UNIVERSITÉ PARIS SUD
Comprendre le monde, construire l'avenir®

Irfu
Institut de recherche sur les lois fondamentales de l'Univers

UNIVERSITÉ PARIS-SUD

Ecole Doctorale : Particules, Noyaux et Cosmos (ED 517)

Institut de Recherche sur les lois Fondamentales de l'Univers (CEA-IRFU)

Discipline : Physique

THÈSE DE DOCTORAT

présentée par

Rémie Hanna

Contributions à une première mesure de la masse du boson W dans le canal électronique auprès du détecteur ATLAS

Soutenue le 29 septembre 2015 devant la commission d'examen composée de :

M.	Reza	ANSARI	président du jury
M.	Maarten	BOONEKAMP	directeur de thèse
M.	Fabio	COSSUTTI	rapporteur
M.	Louis	FAYARD	examinateur
M.	Alessandro	VICINI	examinateur
Mme	Manuella	VINCTER	rapporteur

Abstract

In this document, I present my contributions to a first measurement of the W-mass in the LHC using 4.7 fb^{-1} of 7 TeV data, taken in 2011. I focus on the electron decay channel, $W \to e\nu$. In the first part, I discuss a study regarding the performance of the electromagnetic calorimeter of the ATLAS detector, presenting a novel method to correct the lateral profiles of electron energy deposit, along with various studies of the different Geant4 physics lists versions. In the second part, I introduce the global methodology for the W-mass measurement used in ATLAS, and discuss my contributions in details. I show in a first step the assessment of uncertainties coming from the parton shower modeling in Pythia8, and the optimization of the p_{T}^{ℓ} fitting range in order to reduce the systematic uncertainty. In a second step, I present an elaborate data-driven method for the estimation of the multijet background in the $W \to e\nu$ channel, as well as the corresponding results in terms of event yields and fractions with respect to the signal data. The corresponding uncertainties on the W-mass are also shown. Finally, I show the state of the art of the analysis, by gathering the full breakdown of the uncertainties, in bins of pseudorapidity and average pileup.

Résumé

Dans ce document, je présente mes contributions à une première mesure de la masse du boson W au LHC, exploitant 4.7 fb^{-1} de données à 7 TeV, collectées en 2011. Je me concentre surtout sur le canal électronique, $W \to e\nu$. Dans la première partie, j'aborde des études de performance du calorimètre électromagnétique d'ATLAS, proposant une méthode innovante de correction des profils latéraux de dépôt d'énergie des électrons. Des études de différentes versions de Geant4 sont également abordées. Dans la deuxième partie, je détaille mes contributions après avoir introduit la méthode globale de mesure de la masse du boson W adoptée par ATLAS : je présente dans un premier temps le calcul d'incertitudes systématiques introduites par la modélisation des gerbes de partons dans Pythia8, et une optimisation de l'intervalle d'ajustement en utilisant l'impulsion transverse du lepton, dans le but de réduire les incertitudes correspondantes. Dans un deuxième temps, je présente une estimation de bruit de fond provenant de jets de partons, dans le canal $W \to e\nu$, en développant une méthode basée sur les données, ainsi que les résultats correspondants, en termes de nombre d'événements et de fractions par rapport aux données. Les incertitudes sur la masse du W provenant de cette méthode sont aussi détaillées. Enfin, un état de l'art de l'analyse est montré, en détaillant les incertitudes dans le canal électronique, en fonction de la pseudorapidité et du bruit d'empilement.

Contents

À Vicky

Introduction

The Standard Model of Particle Physics (SM) [1–16] is so far the most predictive theory in fundamental physics. It has successfully and precisely predicted the existence of particles that were later discovered such as the gluon (1978-1979) [17, 18], the W and the Z bosons (1983) [19, 20], the top quark (1995) [21, 22], and lately the Brout-Englert-Higgs (BEH) boson (2012) [23, 24]. These discoveries were achieved with powerful machines and particle accelerators leading to numerous Nobel Prizes and international recognition.

Despite the elegance of the SM, it is far from being the perfect theory. It still has some gaps that haven't been filled yet. Many theoretical and experimental arguments tend to indicate that the SM is an effective model of a more general theory. The main limitations of the SM involve non-exhaustively the following problems. The SM is unable to include the gravitational interaction, described in Einstein's general relativity. This shows that the SM is limited to the Planck scale. The huge difference of scales between the electroweak symmetry breaking scale and the gravitation scale is known as the "hierarchy problem". From the observational point of view, it is assumed that less than 5% of the universe is made of SM particles or "known matter". Almost 26% of the universe is made of unknown matter, called "dark matter", and the remaining 69% are made of an unknown form of energy, the "dark energy". Also, as neutrino oscillations have been measured [25–28], it lead to the conclusion that neutrinos have mass, and the appropriate way to include these masses in the SM remains an open question.

Many other open questions driven by theoretical curiosity and scientific ambition remain, that the SM can't provide answers for. The physics community provides other theories and extensions to the SM in order to try to explain most of these aspects. These extensions include new symmetries, extra-dimensions, ... but no sign of physics beyond the SM has been observed yet, and this topic will not be discussed in this thesis.

All physical parameters that have been predicted by the SM were confirmed and measured by the experiments, however there are many parameters left to be measured with more precision. The Large Hadron Collider (LHC) in general and the ATLAS detector in particular were mainly built to find the Higgs boson, goal achieved in 2012, but also for precision measurements of its properties and other SM parameters, mainly the W boson's mass, a measurement which is the aim of this thesis.

Since its discovery in 1983, the W mass was measured in the Large Electron Positron collider (LEP) [29] and in the TeVatron, a proton-antiproton collider [30], giving the current world average of 80385 ± 15 MeV [31]. The indirect determination of the W mass through an electroweak fit gives an uncertainty of 8 MeV [32], leading to a natural goal at the LHC of reaching an uncertainty less than 10 MeV. This measurement is a challenge for the LHC, due to the inadequate knowledge of parton density functions of the proton, since it is a proton-proton collider. Also,

the large number of interactions per collision makes it more demanding of a well defined analysis strategy. Currently, the analysis is ongoing using the 2011 data at $\sqrt{s} = 7$ TeV, and will also be carried out in a later stage for the 2012 data at $\sqrt{s} = 8$ TeV and for the LHC Run-II data at $\sqrt{s} = 13$ TeV. The studied channels are $W \to e\nu$ and $W \to \mu\nu$ decays.

I present in this thesis my contributions to a first measurement of the W-mass in the LHC using 4.7 fb^{-1} of 7 TeV data, taken in 2011, focusing on the electron decay channel, $W \to e\nu$. In Chapter 1, I introduce the Standard Model and its particles and interactions. The interest of m_W measurement and the W production at LHC are respectively discussed in Sections 1.2 and 1.3. After putting the analysis in context, I talk about the LHC machine and the ATLAS detector in Chapters 2 and 3. In Chapter 4, I propose a shower shape correction method at the electromagnetic calorimeter level, for a perspective on using it in the W mass measurement.

Next, I introduce the global methodology for the W-mass measurement used in ATLAS, in Chapter 5, and discuss my contributions in details in the following chapters. In Chapter 6, a modeling of the boson's transverse momentum is discussed. This observable impacts the lepton p_{T}, directly used in the mass measurement. In this study, Z events are used to model the boson p_{T}, by tuning parton shower parameters in the Pythia [33] generator, and a study of the systematic uncertainties on the W-mass coming from parton showers is detailed. Chapter 7 is were the W signal extraction as well as multijet background assessment are explained. I present an elaborate data-driven method for the estimation of the multijet background in the $W \to e\nu$ channel, as well as the corresponding results in terms of event yields and fractions with respect to the signal data. The corresponding uncertainties on the W-mass are also shown. Finally, I show the results and perspectives in Chapter 8, and gather the full breakdown of the uncertainties, in bins of pseudorapidity and average pileup.

Chapter 1

Standard Model and W Physics at the LHC

1.1 The Standard Model

1.1.1 Parameters of the Standard Model

Four fundamental interactions are found in nature. The Standard Model (SM) was designed to describe in a unified way two of these interactions: the weak and the electromagnetic ones. A third one, the strong interaction, was later added. The fourth fundamental force, gravity, is described in Albert Einstein's theory of general relativity [34], but all attempts to include it in a common framework with the first three have failed so far.

Fundamental particles are classified with respect to the interactions they are sensitive to. Separated into three generations, only the first generation is involved in the ordinary matter. Second and third generation particles are produced in cosmic rays and accelerators.

Matter particles are spin-1/2 fermions, interactions are mediated by spin-1 bosons, also called vector bosons. A spin-0 (scalar) boson, the Brout-Englert-Higgs (BEH) boson, commonly known as the "Higgs boson", is the consequence of the spontaneous symmetry breaking [5–7] discussed later. All the fundamental particles are represented in Table 1.1 and Fig. 1.1. Each fermion has its own antiparticle, with the same mass but opposite charge and quantum number.

The fermions include the leptons (e, μ, τ and their respective neutrinos: ν_e, ν_μ and ν_τ) and the quarks u, d, c, s, t, and b. The vectorial bosons are the Z^0, $W^\pm$, the photon γ and 8 gluons g. These are also called gauge bosons, and they respectively mediate the fundamental forces of the SM: the weak force is carried by the W and Z, the electromagnetic force by the photon, and finally the gluon is the mediator of the strong force. All of these interactions will be presented in this chapter.

Neutrinos interact only via the weak force, while e, μ, τ and quarks interact via the weak and electromagnetic forces. In addition, quarks carry color charge (red, blue or green) and interact via the strong force. They can only be found in bound states called hadrons, having a total color charge of zero. Hadrons are either baryons or mesons, depending on whether they are a bound state of three quarks (like protons and neutrons), or a quark and an anti-quark (like pions and kaons).

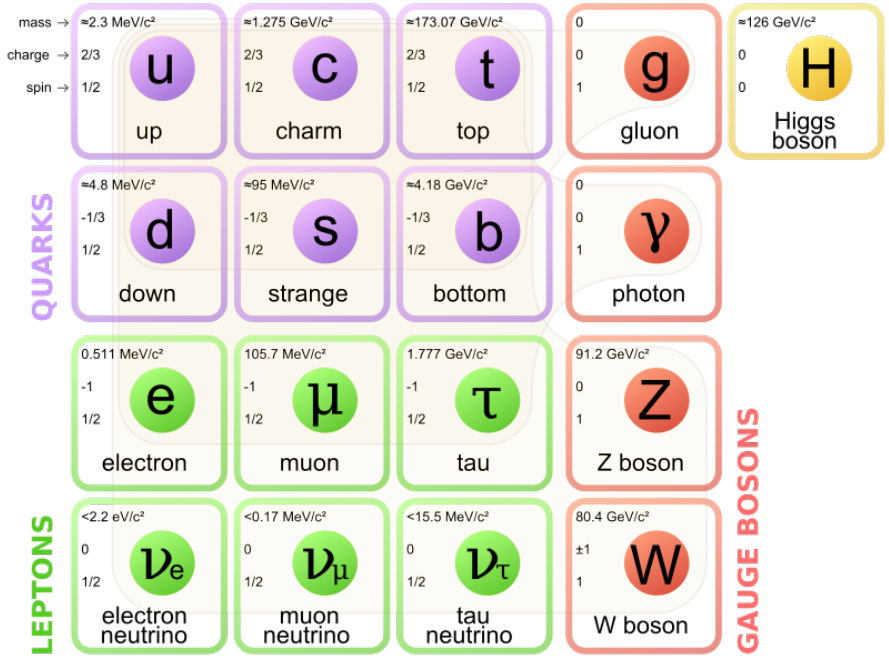

FIGURE 1.1: The Elementary Particles of the Standard Model. This figure shows the leptons in green, the quarks in purple, the gauge bosons in red and the BEH boson in yellow. It shows as well their respective masses, charges and spins [35].

Matter particles: spin$-1/2$ fermions		
	Leptons	Quarks
First Generation	e, ν_e	u, d
Second Generation	μ, ν_μ	c, s
Third Generation	τ, ν_τ	t, b
Force mediators: spin-1 bosons		
Electromagnetic	γ	
Strong	8 gluons	
Weak	W^+, W^-, Z	
Brout-Englert-Higgs: spin-0 boson		

TABLE 1.1: Particles of the Standard Model.

These quarks, defining the quantum number of the hadron, are called "valence quarks". In addition, part of a hadron's momentum is carried by virtual quark-antiquark pairs, called "sea quarks", and gluons. The structure of the hadron (valence and sea quarks, and gluons), is probed at high energy and in particular in the proton-proton collisions in the Large Hadron Collider (LHC).

The SM has 18 free parameters, and any physical observable can be calculated using these parameters:

- 9 fermion masses: m_e, m_μ, m_τ and $m_u, m_d, m_s, m_c, m_b, m_t$.
- 4 CKM parameters: 3 mixing angles θ_{12}, θ_{13} and θ_{23} and the phase parameter δ_{13} determining how quarks of various flavor can mix when they interact. The CKM (Cabibbo-Kobayashi-Maskawa) matrix [36, 37] is a 3×3 unitary matrix, the eigenstates of which mix to form the quark doublets $\{u, d\}$, $\{c, s\}$ and $\{t, b\}$.

- the fine structure constant α, which defines the electromagnetism coupling strength g'
- the Weinberg angle θ_W which relates the electromagnetism coupling constant g' to that of the weak interaction g: $\tan\theta_W = g'/g$
- the strong coupling constant g_s also noted α_S
- the electroweak symmetry breaking energy scale or vacuum expectation value v
- the Higgs self-interacting coefficient λ or alternatively, the Higgs mass m_H

1.1.2 The Standard Model as a Quantum Field Theory

In the formal context, the SM describes all known elementary particles as excited states of the underlying quantum fields. It is written in terms of Lagrangian densities, as a function of quantum fields and their derivatives, and is based on symmetry identifications. Noether's theorem [38] implies that each continuous symmetry results in an associated conservation law. As a consequence, from the symmetry of a system one can predict its dynamics.

Examples of symmetries are the space-time ones such as rotation and translation. Another one is the Poincaré symmetry which is the full symmetry of special relativity and results in the conservation of the 4-momentum. These are global symmetries, *i.e.* do not depend on the position in the space-time.

Unlike global ones, local symmetries are respected locally, they are internal to the studied system, and are the base of the SM. In 1929, Weyl claimed [39] that the electromagnetism can be based on the $U(1)_{EM}$ group. He proclaimed the invariance (already introduced by Fockin 1926) as a general principle and called it "gauge invariance". The gauge symmetries play a major role in the description of the elementary particles and their interactions. Dirac based his studies on this, and later Yang and Mills came up with a more general theory in 1954 based on groups larger than $U(1)$ [1]. They started the present era of non-abelian gauge theories.

These theories gave the Glashow-Weinberg-Salam's theory of electroweak interactions based on a $SU(2)_L \otimes U(1)_Y$ gauge group, combining the electromagnetic and the weak nuclear force into a single model, and the quantum chromodynamic theory [40, 41], based on a $SU(3)_C$ gauge group. The creation of a non-abelian EW theory by Glashow, Weinberg and Salam in the 1960s [11–13] as well as the developments by 't Hooft and Veltman [16] concerning the renormalization was a huge step forward in the gauge theories: the introduction of a gauge invariance into the theory makes the SM a renormalizable quantum field theory, in a way that the theory is computable in terms of a finite number of parameters such as particles masses and coupling constants [42].

The SM is therefore a non-abelian gauge theory based on the symmetry group $SU(3)_C \otimes SU(2)_L \otimes U(1)_Y$: $SU(3)_C$ generates 8 massless gluons carrying the strong nuclear force, C stands for "Color", and the theory describing the strong interaction is the Quantum Chromodynamics (QCD). $SU(2)_L$ generates W bosons responsible for the weak charged currents (L for "Left-handed"), while the linear combination of neutral bosons from $SU(2)_L$ and $U(1)_Y$ produces Z bosons and photons, which mediate respectively the weak neutral currents and the electromagnetic force (Y for "Hypercharge" satisfying the equation $Y = 2(Q - T_3)$, where Q is the electrical charge and T_3 is the third component of weak isospin).

Given that the SM is renormalizable to all orders in perturbation theory, the result of a calculation is a clear prediction of the model. Once all the parameters fixed, the Lagrangian allows to

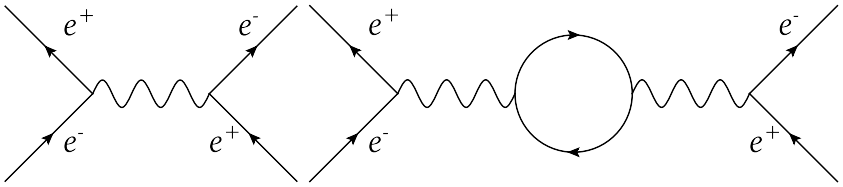

(a) Electron-positron annihilation at leading order.

(b) Electron-positron annihilation at next-to-leading order. Here the electron or the positron emits and reabsorbs a photon.

FIGURE 1.2: Examples of Feynman diagram representations of an electron-positron annihilation at tree-level (1.2(a)) and at next-to-leading order (1.2(b)) .

compute amplitudes for scattering processes and decay rates, using perturbation expansions on power of the coupling constants.

One way to write the SM Lagrangian is:

$$\mathcal{L} = \mathcal{L}_{\text{EW}} + \mathcal{L}_{\text{QCD}}, \text{ where } \mathcal{L}_{\text{EW}} = \mathcal{L}_{\text{gauge bosons}} + \mathcal{L}_{\text{fermions}} + \mathcal{L}_{\varphi} + \mathcal{L}_{\text{Yukawa}} \tag{1.1}$$

The first term, $\mathcal{L}_{\text{EW}}$ represents the $SU(2)_L \otimes U(1)_Y$ electroweak group. It comprises the gauge bosons $W^{\pm}, Z, \gamma$ interactions in $\mathcal{L}_{\text{gauge bosons}}$, the fermion term $\mathcal{L}_{\text{fermions}}$ describing interactions between quarks and leptons, the Higgs sector term $\mathcal{L}_{\varphi}$, and finally $\mathcal{L}_{\text{Yukawa}}$ which describes the Yukawa couplings between single Higgs doublet and various flavors of quarks and leptons. The last term, $\mathcal{L}_{\text{QCD}}$ represents the $SU(3)_C$ group.

The various components of the SM Lagrangian can be directly represented by components of Feynman diagrams (e.g. Fig. 1.2). By using these diagrams, one may compute amplitudes for any interaction process. At higher than the leading order (tree-level), the diagrams contain loops with infinite amplitudes (Fig. 1.2(b)), absorbed by renormalization.

1.1.3 Quantum Chromodynamics

QCD is the theory of strong interactions. It is a non-abelian gauge theory with symmetry group $SU(3)$. An $SU(3)$ group has 8 generators T_a, associated to gauge fields G_μ corresponding to 8 gluons, massless gauge bosons, which carry a quantum number called color charge and can therefore interact with other gluons. Each quark q of given flavor exists in three colors: red (r), green (g) and blue (b). The three color states can be put in a triplet:

$$\begin{pmatrix} q_r \\ q_g \\ q_b \end{pmatrix} \tag{1.2}$$

The QCD Lagrangian is written as:

$$\mathcal{L}_{QCD} = -\frac{1}{4} F^a_{\mu\nu} F^{\mu\nu}_a + \sum_k [i\overline{\psi}_k \gamma^\mu (\partial_\mu - m)\psi + g_s \overline{\psi}_k \gamma^\mu T_a G^a_\mu \psi] \tag{1.3}$$

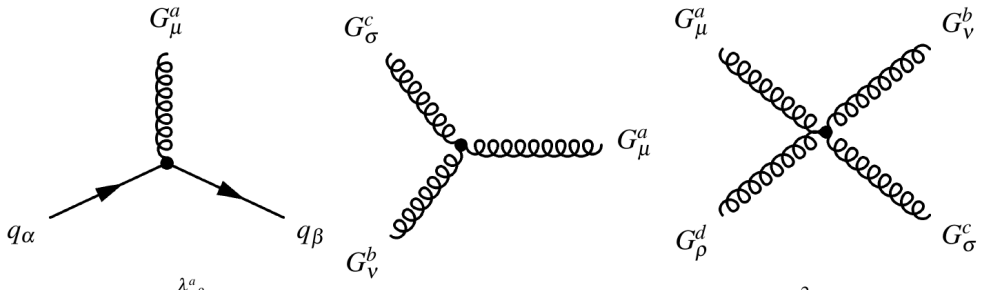

(a) $g_s \frac{\lambda^a_{\alpha\beta}}{2}$ (b) $g_s f_{abc}$ (c) $g_s^2 f_{mab} f_{mcd}$

FIGURE 1.3: The vertices of the strong interaction. q_α and q_β are quark fields, where $\alpha, \beta = r, g, b$. $\lambda^a, a = 1, 2, \ldots, 8$ are the Gell-Mann's matrices, f_{abc} are constant structures and g_s is the strong coupling constant [43].

where $F^a_{\mu\nu}$ is the gluon field tensor, m is the quark mass, G^a_μ are the gluon fields, T_a are the $SU(3)$ generators and g_s is the strong coupling constant, which is universal for all quark flavors. The sum in the second term is done over all the fermions k with color charge, i.e. quarks. The spinor ψ has three components, and a runs over the number of dimensions giving rise to the 8 gluons. This Lagrangian is invariant under $SU(3)$, where the conserved quantum number is the color charge.

The fundamental vertices describing the strong interaction are shown in Fig. 1.3.

In Eq. 1.3, the first term describes the gluon self interaction, while the second term represents the interaction between quarks and gluons with a strength proportional to the strong coupling constant g_s.

One way to write the coupling constant is through the running coupling constant $\alpha_S = g_s^2/4\pi$, given by:

$$\alpha_S(Q^2) = \frac{12\pi}{(11n_c - 2n_f)\log(Q^2/\Lambda^2_{QCD})} \tag{1.4}$$

where Q is the energy transfer, $n_c = 3$ is the number of colors, $n_f = 6$ is the number of quarks, and $\Lambda_{QCD} \approx 200$ MeV is the QCD scale. Fig. 1.4 shows the dependence of α_S on Q.

As a consequence of Eq. 1.4, QCD has two properties:

- **Confinement**, which means that quarks are always found as bound states of hadrons: the force between quarks does not decrease as they are separated. Because of this, when quarks are separated from other quarks, the energy in the gluon field is enough to create another quark pair. This is a consequence of Eq.1.4 as when $Q^2 \to \Lambda^2_{QCD}$, $\alpha_S(Q^2) \to \infty$. In this case, the theory is non-perturbative, and the computations at high orders of α_S is problematic. An approach is proposed to solve this problem, called Lattice QCD.
- **Asymptotic freedom**, which means that at high energies, quarks and gluons almost appear as free particles, creating a quark–gluon plasma. This prediction of QCD was first discovered in 1973 by David Politzer [41], Frank Wilczek and David Gross [44, 45], who were awarded the 2004 Nobel Prize in Physics. In terms of Eq. 1.4, this is the case where $\alpha_S(Q^2) \to 0$ when $Q^2 \to \infty$. In this case, the theory is renormalizable and α_S depends on an energy scale called renormalization scale, μ_R.

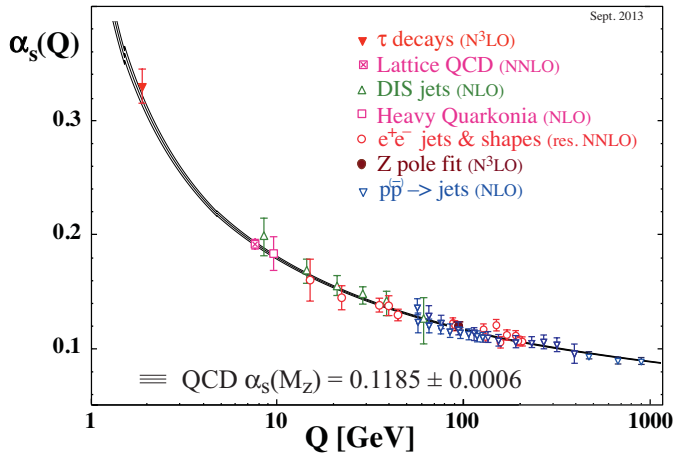

FIGURE 1.4: Summary of measurements of α_S as a function of the energy scale Q [31].

1.1.4 Quantum Electrodynamics

The electromagnetic interaction is described by the Abelian gauge theory Quantum Electrodynamics (QED), based on the $U(1)$ symmetry group. In this theory, fermions and electromagnetic fields interact with each other. Fermions dynamics are described in the Dirac Lagrangian:

$$\mathcal{L}_D = \overline{\psi}(i\partial\!\!\!/ - m)\psi \tag{1.5}$$

where m is the fermion mass, $\partial\!\!\!/ = \gamma^\mu \partial_\mu$, γ^μ are Dirac matrices and ψ are Weyl spinors representing the fermionic field. The interactions between these fermions happen through the exchange of vector bosons, associated to a field A_μ. The Lagrangian describing the vector boson dynamics is the Maxwell Lagrangian:

$$\mathcal{L}_{\text{Maxwell}} = -\frac{1}{4} F_{\mu\nu} F^{\mu\nu} \tag{1.6}$$

where $F_{\mu\nu} = \partial_\mu A_\nu - \partial_\nu A_\mu$. Adding the field A_μ introduces, besides the Lagrangian in Eq. 1.6, an interaction term written in terms of $\overline{\psi}\gamma^\mu \psi A_\mu$. With q being the charge of the fermion, the total QED Lagrangian is written as:

$$\mathcal{L}_{\text{QED}} = \overline{\psi}(i\partial\!\!\!/ - m)\psi + q\overline{\psi}\gamma^\mu \psi A_\mu - \frac{1}{4} F_{\mu\nu} F^{\mu\nu} \tag{1.7}$$

The gauge field A_μ is associated to the electromagnetic force carrier, the photon. A bosonic mass term of the form $\frac{1}{2}\mu_\gamma^2 A^\mu A_\mu$ in the Lagrangian would break the local gauge invariance. The mass of the photon is therefore $\mu_\gamma = 0$, and the interaction range is infinite.

Fig. 1.5 illustrates the electromagnetic interaction. The coupling constant, α, is a running parameter, which is approximately equal to 1/137 at zero momentum transfer, as a first approximation (fine structure constant).

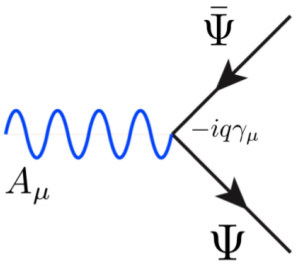

FIGURE 1.5: QED vertex, coupling a fermion (Ψ)-antifermion ($\overline{\Psi}$) pair to a photon A_μ [46].

1.1.5 Electroweak interactions

Weak interactions occur between charged and neutral fermions, and are manifested through phenomena like beta decays and decays of charged pions. They involve both neutral and charged currents, carried by the neutral Z boson and the charged $W^\pm$ bosons. Charged currents are responsible for the flavor transition between up-type and down-type quarks, or leptons, and neutral currents conserve the flavor. The weak interactions only act on left-handed particles and right-handed antiparticles.

Together with the electromagnetic interactions, they are described in a single framework, the electroweak theory, based on the gauge symmetry group $SU(2)_L \otimes U(1)_Y$. The $U(1)$ symmetry here does not exactly correspond to the electromagnetic interaction but its parameter Y, the hypercharge, is connected to the electric charge Q through the relation evoked previously: $Y = 2(Q - T_3)$, involving also the charge associated with $SU(2)$, called weak isospin T_3. This $SU(2)_L \otimes U(1)_Y$ requires the Z and W bosons to be massless, and the $U(1)_{EM}$ symmetry reappears after the spontaneous symmetry breaking of $SU(2)_L \otimes U(1)_Y$ (cf. § 1.1.6).

The three generators of the $SU(2)_L$ group give rise to three gauge bosons, $W_\mu^{1,2,3}$, with a coupling strength g. The generator of $U(1)_Y$ corresponds to another gauge boson B_μ, with coupling g'. The Lagrangian of the electroweak theory is written as:

$$\mathcal{L}_{EW} = i\overline{\psi}_j \gamma^\mu D_\mu \psi_j - \frac{1}{4} W^a_{\mu\nu} W_a^{\mu\nu} - \frac{1}{4} B^{\mu\nu} B_{\mu\nu} \tag{1.8}$$

where the covariant derivative D_μ is equivalent to:

$$D_\mu \psi_j = \left[\partial_\mu - ig \frac{\sigma_a}{2} W^a_\mu - ig' \frac{Y_j}{2} B_\mu \right] \psi_j \tag{1.9}$$

$g(g')$ is the weak (electromagnetic) coupling constant, Y_j the hypercharge, σ_a the Pauli matrices. Also:

$$W^a_{\mu\nu} = \partial_\mu W^a_\nu - \partial_\nu W^a_\mu + g\epsilon^{abc} W_{b\mu} W_{c\nu} \tag{1.10}$$

$$B_{\mu\nu} = \partial_\mu B_\nu - \partial_\nu B_\mu \tag{1.11}$$

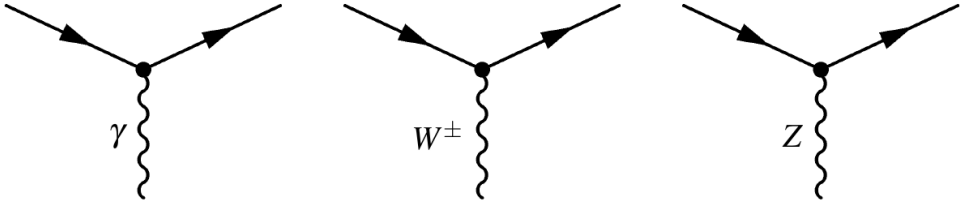

FIGURE 1.6: Electroweak vertices, where fermions couple to a photon γ (left), $W^{\pm}$ (middle) and Z (right) [43].

The $W_{\mu}^{1,2,3}$ and B_{μ} bosons evoked previously are not physical particles, but their linear combinations represent the four gauge bosons *i.e.* the photon, the Z and the $W^{\pm}$ bosons, as the following (θ_W being the weak mixing angle, such that $m_W/m_Z = \cos\theta_W$):

$$A_{\mu} = B_{\mu}\cos\theta_W + W_{\mu}^3 \sin\theta_W \tag{1.12}$$

$$Z_{\mu} = -B_{\mu}\sin\theta_W + W_{\mu}^3 \cos\theta_W \tag{1.13}$$

$$W_{\mu}^{\pm} = \frac{1}{\sqrt{2}}(W_{\mu}^1 \mp iW_{\mu}^2) \tag{1.14}$$

The basic vertices in the electroweak theory are depicted in Fig 1.6.

To preserve QED interactions we must have $g\sin\theta_W = g'\cos\theta_W = e$, known as the electroweak unification condition, e being the charge of the positron.

1.1.6 Electroweak spontaneous symmetry breaking

Bosonic and fermionic mass terms put into the Lagrangian of Eq. 1.8 would break the local gauge invariance. However, the W and Z bosons and the quarks and leptons masses have been measured and found to be non-zero. This problem is solved by introducing the Brout-Englert-Higgs mechanism [5–7]: when a gauge theory is combined with an additional field φ that spontaneously breaks the symmetry, the bosons can consistently acquire a finite mass, and a new particle is introduced, the BEH boson, as the excitation of this scalar field. The EW symmetry is spontaneously broken into the electromagnetic $U(1)_{EM}$ with the introduction of φ.

The idea is to introduce a Higgs doublet allowing to write a potential term with a degenerate ground state. One of these ground states is chosen as the vacuum expectation value (*vev*, denoted v) of the neutral component of the Higgs field. After symmetry breaking, the photon remains massless while the W and Z acquire masses as predicted by the theory given some experimental input. The mass of the W is written as $m_W = vg/2$ and the mass of the Z is $m_Z = v\sqrt{g^2 + g'^2}/2$, g and g' are the weak and electromagnetic coupling constants.

The Higgs field also gives mass to the fermions by Yukawa interactions with the fermion fields. The $U(1)$ and $SU(3)$ symmetries remain unbroken, and therefore their carriers, photons and gluons, remain massless.

W^+ decay modes	Fraction (%)
$e^+\nu_e$	10.71 ± 0.16
$\mu^+\nu_\mu$	10.63 ± 0.15
$\tau^+\nu_\tau$	11.38 ± 0.21
hadrons	67.41 ± 0.27

TABLE 1.2: Main W^+ decay modes. W^- modes are their charge conjugates [31].

With the Higgs discovery in 2012 [23, 24], the SM was proven to be valid at the TeV scale, although it is widely considered as an effective theory of a yet undetermined more general theory.

1.2 W-mass measurement

It is of a great importance to precisely measure the W-mass to test the internal consistency of the Standard Model. A strong test of the consistency of the SM is possible by combining this measurement with other electroweak measurements. Together with the Z-boson mass, m_W sets the energy scale of electroweak symmetry breaking. In this section, the interest and motivation behind the measurement of this mass is discussed in § 1.2.1, and previous measurements and current results are presented in § 1.2.2.

1.2.1 Motivation and interest of the W-mass measurement

The uncertainty on the W mass is related to its short lifetime ($\tau \approx 3 \times 10^{-25}$ s), the mass measurement in particle colliders being performed using the decay products of the W. The main decay channels of the W boson are listed in Table 1.2.

The main motivation behind the need of a high precision in the W-mass measurement is its importance in the consistency test of the SM, through the simultaneous indirect determination of the top mass m_t and the W-mass m_W. When combined with a precise measurement of the top mass, the W-mass measurement can provide critical information on the validity of the SM, or in case of disagreement with the theory, it can indicate the presence of new physics. This aspect is seen in Fig. 1.7, which shows a scan of the confidence level (CL) profile of m_W versus m_t, for the cases where the direct m_H measurement is included in the fit (blue) or not (grey). These contours agree with the direct measurement in green, demonstrating the consistency of the SM, but a small change in the W-mass precision could compromise this agreement and indicate the presence of new physics.

The best measurement of the W-mass is so far 80.387 ± 0.016 GeV, based on TeVatron data [30], yielding the current world average of 80.385 ± 0.015 GeV [31]. The indirect determination of the W-mass, 80.363 ± 0.020 GeV [29], using Z-pole data and m_t measurements, is in agreement with the measured value.

The correlation between W, top quark and Higgs masses are depicted in Fig. 1.8. The dependence of m_W on m_t and m_H is through loop diagrams of top (bottom) quarks and Higgs respectively.

Eq. 1.15 relates, at tree-level (first order), m_W to the fine structure constant $\alpha = e^2/4\pi$, the Fermi constant G_F and the Z mass through the Weinberg angle θ_W, since $m_W/m_Z = \cos\theta_W$.

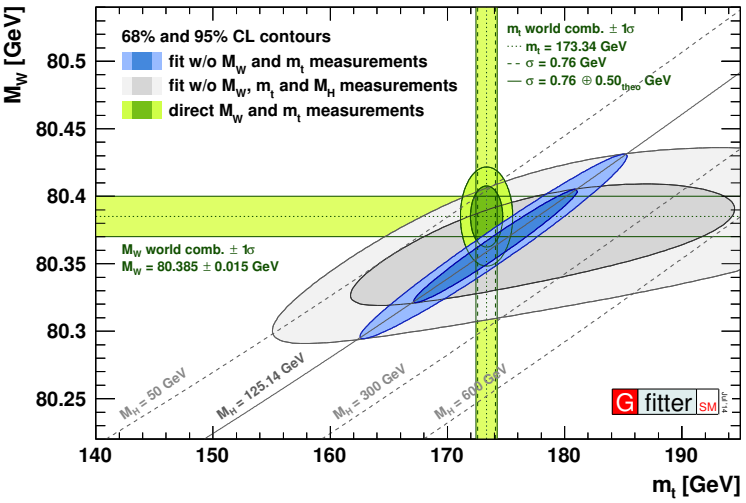

FIGURE 1.7: Contours at 68% and 95% CL obtained from scans of m_W versus the top quark mass, m_t, for the fit including the Higgs mass, m_H,(blue) and excluding m_H (grey), as compared to the direct measurements (vertical and horizontal green bands and ellipses). The theoretical uncertainty of 0.5 GeV is added to the direct top mass measurement. The corresponding direct measurements are excluded from the fit. [32]

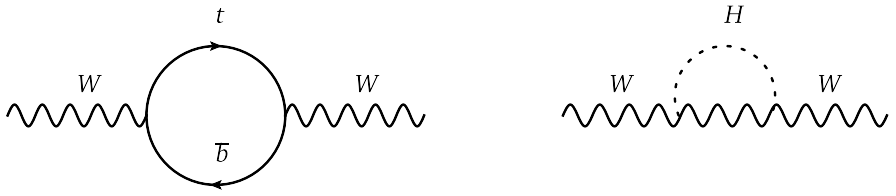

FIGURE 1.8: Lowest order radiative corrections to the W mass involving top and bottom quarks (left) and the Higgs (right).

$$m_W = \sqrt{\frac{\pi\alpha}{\sqrt{2}G_F}}\frac{1}{\sin\theta_W} \tag{1.15}$$

Eq. 1.15 sets a limit on the allowed value of the W mass: since $\sin\theta_W < 1$, we have $m_W > \sqrt{\frac{\pi\alpha}{\sqrt{2}G_F}} \approx 40$ GeV, which is well in agreement with the measurements. If we include higher order corrections as in Fig. 1.8, Eq. 1.15 becomes:

$$m_W = \sqrt{\frac{\pi\alpha}{\sqrt{2}G_F}}\frac{1}{\sin\theta_W\sqrt{1-\Delta r}} \tag{1.16}$$

Here Δr represents the radiative corrections intervening in the diagrams of Fig. 1.8.

1.2.2 Overview of W mass measurements at LEP and TeVatron

Many experiments have measured the W mass since its discovery in 1983, with the goal of improving the precision as much as possible. Currently, the precision on m_W is approximately 0.18‰, almost ten times worse than the 0.02‰ precision on the Z mass. In this paragraph I will focus on the LEP (e^+e^- collider) and the TeVatron ($p\bar{p}$ collider) measurements.

Source	Uncertainty (MeV)
LEP center of mass energy	9
ISR/FSR	7
Hadronization	14
Detector effects	9
Color reconnection	8
Bose-Einstein correlations	2
Others	3
Statistics	25
Total	34

TABLE 1.3: Uncertainties on the W mass for the combined LEP measurements. The numbers don't include information from cross-section measurements [29].

Source	Uncertainty (MeV)
Lepton energy scale and resolution	7
Recoil energy scale and resolution	6
Lepton removal	2
Backgrounds	3
Experimental subtotal	10
$p_T(W)$ model	5
Parton distribution functions	10
QED radiation	4
Production subtotal	12
Total systematics	15
W-boson statistics	12
Total	19

TABLE 1.4: Uncertainties for the final combined result on m_W from the CDF experiment [30].

At e^+e^- colliders, the Ws are produced in W^+W^- pairs to conserve the electric charge. The beam energy being precisely known, it is possible to determine the $e^+e^- \rightarrow W^+W^-$ cross-section as a function of the center of mass energy. On the other hand, the longitudinal momentum being known, the full 3-vector of the neutrino can be reconstructed. These two properties of the e^+e^- collider allows to measure the W mass by taking advantage of the large dependence of the W-pair production cross-section on the W-mass at the center of mass energy of 161 GeV, which is just above the pair production threshold (as it corresponds to twice the W mass), and also at higher energies through the full kinematic reconstruction of its decay products.

At LEP, the main uncertainties are summarized in Table 1.3. The combination of all the experiments measurements gave an average of 80.376 ± 0.033 GeV, shown in the top part of Fig. 1.9.

In the $p\bar{p}$ colliders, the W bosons are produced from the quarks inside the protons. Unlike e^+e^- colliders, the longitudinal momentum of the W is unknown and quantities transverse to the beam direction are used for the mass measurement. At the TeVatron, W production is dominated by $q\bar{q}' \rightarrow W + X$ where X is initial state QCD radiation. $W \rightarrow e\nu$ and $W \rightarrow \mu\nu$ decay modes are studied in CDF experiment, while the DØ experiment only studies $W \rightarrow e\nu$ channel.

Source	Uncertainty (MeV)
Electron energy calibration	16
Electron resolution model	2
Electron shower modeling	4
Electron energy loss model	4
Recoil energy scale and resolution	5
Electron efficiencies	2
Backgrounds	2
Experimental subtotal	18
Parton distribution functions	11
QED radiation	7
$p_T(W)$ model	2
Production subtotal	13
Total systematic uncertainty	22
W-boson statistics	13
Total uncertainty	26

TABLE 1.5: Uncertainties of the D0 m_W measurement determined from the combination of m_{T} and p_{T}^e [30].

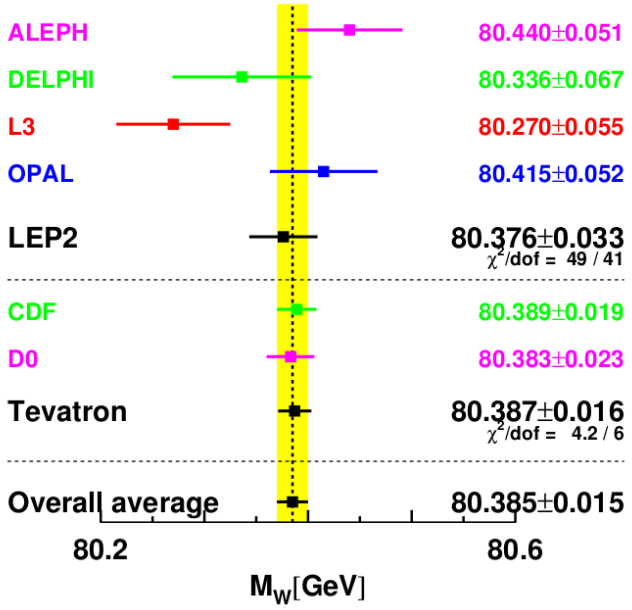

FIGURE 1.9: Measurements of the W-boson mass by the LEP and TeVatron experiments. [31]

In 2012, the CDF and DØ experiments have presented their measurements of the W mass as 80.387 ± 0.019 GeV [47] and 80.375 ± 0.023 GeV [48], respectively. The uncertainties on the measurement are presented in Table 1.4 for CDF and 1.5 for DØ. In the DØ table, the total uncertainty is 26 MeV, as the measurement leading to this result did not include the earlier DØ result from the first TeVatron run [49]. The bottom part of Fig. 1.9 shows the TeVatron results and their combination 80.387 ± 0.016 GeV. The combined world average, assuming no common systematic uncertainties between the LEP and the TeVatron measurements, is currently 80.385 ± 0.015 GeV.

1.3 W and Z production at the LHC in the context of the strong sector

1.3.1 Proton-proton collisions

Protons are composed of two quarks u and one quark d, called *valence quarks*. The gluons interchanged between these quarks can split forming virtual quark-antiquark pairs, called *sea quarks*. A proton-proton collision can be either elastic or inelastic. In the first case, the protons are not dissociated, and a small amount of momentum is transferred. In the second case, at least one of the protons dissociate. The inelastic scattering can be soft or hard, with the QCD being the underlying theory for both processes.

In soft scattering events, one or two protons dissociate into a system of particles with low transverse momentum. They are dominant processes at the LHC and include diffraction, Multiple-Partonic Interactions (MPI), soft initial- and final-state radiation (ISR/FSR), and beam-beam remnants. These phenomena are grouped according to experimental trigger. For example, minimum bias interactions are the processes that are selected with a loose trigger intended to select inelastic collisions with as little bias as possible. The Underlying Event (UE) is the collection of all the soft processes that accompany a high-transverse momentum interaction of interest. It is typically studied as a function of the highest-transverse momentum particle in the event. On the other hand, in the hard scattering events, like Drell-Yan processes, Higgs production, *etc.*, high transverse momentum particles are produced. The rates and properties for the hard processes can be predicted with good precision using the perturbation theory, due to the asymptotic freedom property where quarks interact as free particles at large energy scales.

Soft processes are dominated by non-perturbative QCD effects, which are less well understood. Even though W and Z production are considered hard processes, they are usually accompanied by underlying events. An understanding of this soft physics is interesting in its own right but is also essential for precision measurements of hard interactions.

The structure of the proton is described by the parton distribution functions (PDFs), $f_q(x, Q^2)$, which represent the probability to extract a parton of a given flavor q with a fraction x -also called Bjorken-x- of the proton momentum. This proton structure depends on the energy scale Q at which the proton is probed. The DGLAP [50] equations predict the evolution of the PDF as a function of Q^2. However, the PDFs themselves cannot be calculated, but are determined from fits to experimental data. Several PDF sets are calculated by collaborations such as CTEQ, MSTW (MMHT), and NNPDF.

Usually the valence quarks, u and d, carry the large part of the momentum, while gluons dominate the region of small x. Gluon contributions become more important as Q^2 increases. All these properties are shown in Fig. 1.10, taken from Ref. [51] for the CT10NNLO PDFs.

The impact of valence contribution in the lepton transverse momentum distribution in a $W \to \ell\nu$ decay is shown in Figure 1.11. In this figure, the natural distribution is compared to the one obtained in the hypothetical case where valence quark contributions to the PDF are excluded.

Fig. 1.12 suggests a schematic description of a proton-proton collision, where hard scattering events involve some soft interactions as well.

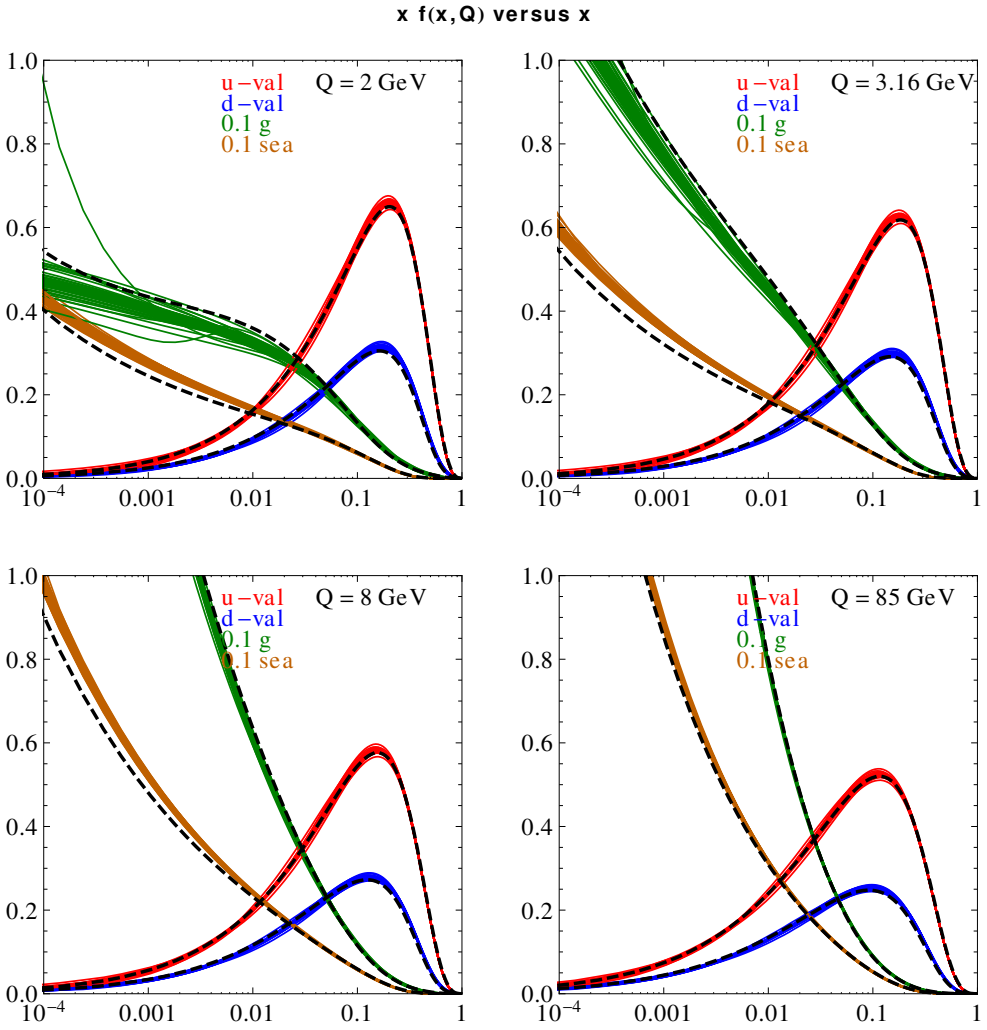

FIGURE 1.10: CT10 parton distribution functions at next-to-next-to-leading order (NNLO). Each graph shows the PDFs of the valence u and d quarks, as well as of the gluons and sea quarks as functions of x, for a fixed value of Q. The values of Q are 2, 3.16, 8 and 85 GeV [51].

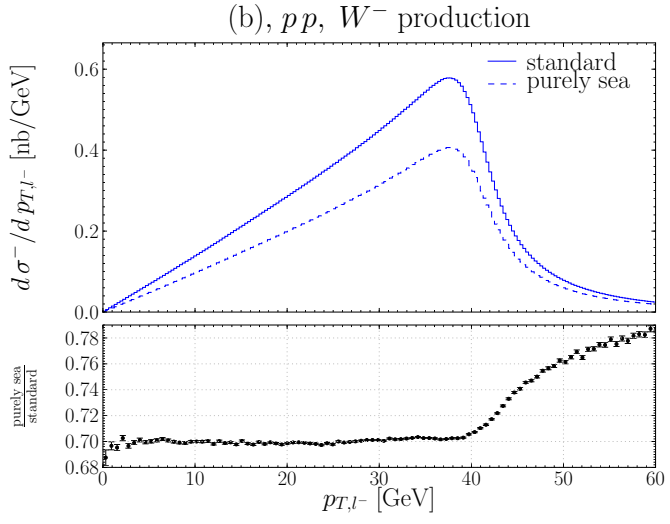

FIGURE 1.11: Lepton transverse momentum distributions in W^- decays, with and without valence contributions [52].

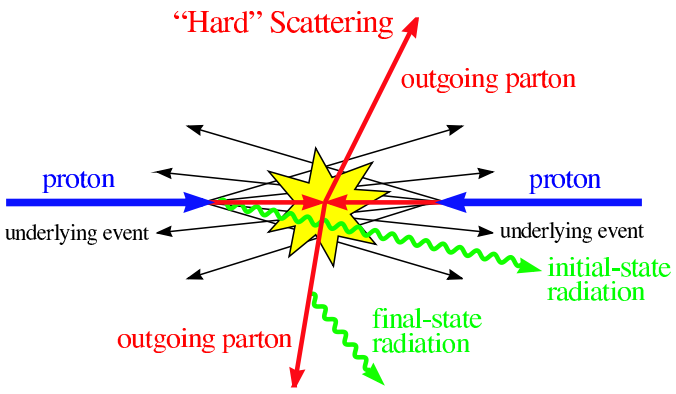

FIGURE 1.12: Schematic diagram of a proton-proton collision [53].

1.3.2 The QCD factorization theorem

The QCD factorization theorem introduced by Drell and Yan can be used to calculate a wide variety of hard scattering cross sections in hadron-hadron collisions [54]. It implies that the cross section of a hard-scattering $pp \to X$ in proton-proton collisions can be factorized into two contributions: one corresponding to the cross section of the parton interaction (Hard Scattering) and one representing the momentum distribution of the partons inside the incoming protons, the PDFs. In other terms, the hadronic cross-section $\sigma_{pp\to X}$ could be obtained by weighting the sub-process cross-section $\hat{\sigma}_{q\bar{q}\to X}$ with the parton distribution functions (PDF) $f_{a/A}$ extracted from deep inelastic scattering (DIS), which is a hard scattering event.

The cross section $\sigma_{pp\to X}$ in the leading logarithm approximation can therefore be written as:

$$\sigma_{pp\to X} = \sigma_{HS} \otimes PDF = \sum_q \int dx_1 dx_2 f_{a/A}(x_1, Q^2) f_{b/B}(x_2, Q^2) \otimes \hat{\sigma}_{q\bar{q}\to X} \tag{1.17}$$

where A and B are the protons, $X = \ell^+\ell^-$ and $ab = q\bar{q}, \bar{q}q$ for the Drell-Yan process illustrated in Fig. 1.13 and Fig. 1.17. Q^2 is the momentum scale that characterizes the hard scattering. x_1 and x_2 are the momentum fractions of the protons carried by the partons q and $\bar{q}$ respectively, and $f_{a/A}$ and $f_{b/B}$ are the momentum fraction distributions of a and b, respectively. Eq. 1.17 is diagrammatically depicted in Fig. 1.14. It can also be rewritten as:

$$\sigma_{pp\to X} = \sum_q \int dx_1 dx_2 f_{a/A}(x_1, \mu_F) f_{b/B}(x_2, \mu_F) \otimes \hat{\sigma}(\mu_F, \mu_R)_{q\bar{q}\to X} \tag{1.18}$$

where μ_F is the factorization scale, which separates short (parton level) and long (hadron level) distance physics, and is usually taken as the mass of the outgoing system of particles, and μ_R is the renormalization scale which defines the QCD running coupling $\alpha_S(Q)$ (cf. Eq. 1.4) and the renormalization. $\hat{\sigma}(\mu_F, \mu_R)_{q\bar{q}\to X}$ depends on both of these scales. The convention is to take μ_F and μ_R to be of the same order as the typical momentum transfer in the hard scattering process, *e.g.* the mass of the Z boson.

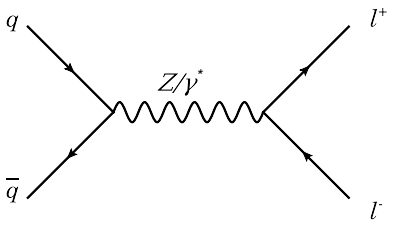

FIGURE 1.13: Feynman diagram representing the basic Drell-Yan process, where a quark from one hadron and an antiquark from another annihilate, creating a virtual photon or Z boson which then decays into a pair of oppositely-charged leptons.

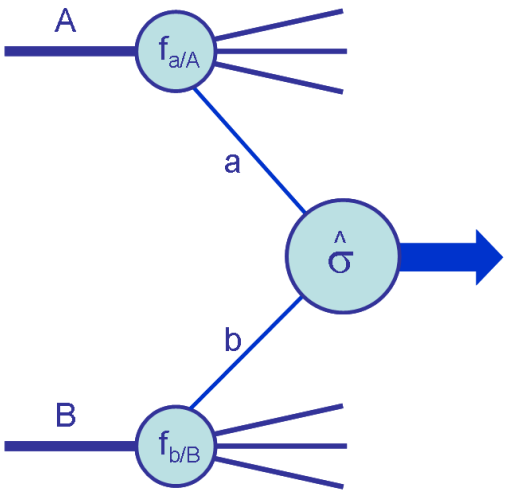

FIGURE 1.14: Diagrammatic structure of a generic hard scattering process [53].

At high energies, the strong coupling constant is such that $\alpha_S << 1$, and the perturbation theory can be applied. The partonic cross sections are thus expressed as a power series expansion of α_S:

$$\hat{\sigma}_{pp\to X} = \hat{\sigma}_0 + \alpha_S\hat{\sigma}_1 + \alpha_S^2\hat{\sigma}_1 + O(\alpha_S^3) \tag{1.19}$$

where the first contribution ($\hat{\sigma}_0$) represents calculations at Leading Order (LO), the second one represents the Next-to-Leading Order (NLO) and the the third contribution refers to Next-to-Next-to-Leading Order (NNLO) calculations.

Fig. 1.15 presents the different cross-sections of the main SM processes involved in the LHC (pp collider) and TeVatron ($p\bar{p}$ collider), calculated at next-to-leading order (NLO) in perturbation theory, *i.e.* including also the $\hat{\sigma}_1$ term in 1.19. One of the benefits of performing a calculation to higher order in perturbation theory is the reduction of the dependence of related predictions on the unphysical renormalization (μ_R) and factorization (μ_F) scales.

1.3.3 W and Z production

In proton-proton collisions, at leading order, the W is produced after the annihilation of a quark q and an anti-quark $\bar{q'}$ from the sea. The quark composition of the proton (uud) makes it more

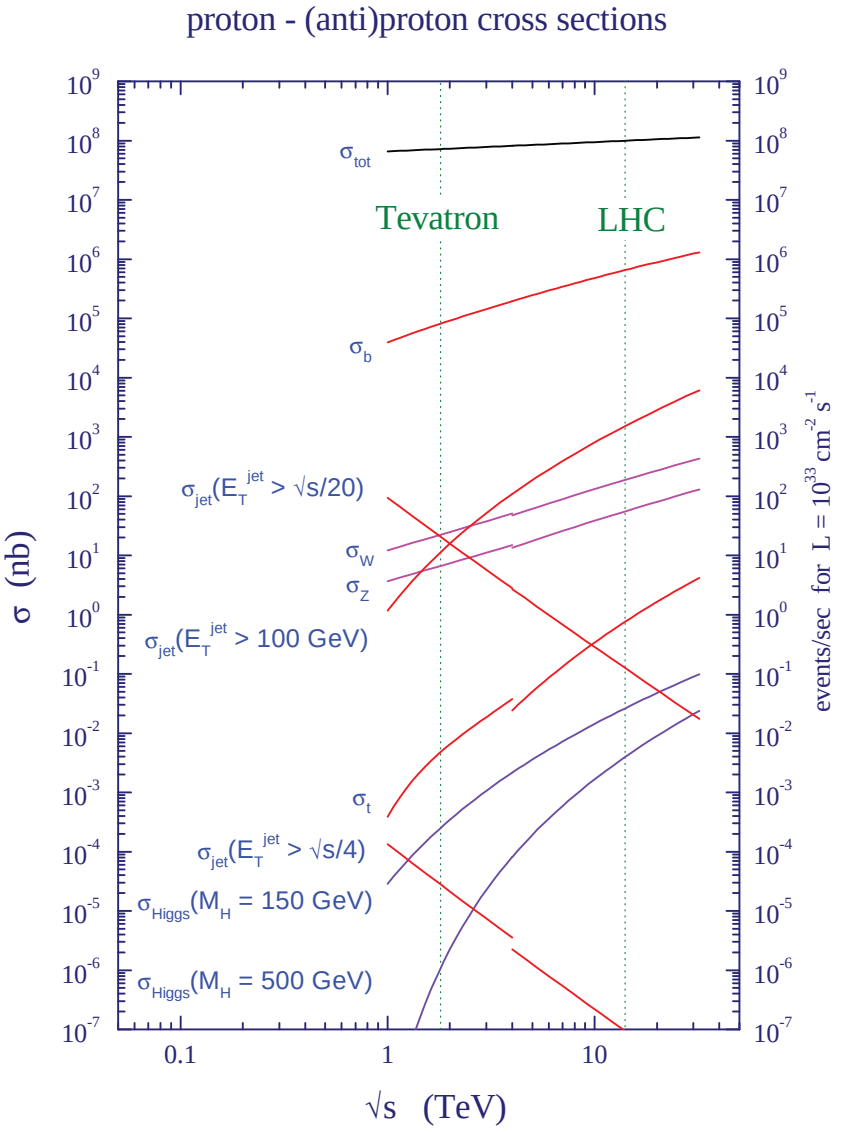

FIGURE 1.15: SM cross sections at the TeVatron and the LHC colliders [53].

likely to have $u\bar{d}$ annihilations than $\bar{u}d$. This results in producing more W^+ than W^-. W bosons are also produced through strange-charm annihilation. The decomposition of the W^+ and W^- cross-sections in terms of quark contributions is shown in Fig. 1.16.

Fig. 1.17 shows the production of W^+ and W^- at leading order at the LHC. Here, only the leptonic decays are depicted, as they are the subject of this thesis. The cross-section $\hat{\sigma}$ of such process can be written as:

$$\hat{\sigma}(q\bar{q}' \to W) = 2\pi|V_{qq'}|^2 \frac{G_F}{\sqrt{2}} m_W^2 \ . \ \delta\left(Q^2 - m_W^2\right) \tag{1.20}$$

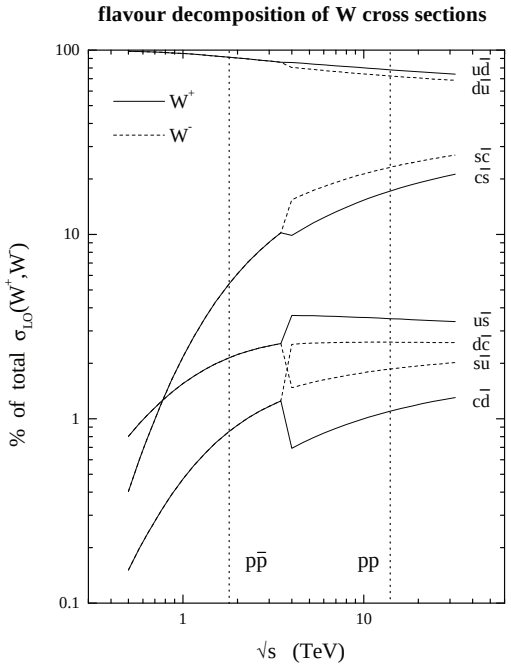

FIGURE 1.16: Parton flavor decomposition of the W^+ (solid line) and W^- (dashed line) total cross-sections in $p\bar{p}$ and pp colliders as functions of the center of mass energy. In $p\bar{p}$ collisions the decomposition is the same for W^+ and W^-. This plot is based on the MRST99 PDF set [55].

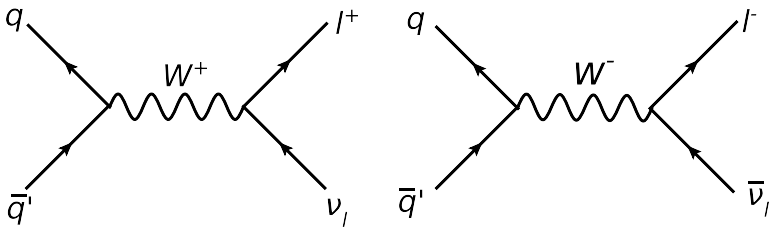

FIGURE 1.17: Leading Order Feynman diagrams representing the main production channels of W^+ (left) and W^- (right) at the LHC.

where $|V_{qq'}|$ is the relevant element from the CKM quark mixing matrix, G_F is the Fermi constant, m_W is the mass of the W and δ is the Dirac delta function.

One should also take into account corrections at higher orders. Three types of QED corrections intervene in the W production at Leading Order: Initial State Radiations (ISR), Internal Radiations, and Final State Radiations (FSR), all of them illustrated in Fig. 1.18. QCD corrections at Leading Order are needed in the case where gluons or quarks are emitted, like in the $q\bar{q} \to Wg$ and $qg \to Wq$ processes, and also at higher orders like in the $q\bar{q} \to q\bar{q}W$, $gg \to q\bar{q}W$ and $q\bar{q} \to ggW$ processes. These corrections need to be taken into account, but the higher the order, the smaller the impact of the correction.

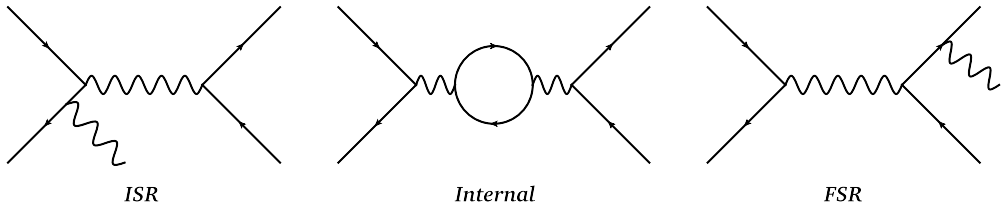

FIGURE 1.18: Feynman diagrams of the QED corrections at LO.

1.3.4 W and Z transverse momentum distributions

W and Z bosons are produced with relatively small transverse momentum $p_{\mathrm{T}}^{V} << m_V$ [53], where m_V denotes the vector boson's mass, V being either W or Z. At leading order, the colliding partons are assumed to be exactly collinear with the colliding protons, and the gauge bosons are produced with zero transverse momentum.

At higher orders, one must account for the non-perturbative transverse motion of the quarks and gluons inside the colliding protons, and the recoil against additional energetic partons produced in the hard scattering, generating large transverse momentum. The W and Z distributions are determined by the PDFs of the proton and the initial state interactions of the colliding partons. A full flavour decomposition of the proton PDFs and a mapping of their Bjorken-x dependence are needed for an accurate p_{T}^{V} description.

Figure 1.19 shows the expected p_{T}^{Z} and p_{T}^{W} distributions for different initial parton flavors. In particular, in $cs \to W$ events, the c quark involved has on average higher transverse momentum than the light quarks. This results in a harder p_{T}^{V} compared to contributions from u and d, by an amount of order m_c (charm quark mass). As a consequence, the p_{T}^{ℓ} distributions reflecting the underlying p_{T}^{V} distributions differ between processes with and without heavy quark contributions. This effect is illustrated in Figure 1.20, where the natural p_{T}^{ℓ} distribution is compared to the one obtained with $ud \to W$ only.

One should also consider the interactions between the colliding partons, resulting in soft gluons radiations, or "parton showers". These initial state radiations contribute to the p_{T}^{V} distribution. Since this process is not fully predictable, the Z samples are used to constrain the model parameters. However, the extrapolation of Z-based constraints to W should take into account aspects such as a possible mis-modeling of the b-quark fraction in Z production, which generates a distortion in the predicted p_T^Z distribution. This distortion is absorbed in the fitted parton shower parameters, and hence propagated to the p_T^W prediction, although the b-quark contribution to W production is negligible. This aspect is not taken into account in Chapter 6 where a parton shower parameters tuning is discussed.

The differential cross section as a function of p_{T}^{V} has been calculated including higher order corrections up to second order in α_{S}. However, the perturbative expansion of the cross section includes terms proportional to $\alpha_{\mathrm{S}}^{n} \log^{m}(m_V^2/p_{\mathrm{T}}^{V2})$ with $m \leq 2n-1$ at each order n. For $p_{\mathrm{T}}^{V} << m_V$ these higher order terms diverge, since the logarithm becomes large and compensates for the small α_{S}. A resummation technique is applied to solve this problem. It has been developed to include all contributions up to next-to-next-to-leading-logarithmic (NNLL) accuracy.

At high momentum ($p_{\mathrm{T}}^{V} > m_V/2$), the dominant processes are the hard parton emissions, and the p_T^V distribution can be calculated using perturbative QCD (pQCD). In the end, in order to have a full theoretical picture and a consistent result for small and large p_{T}^{V} values, the prediction for

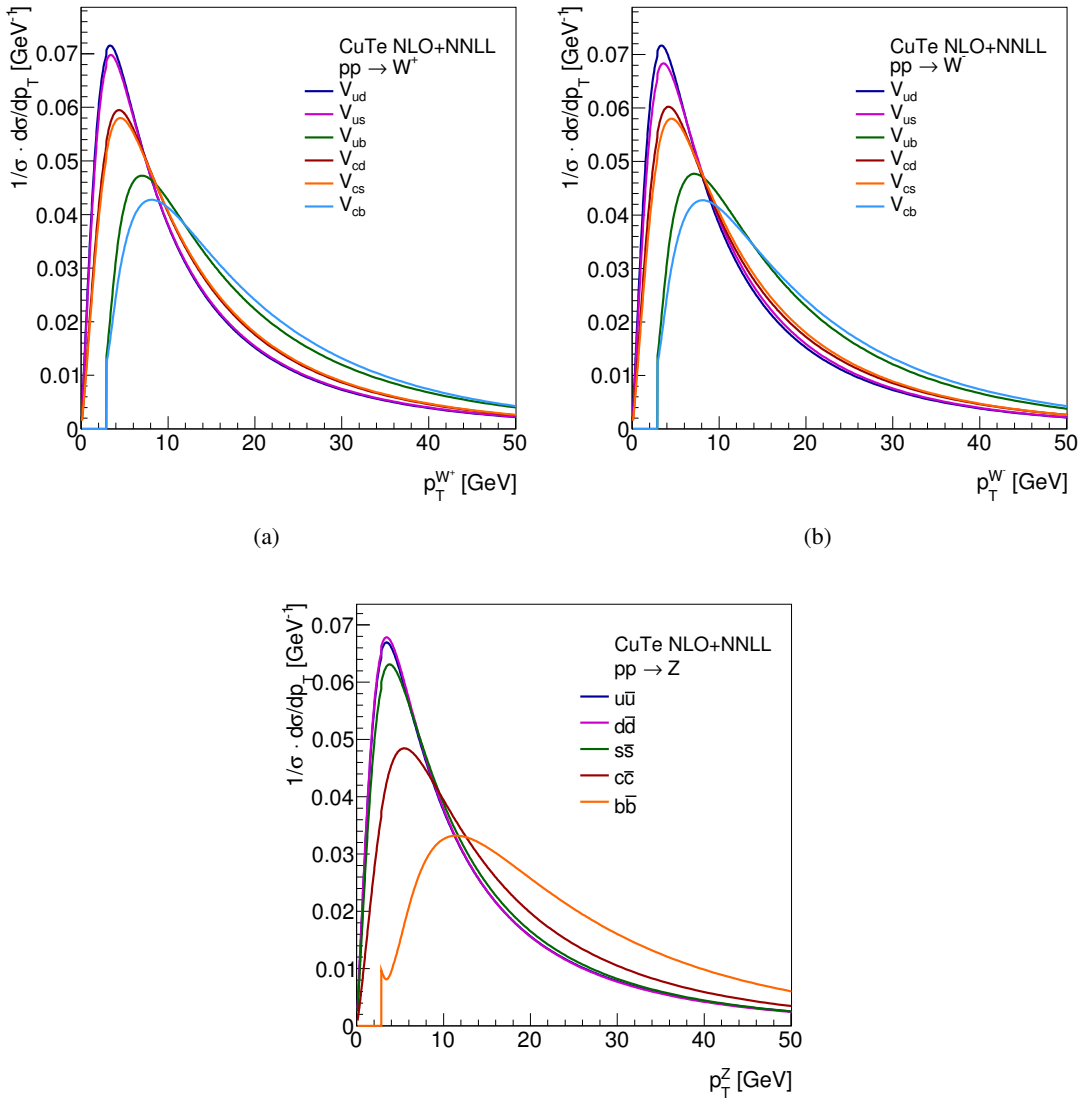

FIGURE 1.19: Differential cross sections as a function of $p_{\mathrm{T}}^{W,Z}$ for (a) W^+, (b) W^-, and (c) Z production for different initial parton flavours, as evaluated by CuTe at NLO+NNLL. All distributions are normalized to the same area. [56]

low p_{T}^{V} (resummed cross-section) has to be matched with the pQCD prediction. The differential spectrum is written as:

$$\left(\frac{d\sigma}{dp_{\mathrm{T}}^{V}}\right) = \left(\frac{d\sigma}{dp_{\mathrm{T}}^{V}}\right)_{\mathrm{pQCD}} + \left(\frac{d\sigma}{dp_{\mathrm{T}}^{V}}\right)_{\mathrm{resumm.}} \tag{1.21}$$

For low momenta, the measured spectrum allows to test the validity of the resummation schemes. For high momenta, the spectrum is sensitive to pQCD contributions and the emission of additional hard partons. Theoretical predictions are limited in precision due to the unknown contributions of higher order terms that are not included in the calculation. Data is used to perform fits and improve the understanding of such contributions.

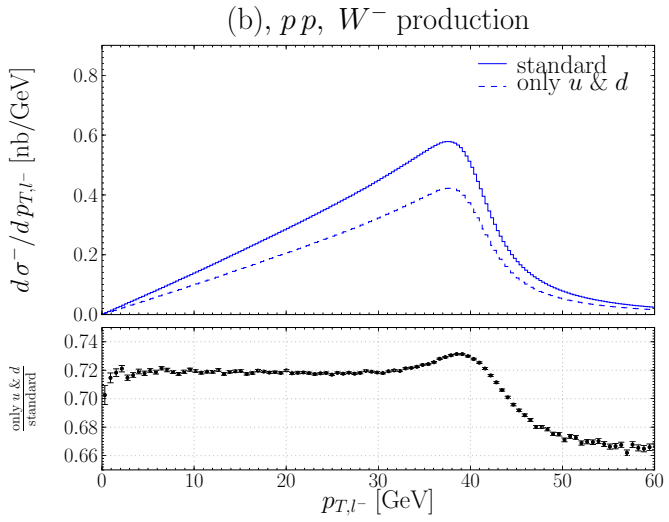

FIGURE 1.20: Lepton transverse momentum distributions in W^- decays, with and without contributions from second generation quarks [52].

Chapter 2

The Large Hadron Collider

The Large Hadron Collider (LHC) [57] is a superconducting hadron accelerator and collider and the most powerful tool so far built for particle physics research. It is located between 45 and 170 meters under the french and swiss territories, between the Jura mountains and the Léman lake. It was built in the 26.7 km tunnel used for the LEP machine, with the purpose of discovering the -at the time- missing scalar boson and studying its properties, exploring new physics at higher energies, as well as increasing the precision on the known fundamental parameters.

The first part of this chapter is about the design performance of the LHC, operating at a center of mass energy of 14 TeV, and the last part (Section 2.4) is about its actual performance in Run I (2010-2012) at 7 and 8 TeV, as the studies described in the following chapters involve 2011 and 2012 data. A detailed and technical description of the LHC machine can be found in the three-volume LHC Design Report in Ref. [58–60].

2.1 Injector and accelerator complex

The LHC machine accelerates and collides protons, and sometimes lead ions (Pb). It is linked to the CERN accelerator complex by a 2.5 km tunnel. This acceleration/injection chain is a succession of devices that provides the LHC with protons. The chain is represented in Fig. 2.1 and works as follows:

1. The protons are produced by a duoplasmatron source at 100 KeV and injected into the chain.
2. They enter an 80 m long linear accelerator, LINAC2, and are accelerated to 50 MeV.
3. A circular accelerator of a 157 m circumference, the Proton Synchrotron Booster (PSB) accelerates the protons up to 1.4 GeV.
4. The protons then enter the Proton Synchrotron (PS), a 628 m perimeter circular accelerator and get to 26 GeV.
5. The last point of the injection chain is the Super Proton Synchrotron (SPS), a 6.9 km circumference ring accelerator that increases the protons energy to 450 GeV before injecting them in the LHC.

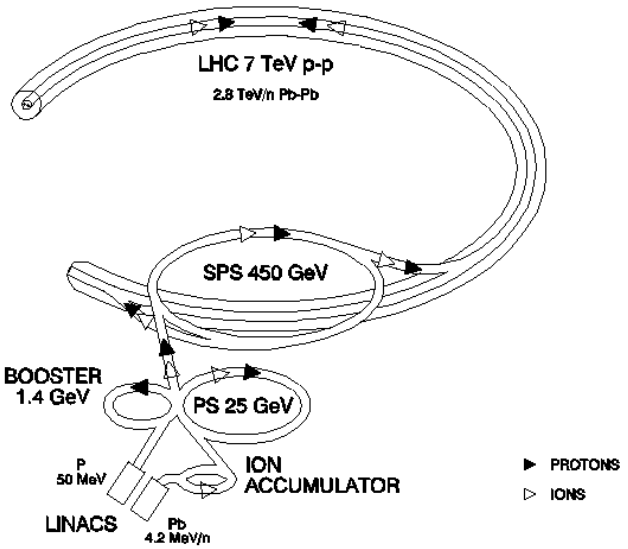

FIGURE 2.1: The LHC injector complex [57]. The full triangles represent the protons acceleration process. The empty triangles represent the lead ions acceleration, which is not in relevance to this thesis.

2.2 Design operation

The accelerated protons enter the two-ring LHC tunnel in the form of two counter-rotating beams until they reach 7 TeV each, giving at every collision a center of mass energy of $\sqrt{s} = 14$ TeV. This energy is the original design energy of the LHC. However, for practical reasons, this energy has been limited to 13 TeV. Each beam nominally contains 2808 proton bunches, separated by 25 ns, with small transverse and well defined longitudinal emittances, and each bunch contains approximately 1.15×10^{11} protons (This number exceeded its nominal value in 2012 to reach 1.5×10^{11} protons per bunch). These protons are kept in acceleration in order to be collided in four collision points, corresponding respectively to the four main detectors of the LHC: ATLAS [61], CMS [62], LHCb [63], and ALICE [64]. These points can be seen in Fig. 2.2. The design instant luminosity is $\mathscr{L} = 10^{34}$ cm^{-2} s^{-1}, a variable defined in Eq. 2.2. In one year of optimal functioning, the LHC machine could produce a luminosity of more than 200 fb^{-1}.

The acceleration of charged particles in a circular accelerator involves the use of magnets. The LHC relies on more than 9000 magnets that are at the edge of present technology, divided into "lattice" and "insertion" magnets. The main lattice magnets are 1232 superconducting dipoles cooled with liquid helium to 1.9 K. These dipoles are 15 meters long, weigh approximately 35 tonnes each, and can produce a magnetic field of 8.33 T needed for 7 TeV beams. The focusing of the beams is controlled by 392 quadrupoles. A dipole cross-section schema is shown in Fig. 2.3 as an example. The remaining magnets are responsible for keeping the beams stable and precisely aligned, keeping the particles in a tight beam, and squeezing the beam either vertically or horizontally. Dipoles are also equipped with sextupole, octupole and decapole magnets, which correct for small imperfections in the magnetic field at the extremities of the dipoles.

The insertion magnets intervene when the particle beams enter the detectors, to squeeze the particles closer together so that they collide with the particles coming from the opposite direction. Three quadrupoles are used to create a system called an inner triplet. There are eight inner triplets, two of which are located at each of the four large LHC detectors, ALICE, ATLAS, CMS

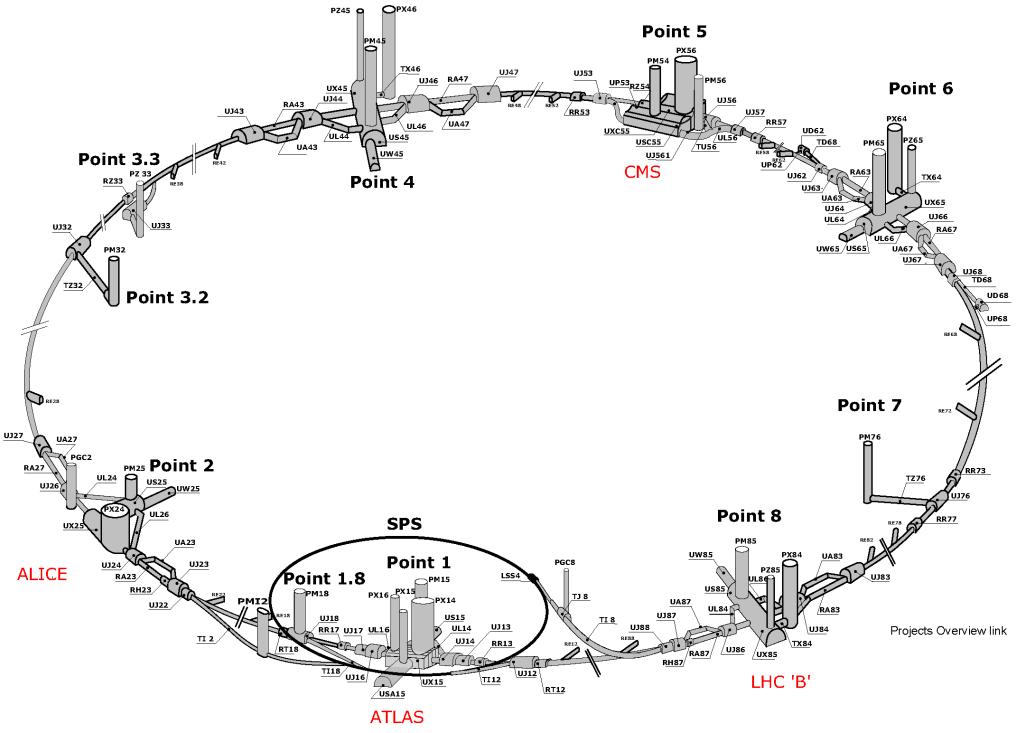

FIGURE 2.2: The different interaction points of the LHC. The ATLAS detector is at Point 1, ALICE at Point 2, CMS at Point 5 and LHCb at Point 8. The remaining points are strategic locations for technical purposes. [65]

and LHCb. Their role is to tighten the beam from 0.2 millimeters down to 16 micrometers. After the collision, the magnetic field helps in the charge and momentum measurements of the particles. The particle beams are later separated again by dipole magnets. Other magnets minimize the spread of the particles from the collisions. Insertion magnets are also responsible for beam cleaning, to ensure that no stray particle comes in contact with the LHC's sensitive components.

The particles are finally deflected from the LHC along a straight line towards the beam dump, in order to dispose of them. A dilution magnet reduces the beam intensity by a factor of 100,000 before the beam collides with a block of concrete and graphite composite for its final stop.

The four main experiments of the LHC have different goals each. ATLAS (A Toroidal LHC Apparatus System) and CMS (Compact Muon Solenoid) are general purpose detectors, they are designed to make use of the highest luminosity in order to explore many physics topics. LHCb is, as its name implies, built to study B-physics. ALICE (A Large Ion Collider Experiment) is specifically designed to study heavy ion (lead) collisions, and to explore the properties of a quark-gluon plasma. Two other experiments found on the LHC ring, TOTEM (TOTal Elastic and diffractive cross-section Measurement) and LHCf (LHC forward), study particles produced in the forward direction by collisions in the LHC. TOTEM is divided into four locations on either side of the collision point of the CMS experiment, LHCf is located at 140 m on either side of the ATLAS detector.

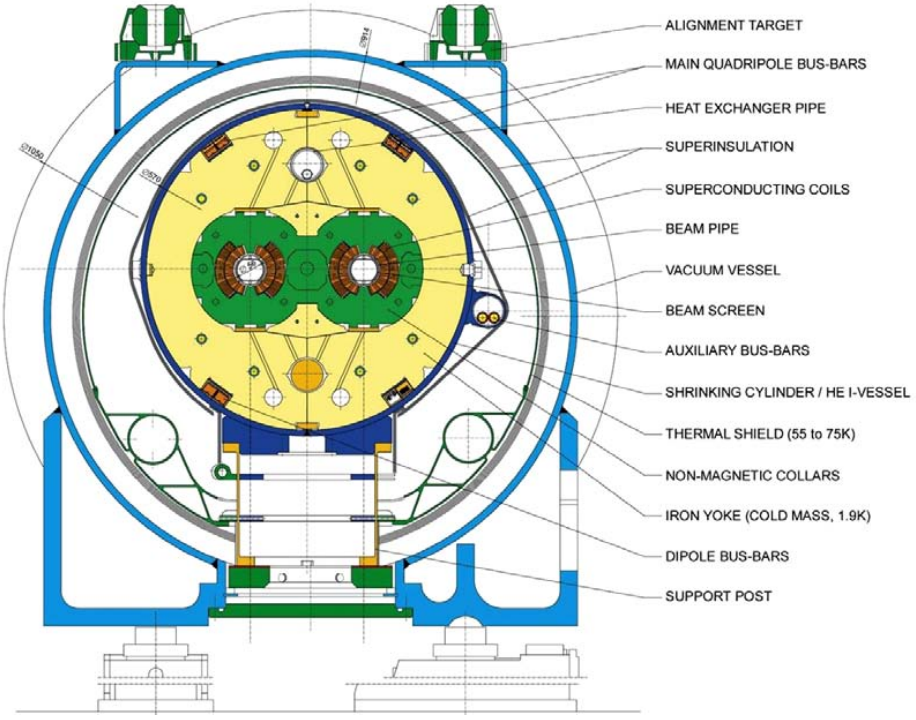

FIGURE 2.3: Cross-section of a dipole magnet [57].

2.3 Luminosity

The most important parameters in a particle accelerator are the center of mass energy and the number of events (or physics processes) per second (N_{events}) which are directly related to the luminosity $\mathscr{L}$:

$$N_{\text{events}} = \sigma_{\text{event}}(s) \times \mathscr{L} \tag{2.1}$$

where $\sigma_{\text{event}}(s)$ is the cross-section of the event under study, characterizing the scattering process and depending on the center of mass energy. The luminosity solely depends on the beam parameters, and considering a Gaussian beam, we can write:

$$\mathscr{L} = \frac{N_{\text{p}}^2 n_{\text{b}} f_{\text{rev}} \gamma_{\text{r}}}{4\pi \epsilon_{\text{n}} \beta^*} F \tag{2.2}$$

where:

- N_p is the number of protons per bunch, nominally 1.15×10^{11},
- n_b is the number of bunches per beam, nominally 2808 for a bunch spacing of 25 ns,
- f_{rev} is the revolution frequency, equal to 11.245 kHz for a circumference of 26.7 km,
- γ_{r} is the relativistic gamma factor E/m_p,
- ϵ_{n} is the normalized transverse emittance which shows the spread of particles in position and momentum phase space,

- β^* is the beta function at collision point, it measures the beam focalization, nominally 1.1m for 7 TeV and 0.55m for 14 TeV.
- Finally, F is the geometric luminosity reduction factor, which is due to the crossing angle at the interaction point:

$$F = \left(1 + \left(\frac{\theta_c \sigma_z}{2\sigma^*}\right)^2\right)^{-1/2} \tag{2.3}$$

  θ_c is the full crossing angle at the interaction point, σ_z is the bunch length RMS, and σ^* is the transverse RMS beam size at the interaction point. This expression of the F factor is done with the following assumptions: the beams are round, $\sigma_z \ll \beta$, and the beam parameters are equal for both beams.

Exploring rare physics processes requires high beam energy and high luminosity. One disadvantage of the high luminosity is the "pile-up" event, which degrades the energy resolution of the detectors. With an inelastic pp cross-section of 80 mb, the LHC will produce a total rate of 10^9 inelastic events per second at design luminosity. This implies that every candidate event for new physics will be accompanied on average by 23 inelastic events per bunch-crossing, at 14 TeV. Beside the pile-up problem, the nature of pp collisions implies that QCD jet production cross-sections will be dominant over rare processes. Overcoming these problems requires huge efforts to identify the experimental signatures of searched events and count on the robust capabilities of the different detectors.

2.4 Performance in Run I

The first long run of the LHC lasted from march 2010 to December 2012. During Run I, the proton-proton luminosity increased in distinct phases, starting with basic commissioning in 2010 and moving on to full physics production running in 2012. In this section I will only focus on proton-proton collisions.

The year 2010 was devoted to commissioning and establishing confidence in operational procedures and the machine protection system. The first collisions at $\sqrt{s} = 7$ TeV were established on March 30, at 3.5 TeV per beam, and β^* was reduced to 2m in all four interaction points (cf. Eq. 2.2 for the definition of β^*). The proton run for this year finished with beams of 368 bunches of around 1.2×10^{11} protons per bunch and a peak luminosity of $2.1 \times 10^{32}\text{cm}^{-2}\text{s}^{-1}$. The total integrated luminosity for both ATLAS and CMS in 2010 was around 0.04 fb^{-1}, and is illustrated in Fig. 2.4(a).

In 2011 the beam energy remained at 3.5 TeV, giving a center of mass energy of $\sqrt{s} = 7$ TeV. The machine ran with a 50 ns bunch spacing, and the number of bunches reached 1380, the maximum possible with such bunch spacing, by the end of June. A peak luminosity of $2.4 \times 10^{33}\text{cm}^{-2}\text{s}^{-1}$ was achieved, followed by a reduction in β^* in ATLAS and CMS from 1.5m to 1m. Lowering β^* and increasing the bunch intensity produced a peak luminosity of $3.7{\times}10^{33}\text{cm}^{-2}\text{s}^{-1}$. ATLAS and CMS received around 5.6 fb^{-1}each by the end of the proton-proton run in 2011, as seen in Fig. 2.4(b).

The start of operations in 2012 was marked with an increase in beam energy to 4 TeV. The number of 1380 bunches was kept with a bunch spacing of 50 ns. β^* was squeezed to 0.6m. About 23 fb^{-1}were delivered to both ATLAS and CMS during a long operational year which ended in December. Fig. 2.4(c) shows the luminosity over the year 2012.

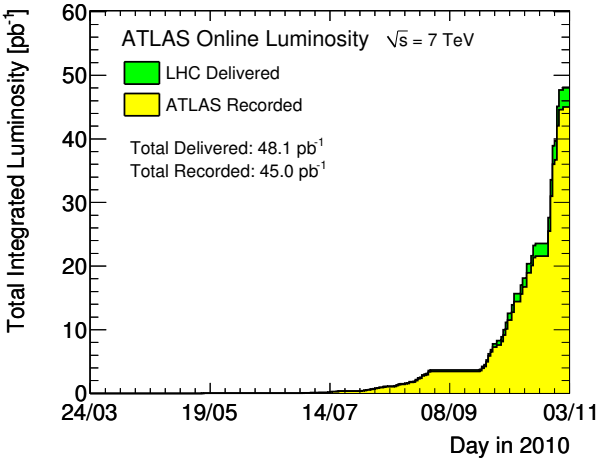

(a) 2010

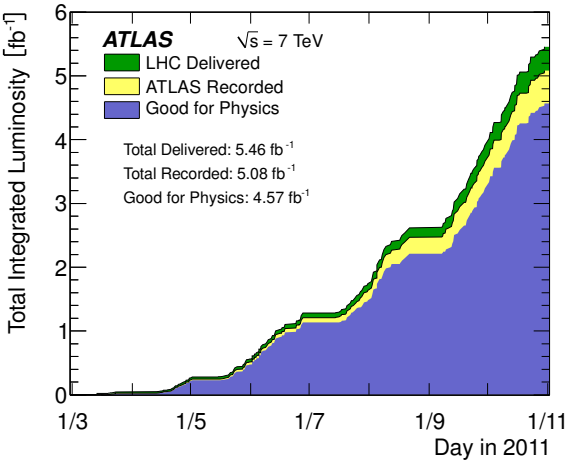

(b) 2011

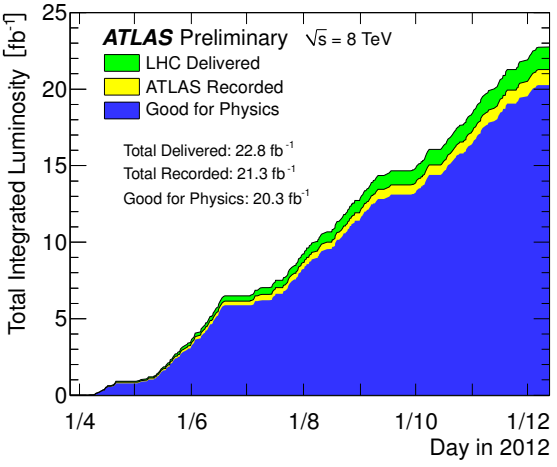

(c) 2012

FIGURE 2.4: Total integrated luminosity as delivered by LHC (green), recorded in ATLAS (yellow) and the part that was used for the physics analyses (blue) [66], versus the day, for 2010, 2011 and 2012.

Parameter	2010	2011	2012	Design Value
Beam energy	3.5	3.5	4	7
β^* in IP 1 and 5 (m)	2.0/3.5	1.5/1.0	0.6	0.55
Bunch spacing (ns)	150	75/50	50	25
Max. number of bunches	368	1380	1380	2808
Max. bunch intensity (protons per bunch)	1.2×10^{11}	1.45×10^{11}	1.7×10^{11}	1.15×10^{11}
Normalized emittance at start of fill (mm mrad)	≈ 2.0	≈ 2.4	≈ 2.5	≈ 3.75
Peak luminosity ($cm^{-2}s^{-1}$)	2.1×10^{32}	3.7×10^{33}	7.7×10^{33}	1×10^{34}
Max. mean number of events per bunch crossing	4	17	37	19
Stored beam energy (MJ)	≈ 28	≈ 110	≈ 140	362

TABLE 2.1: Values for the main performance-related parameters of the LHC from 2010 to 2012 and the design values. IP 1 and 5 represent ATLAS and CMS collision points. [67]

Table 2.1 shows the values for the main luminosity-related parameters at peak performance of the LHC from 2010 to 2012 and the design values. It shows that, even though the beam size is naturally larger at lower energy, the LHC has achieved 77% of design luminosity at four-sevenths of the design energy with a β^* of 0.6m (compared with the design value of 0.55m) with half of the nominal number of bunches. The table is taken from Ref. [67]

Chapter 3

The ATLAS detector

ATLAS is a general-purpose detector, using the full luminosity delivered by the LHC machine to explore a broad spectrum of particle physics. Its dimensions are 25 m in height, 44 m in length and it weighs approximately 7000 tonnes. Fig. 3.1 represents an illustration of the detector with its different sub-detectors and components.

The ATLAS detector is an arrangement of several sub-detectors, each one playing a different role in the detection of different particles. Starting from the interaction point, a tracking system is used to identify the charged particles trajectories, then come the electromagnetic and the hadronic calorimeters, and on the outside is the muon system specially designed to identify and reconstruct muons. Fig. 3.2 shows a transverse representation of the different detectors. The detectors are placed in a magnetic field provided by the ATLAS magnet system, and the detections are controlled by a trigger system that chooses whether to keep the detected signals or not. All of these components will be presented in this chapter.

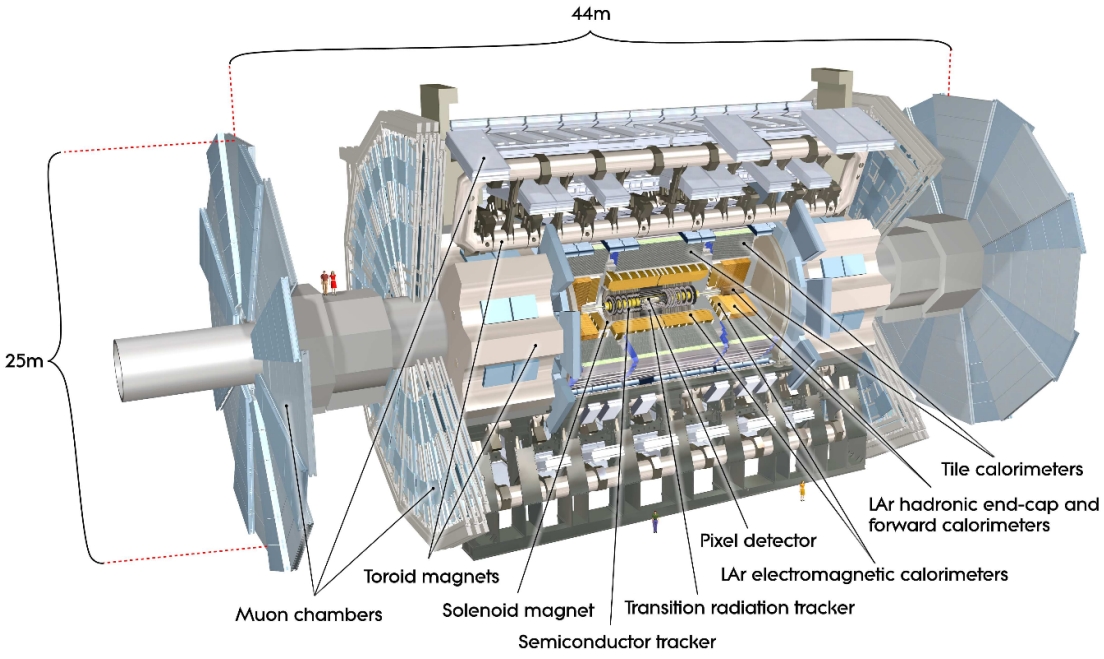

FIGURE 3.1: Cut-away view of the ATLAS detector [61].

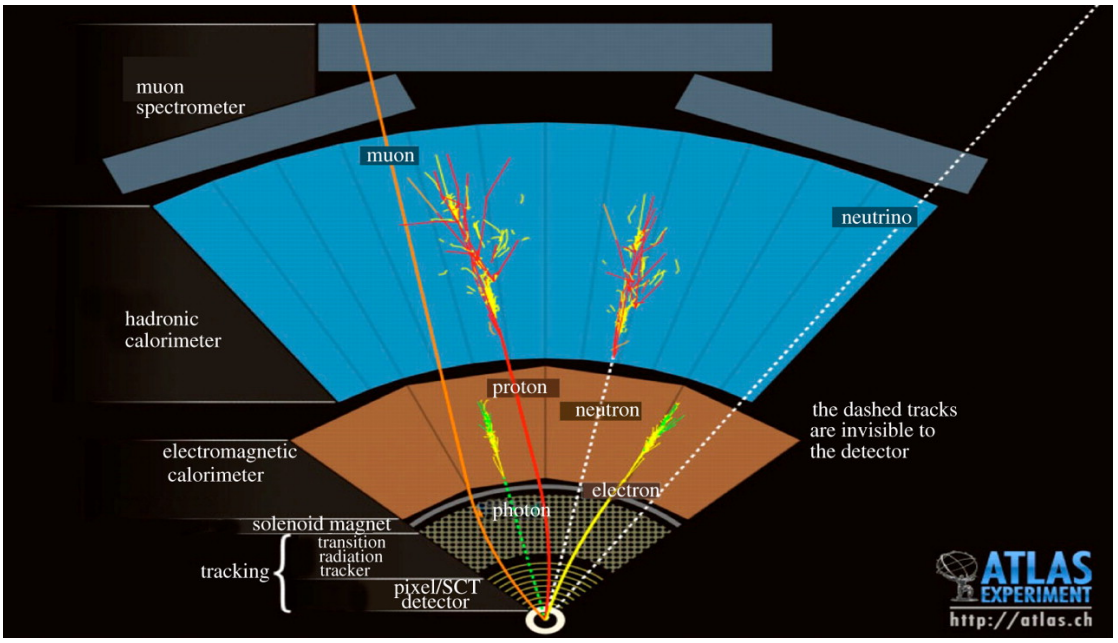

FIGURE 3.2: Transverse representation of the ATLAS detector [68]. Photons and electrons are detected in the electromagnetic calorimeter. The hadronic calorimeter detects protons, neutrons and other hadrons, and the muons are detected when they reach the muon spectrometer. Invisible particles like neutrinos cannot be detected directly.

3.1 Coordinate system

The coordinate system of the ATLAS detector is centered around the interaction point, and the detector is forward-backward symmetric with respect to its center. The positive x-axis is defined as pointing from the interaction point to the center of the LHC ring, with the positive y-axis pointing upward. The system is right-handed, and the z-axis is defined by the beam direction. The most commonly used angular coordinates are:

- ϕ, the azimuthal angle measured around the beam axis,
- θ, the polar angle from the beam axis,
- y, the rapidity defined as $y = 1/2\ \ln[(E + p_z)/(E - p_z)]$,
- η, the pseudo-rapidity equal to $-\ln\tan(\theta/2)$

All the transverse physics observables are defined in the (x, y) plane. A commonly used distance in the (η, ϕ) plane is defined by $\Delta R = \sqrt{(\Delta\eta)^2 + (\Delta\phi)^2}$.

3.2 Magnet system

The magnet configuration of the ATLAS detector determined its original design (Fig. 3.3(a)). The magnet system consists of a thin superconducting solenoid surrounding the inner detector (tracking system), which is aligned with the beam axis and provides a 2T axial magnetic field for the inner detector, and three large superconducting toroids (where ATLAS got its name from): one barrel and two endcaps, producing a toroidal magnetic field of approximately 0.5T in the

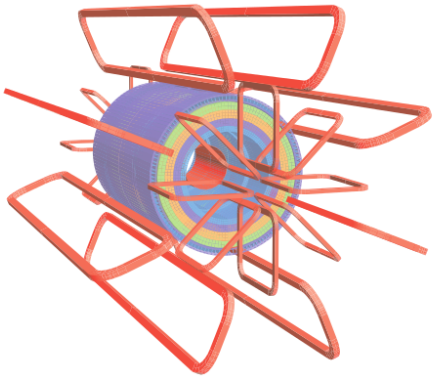

(a) Geometry of the magnets: the eight barrel toroids and the endcap coils are visible in red. The solenoid is placed inside the calorimeter.

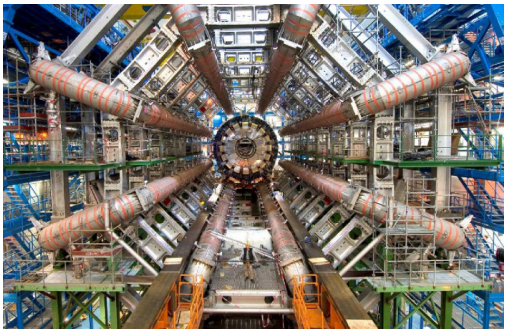

(b) Picture showing the symmetry of the toroidal magnets.

FIGURE 3.3: A schematic representation of the magnet system (left) and a picture of the toroids (right) [68].

barrel and 1T in the endcap for the muon detectors. The toroids are arranged in an eight-fold azimuthal symmetrical disposition around the calorimeters, which can be seen in Fig. 3.3(b).

The magnetic field volume defined as the region in which the field exceeds 50 mT, covers approximately 12,000 m^3.

3.3 Tracking system

The Inner Detector (ID) has the task of reconstructing charged particles and performing vertex and momentum measurements. It covers the pseudo-rapidity region of $|\eta| < 2.5$ and is composed of a pixel detector (Pixel), semiconductor tracker (SCT) and a transition radiation tracker (TRT), arranged in a concentric shell disposition around the beam axis in the barrel region (low-η region), while in the endcap regions (higher-η region) they are located on disks perpendicular to the beam axis. The ID is contained inside the central solenoid magnet generating a 2T magnetic field. Fig. 3.4 shows the layout of the ID and its different components.

The trackers are characterized by a fine granularity and provide high-precision measurements to cope with the large track density created by the particles emerging from the collisions at a rate of approximately 1000 particles every 25 ns, for $|\eta| < 2.5$. They provide tracking measurements in a range matched by the precision-measurements of the electromagnetic calorimeter.

The highest granularity is achieved around the vertex region using three layers of identical pixel sensors. The innermost layer of the pixels enhance the secondary vertex measurement at a radius of about 5 cm. The SCT consists of four double layers of silicon strip sensors made of two sensors each, allowing to measure both R and ϕ. It also allows impact parameter measurements and vertexing for heavy-flavour- and τ-tagging. The TRT is formed with straw tubes oriented in the z direction in the barrel and radially in the disks. The xenon-based gas mixture in the straw tubes allows an electron identification enhanced by the transition-radiation photons.

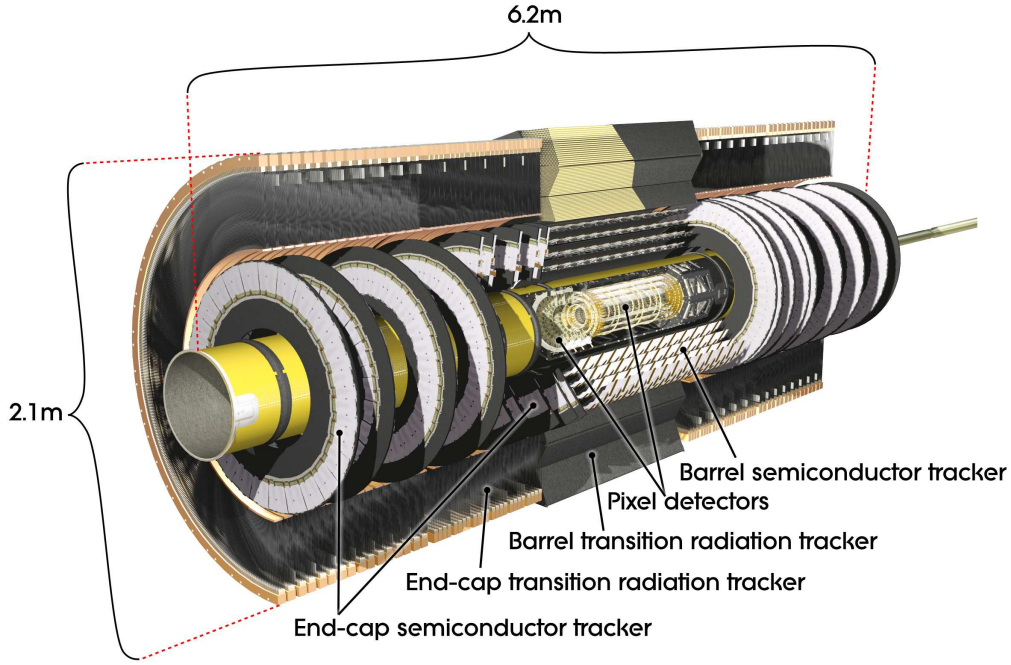

(a) Layout of the Inner Detector.

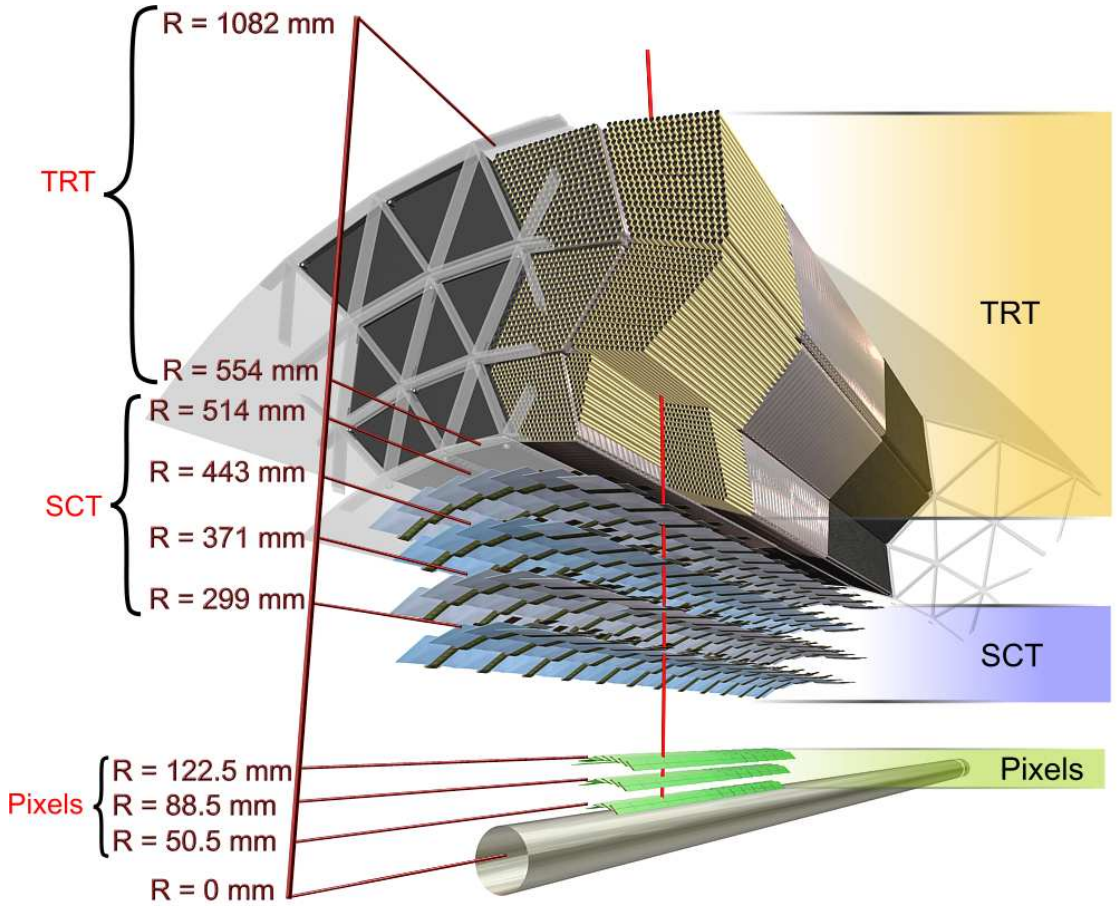

(b) Drawing of a charged particle (in red, p_T = 10 GeV) traversing the different layers of the inner detector. A reconstructed track in the barrel would typically have 3 pixel hits, 8 SCT strip layer hits, and 36 TRT straw hits.

FIGURE 3.4: Representations of the ATLAS Inner Detector [68].

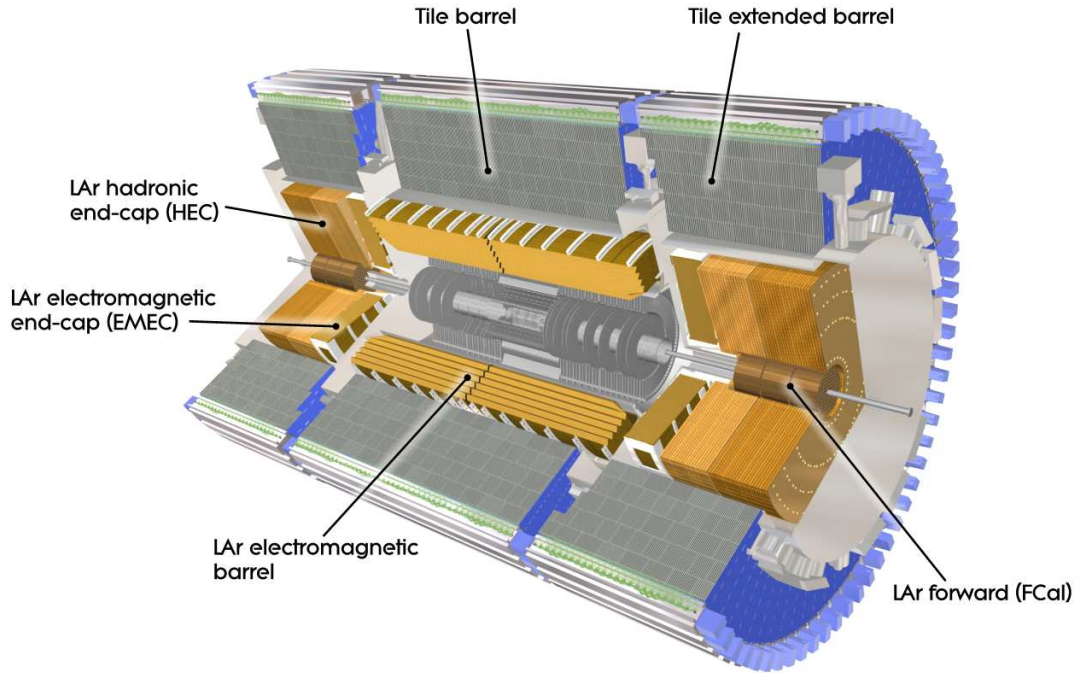

FIGURE 3.5: Layout of the electromagnetic and the hadronic calorimeters [68].

3.4 Calorimetry

This part of the detector consists of the electromagnetic calorimeter (EMC) on the inside and the hadronic calorimeter (HC) on the outside. The main component of the calorimeters is the liquid argon (LAr), chosen for its intrinsic linear behaviour, the stability of its response over time and its intrinsic radiation-hardness. It is designed to measure with high accuracy the properties of electrons and photons in a wide pseudorapidity (η) region, $0 < |\eta| < 2.5$. A study on the EMC performance is detailed in Chapter 4. The calorimetry system also significantly contributes to the performance of jet and missing transverse momentum measurements in the extended pseudorapidity range ($|\eta| < 4.9$). The ATLAS LAr calorimeter played a major role in the discovery of the Higgs boson in 2012 [23].

The calorimeters are sampling detectors with full ϕ-symmetry and coverage around the beam axis. They provide excellent performance in terms of energy and position resolution, and cover the range $|\eta| < 3.2$. The HC is mainly composed of scintillator-tile calorimeters ($|\eta| < 1.7$). In the endcaps ($|\eta| > 1.5$), LAr is also used to match the outer $|\eta|$ limits of the EMC. The pseudorapidity coverage is extended by forward LAr electromagnetic and hadronic calorimeters, covering up to $|\eta| = 4.9$. Both calorimeters are represented in Fig. 3.5 and 3.6.

Calorimeters are sufficiently thick to completely stop hadronic particles and limit related activity ("punch-through") into the muon system. The total thickness of the EMC is more than $22X_0$ in the barrel and more than $24X_0$ in the endcaps. X_0 is the radiation length, defined by the travelled distance inside the medium by an energetic electron/positron in a way to keep $1/e$ of its energy. It directly depends on the nature of the traversed medium.

3.4.1 The Electromagnetic Calorimeter

The EMC is highly granular over the η region matching the ID. This is ideally suited for precision measurements of electrons and photons. For the rest of the calorimeter, the granularity is coarser but sufficient to satisfy the physics requirements for jet reconstruction and missing transverse energy measurements. A detailed description of the EMC can be found in § 4.1, and its performance as well as a proposed correction for the lateral profiles of the electronic clusters are reported in § 4.2.

3.4.2 The Hadronic Calorimeter

The HC is composed of three independent components:

- Tile Calorimeter (TileCal): It is placed directly outside the EMC envelope. It covers the range $|\eta| < 1.7$, and uses steel as the absorber and scintillating tiles as the active material. The Tile Calorimeter is located between a radius of 2.28m to 4.25m, and is composed of a main barrel and an extended barrel. The total detector thickness is 9.7λ at $\eta = 0$, where λ is the interaction length which depends on the number of protons and neutrons in the calorimeter and on the cross-section of the inelastic collision between the atoms of the calorimeter and the traversing particle.
- Hadronic EndCap Calorimeter (HEC): It consists of two independent wheels per endcap. Each wheel is divided into two layers, and is made of copper plates interleaved with LAr gaps, which provide the active medium for this sampling calorimeter.
- Forward Calorimeter (FCal): It is a sampling calorimeter consisting of three wheels in the endcap: one made of copper, for electromagnetic measurements, and two made of tungsten to measure the energy of hadronic interactions. The LAr gaps between the absorber are very thin to avoid ion build-ups and to provide at the same time the highest possible detector density.

The main characteristics of the ATLAS calorimeters are summarized in Table 3.1.

3.5 Muon system

The calorimeter is surrounded by the muon system. The latter is designed to detect charged particles which have passed through the calorimeters, and to measure muon momentum up to $|\eta| < 2.7$. It also provides trigger capability up to $|\eta| < 2.4$, and was designed with the performance goal of 10% momentum resolution for 1 TeV tracks. The low momentum limit for muons to reach the muon system is approximately 3 GeV, due to energy loss in the calorimeter.

The muon momentum measurement is based on the magnetic deflection of muon tracks in the large superconducting air-core toroid magnets, instrumented with separate trigger and high-precision tracking chambers. The air-core toroid system, with a long barrel and two inserted endcap magnets, generates strong bending power in a large volume within a light and open structure. The barrel toroid covers the region $|\eta| < 1.4$ and the two endcap toroids cover the region $1.6 < |\eta| < 2.7$, the magnetic field in between is produced by the overlap of barrel and

	Barrel		End-cap	
EM calorimeter				
Number of layers and $\|\eta\|$ coverage				
Presampler	1	$\|\eta\| < 1.52$	1	$1.5 < \|\eta\| < 1.8$
Calorimeter	3	$\|\eta\| < 1.35$	2	$1.375 < \|\eta\| < 1.5$
	2	$1.35 < \|\eta\| < 1.475$	3	$1.5 < \|\eta\| < 2.5$
			2	$2.5 < \|\eta\| < 3.2$
Granularity $\Delta\eta \times \Delta\phi$ versus $\|\eta\|$				
Presampler	0.025×0.1	$\|\eta\| < 1.52$	0.025×0.1	$1.5 < \|\eta\| < 1.8$
Calorimeter 1st layer	$0.025/8 \times 0.1$	$\|\eta\| < 1.40$	0.050×0.1	$1.375 < \|\eta\| < 1.425$
	0.025×0.025	$1.40 < \|\eta\| < 1.475$	0.025×0.1	$1.425 < \|\eta\| < 1.5$
			$0.025/8 \times 0.1$	$1.5 < \|\eta\| < 1.8$
			$0.025/6 \times 0.1$	$1.8 < \|\eta\| < 2.0$
			$0.025/4 \times 0.1$	$2.0 < \|\eta\| < 2.4$
			0.025×0.1	$2.4 < \|\eta\| < 2.5$
			0.1×0.1	$2.5 < \|\eta\| < 3.2$
Calorimeter 2nd layer	0.025×0.025	$\|\eta\| < 1.40$	0.050×0.025	$1.375 < \|\eta\| < 1.425$
	0.075×0.025	$1.40 < \|\eta\| < 1.475$	0.025×0.025	$1.425 < \|\eta\| < 2.5$
			0.1×0.1	$2.5 < \|\eta\| < 3.2$
Calorimeter 3rd layer	0.050×0.025	$\|\eta\| < 1.35$	0.050×0.025	$1.5 < \|\eta\| < 2.5$
Number of readout channels				
Presampler	7808		1536 (both sides)	
Calorimeter	101760		62208 (both sides)	
LAr hadronic end-cap				
$\|\eta\|$ coverage			$1.5 < \|\eta\| < 3.2$	
Number of layers			4	
Granularity $\Delta\eta \times \Delta\phi$			0.1×0.1	$1.5 < \|\eta\| < 2.5$
			0.2×0.2	$2.5 < \|\eta\| < 3.2$
Readout channels			5632 (both sides)	
LAr forward calorimeter				
$\|\eta\|$ coverage			$3.1 < \|\eta\| < 4.9$	
Number of layers			3	
Granularity $\Delta x \times \Delta y$ (cm)			FCal1: 3.0×2.6	$3.15 < \|\eta\| < 4.30$
			FCal1: ~ four times finer	$3.10 < \|\eta\| < 3.15$, $4.30 < \|\eta\| < 4.83$
			FCal2: 3.3×4.2	$3.24 < \|\eta\| < 4.50$
			FCal2: ~ four times finer	$3.20 < \|\eta\| < 3.24$, $4.50 < \|\eta\| < 4.81$
			FCal3: 5.4×4.7	$3.32 < \|\eta\| < 4.60$
			FCal3: ~ four times finer	$3.29 < \|\eta\| < 3.32$, $4.60 < \|\eta\| < 4.75$
Readout channels			3524 (both sides)	
Scintillator tile calorimeter				
	Barrel		Extended barrel	
$\|\eta\|$ coverage	$\|\eta\| < 1.0$		$0.8 < \|\eta\| < 1.7$	
Number of layers	3		3	
Granularity $\Delta\eta \times \Delta\phi$	0.1×0.1		0.1×0.1	
Last layer	0.2×0.1		0.2×0.1	
Readout channels	5760		4092 (both sides)	

TABLE 3.1: Main parameters of the calorimetry system [61].

endcap toroid fields. The advantage of using toroid magnets is that the magnetic field created by them is orthogonal to the muon tracks in most regions. At the same time, the toroid design uses relatively little material thereby minimizing multiple scattering. For high energy tracks the performance is determined by the bending power of the magnets, given by the integrated magnetic field strength along the tracks, which ranges from 1 to 7.5 Tm.

Fig. 3.7 represents a cross section of the muon system. Precision-tracking chambers in the barrel region are located between and on the eight coils of the superconducting barrel toroid magnet, while the endcap chambers are in front and behind the two endcap toroid magnets.

The precision momentum measurement in the bending plane is performed by Monitored Drift Tubes (MDT) chambers, which cover the innermost endcap layers at $|\eta| < 2.0$, and the outer layers at $2.0 < |\eta| < 2.7$. The MDT chambers combine high measurement accuracy, predictability

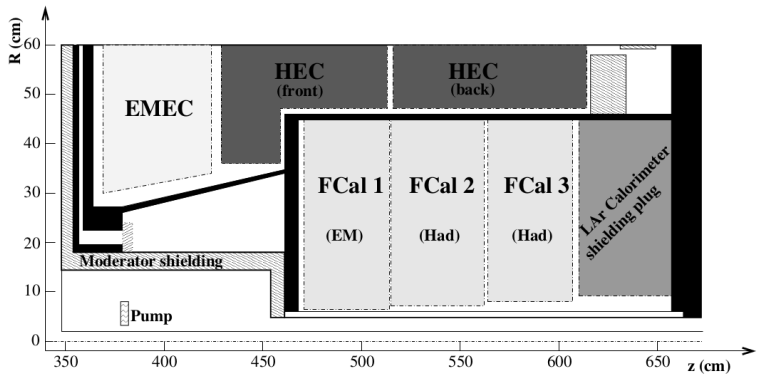

(a) Schematic diagram showing the three FCal modules located in the endcap. The diagram has a larger vertical scale for clarity.

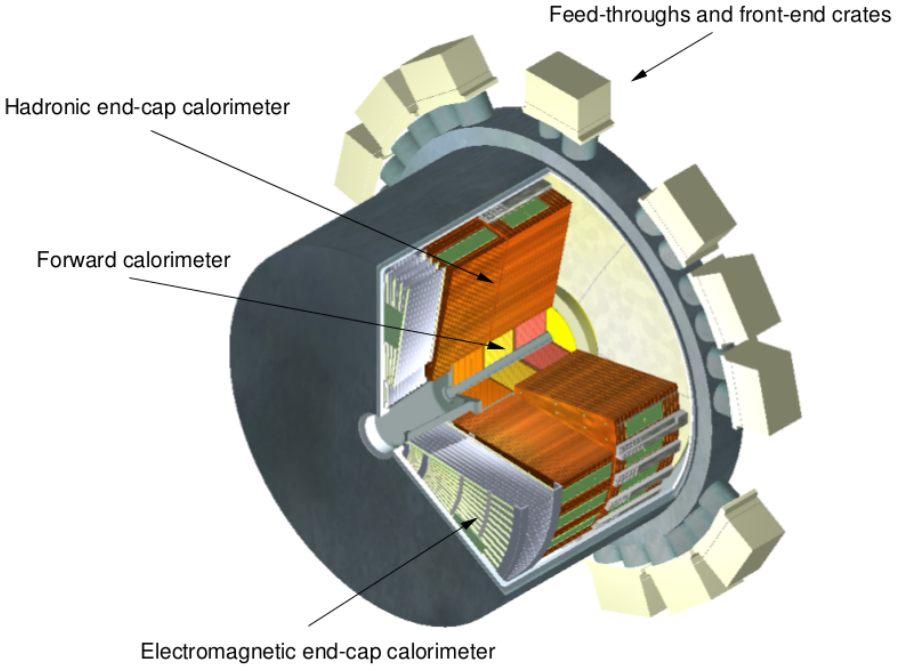

(b) Cut-away view showing the positions of the three endcap calorimeters.

FIGURE 3.6: Two different representations of the endcap calorimeters [68].

of mechanical deformations and simplicity of construction. They consist of 3 to 8 layers of drift tubes, operated at an absolute pressure of 3 bar.

The precision measurements in the forward regions ($2 < |\eta| < 2.7$) are performed using Cathode-Strip Chambers (CSC) that are able to deal with the higher rates and have better time resolution. They are multiwire proportional chambers with readout over segmented cathodes. The CSC measure both track coordinates, from the induced-charge distribution.

An essential design criterion of the muon system is the capability to trigger on muon tracks. The precision-tracking chambers have therefore been complemented by a system of fast trigger chambers capable of delivering track information within a few tens of nanoseconds after the passage of the particle. Trigger capability in the barrel region ($|\eta| < 1.05$) is added by Resistive Plate Chambers (RPC), and in the endcap region ($1.05 < |\eta| < 2.4$) by Thin-Gap Chambers

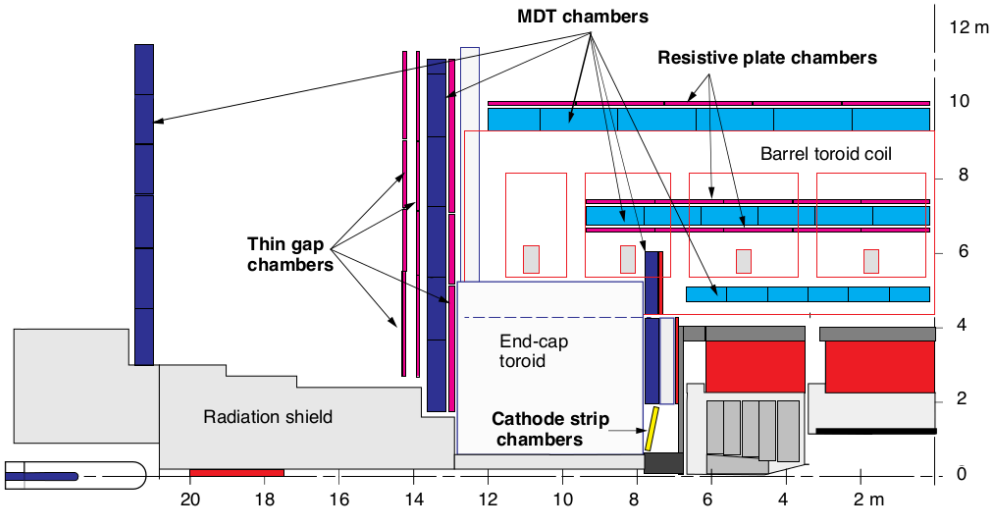

FIGURE 3.7: Cross section of the muon system in an $R - z$ plane [68].

(TGC). The design goal was to keep contributions from signal propagation and electronics low enough for reliable beam-crossing identification with $\geq 99\%$ probability.

3.6 Trigger system

The task of the trigger system is to reduce the event rate from the 40 MHz bunch crossing rate (in Run I, and 1 GHz event rate at design luminosity) down to 200 Hz which is the limit of the data recording rate of ATLAS. It is implemented in three levels, Level 1 (L1), Level 2 (L2) and the Event Filter (EF), each refining the decision made by the previous level and reducing the rate.

The L1 trigger system uses a subset of the total detector information to make a decision on whether or not to continue processing an event, reducing the data rate to approximately 75 kHz. It is based on custom electronics and uses fast algorithms on a subset of the detector information enabling it to reach a trigger decision in 2.5 μs. The L1 trigger searches for high transverse-momentum muons, electrons, photons, jets, and τ-leptons decaying into hadrons, as well as large missing and total transverse energy. Events passing the L1 trigger selection are transferred to the next stages of the detector-specific electronics. In each event, the L1 trigger also defines one or more Regions-of-Interest (RoI), i.e. the geographical coordinates in η and Φ, of those regions within the detector where its selection process has identified interesting features. The RoI data include information on the type of feature identified and the criteria passed, e.g. a threshold. This information is subsequently used by the higher level triggers, i.e. L2 and EF.

The L2 and EF, together referred to as high-level trigger (HLT), are implemented in software and use full-granularity readout to allow reconstruction close to the offline reconstruction. L2 selections use, at full granularity and precision, all the available detector data within the RoI's (approximately 2% of the total event data). The L2 menus are designed to reduce the trigger rate to approximately 3.5 kHz, with an event processing time of about 40 ms, averaged over all events. The final stage of the event selection is carried out by the event filter, which reduces the event rate to roughly 200 Hz. With access to the full event data and calibration databases,

the event filter reconstructs the entire event and applies offline analysis procedures within an average event processing time of the order of four seconds.

Chapter 4

Performance of the Electromagnetic Calorimeter

4.1 The electromagnetic calorimeter

The EMC has an accordion shape, and is made of Lead and Liquid Argon (LAr). This geometry provides it with complete ϕ symmetry, without azimuthal cracks, and a fast extraction of the signal at the rear and at the front of the electrodes. The only cracks are along η, at $|\eta| = 0$ (between the two half-barrels), $1.37 < |\eta| < 1.52$ (between the barrel and the endcap) and the last crack is between the inner and the outer wheel, at $|\eta| = 2.5$. The EM calorimeter has three longitudinal layers (strip, middle and back layers) and a fine segmentation in the lateral direction of the showers within the inner detector coverage, as can be seen from Fig. 4.1. The first layer is finely segmented along η, as for example in the barrel where there are eight strips in front of a middle cell. One can note however the coarser granularity of the first layer in the edge zones of the barrel and end-caps as explicitly given in Table 3.1. The second layer collects the largest fraction of the energy of the electromagnetic shower, and the third layer collects only the tail of the electromagnetic shower and is therefore less segmented in η.

4.1.1 Barrel geometry

The barrel electromagnetic calorimeter is centered around the beam axis, and is made of two half-barrels, covering the pseudo-rapidity region $0 < |\eta| < 1.475$, and measuring 3.2 m in length each. The half-barrels have an inner diameter of 2.8 m and an outer diameter of 4 m, and weigh 57 tonnes individually. A half-barrel is made of 1024 accordion-shaped absorbers, interleaved with readout electrodes.

A half-barrel presents no discontinuity along the azimuthal angle ϕ. However, for ease of construction, each half-barrel has been divided into 16 modules, each covering a $\Delta\phi = 22.5°$. The total thickness of a module is at least 22 radiation lengths (X_0), increasing from $22X_0$ to $30X_0$ between $|\eta| = 0$ and $|\eta| = 0.8$ and from $24X_0$ to $33X_0$ between $|\eta| = 0.8$ and $|\eta| = 1.3$. Each module has three layers (front, middle and back as viewed from the interaction point) as seen in Fig. 4.1. The readout granularity of the different layers is shown in Table 3.1. In total, there are 3424 readout cells per module, including the presampler cells.

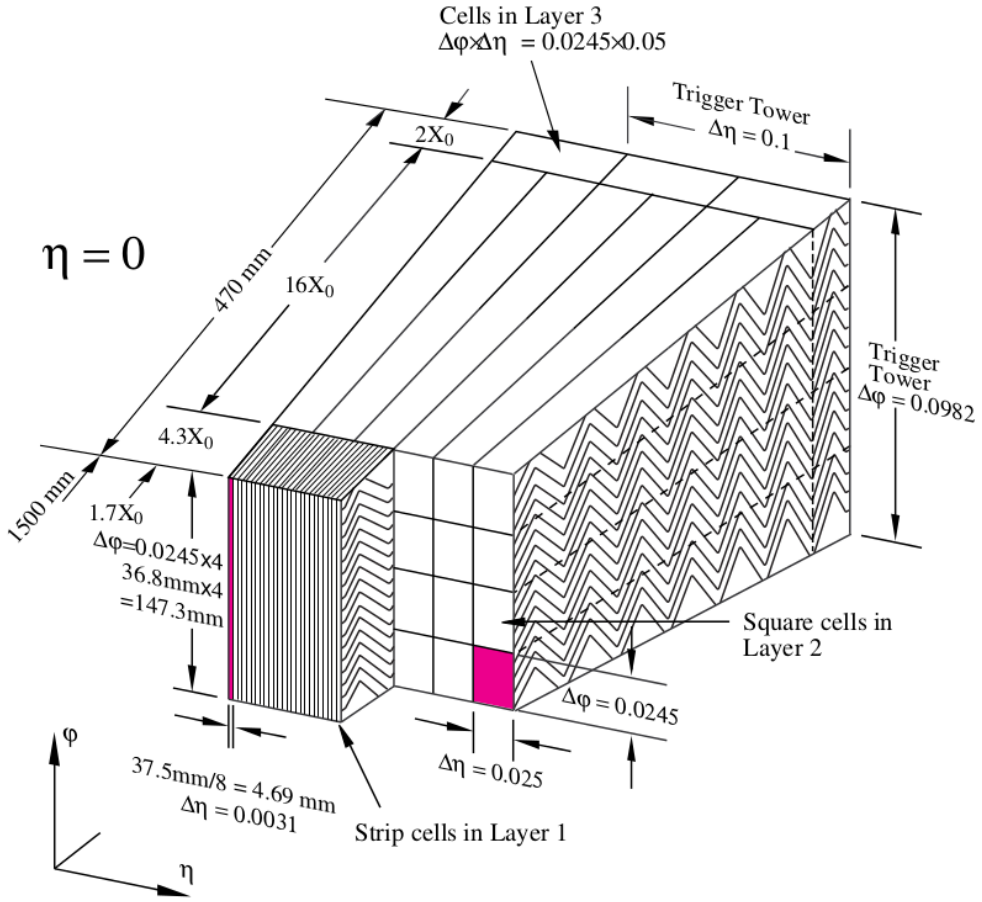

FIGURE 4.1: Sketch of a barrel module where the different layers are clearly visible [68]. The granularity in η and ϕ of the cells is also shown.

The presampler is a separate thin LAr layer (11 mm in depth), which provides shower sampling in front of the active electromagnetic calorimeter and inside the barrel cryostat. It is composed of eight modules of different sizes, with a length increasing with $|\eta|$ to obtain a constant η-granularity of $\Delta\eta = 0.2$ for each module, except for the module at the end of the barrel, for which the η-coverage is reduced to 0.12.

4.1.2 Endcap geometry

The endcap calorimeters consist of two wheels, one on each side of the electromagnetic barrel. Each wheel is 63 cm thick and weighs 27 tonnes, and covers the region $1.375 < |\eta| < 3.2$. At ambient temperature, the internal radius of each wheel is 330mm, and the external radius is 2098mm. In the transition region between the barrel and the endcap calorimeters, the material in front of the calorimeter amounts to several radiation lengths. In order to improve the energy measurement in this region, a LAr presampler is implemented in front of the endcap calorimeter, covering the range $1.5 < |\eta| < 1.8$.

The total active thickness of an endcap calorimeter is greater than $24X_0$ except for $|\eta| < 1.475$. The thickness increases from 24 to $38X_0$ as $|\eta|$ increases from 1.475 to 2.5 (outer wheel) and from 26 to $36X_0$ as $|\eta|$ increases from 2.5 to 3.2 (inner wheel).

As for the barrel electromagnetic calorimeter, the precision region in the end-cap electromagnetic calorimeters ($1.5 < |\eta| < 2.5$) is divided in depth into three longitudinal layers. The front layer, about $4.4X_0$ thick, is segmented with strips along the η direction. The transverse size of the projective cell in the middle layer is the same as defined in the barrel electromagnetic calorimeter, $\Delta\eta \times \Delta\phi = 0.025 \times 0.025$. The back layer has a twice coarser granularity in η. The outermost region $|\eta| < 1.5$ of the outer wheel and the inner wheel ($2.5 < |\eta| < 3.2$) are segmented in only two longitudinal layers and have a coarser transverse granularity. Table 3.1 summarizes the longitudinal and transverse readout granularities of the electromagnetic endcap calorimeter as a function of $|\eta|$.

Each endcap presampler consists of 32 identical azimuthal sectors or modules. The granularity of the presampler is $\Delta\eta \times \Delta\phi = 0.025 \times 0.1$.

4.2 Electron reconstruction and energy measurement

Calorimeter clusters are built from energy deposits in the calorimeter cells of the second layer. There are two clustering algorithms [69]:

- Sliding window clustering algorithm. It builds fixed size clusters from selected seeds, which is fast and useful for objects with a well defined energy deposition pattern, such as electromagnetic showers from electrons and photons (details in this section),
- The topological clustering algorithm. It is more used for hadron reconstruction such as hadronic jets, since hadronic showers have a more varied energy response.

Electrons used in this analysis are reconstructed in the central region of the detector, $|\eta| < 2.5$. The standard (sliding window) electron reconstruction algorithm is used. It starts from cell clusters in the EMC determined by the sliding window algorithm, which are then associated with reconstructed tracks with $p_{\mathrm{T}} > 0.5$ GeV from the ID, based on their (η, ϕ) coordinates. This algorithm only takes into account clusters with an energy deposit of more than 2.5 GeV.

In the precision measurement region, $0 < |\eta| < 2.5$, one can get an accurate position measurement for particles such as photons and neutral particles. The granularity of the second layer (0.025×0.025 in $\eta \times \phi$ space, for $|\eta| < 2.5$) allows the electrons to deposit their energy in a 3×7 cluster[1] in the barrel, and a 5×5 cluster in the endcap.

This cluster is matched to the electron track, and built around the most energetic cell in the neighborhood of the electron. The electron is reconstructed if one or more tracks from the ID are matched to the seed cluster. Together with the surrounding 7×11 cluster, *i.e.* the wider cluster containing the 3×7 one, they provide important information about the electromagnetic shower energy profiles, and the lateral energy leakage outside of the electronic cluster. Background and fake electrons rejection is discussed in detail in sections 7.1.4 and 7.2.

4.3 Shower shapes studies

The electrons and photons are detected in the form of energy showers, which allow us to define the following shower shape variables:

[1] This only applies to electrons with energy < 100 GeV. For $E_e > 100$ GeV, the cluster size is 5×5 [70].

- Lateral width:

$$w_{\eta 2} = \sqrt{\frac{\sum E_i \eta_i^2}{\sum E_i} - \left(\frac{\sum E_i \eta_i}{\sum E_i}\right)^2} \tag{4.1}$$

  where i is the cell index, E and η its energy and pseudo-rapidity respectively. This variable measures the shower lateral width along η over a window of 3×5 cells, around the cluster center. An example of a $w_{\eta 2}$ distribution is shown in Fig. 4.2(a).

- η energy ratio:

$$R_\eta = \frac{E_{3\times 7}}{E_{7\times 7}} \tag{4.2}$$

  where $E_{3\times 7}$ is the reconstructed energy in 3×7 cells around the cluster center and $E_{7\times 7}$ that of 7×7 cells. It is used to study the energy leaked outside the cluster along η, and is illustrated in Fig. 4.2(b).

- ϕ energy ratio:

$$R_\phi = \frac{E_{3\times 3}}{E_{3\times 7}} \tag{4.3}$$

  where $E_{3\times 3}$ is the reconstructed energy in 3×3 cells and $E_{3\times 7}$ that of 3×7 cells centered on the cluster. It measures the distribution along ϕ of the energy inside and outside the cluster. This variable is represented in Fig. 4.2(c).

The precise knowledge of these variables is highly important, for they are used for particle identification, background rejection, etc. This study has been conducted on $Z \to ee$ electrons, but a few results validations have been made on photons (section 4.3.1). R_ϕ being sensitive to the material in front of the EMC, we focused only on $w_{\eta 2}$ and R_η, which carry more intrinsic information on the width of the shower.

The electron shower shape study was motivated by the discrepancy in the $m_{e^+e^-}$ tails between data and Monte Carlo simulation, as shown in Fig. 4.3. In this figure, the right plot representing the data to MC ratio of the di-electron invariant mass in 2012 shows a $\approx 10\%$ discrepancy for the low tails. A first explanation was attempted by correcting the lateral profile of the electron clusters. The data to simulation discrepancy in the shower's lateral development is due to an imperfect simulation or to material effects upstream of the EMC, but correcting it didn't provide a solution to the $m_{e^+e^-}$ discrepancy. A second attempt was performed by testing different `GEANT4` versions on shower shapes after implementing several corrections to the physics simulation, which gave a more acceptable explanation on the $m_{e^+e^-}$ discrepancy (`GEANT4` is a software used to simulate the detector and the collisions. The name stands for GEometry ANd Tracking).

In the following sections, the first part involves correcting the lateral profile of the electron clusters in the middle layer of the ATLAS electromagnetic calorimeter. This correction uses weights computed from data to simulation energy ratios, and is applied to Monte Carlo. Next are a few studies regarding the Z-lineshape and $m_{e^+e^-}$ tails, and then a correction to the lateral shower width η-modulation is proposed to increase the cuts and selections efficiency. The corrections were later implemented at the reconstruction level in the ATLAS software, in the purpose of using them in an Integrated Simulation Framework to be used in future W studies. The last study is about testing different `GEANT4` versions and their impact on the lineshape.

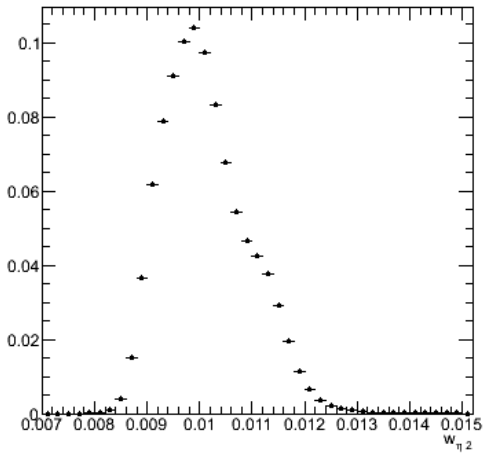

(a) $w_{\eta 2}$

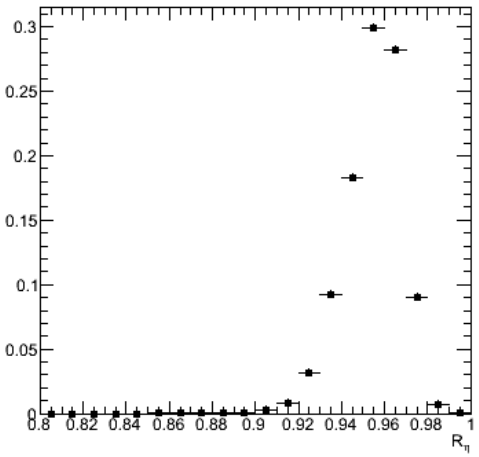

(b) R_{η}

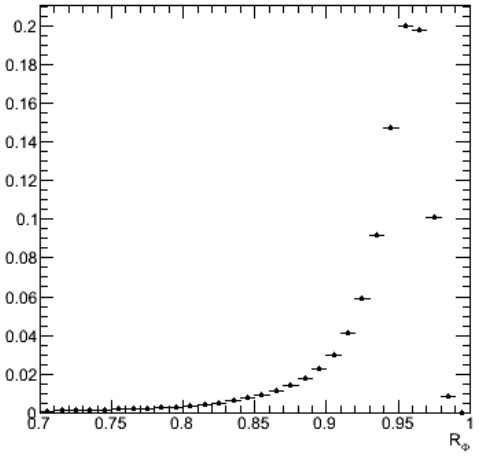

(c) R_{ϕ}

FIGURE 4.2: Distributions of electron shower shape variables. The plots are from $Z \rightarrow ee$ 2012 Monte Carlo simulation. All plots are normalized to unity.

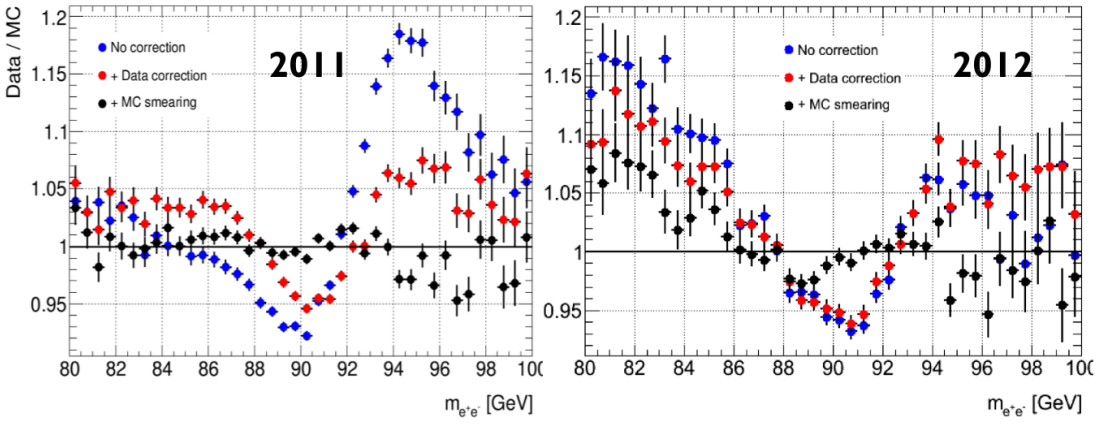

FIGURE 4.3: Data to MC di-electron invariant mass ratios before any correction (blue), with data correction (red) and also with MC smearing (black) - J.B. de Vivie

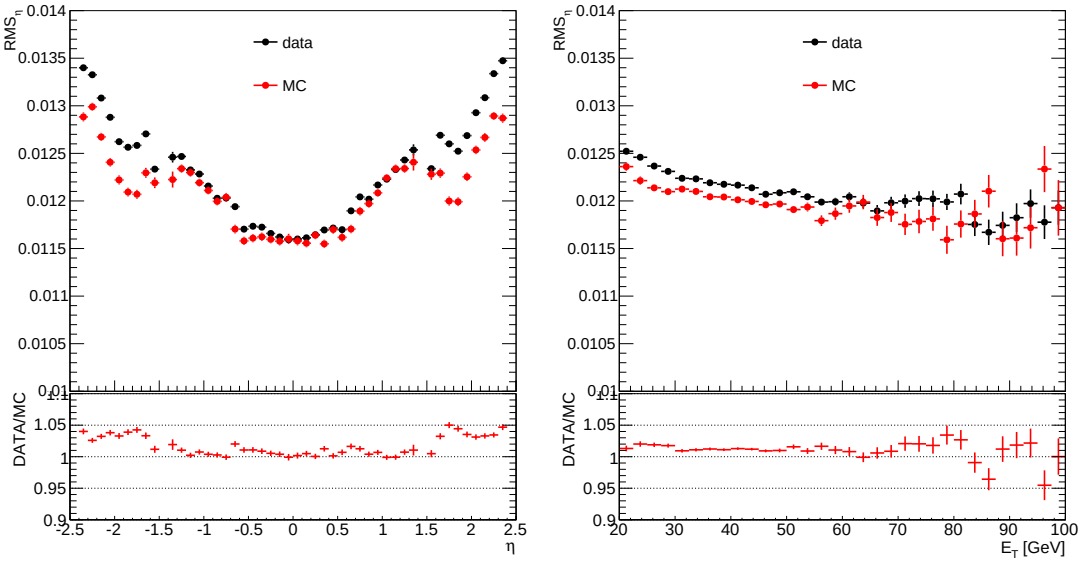

(a) η-profile

(b) E_{T}-profile

FIGURE 4.4: RMS of the cells energies along η, in a 3×7 cluster. Profiles vs. η (left) and the cluster transverse energy, E_{T} (right), for collision data and simulated samples. The bottom plots show the ratios of data to simulation.

4.3.1 Energy corrections and lateral leakage

The discrepancy between collision data and simulation concerning calorimeter shower shapes is a recurrent topic of study [71]. For instance, in the second sampling of the electromagnetic calorimeter, the predicted lateral shower shapes are narrower than what is measured, as seen in Fig. 4.4 and 4.6. An attempt to correct these discrepancies by modifying the physics lists in the simulation turned out to be ineffective, this aspect will be discussed in section 4.3.3. Fig. 4.4 shows the Root Mean Square ($\mathrm{RMS}_\eta = \sqrt{\sum_i E_i(\eta_i - \langle\eta\rangle)^2 / \sum_i E_i}$) of the cell energies along eta in a 3×7 cluster. As shown in the right hand plots, the dependency on the transverse energy is almost flat, unlike the η dependency (on the left). These profiles show that a valid correction can be done regardless of the energy range, but should take the η regions into account. The corrective approach developed here is based on this concept. It mainly consists in reweighting Monte Carlo to Data in terms of the cell energies, summed over ϕ, in 12 different η regions: $|\eta| \in [0.0-0.2], [0.2-0.4], [0.4-0.6], [0.6-0.8], [0.8-1.0], [1.0-1.2], [1.2-1.37], [1.52-1.7], [1.7-1.9], [1.9-2.1], [2.1-2.3], [2.3-2.47]$.

The study has been conducted on central electrons ($|\eta| < 2.47$), covering the tracking system of the detector, the barrel ($|\eta| < 1.475$) and endcap outer-wheels ($|\eta| > 1.375$) electromagnetic calorimeters. The events inside the middle crack ($1.37 < |\eta| < 1.52$) will not be considered. Since the electromagnetic showers deposit most of their energy in the second layer of the EMC, the study was focused on this layer, using the variables listed above.

The Z mass being precisely known from LEP, and having a good prediction on the Z lineshape, the data to Monte Carlo comparisons give useful informations on the experiment and its simulation. Based on that, $Z \to ee$ samples have been used in this study. The corresponding datasets are 2012 collision data and Monte Carlo simulated samples (MC), with a center of mass energy of $\sqrt{s} = 8$ TeV. The selected electrons have a transverse momentum of more than 20 GeV, an invariant mass between 80 and 100 GeV, and must fall in the pseudorapidity acceptance.

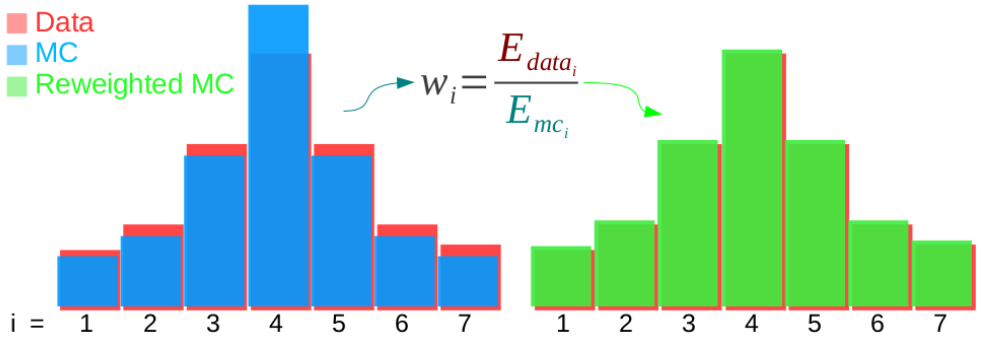

FIGURE 4.5: Illustrative example of the reweighting method. This provides, for each eta region, 7 weights w_i, which will be used to correct the MC energies: $E_{\text{reweighted MC}} = w_i \times E_{\text{original MC}}$.

Every electron is matched to a cluster in the middle layer. The cluster sizes are 3×7 in the barrel and 5×5 in the endcap, in $\eta\times\Phi$ space. But in order to study the lateral energy leakage (details in section 4.3.1), 7×11 clusters are built at first, according to the method that follows:

First step is to search for the cluster's central cell. For that, we look for the closest cell to the electron that has passed the selections. In the second sampling, the cell corresponding to the minimal $\Delta R = \sqrt{(\Delta\eta)^2 + (\Delta\phi)^2}$ with the electron's cluster direction is kept. Within $\Delta R < 0.5$ of this cell, the cell energies are compared with each other and the highest energy in this area corresponds to the central cell of our seeked cluster.

In the next step we build the 7×11 cluster around the central cell defined earlier. The energy, η and ϕ for each of the 77 cells is saved. To prevent having incomplete clusters, only clusters containing exactly 77 cells are kept.

The short-term purpose of this study is to find a correction for predicted energies in order to match the measured values. The goal was achieved by reweighting the energy deposited in the MC 7×11 clusters. The weights were calculated as described in Fig. 4.5. The same procedure has been repeated in 12 eta regions of $\Delta\eta = 0.2$ each, providing 12×7 weights, which once applied to Monte Carlo make the summed cell energies match the data exactly, by construction.

Fig. 4.6 shows an example of a corrected cluster. The reweighted plot (in blue) matches perfectly the data by construction. The new corrected clusters can now be used to study the impact of this correction on the shower shapes.

- Impact on the shower shapes

  When the cell energies are reweighted, shower shapes variables (R_η and $w_{\eta2}$) are computed from the corrected energies to check if the applied correction is efficient. In Fig. 4.7, 4.8 and 4.9, it is obvious that the correction brings the MC closer to data, as shown in the bottom plots of each of these figures, where the data to MC ratios tend to be flat around unity level for the corrected variables.

- Lateral leakage

  In the purpose of studying the energy distribution after the correction, let us define a leakage factor, k, as the ratio of the 3×7 (respectively 5×5) cluster energy after applying the weights with respect to the original energy (before reweighting), in the barrel where $|\eta| < 1.37$ (respectively in the endcap, where $|\eta| > 1.52$). For each event, two k-factors are

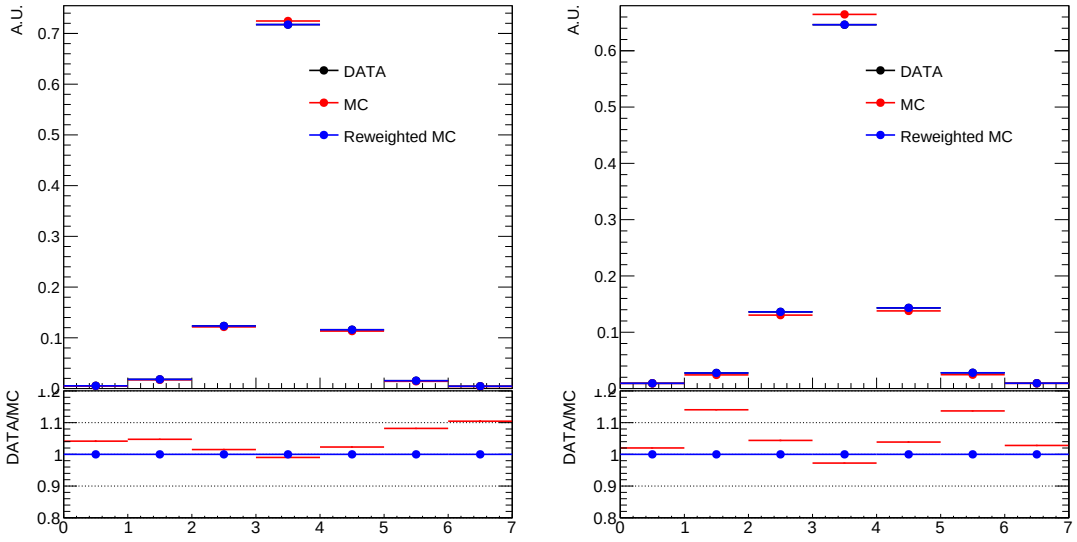

(a) $0.6 < |\eta| < 0.8$ (b) $2.1 < |\eta| < 2.3$

FIGURE 4.6: Corrected (blue) and original (red) MC cluster energies, compared to data (black). Left plot represents a bin in the barrel and the right one represents a bin in the endcap. Bottom plots are data to MC ratios. The x-axis represents the cluster cells in η, with the bin content being the energy summed over ϕ in a $\eta \times \phi = 7 \times 11$ cells cluster. Histograms are normalized to unity.

saved, corresponding to the two electrons. If k represents the remaining energy fraction inside the cluster, $1 - k$ represents the leaked fraction outside the cluster.

Fig. 4.10 shows the k-factors. The tails in these distributions make it interesting to study their impact on the $m_{e^+e^-}$ tails, as shown in Fig. 4.11, where the black dots are the nominal lineshape, and the blue dots correspond to the reweighted lineshape, where each of the two electrons is reweighted using its matching k-factor. To get the green dots, we then apply $1/\langle k_i \rangle$ as a scale on the blue plot, where $\langle k_i \rangle$ is the mean of all the k-factors, in the concerned pseudorapidity region. This plot shows that this correction does not affect the energy tails.

In Fig. 4.12, $1 - k$ is compared to the real leakage (the actual leakage in the calorimeter), where k is the mean of the two values corresponding to the two electrons. The leakage is well represented by the reweighting correction: the discrepancy in the barrel is around 0.1‰, and less than 0.2% in the endcap.

- Impact on photons

  In order to check whether this correction can be extrapolated to photons, a few basic verifications have been applied to photons clusters. Fig. 4.13 shows that this approach brings the simulated energy closer to the real data, but it doesn't completely correct it at this level. No further studies were carried out on this aspect.

4.3.2 Implementing the correction in the ATLAS software

The corrective approach described in 4.3.1 has only been applied to final $Z \to ee$ event samples, which are directly used in most physics analyses. In order to implement the correction at the

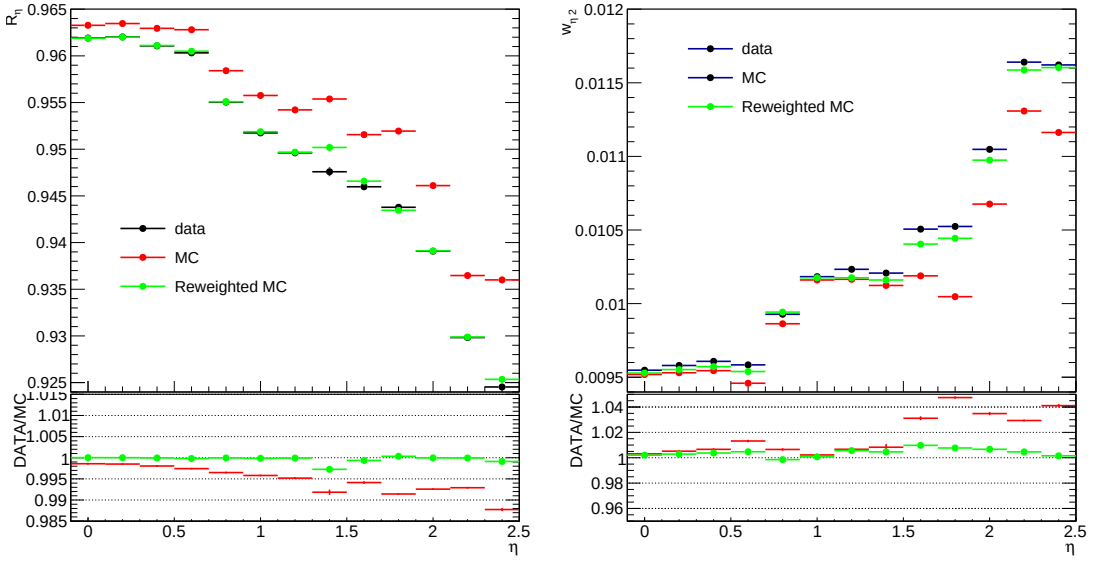

(a) R_η (b) $w_{\eta 2}$

FIGURE 4.7: η-profiles for R_η (left) and $w_{\eta 2}$ (right), for data and MC before and after correction. Bottom plots are data to MC ratios.

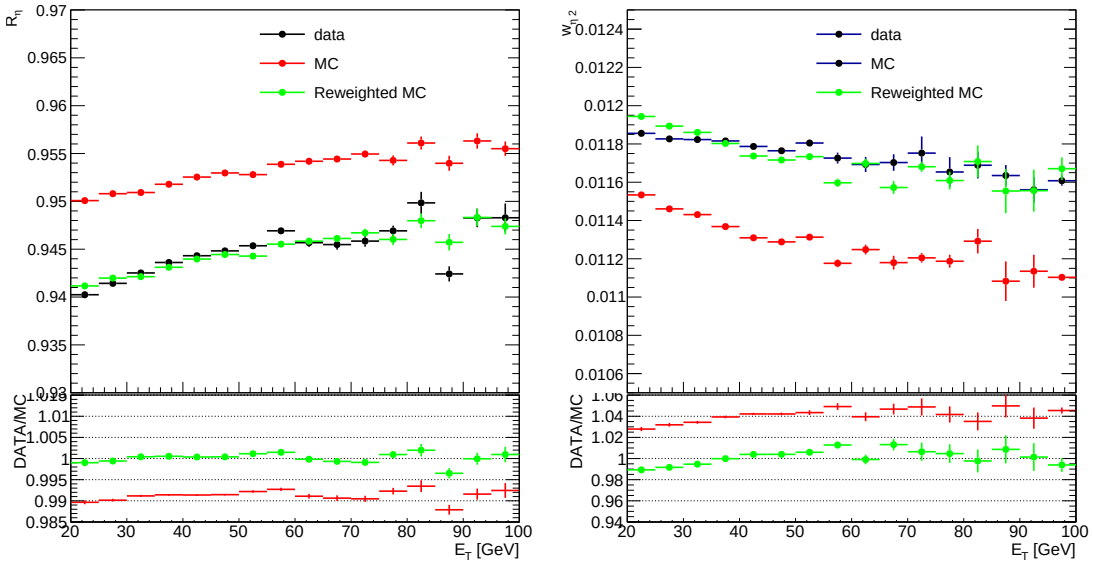

(a) R_η (b) $w_{\eta 2}$

FIGURE 4.8: E_T-profiles for R_η (left) and $w_{\eta 2}$ (right), for data and MC before and after correction, in two random pseudorapidity bins. Bottom plots are data to MC ratios.

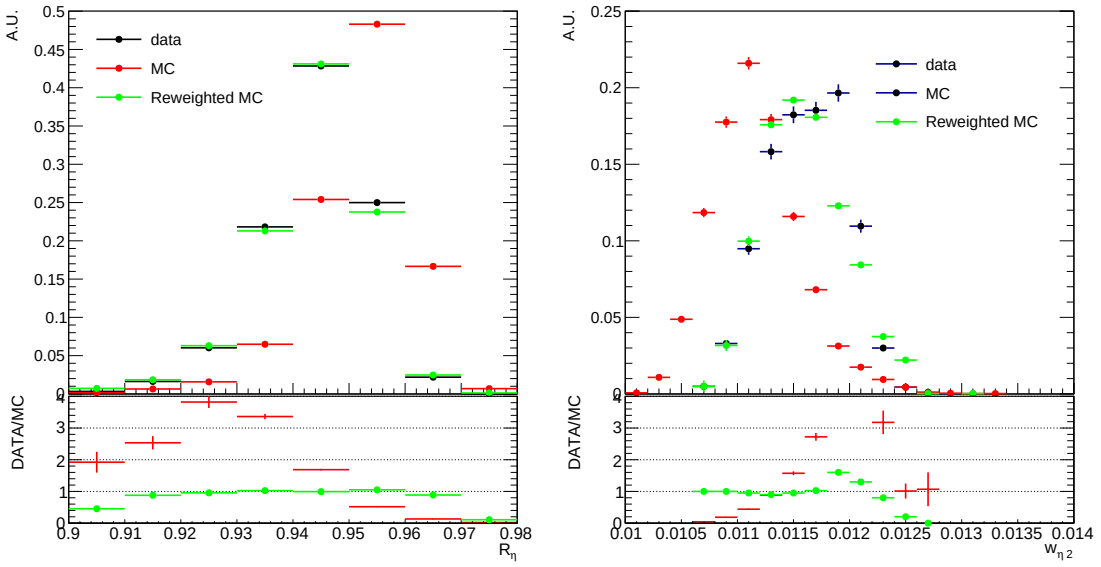

(a) R_η (b) $w_{\eta 2}$

FIGURE 4.9: Distributions of R_η (left) and $w_{\eta 2}$ (right), for data and MC before and after correction, in two random pseudorapidity bins, normalized to unity. Bottom plots are data to MC ratios.

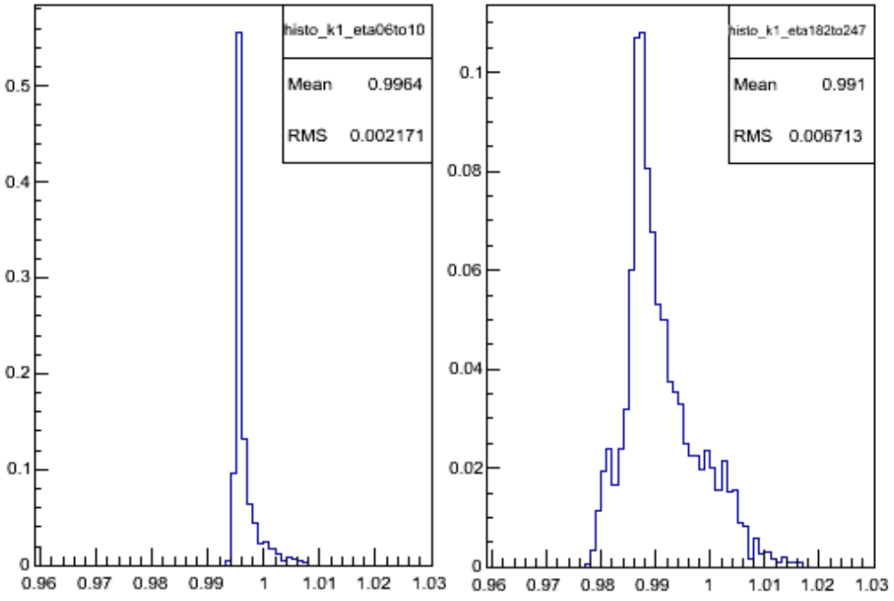

(a) $0.6 < |\eta| < 1.0$ (b) $1.82 < |\eta| < 2.47$

FIGURE 4.10: Distributions of the k-factor, for one electron, in one typical bin in the barrel (4.10(a)) and another one in the endcap (4.10(b)). Plots are normalized to unity.

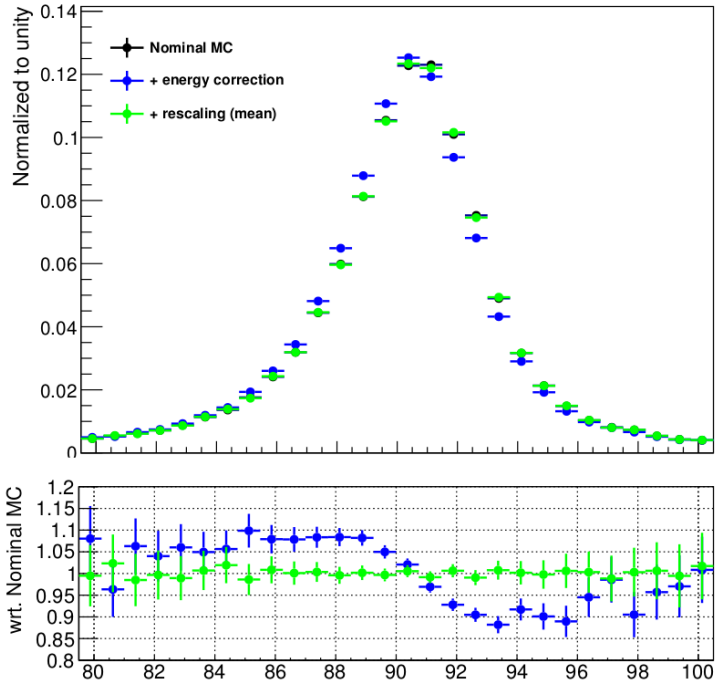

FIGURE 4.11: Z-lineshape distributions (normalized to unity), in one typical bin in the barrel ($0.0 < |\eta| < 0.6$). Black dots are nominal MC distributions, blue dots are obtained after reweighting using the k-factors, and the green dots are reweighted and rescaled distributions (more details in text). The bottom plots are ratios with respect to nominal.

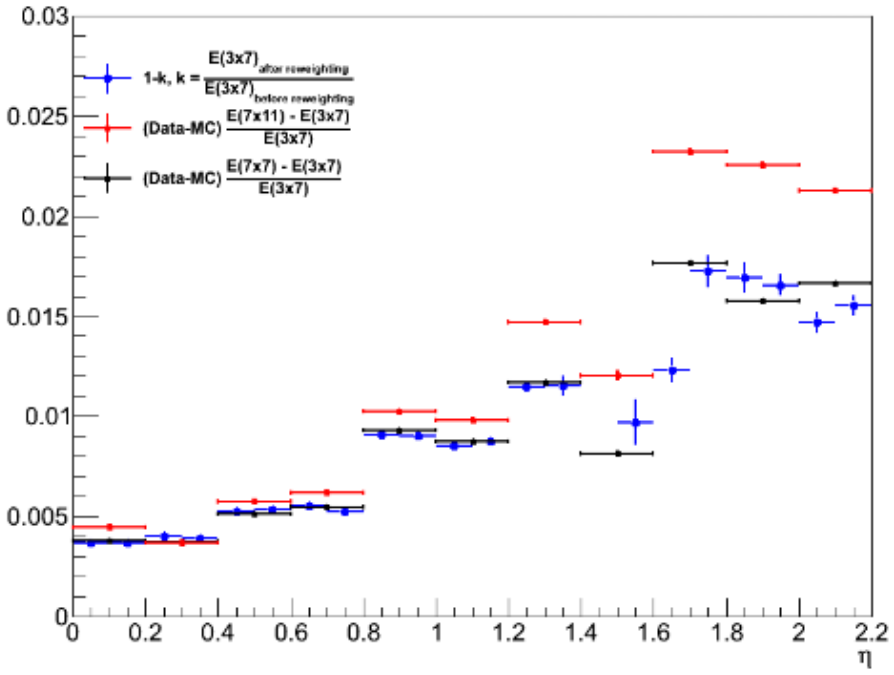

FIGURE 4.12: Comparison of $1-k$ (in blue) to the real leakage (in black) along η obtained from a study by C. Becot. The red plot (also by C. Becot) represents the leakage along η and ϕ , and is shown here for information only.

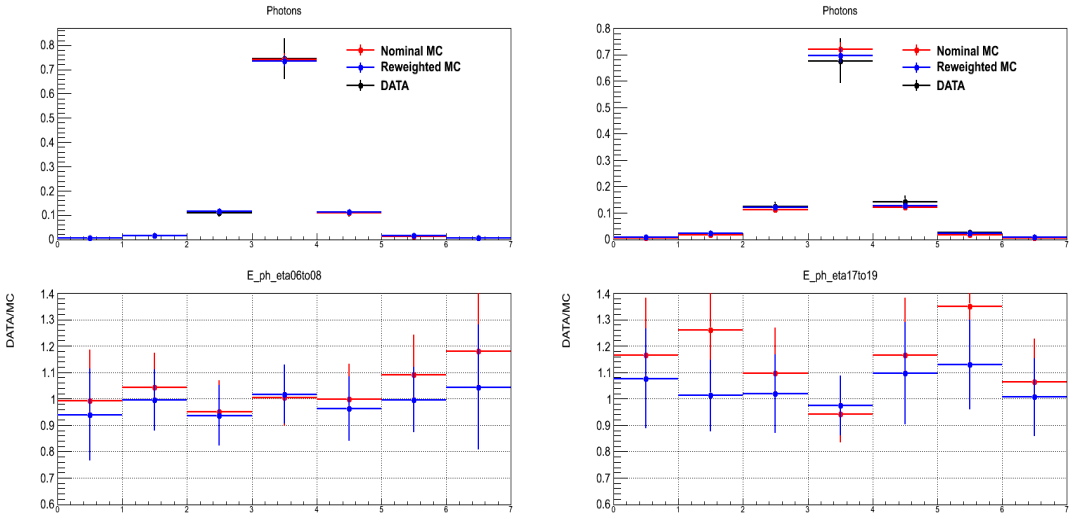

(a) $0.6 < |\eta| < 0.8$ (b) $1.7 < |\eta| < 1.9$

FIGURE 4.13: Lateral energies for photon clusters, for data (in black), and MC before (red) and after (blue) correction, which is applied using the weights extracted from electrons. Distributions are normalized to unity. Bottom plots are data to MC ratios. The error bars are mostly originated by the low statistics (500k total events).

electron reconstruction level, one has to work on unrefined samples, which will be taken as input for the reconstruction software. The expected output is a set of final samples containing the corrected shower shapes. The samples and selections are similar to the above, except for the unrefined nature of the samples.

The global procedure is similar to the one applied at the final level. Fig. 4.14 schematically describes the method used here to define the clusters. The final result is a set of 7×11 corrected cells, corrected electron clusters and corrected electrons.

Fig. 4.15 shows the checks that were made in order to verify the weights and the corrected energy profiles, at unrefined level.

At this point, the cell energies are now corrected at unrefined level. To make use of this correction, the final samples were built using the newly corrected electrons and cells collections in the reconstruction software. Fig. 4.16, 4.17 and 4.18 show the impact of this correction on R_η and $w_{\eta 2}$, in the newly built final samples. These plots confirm the efficiency of such correction when implemented in the software.

4.3.3 Studies of GEANT4 physics lists

This section is about checking the impact of several GEANT4 software versions on shower shapes and $m_{e^+e^-}$ tails, where the main differences between the versions are regarding electron scattering angles, Bremsstrahlung and/or photon conversion description. In a more relevant context to what was discussed above, this study was at first an attempt to better describe the shower shapes using different GEANT4 physics description.

The exact definitions of each of the versions will not be discussed in detail. Nevertheless, the following definitions will be used:

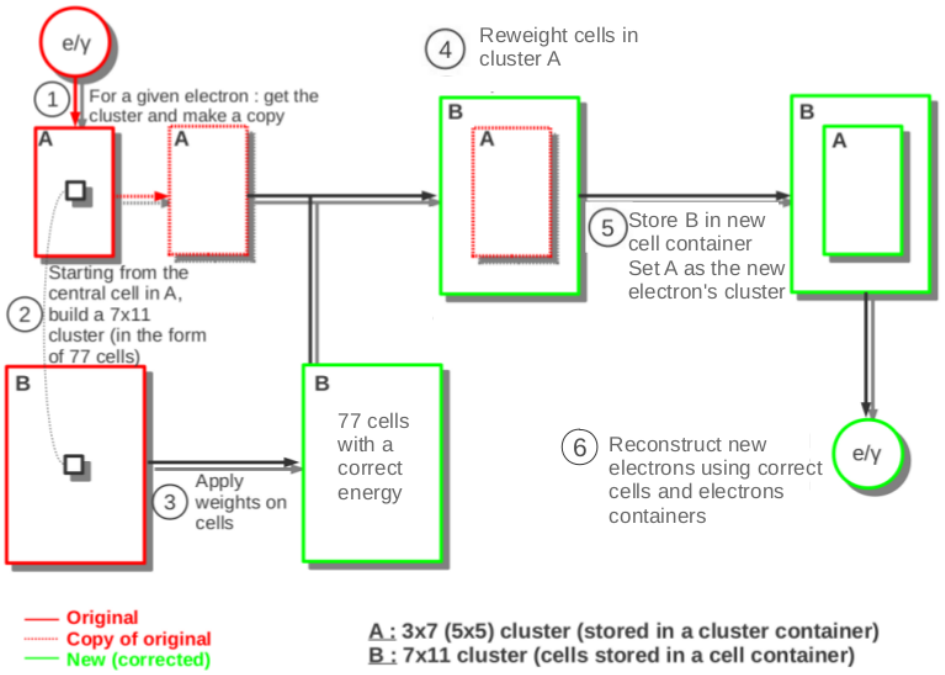

FIGURE 4.14: Diagram showing the concept of the algorithm to save corrected clusters and cells. These new clusters and cells have been used to reconstruct electrons and to obtain corrected shower shapes.

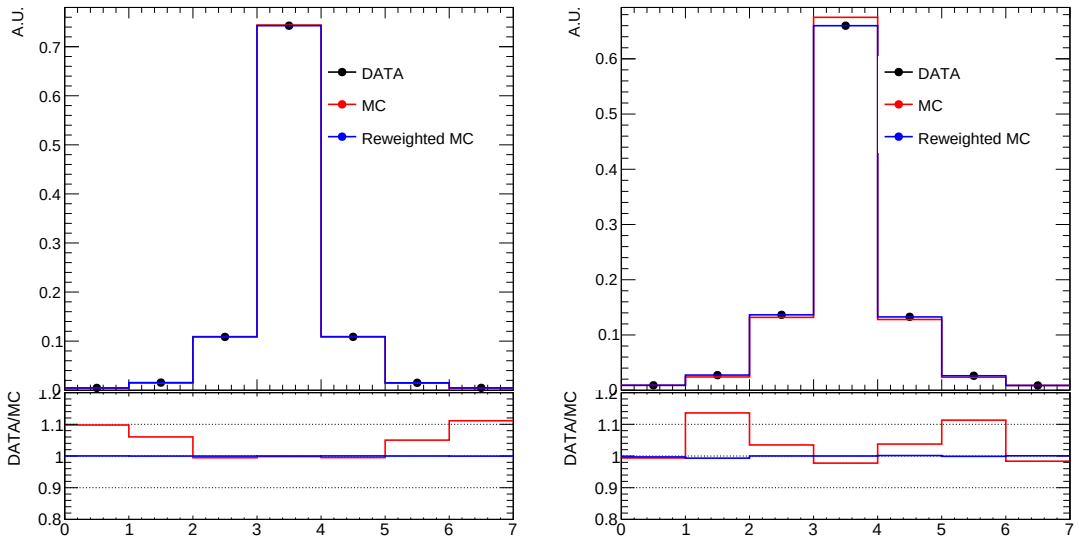

(a) $0.0 < |\eta| < 0.2$ (b) $2.1 < |\eta| < 2.3$

FIGURE 4.15: Lateral energies for electron clusters, for data (in black), and MC before (red) and after (blue) correction, in the unrefined samples. Distributions are normalized to unity. Bottom plots are data to MC ratios.

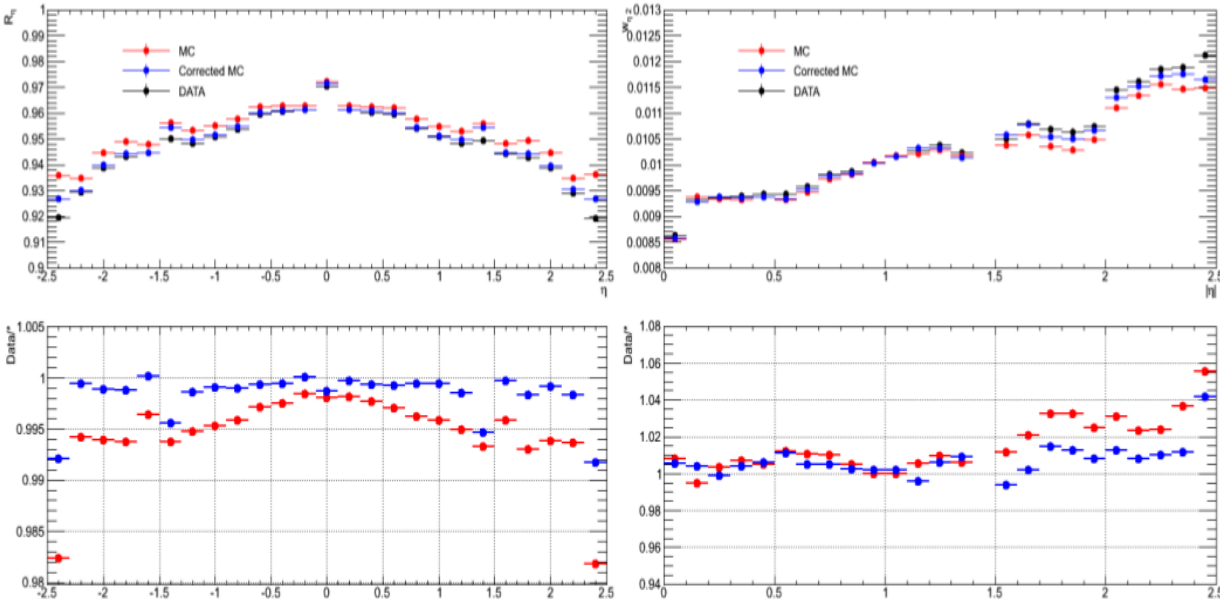

FIGURE 4.16: η-profiles for R_η (left) and $w_{\eta 2}$ (right), for data and MC before and after correction. Bottom plots are data to MC ratios.

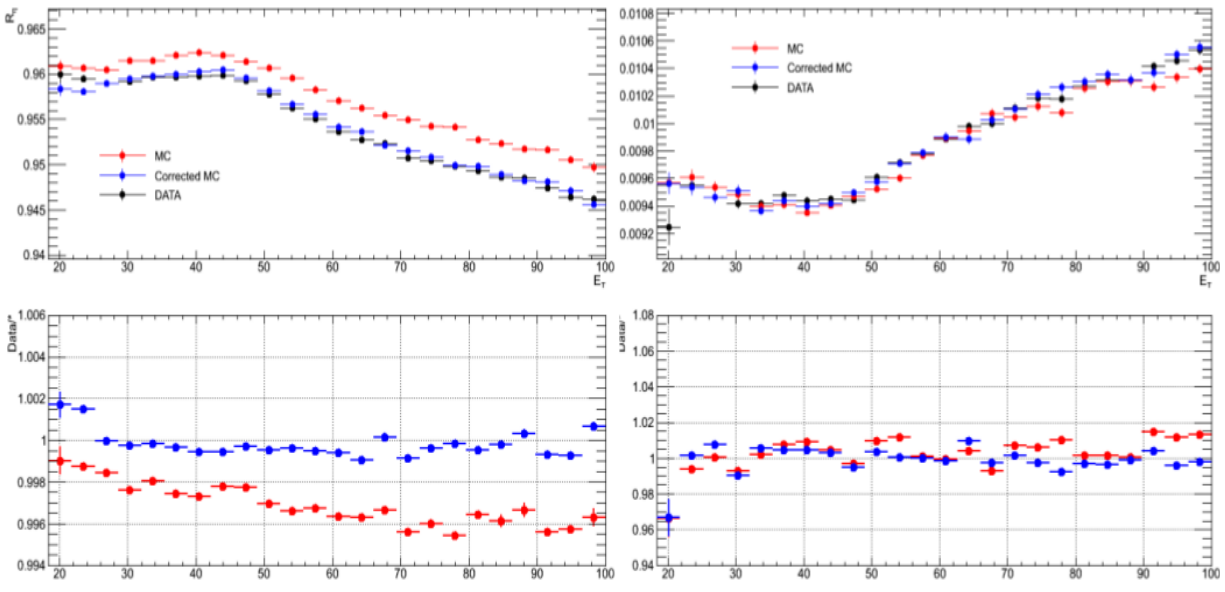

FIGURE 4.17: p_T-profiles for R_η (left) and $w_{\eta 2}$ (right), for data and MC before and after correction, in two particular eta bins. Bottom plots are data to MC ratios.

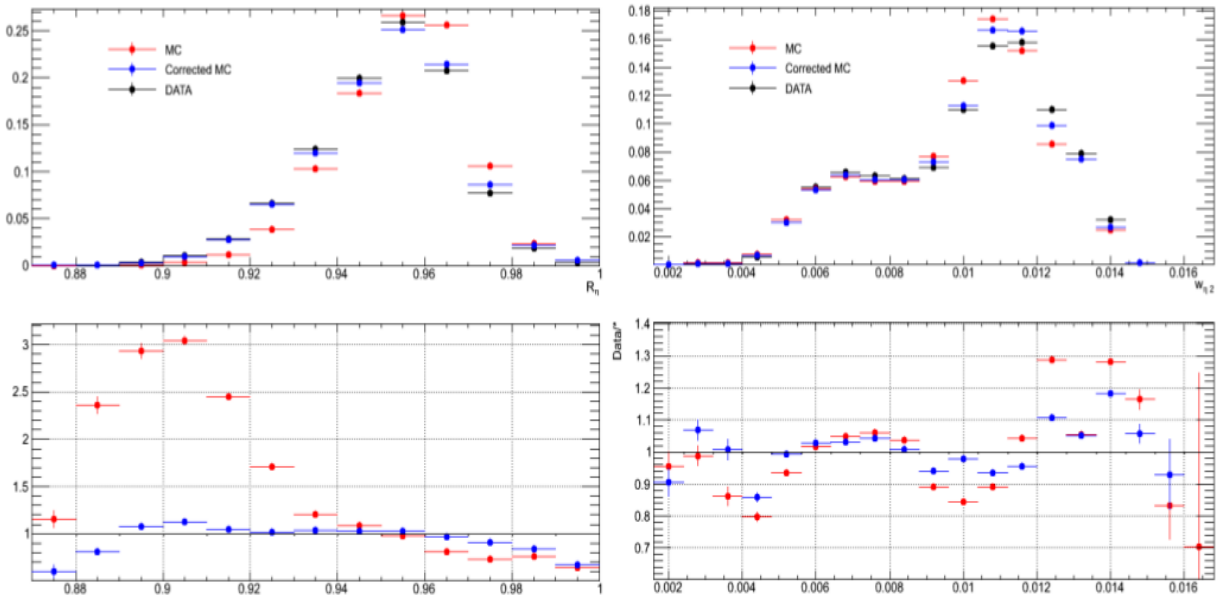

FIGURE 4.18: Distributions of R_η (left) and $w_{\eta 2}$ (right), for data and MC before and after correction, in two particular eta bins. Distributions are normalized to unity. Bottom plots are data to MC ratios.

- **Urban** is used to define the electron scattering version,
- **Brem** determines which Bremsstrahlung definition is used,
- **Conv** precises the used photon conversion description.

The different versions are either 93 or 95, referring to `GEANT4` versions number 9.3 or 9.5. The used samples are generated using POWHEG+PYTHIA8 [33, 72] Monte Carlo generators. They contain $Z \rightarrow ee$ processes, with 500000 events each, and using different combinations of Urban93/Urban95, Brem93/Brem95 and Conv93/Conv95.

In 2011, a better data to MC agreement than in 2012 was noticed in the di-electron invariant mass distribution in Z events, as seen in Fig. 4.3.

The effect reported in Fig. 4.3 as well as the tails seen in shower shapes distributions (cf. section 4.3.1) make it interesting to study the invariant mass tails in the different samples described above. Results are shown in Fig. 4.19, 4.20 and 4.21.

These plots show that there's a significant mass decrease going from Urban93 to Urban95, while a variation in Brem and Conv physics has a less than 5% effect on the tails, confirming that the largest effect on energy response is from Urban95, which makes it useful to better quantify tails with this model.

Several validation studies have also been fulfilled to test whether the different physics lists variations impact the shower shapes or not. In the bottom plots of Fig. 4.22, 4.23, 4.24 and 4.25, the effect of changing the physics list is nothing more than 5‰ when it comes to R_η and $w_{\eta 2}$. This shows that `GEANT4` cannot by itself fix the shower shapes discrepancy, hence the need for an independent correction, like the one proposed in section 4.3.1.

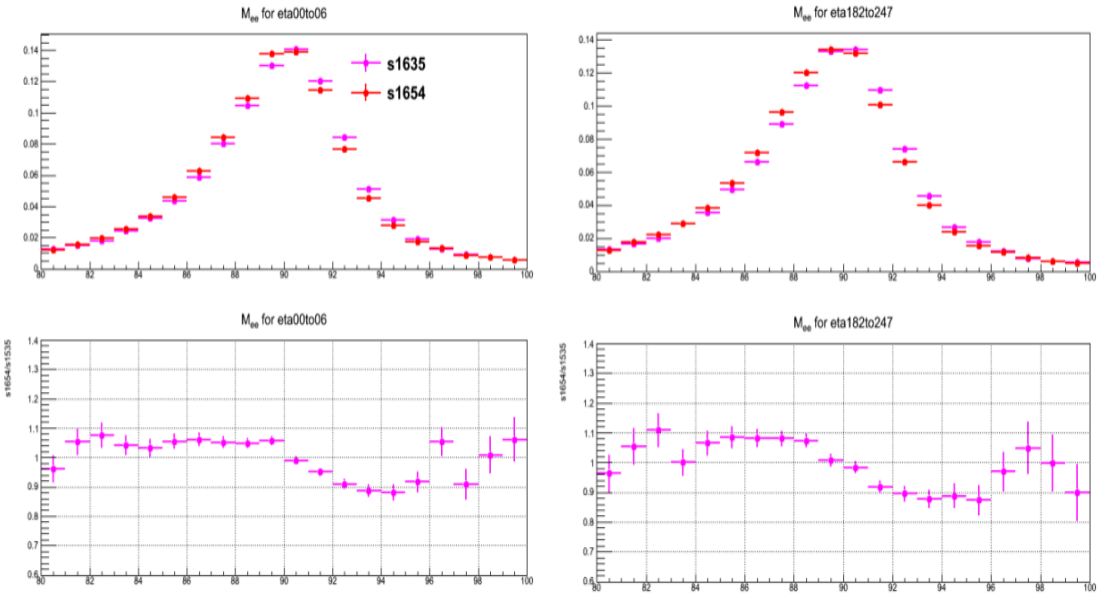

(a) $0.6 < |\eta| < 1.0$ (b) $1.82 < |\eta| < 2.47$

FIGURE 4.19: $m_{e^+e^-}$ distributions, for Urban93 (pink) vs. Urban95 (red) with Brem93 and Conv93, in one typical bin in the barrel (4.19(a)) and another one in the endcap (4.19(b)). Bottom plots are Urban95/Urban93 ratios.

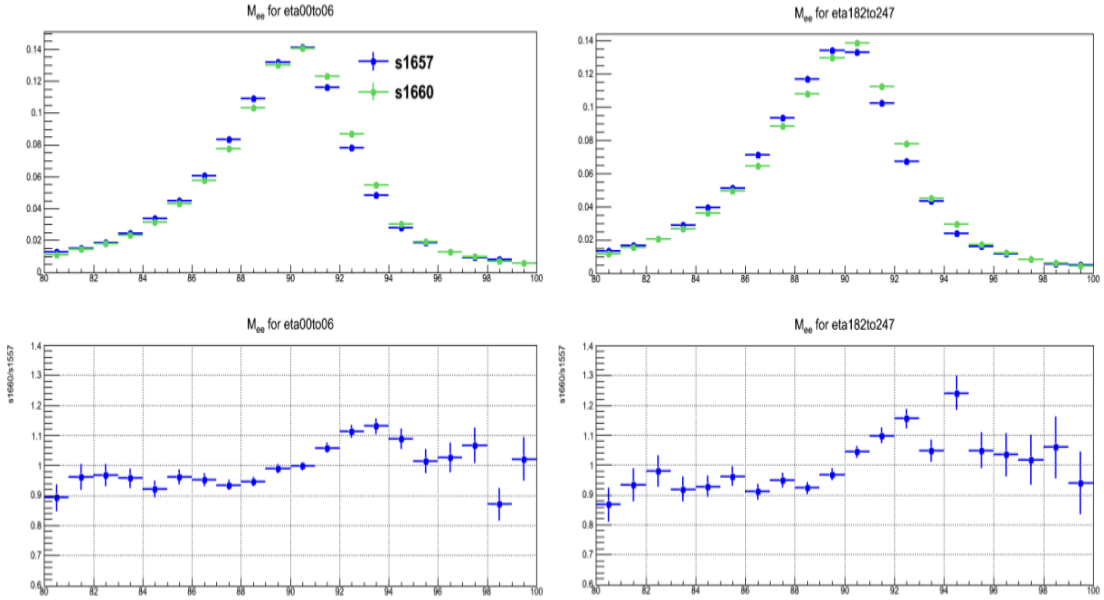

(a) $0.6 < |\eta| < 1.0$ (b) $1.82 < |\eta| < 2.47$

FIGURE 4.20: $m_{e^+e^-}$ distributions, for Urban93 (green) vs. Urban95 (blue) with Brem95 and Conv95, in one typical bin in the barrel (4.20(a)) and another one in the endcap (4.20(b)). Bottom plots are Urban93/Urban95 ratios.

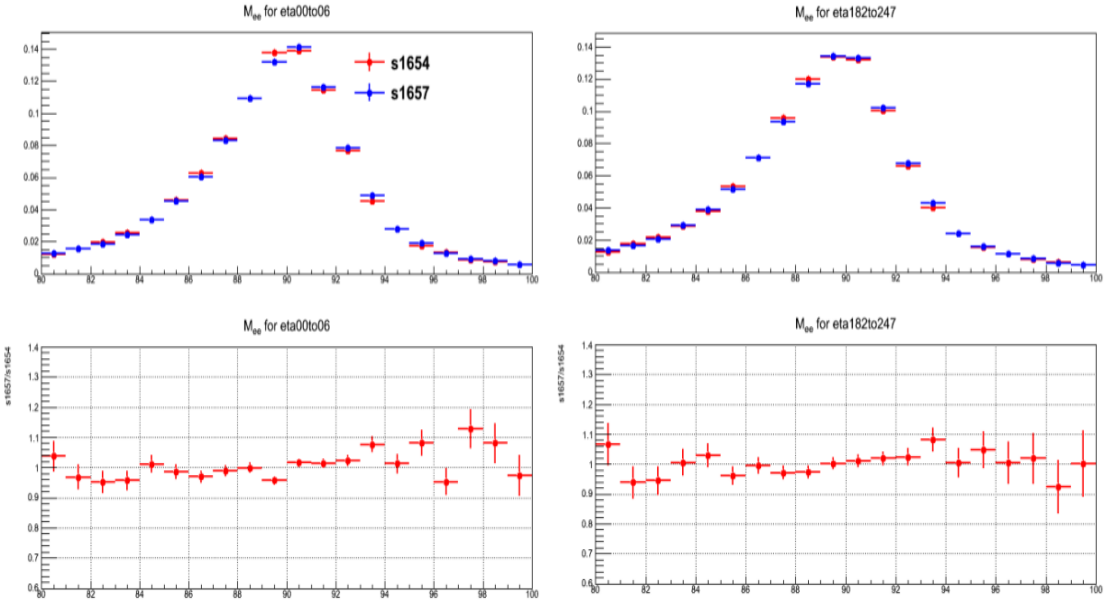

(a) $0.6 < |\eta| < 1.0$ (b) $1.82 < |\eta| < 2.47$

FIGURE 4.21: $m_{e^+e^-}$ distributions, both for Urban95, showing Brem93+Conv93 in red and Brem95+Conv95 in blue, in one typical bin in the barrel (4.21(a)) and another one in the endcap (4.21(b)). Bottom plots are Brem95+Conv95 to Brem93+Conv93 ratios.

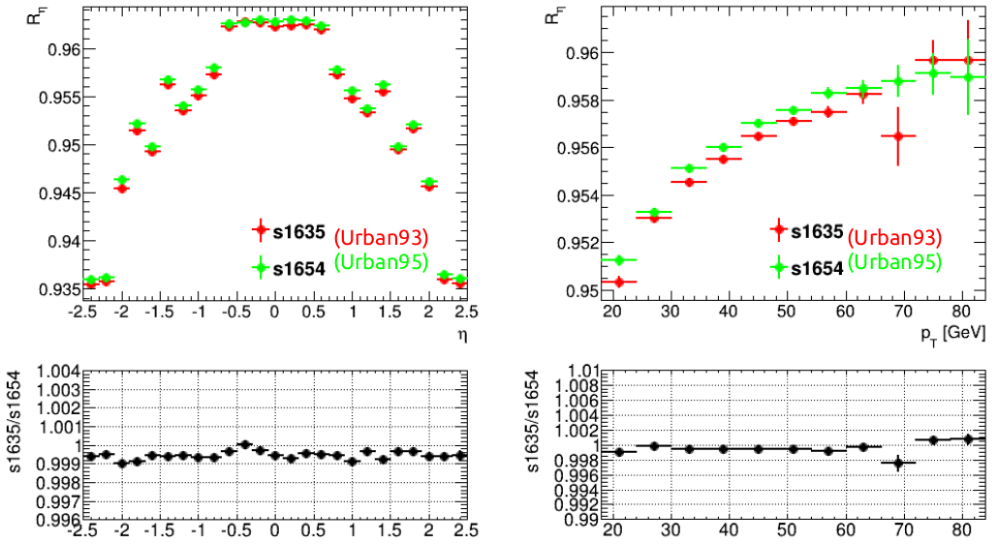

FIGURE 4.22: η-profiles (left) and p_T-profiles (right) for R_η, for Urban93 (red) and Urban95 (green). Both samples have Brem93 and Conv93. Bottom plots are Urban93/Urban95 ratios.

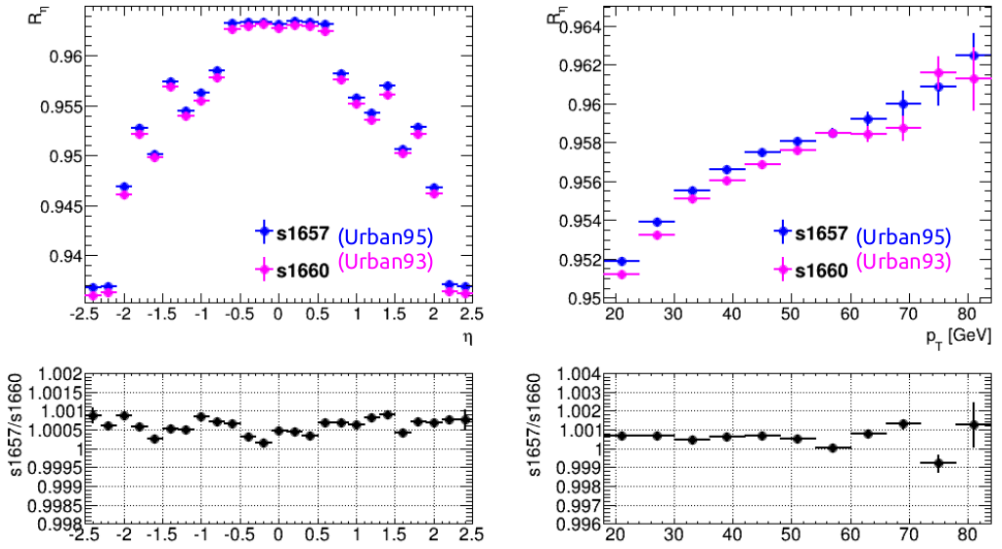

FIGURE 4.23: η-profiles (left) and p_T-profiles (right) for R_η, for Urban93 (pink) and Urban95 (blue). Both samples have Brem95 and Conv95. Bottom plots are Urban95/Urban93 ratios.

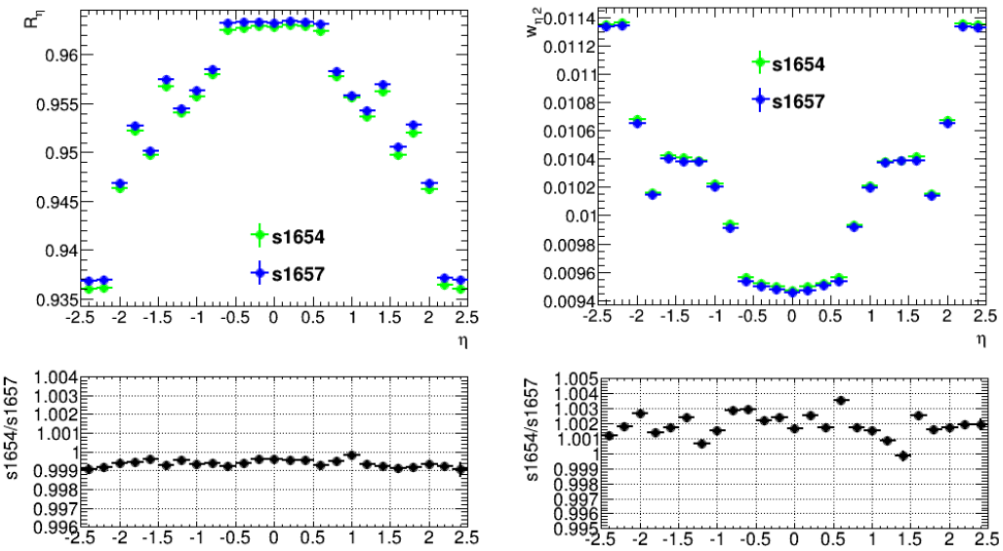

FIGURE 4.24: η-profiles for R_η (left) and $w_{\eta 2}$ (right), for Urban95. The green plots have Brem93 and Conv93, the blue plots have Brem95 and Conv95. Bottom plots are Brem93+Conv93/Brem95+Conv95 ratios.

4.3.4 Optimization of the $w_{\eta 2}$ correction implemented in the ATLAS software

This section suggests a correction function to be applied to the $w_{\eta 2}$ width modulation, in the purpose of increasing the selection efficiency. Fig. 4.26 (top) shows the modulation of $w_{\eta 2}$ vs. η_{rel} , the relative pseudorapidity of the electron inside a given cell, and the corresponding distributions (bottom). Without any corrections (in red), $w_{\eta 2}$ has a quite large modulation. The variable reconstructed with ATLAS software, called here "el_weta2" (in black), has an obviously narrower distribution. This variable is already corrected with a certain function implemented in the software. The goal of the proposed correction is to have the same mean value as el_weta2, while making the η_{rel} modulations as flat as possible (as shown in green).

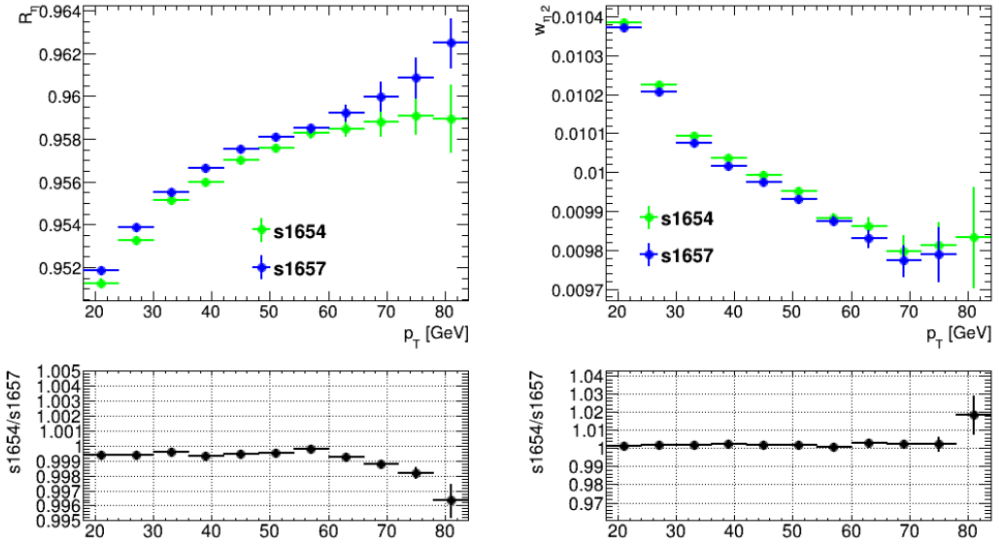

FIGURE 4.25: p_T -profiles for R_η (left) and $w_{\eta 2}$ (right), for Urban95. The green plots have Brem93 and Conv93, the blue plots have Brem95 and Conv95. Bottom plots are Brem93+Conv93/Brem95+Conv95 ratios.

For consistency purposes, the same datasets have been used as in section 4.3.1: 2012 $Z \rightarrow ee$ samples at $\sqrt{s} = 8$ TeV. The same selections are applied as well.

In the following, the variables will be designated as follows: $w_{\eta 2}$ represents the raw value of the variable, without any corrections (ie. computed directly from the cells energies). $w_{\eta 2}^{soft}$ is the software variable, and $w_{\eta 2}^{corr}$ is the one on which the proposed correction is applied.

The method used here is somehow similar to what have been used to get $w_{\eta 2}^{soft}$ (As detailed in [73] and [74]). This new correction involves the use of parameters calculated in 12 eta bins[1], as follows: The η_{rel} profile is divided into three regions: $0 \leq \eta_{rel} < 0.1$, $0.1 \leq \eta_{rel} < 0.9$ and $0.9 \leq \eta_{rel} < 1.0$, and each of the three regions is fitted into a parabola. The extracted parameters are then used to correct $w_{\eta 2}$.

The corrected profiles ($w_{\eta 2}^{corr}$) are compared to $w_{\eta 2}^{soft}$, as shown in the left plots of Fig. 4.27 and 4.28. The same correction has later on been applied to data. The results are in the right hand plots of the same figures, which shows that this approach works for data as well.

4.3.5 Discussion and perspective for m_W measurement

It has been shown that changing the physics lists in `GEANT4` does not significantly affect the shower shapes, but explains the data to MC differences in $m_{e^+e^-}$ tails, when changing from Urban93 to Urban95. This has lead to suggesting two new corrective approaches: one that is extracted from data to simulation ratios, and which corrects the shower variables to give out values that match the experimental data, and another one that, once applied to the $w_{\eta 2}$ variable, reduces its modulations and thus optimizes the efficiency of the selections.

The importance of this work in a W mass measurement context is that it helps to better define electron energies, which is essential for high precision measurements done in the electron

[1] $|\eta| \in [0.0-0.2], [0.2-0.4], [0.4-0.6], [0.6-0.8], [0.8-1.0], [1.0-1.2], [1.2-1.37], [1.52-1.7], [1.7-1.9], [1.9-2.1], [2.1-2.3], [2.3-2.47]$

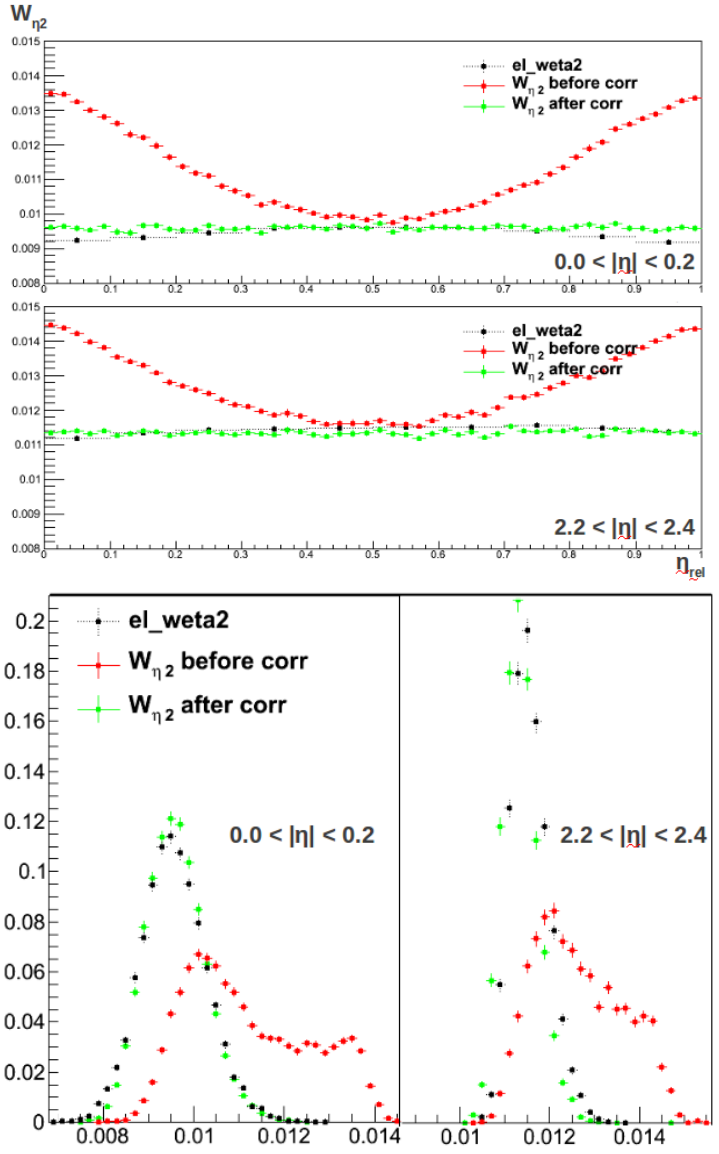

FIGURE 4.26: $w_{\eta 2}$ vs. η_{rel} (top), and $w_{\eta 2}$ distributions, normalized to unity (bottom) for $0.0 < |\eta| < 0.2$ and $2.2 < |\eta| < 2.4$.

channel. The achieved corrections are to be used in an ongoing study on Integrated Simulation Framework which allows to combine accurate and fast detector simulation.

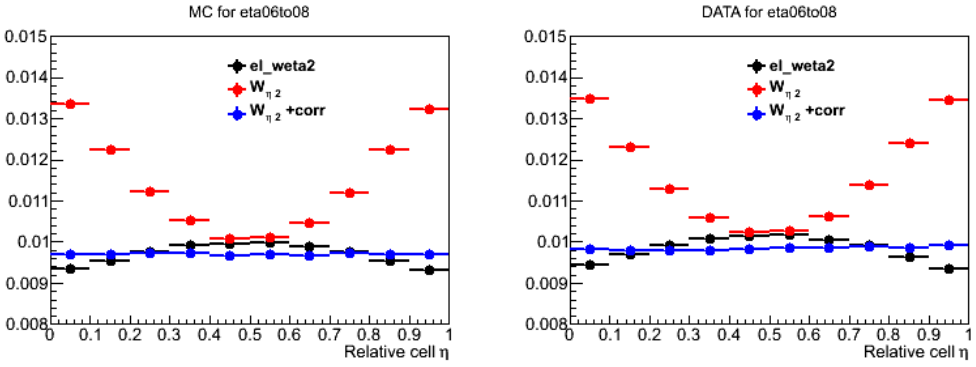

(a) $0.6 < |\eta| < 0.8$

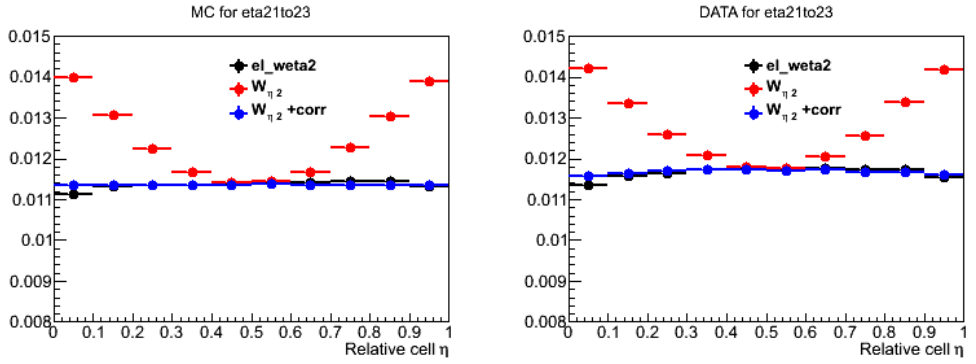

(b) $2.1 < |\eta| < 2.3$

FIGURE 4.27: $w_{\eta 2}$ vs. η_{rel} profiles for MC (left) and data (right). $w_{\eta 2}$ is in red, $w_{\eta 2}^{soft}$ is in black and $w_{\eta 2}^{corr}$ is in blue. Fig. 4.27(a) represents a bin in the barrel, while 4.27(b) is for a bin in the endcap.

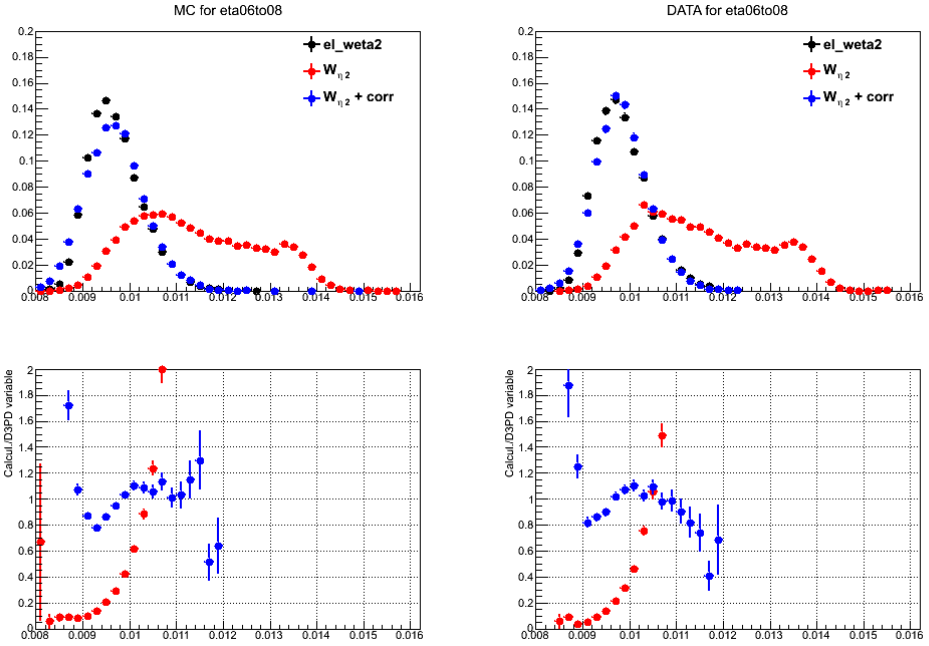

(a) $0.6 < |\eta| < 0.8$

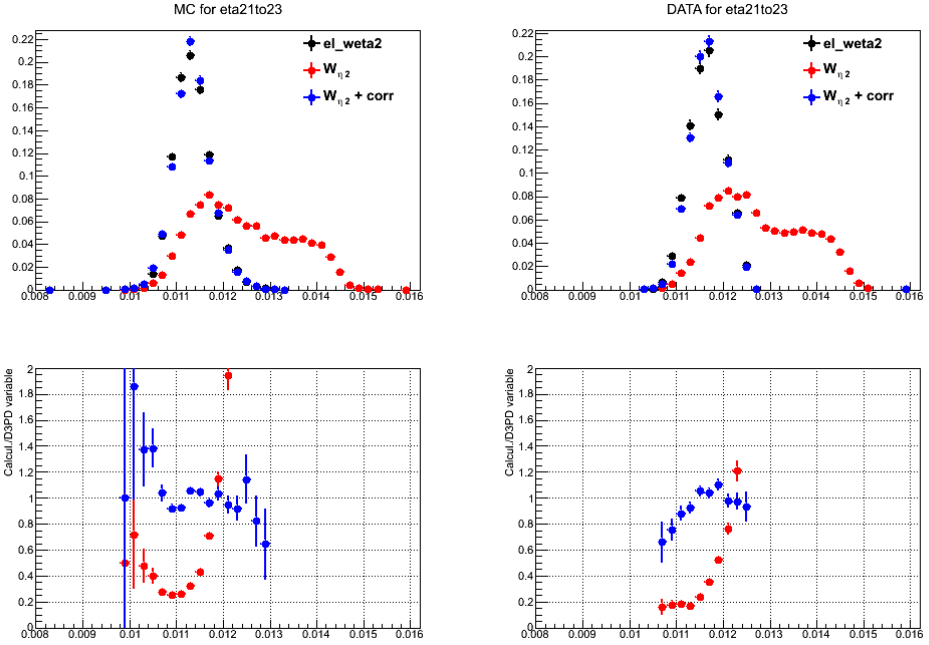

(b) $2.1 < |\eta| < 2.3$

FIGURE 4.28: $w_{\eta 2}$ vs. η_{rel} distributions, normalized to unity, for MC (left) and data (right). $w_{\eta 2}$ is in red, $w_{\eta 2}^{soft}$ is in black and $w_{\eta 2}^{corr}$ is in blue. Bottom plots are ratios wrt. $w_{\eta 2}^{soft}$. The plots show one bin in the barrel (4.28(a)) and another one in the endcap (4.28(b))

Chapter 5

Methodology for the W-Mass Measurement

5.1 Observables used in the Z- and W-mass measurements

W and Z events are detected through their decay products. The decay channel for these two bosons involved in this study is the leptonic channel, where the final state is $\ell\nu_\ell$ for W and $\ell\ell$ for Z, ℓ being either an electron or a muon. The hadronic decays suffer from large backgrounds from jet production, and even if τ modes can be detected, it is not easy to use them for the reason that the τ-lepton produces additional undetected particles in the final state.

Since the parton-parton effective energy in the longitudinal direction cannot be measured, and therefore we cannot reconstruct the longitudinal momentum of the neutrino, it is interesting to reconstruct the observables in the transverse plane with respect to the beam direction. Several observables are used in the m_W measurement, mainly the reconstructed lepton transverse momentum p_{T}^{ℓ}, the reconstructed W transverse mass m_{T} and the missing transverse energy, $E_{\mathrm{T}}^{\mathrm{miss}}$, taking advantage of their Jacobian shape, where the Jacobian peak position holds information on the mass. For Z events, the observables most sensitive to the mass are the lepton p_{T} and the di-lepton invariant mass $m_{\ell\ell}$.

- **Lepton transverse momentum, p_{T}^{ℓ}**
  The transverse momentum of the lepton is the lepton momentum in the plane orthogonal to the beam. For the muon, it is taken as the track momentum $p_{\mathrm{T}}^{\mu} = p_{\mathrm{T}}^{\mu\ (track)}$, and for the electron, it is the ratio of the cluster energy $E_T^{(cluster)}$ measured in the calorimeter with respect to the hyperbolic cosine of the track pseudorapidity $\eta^{(track)}$:

  $$p_{\mathrm{T}}^{e} = \frac{E_T^{(cluster)}}{\cosh \eta^{(track)}} \tag{5.1}$$

  It is illustrated in Fig. 5.1(a). The Jacobian peaks at around $m_W/2$. Measuring the W-mass by means of the lepton transverse momentum requires a good control of the W-p_{T}. In addition, a well-defined detector calibration and energy resolution is needed for an accurate momentum reconstruction (§ 5.3).

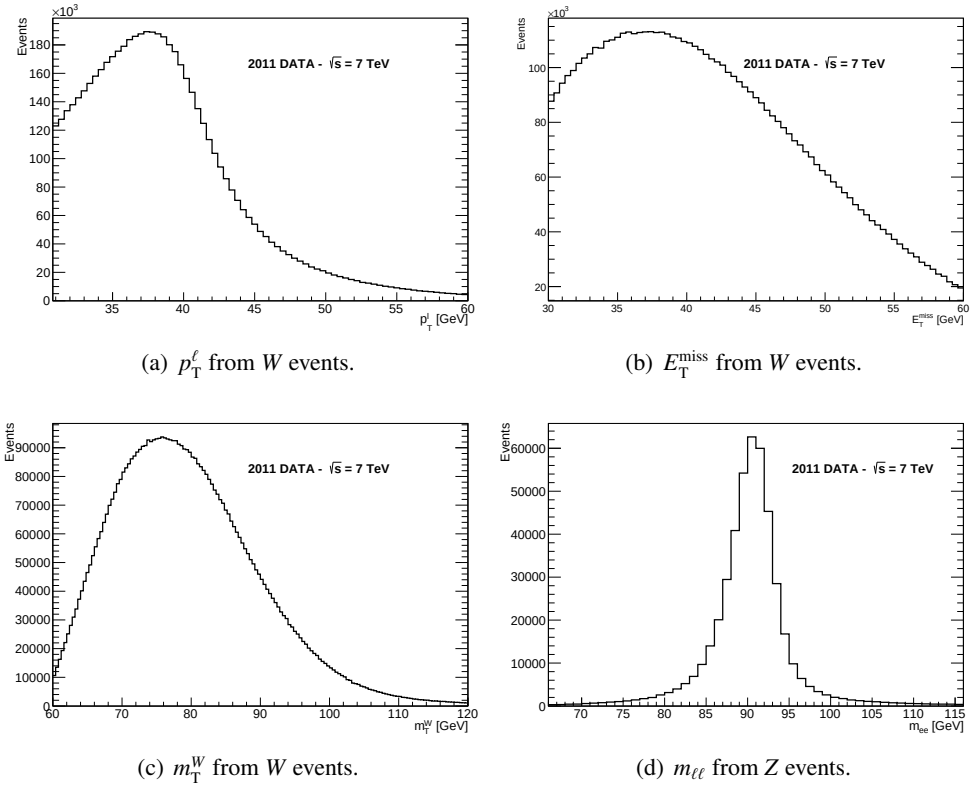

(a) p_{T}^{ℓ} from W events.

(b) $E_{\mathrm{T}}^{\mathrm{miss}}$ from W events.

(c) m_{T}^{W} from W events.

(d) $m_{\ell\ell}$ from Z events.

FIGURE 5.1: Distributions of the observables used in the Z and W mass measurements.

- **Missing transverse energy, $E_{\mathrm{T}}^{\mathrm{miss}}$**
  In the case of production of invisible particles, the transverse momentum of the latter is equal to the missing transverse energy, $\overrightarrow{E_{\mathrm{T}}^{\mathrm{miss}}}$ given by:

$$\overrightarrow{E_{\mathrm{T}}^{\mathrm{miss}}} = -\sum_{i} \overrightarrow{p_{\mathrm{T}}(i)} \tag{5.2}$$

  where i represents all visible final state particles and $\overrightarrow{p_{\mathrm{T}}(i)}$ their transverse momentum.

  This variable is useful in W-studies since a large $E_{\mathrm{T}}^{\mathrm{miss}}$ value signals the presence of the undetected neutrino: it is inferred from the transverse energy imbalance between the initial and the final states. In an analogy with the detected lepton transverse momentum, this observable is seen as the neutrino transverse momentum and used to reconstruct the boson mass. However, at the LHC, given the large amount of interactions per bunch crossing, this distribution suffers from a poor resolution and is not used in this study. It is illustrated in Fig. 5.1(b).

- **Transverse mass, m_{T}**
  The transverse mass is given by the following expression:

$$m_{\mathrm{T}} = \sqrt{2p_{\mathrm{T}}^{\ell}E_{\mathrm{T}}^{\mathrm{miss}}(1-\cos(\Delta\phi))} \tag{5.3}$$

  where $\Delta\phi$ is the azimuthal angle between the lepton and the neutrino, p_{T}^{ℓ} the previously defined transverse momentum of the lepton, and $E_{\mathrm{T}}^{\mathrm{miss}}$ the missing transverse energy deduced from the hadronic recoil (§ 5.3.4) and corrected as described in § 5.4. If well

C.L.	1 parameter	2 parameters	3 parameters
68% (1σ)	1.00	2.30	3.50

TABLE 5.1: χ^2 differences (δ) above minimum, at 68% confidence level, for one, two and three parameters.

defined, the corresponding distribution is a Jacobian and peaks at m_W (Fig. 5.1(c)).

- **Invariant mass, $m_{\ell\ell}$**
  In Z studies, the dilepton invariant mass $m_{\ell\ell}$ (Fig. 5.1(d)) is used to calculate the Z-mass. $m_{\ell\ell}$ peaks at m_Z and is defined as:

$$m_{\ell\ell} = \sqrt{2E_1E_2(1-\cos\theta_{12})} \tag{5.4}$$

  where E_1 and E_2 are the energies of the first and second lepton, and θ_{12} is the angle between them.

5.2 Measurement method and uncertainty propagation

5.2.1 Mass fits and statistics

The W mass measurement method adopted in the ATLAS collaboration is described in detail in Ref. [75–81] and summarized in this chapter.

The mass measurement is done by comparing the previously described observables between data and a set of templates. These templates are built by reweighting the distributions of these observables to different values of W-mass, in known steps within a known interval around a reference mass, m_{ref}, usually taken as the world average (80385 MeV). The template which best fits the data gives the value of the extracted mass.

The statistical comparison of the signal to the templates can be performed in various ways. Throughout this study we will use a Least Squares method, represented by the χ^2 function. χ^2 is computed for a given histogram as follows:

$$\chi^2 = \sum_{i=1}^{N} \frac{(n_i^{obs} - n_i^{exp})^2}{\sigma_i^2} \tag{5.5}$$

where i represents each bin, N the total number of bins, n_i^{obs} and n_i^{exp} are respectively the number of entries in bin i observed in the signal and expected from the template. $\sigma_i = \sigma_i^{obs} \oplus \sigma_i^{exp}$ is the statistical uncertainty on $n_i^{obs} - n_i^{exp}$. This approach is valid when all uncertainties are Gaussian. We can justify the use of a Gaussian approach by the availability of large statistics used in this study.

The Least Squares method consists of minimizing the χ^2 *i.e.* minimizing the difference between n_i^{obs} and n_i^{exp}. The contour in the parameter space corresponding to one standard deviation (at 68% Confidence Level) from the minimal χ^2 is $\chi^2 + \delta$, where δ is given in Table 5.1 depending on the number of parameters. In the case of one parameter, the number of degrees of freedom is equal to $n_{\text{dof}} = N - 1$.

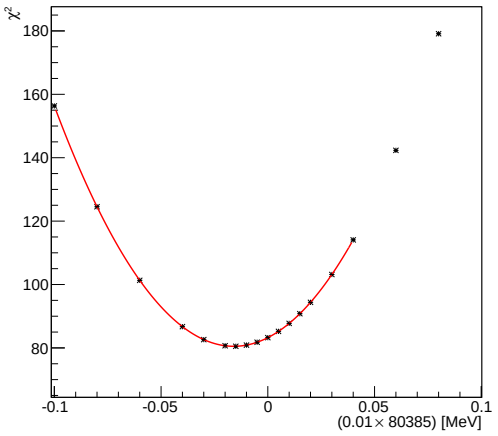

FIGURE 5.2: Example of a χ^2 profile fitted with a parabola (red line). The minimum of the χ^2 gives the value of the extracted mass.

The reason behind the usage of this method is mainly the absence of knowledge of an analytical description of the kinematic distributions used for the measurement. Fig. 5.2 is an example of a χ^2 profile, fitted with a parabolic function, and where each point represents a given template.

The total statistical uncertainty can be estimated from the width of the χ^2 parabola:

$$\sigma_i = \sigma_i^{obs} \oplus \sigma_i^{exp} \tag{5.6}$$

In order to minimize the possibility of a personal and subjective bias in the measurement, a blinding was introduced by shifting the reweighted mass by a random value. The same blinding shift is introduced to W^+ and W^-, and is reflected in the fitting results. The unblinding happens when the results give the same mass for W^+ and W^-, when the mass shows a consistent value in all analysis regions (the analysis is performed in bins of pseudorapidity and average number of interactions per bunch crossing, see Chapter 7) and finally when the electron and muon channels give similar results.

5.2.2 Systematic uncertainty propagation

Systematic uncertainties are extracted with a χ^2 method similar to the one described in § 5.2.1. In some cases, the uncertainty δm is parametrized by a single parameter P. However, one can also encounter a case where the uncertainty is parametrized by multiple parameters, P_i, usually correlated. Both of these scenarios, as well as a treatment for correlated uncertainties, are detailed in what follows.

1. **Single parameter case: "Offset Method"**

   The systematic uncertainty relies on a single parameter when the kinematic distributions for a given m are affected by a physics effect which can be summarized in one parameter, P. Suppose P takes the values $p \pm \delta p$. Instead of fitting the different templates to the signal data, one fits a nominal template with the central value p injected, with templates

containing variations of P within $p \pm \delta p$, called pseudo-data. If we call m_0 the extracted mass with the nominal template and m the mass from the pseudo-data, the largest bias $\delta m = m - m_0$ is noted as an uncertainty induced by the parameter P.

This procedure introduces an "offset" to the parameter value which is propagated to the mass *via* the pseudodata used in the mass fit, and will result in the mass bias extracted as an uncertainty. An example for using this method is when dealing with the energy scale uncertainties (detailed in § 5.3.2).

2. **Multiple parameters: "Toy Monte-Carlo"**

When dealing with systematics deriving from multiple parameters, such as the efficiency scale factors (discussed in § 5.3.2), another uncertainty propagation method needs to be adopted. Considering a multiple parameters scenario, where P_i are the said parameters taking the values $p_i \pm \delta p_i$, an idea is to use a Monte-Carlo method called "Toy Monte-Carlo", to propagate the uncertainty from the parameters to the mass, without having to generate new samples for every configuration of the different $p_i \pm \delta p_i$ values.

In this case, a simplified model of the measurement is adopted and a large number N of toys are built, such that the parameters values p_i for each of the N toys are modified as follows:

$$\widetilde{p_i^k} = p^k + \Delta p^k_{\text{stat+uncorr}} \cdot g_i + \sum_{s=1}^{S} \Delta p^k_{\text{cor},s} \cdot g_{i,s} \tag{5.7}$$

In eq. 5.7, $\widetilde{p_i^k}$ is the variation of the parameter value for the toy i, for each bin k of a given distribution. p^k is the central value in this bin, and the toys are generated with a random seed following a Gaussian $g_i \in \text{Gauss}(0, 1)$. $g_{i,s}$ is the same random number for all bins k in a given Toy Monte Carlo i. This procedures takes into account uncorrelated ($\Delta p^k_{\text{stat+uncorr}}$) and correlated ($\Delta p^k_{\text{cor},s}$) uncertainties.

The propagation of the uncertainties on the mass gives a gaussian m_W behavior. The resulting uncertainty is therefore estimated from the RMS of the fitted m_W distribution.

3. **Combining correlated parameters: covariance matrix diagonalization**

One can encounter a case where several correlated parameters give rise to correlated uncertainties. This is the case of PDF uncertainties (§ 5.4.3) and the uncertainties arising from Parton Shower modeling (§ 5.4.4), where it is essential to have the parameters decorrelated.

Suppose we have a set of n parameters $x_1, \ldots, x_n$, and their covariance matrix:

$$V_{ij} = \text{cov}[x_i, x_j] = E[(x_i - \mu_i)(x_j - \mu_j)] \tag{5.8}$$

where $\mu_i = E[x_i]$ is the expected value of x_i. If the x_i are correlated, the off-diagonal elements of the covariant matrix are non-zero. In this case, we define a new diagonal covariance matrix $U_{ij} = \text{cov}[y_i, y_j]$ for a new set of n parameters, y_i that are not correlated. This transition is always possible with a linear transformation [82]:

$$y_i = \sum_{j=1}^{n} A_{ij} x_j, \tag{5.9}$$

where A_{ij} are the combination coefficients of y_i and x_j. The covariance matrix for the new parameters y_i will be:

$$U_{ij} = \text{cov}[y_i, y_j] = \sum_{k,l=1}^{n} A_{ik} V_{kl} A_{lj}^T = AVA^T \tag{5.10}$$

For the equation 5.10 to be solved, we find a matrix A such that $U = AVA^T$ is diagonal, having:

$$A_{ij} = \frac{\partial y_i}{\partial x_j} \tag{5.11}$$

The eigenvalues of each of the found A matrices will be used to generate pseudo-data, which will later be fitted to the original template. This method is used in Chapter 6.

5.3 Detector-level corrections and uncertainties in the electron channel

The uncertainties arising in the course of a measurement are due to the detector's imperfect calibration or to imperfect methods of observation, they could also result from a weak estimate of a physics law. A precise measurement relies on well-evaluated uncertainties. On the other hand, the fitted observables in the W-mass measurement need to be accurately reconstructed from data and modeled in MC. Several corrections and reweightings are performed throughout the analysis before getting to the mass measurement. The main corrections as well as sources of uncertainties involved in the W-mass measurement are summarized hereafter.

5.3.1 Pile-up and Primary Vertex z-position reweighting

The effect of multiple interactions per bunch crossing ("pile-up") is modeled by overlaying simulated minimum bias events over the original hard-scattering event. A reweighting is applied to reproduce the distribution of the average number of interactions per bunch crossing in data. Furthermore, the simulation is reweighted such that the vertex z position match the one observed in the data. These two reweightings are purely correctional and do not directly induce uncertainties on the mass measurement.

5.3.2 Energy scale and resolution

A disagreement was observed between data and Monte Carlo in Z decays. The detector calibration needs to be understood and optimized: a complete electron and photon calibration study for the first run of the LHC is described in Ref. [83], and summarized hereafter for electrons.

The main corrections are applied on the energy scale and resolution of the Z resonance. The measured electron energy is given by:

$$E^{meas} = E^{data} = E^{true}(1 + \alpha_i) \tag{5.12}$$

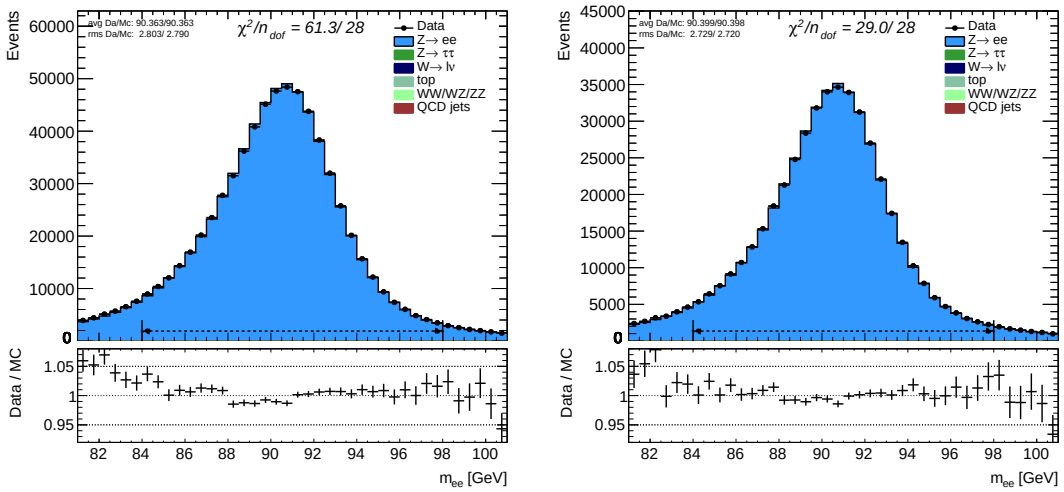

(a) $0.0 < |\eta| < 1.37 + 1.52 < |\eta| < 2.47$

(b) $0.0 < |\eta| < 1.2 + 1.82 < |\eta| < 2.47$

FIGURE 5.3: Agreement between data and simulation for m_{ee} excluding only the nominal transition region, 1.37< $|\eta|$ <1.52 [5.3(a)], and excluding the region 1.2< $|\eta|$ <1.82 [5.3(b)].

E^{true} is the true electron energy and α_i is the energy scale in a phase space i, usually corresponding to a region in pseudorapidity. α_i reflects the mis-calibration due to calorimeter inhomogeneities or imperfect simulation of passive material.

The fractional energy resolution is parametrized as:

$$\frac{\sigma_E}{E} = \frac{a}{\sqrt{E}} \oplus \frac{b}{E} \oplus c \tag{5.13}$$

where a is the sampling term, b is the noise term and c is the constant term and a, b and c are η-dependent. A smearing correction is derived for the MC under the assumption that the sampling term a is well modeled by the simulation. The noise term b used in the simulation is taken from calibration runs, so that any additional resolution correction must be proportional to the energy, as an additional constant term c_i in a range in pseudorapidity labelled i, *i.e.*

$$\sigma_E^{data} = \sigma_E^{MC} \oplus c_i \times E \tag{5.14}$$

Fig. 5.3(a) shows the invariant mass of the di-electron system in the $[0.0 - 1.37] \cup [1.52 - 2.47]$ absolute pseudorapidity region. The result is not at the level of precision needed for the W boson mass measurement. Several tests were performed, only to find that excluding the $1.2 < |\eta| < 1.82$ region, which is the least understood part of the detector, improves the data-simulation agreement to a sufficiently satisfying level for the W mass measurement. The improved agreement is shown in Figure 5.3(b).

The energy scale measurement uncertainties are summarized in Table 5.2, along with the statistical precision on the energy scales and the corresponding estimation of their impact on the W mass. In this table, "EW background" refers to the electroweak background impact, "Mass window" shows the uncertainties coming from varying the invariant mass range over which the

Variation \ η-bin	[-2.4,-1.82]	[-1.2,-0.6]	[-0.6,0.0]	[0.0,0.6]	[0.6,1.2]	[1.82,2.4]	Total
EW background (10^{-5})	5.0						
Mass window (10^{-5})	4.3	-2.9	2.4	-1.4	-4.9	-1.9	1.3
Closure (10^{-5})	2.4	2.0	8.7	-0.5	-1.8	10.0	2.1
Statistic (10^{-5})	24.6	16.9	14.7	14.9	16.9	24.6	7.2
Total$^{\text{Syst}}$ (10^{-5})	26.2	18.0	18.5	15.8	18.4	27.4	9.2
δ^{Syst}m$_W$ (MeV)	22.0	15.1	15.6	13.3	15.5	23.0	7.7
m$_Z$ uncertainty (MeV)	2.1						
FSR $O(\alpha)$ (MeV)	0.4						
δ^{total}m$_W$ (MeV)	22.1	15.3	15.7	13.5	15.6	23.1	8.0

TABLE 5.2: Summary of electron energy scale uncertainties as estimated from $Z \to ee$ decays and expected impact on the measurement of m_W in different bins of pseudo-rapidity.

fit was performed, "Closure" refers to the non-closure problem in the resolution difference between data and Monte Carlo, detailed in Ref. [84]. The "m_Z uncertainty" and "FSR" (Final State Radiation) are modeling uncertainties and will be discussed in § 5.4.

In Table 5.2, the first block shows the uncertainty considered as correlated within a large η-bin but uncorrelated from one large η-bin to another, whereas the second block shows correlated uncertainties. The total shown as last column is a combination made using the number of events per bin. The impact on m_W is assessed using p_{T}^{ℓ} fits, similar results are obtained with m_{T}^{W} fits.

Other sources of uncertainties, not shown in Table 5.2, impact the calibration. They regard passive material uncertainties, liquid argon cell calibration, the relative layer calibration, electronics gain, etc., and are noted by "Detec" in what follows. The detector uncertainties are shown in Table 5.3 using p_{T}^{ℓ} fits and Table 5.4 using m_{T} fits. The total resulting numbers are gathered in Table 5.5 along with the ones from energy scale and their combination is performed to get the total systematic uncertainties on the W mass measurement, due to the calibration procedure.

Variation \ $\lvert\eta\rvert$-bin	[0,0.6]	[0.6,1.2]	[1.82,2.4]	η-combined
Total δm_W (MeV)	4.9	7.4	4.6	4.2
Stat (MeV, for info only)	14.0	14.0	16.0	8.0

TABLE 5.3: Combination of the detector systematic uncertainty sources in $|\eta|$-bins, using p_{T}^{ℓ} distribution, and the statistical uncertainty.

Variation \ $\lvert\eta\rvert$-bin	[0,0.6]	[0.6,1.2]	[1.82,2.4]	η-combined
Total δm_W (MeV)	5.4	7.2	5.1	4.5
Stat (MeV, for info only)	19.0	20.0	22.0	12.0

TABLE 5.4: Combination of the detector systematic uncertainty sources in $|\eta|$-bins, using m_{T}^{W} distribution, and the statistical uncertainty.

5.3.3 Electron selection efficiency

The electron selection efficiency is the ratio of the number of electrons passing specific selection criteria to the number before selection. The electron reconstruction and identification efficiency

	p_{T}^{ℓ}	m_{T}^{W}
$\delta^{\mathrm{Detect}} m_W$ (MeV)	4.2	4.5
$\delta^{\mathrm{Escale}} m_W$ (MeV)	8.0	8.0
$\delta^{\mathrm{Calib}} m_W$ (MeV)	9.0	9.2

TABLE 5.5: Uncertainty on W mass measurement obtained with transverse lepton momentum and transverse mass coming from the calibration procedure and the energy scales estimation. Their combination is shown as a final estimation for the complete calibration procedure for electrons.

measurements and systematics are detailed in Ref. [85]. In the m_W context, the efficiencies dependence on the transverse energy induces a direct experimental uncertainty on the lepton transverse momentum, and has a small impact on the transverse mass.

The electron efficiency factor ε_{e} is given by:

$$\varepsilon_{\mathrm{e}} = \prod_{i=0}^{n} \varepsilon_i \tag{5.15}$$

where i represents any selection such as cluster reconstruction, electron reconstruction, electron identification (which comprises several conditions including shower shape variables, the electron's energy, track and isolation. Such conditions are labelled "*loose*", "*medium*" or "*tight*" depending on the strictness of the selections. They are detailed in Table 7.2. Only tight scale factors are discussed here since the analysis involve tight electrons), trigger, isolation, etc. and ε_i in eq. 5.15 would therefore be:

- $\varepsilon_{\mathrm{cluster}}$ = efficiency to reconstruct an electromagnetic cluster.
- $\varepsilon_{\mathrm{reco}}$ = electron reconstruction algorithm efficiency given the cluster.
- $\varepsilon_{\mathrm{id}}$ = efficiency of identification criteria with respect to the reconstructed electron candidates.
- $\varepsilon_{\mathrm{trig}}$ = efficiency of trigger selection with respect to the reconstructed electron candidates passing the identification criteria.
- $\varepsilon_{\mathrm{iso}}$ = efficiency of the applied isolation cuts.

The efficiencies of the selections differ between data and simulation, and therefore efficiency scale factors (SF) need to be computed as data to simulation efficiency ratios:

$$\mathrm{SF}_i = \frac{\varepsilon_i^{\mathrm{data}}}{\varepsilon_i^{\mathrm{MC}}} \tag{5.16}$$

In the m_W analysis, the involved scale factors are those of the electron reconstruction, identification and isolation, and of the trigger. The computation in Ref. [85] was performed for three channels ($Z \to ee$, $W \to e\nu$, $J/\psi \to ee$) in bins of transverse energy (E_{T}) and pseudorapidity (η).

η range	-2.4, -1.8	-1.2, -0.6	-0.6, 0	0, 0.6	0.6, 1.2	1.8, 2.4	Full range
Reco	18	12	11	13	14	17	6.8
ID (Tight)	19	15	13	13	15	20	6.7
Trigger (w.r.t Tight)	1.7	0.3	0.2	0.2	0.3	2.0	0.8
δm_{W} (Tight)	26	19	17	18	21	26	9.5

TABLE 5.6: Impact of electron efficiency scale factor uncertainties on the measurement of m_{W}, in MeV, when using the electron p_{T} distribution, in different η ranges.

η range	-2.4, -1.8	-1.2, -0.6	-0.6, 0	0, 0.6	0.6, 1.2	1.8, 2.4	Full range
Reco	15	10	10	11	12	15	6.0
ID (Tight)	15	12	11	11	12	17	5.7
Trigger (w.r.t Tight)	1.7	0.5	0.5	0.5	0.5	2.2	0.9
δm_{W} (Tight)	21	16	15	16	17	23	8.3

TABLE 5.7: Impact of electron efficiency scale factor uncertainties on the measurement of m_{W}, in MeV, when using the M_T distribution, in different η ranges.

The uncertainty propagation is achieved through a set of toy experiments as described in § 5.2.2, by creating pseudodata distributions for a fixed value of m_W, but randomly varying the efficiency corrections within their uncertainties. A template fit is performed for each pseudo-experiment, using template with nominal efficiency corrections, and the spread of the fit results is used to estimate the induced uncertainty. A few of these spreads are shown in Fig. 5.4 when using p_{T}^{ℓ} fits and in Fig. 5.5 when using m_{T}^{W} for different scale factors in one particular η-bin ($0.0 < |\eta| < 0.6$). The induced uncertainties on the W-mass based on 2500 toys and in the region $0.0 < |\eta| < 1.2 \cup 1.8 < |\eta| < 2.4$ are noted in Table 5.6 for the p_{T}^{ℓ} fits, and Table 5.7 for the m_{T}^{W} fits.

5.3.4 Recoil energy scale and resolution

The hadronic recoil is calculated as the vectorial sum of all reconstructed transverse energies in the calorimeter system:

$$\vec{u} = \sum_{i=0}^{N} \overrightarrow{E_T^i} \tag{5.17}$$

where i represents all topo-clusters (noise-suppressed clusters required to have one cell with a threshold of 4σ deviation from the baseline noise rate) in the calorimeter, excluding those close to the decay leptons and those from secondary vertices. The reconstructed hadronic recoil is decomposed into parallel ($u_{\parallel} = u_x.v_y - u_y.v_x$) and perpendicular ($u_{\perp} = \vec{v_{xy}}.\vec{u}$) components, by projecting on the transverse momentum of the vector boson as illustrated in Fig. 5.6. On average, the perpendicular component is zero, while the parallel component reflects the negative absolute value of the vector boson transverse momentum.

Since the transverse momentum of the Z boson can be determined via the hadronic recoil measurement, but also via the precise measurement of the 4-vectors of its decay leptons, a data-driven calibration of the hadronic recoil measurements is possible. The reconstruction of the

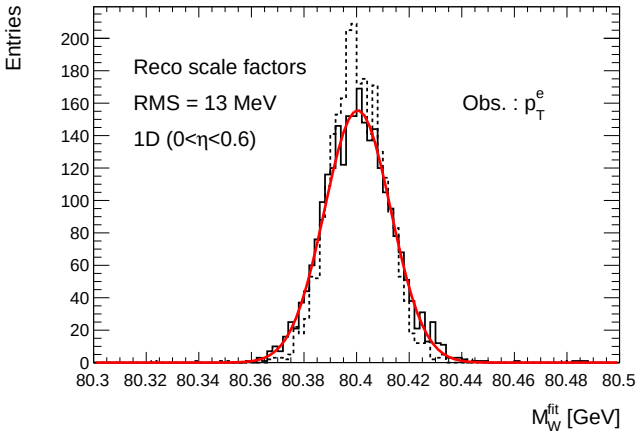

(a) Reco SF

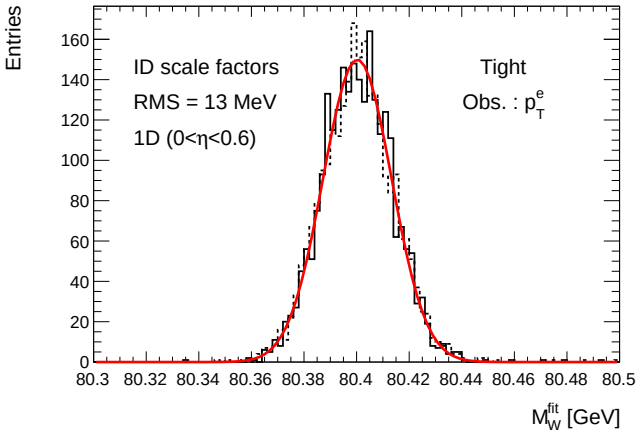

(b) Tight ID SF

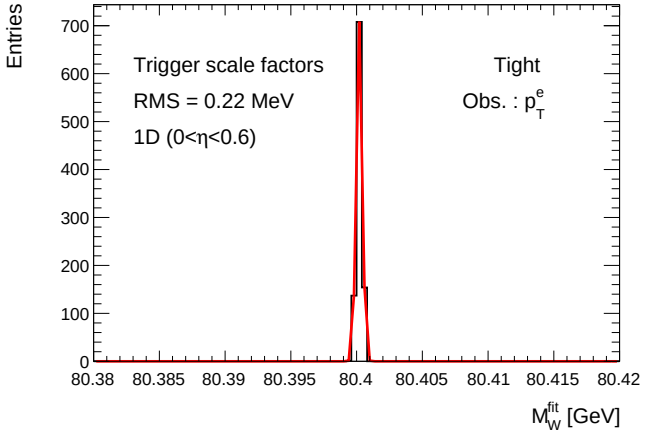

(c) Tight Trigger SF

FIGURE 5.4: W boson mass distribution extracted from different efficiency scale factor variations, when the mass fit is performed using the electron p_T distribution for $30 < p_T < 50$ GeV [77]. The RMS of the fitted distribution indicates the corresponding uncertainty.

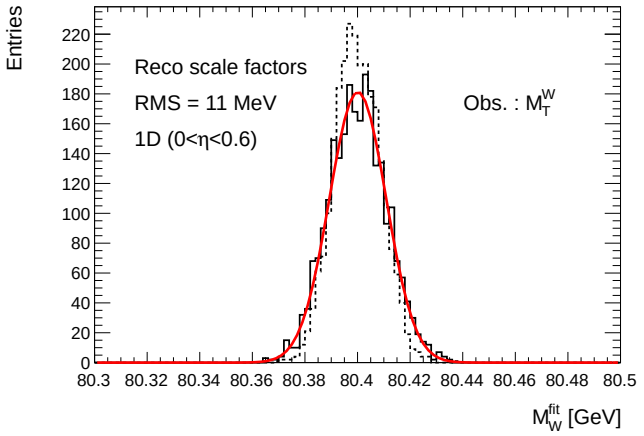

(a) Reco SF

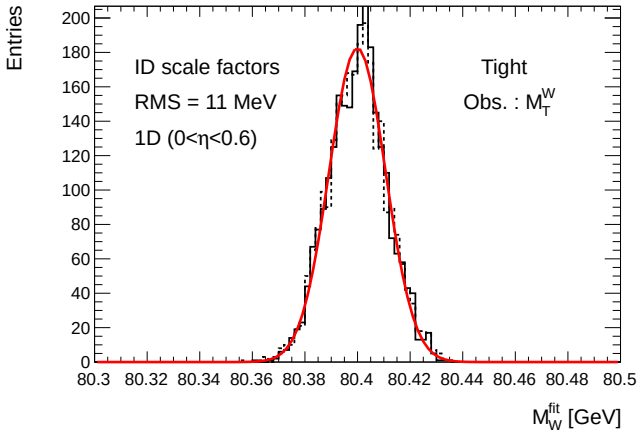

(b) Tight ID SF

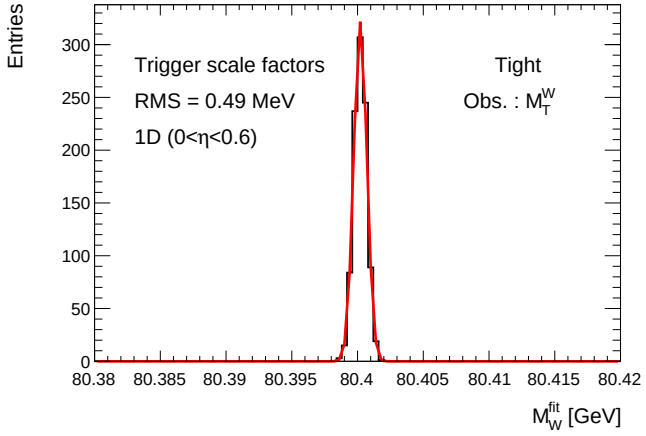

(c) Tight Trigger SF

FIGURE 5.5: W boson mass distribution extracted from different efficiency scale factor variations, when the mass fit is performed using the W transverse mass distribution for $60 < m_T < 110$ GeV [77]. The RMS of the fitted distribution indicates the corresponding uncertainty.

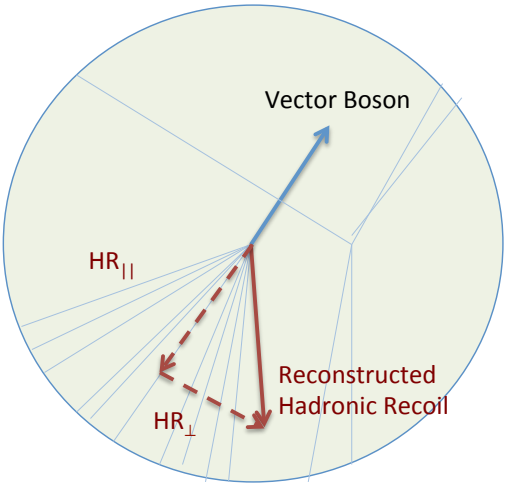

FIGURE 5.6: Projection of Hadronic Recoil on vector boson for the definition of $HR_{\parallel} = u_{\parallel}^{V}$ and $HR_{\perp} = u_{\perp}^{V}$ [78].

Z boson transverse momentum via its decay leptons allows for a precise determination of the expected hadronic recoil, as the typical resolution for the reconstructed vector boson p_{T} through the leptons is almost 10 times better than the resolution of the measured hadronic recoil.

In the following, $u_{\perp}^{V}$ and $u_{\parallel}^{V}$ ($u_{\perp}^{\ell}$ and $u_{\parallel}^{\ell}$) will refer to the perpendicular and parallel components with respect to the transverse momentum of the vector boson (reconstructed lepton).

The hadronic recoil calibration procedure as adopted in the analysis of this thesis was done with the following steps:

1. Correct the mismodeling of vertex multiplicity in data and MC:
   This is done by rescaling the average number of interactions per bunch crossing, $\langle\mu\rangle$, by a factor 1.1. The value of this data scale factor is in agreement with the default ATLAS value (1.11 ± 0.03). It is optimal for correcting distributions sensitive to resolution ($\sum E_{\mathrm{T}}$ and u_{perp}) and distributions sensitive to boson p_{T} (u and $u_{\parallel}$).

2. Correct the residual discrepancies of the $\sum E_{\mathrm{T}}$ distribution:
   The $\sum E_{\mathrm{T}}$ variable is the scalar sum of the transverse energies of all activity in the calorimeter without counting the lepton's energy. It is corrected by defining a Smirnov transformation for the MC distributions to match the data: this correction assumes that the mismodeling of $u_{\perp}$ and $u_{\parallel}$ mostly comes from the $\sum E_{\mathrm{T}}$ mismodeling.

3. Correct the mean and the resolution of the hadronic recoil distribution based on data to MC comparisons:
   The difference in means $\langle u_{\parallel} + p_{\mathrm{T}}\rangle_{\mathrm{data}} - \langle u_{\parallel} + p_{\mathrm{T}}\rangle_{\mathrm{MC}}$ is used to correct $\langle u_{\parallel}\rangle$, and the resolution ratio $\sigma(u_{\perp})_{\mathrm{data}}/\sigma(u_{\perp})_{\mathrm{MC}}$ is used to correct both $u_{\perp}$ and $u_{\parallel}$.

The overall correction procedure is illustrated in Figure 5.7. The systematic uncertainties induced by the recoil correction come from the $\langle\mu\rangle$ scale factor choice, the $\sum E_{\mathrm{T}}$ transform and the resolution and bias corrections, and the total systematic uncertainty is shown in Fig. 5.8 for the hadronic recoil as well as its parallel and perpendicular projection with respect to the lepton p_T. Statistical uncertainty is propagated via toys.

Bin	p_{T}^{l+}	p_{T}^{l-}	$p_{\mathrm{T}}^{l\pm}$	m_{T}^{W+}	m_{T}^{W-}	$m_{\mathrm{T}}^{W\pm}$
	Total Uncertainty					
$2.5 < \langle\mu\rangle < 6.5$	6.2	5.6	6.0	23.2	18.8	20.7
$6.5 < \langle\mu\rangle < 9.5$	4.1	4.4	4.3	16.3	12.2	13.9
$9.5 < \langle\mu\rangle < 16$	3.3	3.3	3.4	15.9	8.5	11.9
Inclusive	4.4	4.4	4.6	14.4	12.5	13.0

TABLE 5.8: Impact (in MeV) of the recoil correction on the W mass, in pile-up bins and inclusively, for p_{T}^{ℓ} and m_{T}^{W} fits.

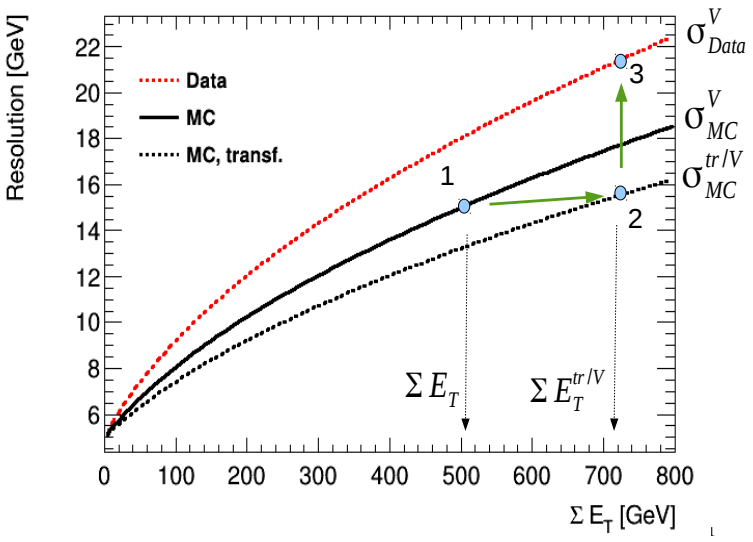

FIGURE 5.7: Schematic view of the correction procedure [81]: this figure illustrates the resolution of $u_{\perp}$ as a function of ΣE_T. The dotted red curve represents data resolution (σ^{V}_{Data}), solid black is nominal MC (σ^{V}_{MC}) and dotted black is MC as a function of transformed ΣE_T ($\sigma^{tr/V}_{MC}$). The transformation of ΣE_T in MC is represented in the step from point 1 to point 2, while step form point 2 to point 3 represents the resolution correction value, which is the difference in resolution between data and MC for a given ΣE_T value.

The correction procedure was repeated in bins of average interactions per bunch-crossing $\langle\mu\rangle$ ("pile-up"). The chosen binning is $2.5 < \langle\mu\rangle < 6.5$, $6.5 < \langle\mu\rangle < 9.5$, and $9.5 < \langle\mu\rangle < 16$ dividing the total statistics into 40%, 30% and 30% in each $\langle\mu\rangle$ bin. The impact of the recoil correction on the W-mass is summarized in Table 5.8.

5.3.5 Background determination

The background in W-events consists of the electroweak, top, and multijet processes having a final state seen as a lepton and missing transverse energy. Table 5.9 represents the sensitivity of the mass fit to the background normalization, estimated by varying this normalization within the cross-section uncertainties. A variation of ±5% is considered for $Z \to \tau\tau$, $Z \to ee$, dibosons and $t/t\bar{t}$ channels, and of ±2.37% for $W \to \tau\nu$, equal to the uncertainty on the ratio of $W \to \tau\nu$ and $W \to e\nu$ branching ratios. This table doesn't include the multijet background, which is difficult to model and will be discussed in details in Chapter 7, where it is estimated in a data-driven method. Also, the table doesn't consider the impact of the shape of the kinematic

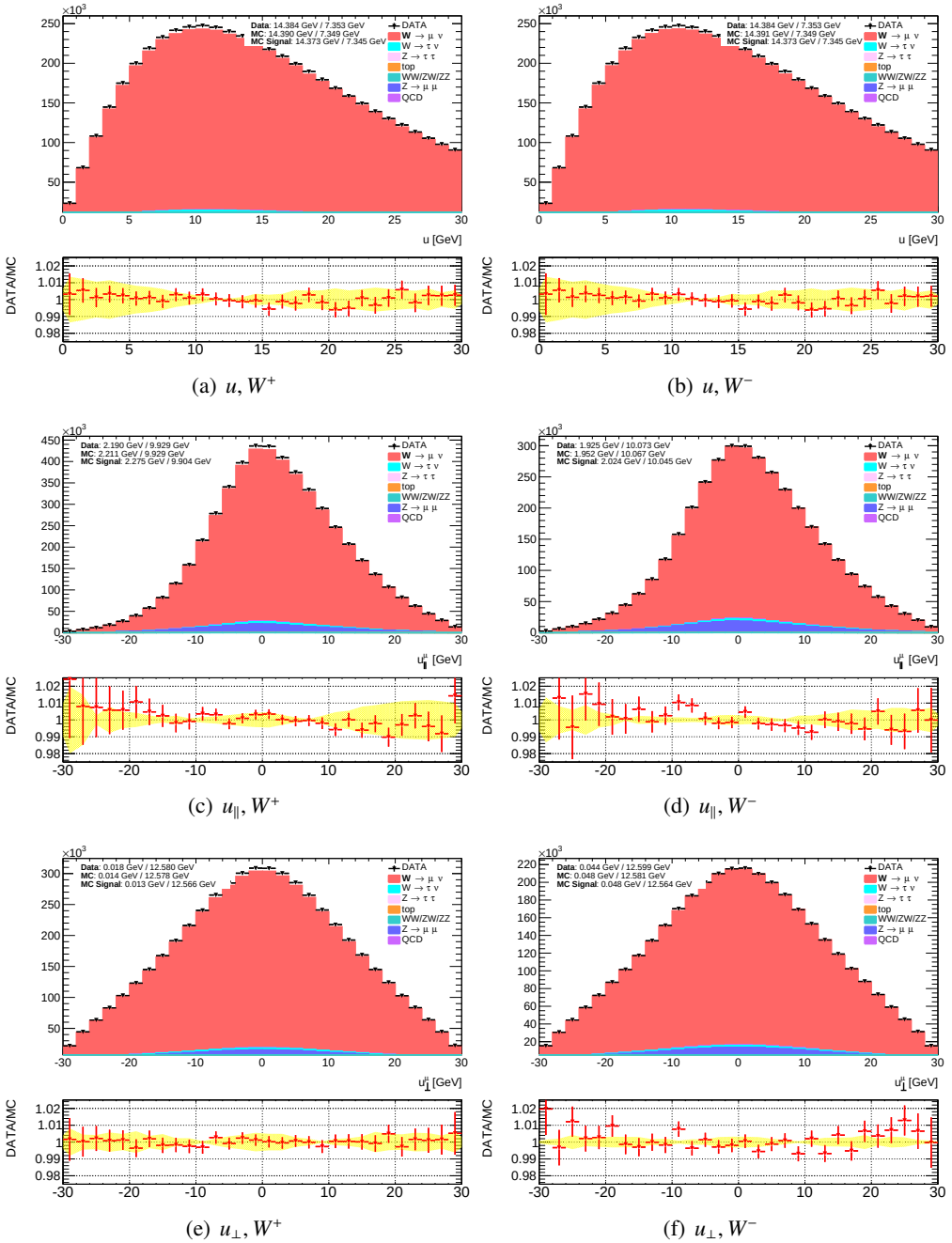

(a) u, W^+ (b) u, W^-

(c) $u_\parallel, W^+$ (d) $u_\parallel, W^-$

(e) $u_\perp, W^+$ (f) $u_\perp, W^-$

FIGURE 5.8: Hadronic recoil distribution u and its projections $u_\parallel^\ell$ and $u_\perp^\ell$ with respect to the lepton p_T for W^+ and W^- after recoil corrections with systematics uncertainties (yellow bands) due to variation of all corrections [81].

	$W \to \tau\nu$	$Z \to \tau\tau$	$Z \to ee$	Diboson	$t/t\bar{t}$
Impact (MeV)	$\mp$ 2.61	$\mp$ 0.5	$\pm$ 0.5	$\pm$ 0.2	$\pm$ 0.3

TABLE 5.9: Impact of a background normalization variation on the mass average determination.

Generator	α_{em}	G_μ [GeV^{-2}]	m_Z [GeV]	Γ_Z [GeV]	m_W [GeV]	Γ_W [GeV]	Breit-Wigner form
PYTHIA	Running	Running	91.1876	2.4812	80.399	2.072	Running-width
POWHEG	1/127.9	1.166×10^{-5}	91.1876	2.4952	80.399	2.085	Fixed-width
MC@NLO	Running	1.166×10^{-5}	91.1876	2.4952	80.399	2.085	Fixed-width
ALPGEN	1/132.3	1.166×10^{-5}	91.1880	2.4409	80.419	2.047	Fixed-width
SHERPA	1/128.8	1.166×10^{-5}	91.1876	2.4952	80.399	2.085	Fixed-width

TABLE 5.10: Electroweak parameter settings implemented in different MC generators [79].

distributions used for the fit. However, such an impact is well modeled for the Monte Carlo based backgrounds, but not for the jets.

5.4 Physics corrections and uncertainties

5.4.1 Lineshape and resonance correction - QED Final State Radiation

Several generators are used in this analysis (cf. Table 7.1). The main MC, POWHEG+PYTHIA8 [33, 72], includes higher order QCD corrections, but only leading order EW couplings, hence the need to correct the W and Z lineshapes description. The correction is done at particle level at first, and then takes into account the QED radiations in a later step, with the help of the PHOTOS [86] generator.

The motivation behind using a reweighting procedure instead of simulating different mass hypotheses, is the required large statistics for the W analysis. It is therefore more efficient to simulate a single mass point (usually equal to the world average m_W = 80.385 GeV), and reweight the boson invariant mass using the physics mass and width, and effective couplings measured with the Z resonance.

The lineshape reweighting has the purpose of:

- incorporating the non-simulated next-to-leading order EW effects in the resonance lineshape,
- taking into account the differences in the mass and width definitions between the different generators, which do not all start from the same electroweak parameter settings (see Table 5.10). The values of the W and Z masses and widths, the CKM matrix elements and the strong and electromagnetic coupling constants being taken as the world average, most leading order generators do not make use of these parameters in their internal calculations the same way, which generates discrepancies in the resulting resonance lineshapes,
- and finally giving the possibility to generate kinematic distributions with different mass hypotheses without generating new samples.

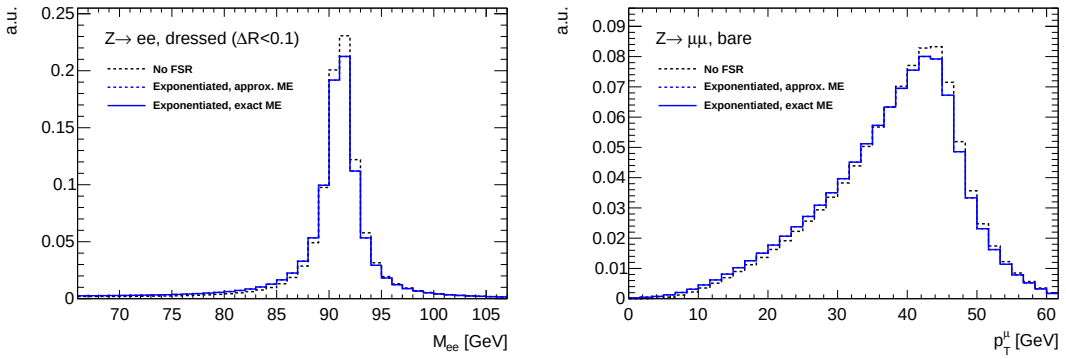

FIGURE 5.9: Comparison of the electron pair invariant mass distribution (left) and the muon transverse momentum distribution (right) at various levels of QED corrections [79].

In the reweighting procedure [79] we define the photon coupling as a function of the available energy s, $\alpha_{em}(s)$ as:

$$\alpha_{\mathrm{em}}(s) = \frac{\alpha_{\mathrm{em}}(0)}{1 - \Delta\alpha(s)} \tag{5.18}$$

where:

$$\Delta\alpha(s) = \frac{\alpha_{\mathrm{em}}(0)}{3\pi}\,(13.4955 + 3\ln s) + 0.00165 + 0.00299\ln(1+s) \tag{5.19}$$

and take the experimental value of G_μ for the weak boson couplings, and use the masses and widths of the gauge bosons in the running-width Breit-Wigner parametrization. However, this procedure doesn't account for photon emission correction. This is done using the PHOTOS generator, which generates photon emissions starting from the already generated events (with no QED radiations) and modifies the final state lepton kinematics accordingly.

Two NLO treatments are compared to evaluate the systematic uncertainty on the analysis: the first one involves approximate NLO calculations [87] and the second uses exact NLO QED matrix elements [88]. The differences between these two settings, and the one without final state radiation are compared in figure 5.9. In this figure, "No FSR" refers to generator-level leptons, "approx" and "exact ME" refer to the implementations of references [87] and [88]. "Bare" means the lepton is taken after FSR-induced momentum loss, and "dressed (ΔR < 0.1)" means a recombination of the bare lepton with all photons emitted within a cone of ΔR < 0.1. It was verified that for each lepton flavor, the size of the correction does not depend on whether the leptons are considered bare or dressed.

The PHOTOS calculations take into account the final state QED radiations (FSR), and do not address photon radiation in the initial state (ISR), the interference of the ISR with the FSR, nor the interference between successive FSR photons. The dominant higher-order QED correction in the W and Z production is however the FSR calculation, but the size of the uncertainty due to the unaccounted effects is estimated by fitting p_{T}^{ℓ} in the range $30 < p_{\mathrm{T}}^{\ell} < 50$ GeV for W and $25 < p_{\mathrm{T}}^{\ell} < 55$ GeV for Z, and the transverse/invariant mass in $60 < m_{\mathrm{T}} < 100$ GeV for W and $80 < m_{\ell\ell} < 100$ GeV for Z. As described in § 5.2, the difference between the injected mass and the fitted mass for each pseudo-data sample is taken as the corresponding uncertainty. The estimated uncertainties are summarized in Tables 5.11 and 5.12 (tables to be updated).

Source (Z events)	m_{ee}	p_T^e
FSR (real)	0.4×10^{-5}	3×10^{-5}
FSR (pair production)	2×10^{-5}	4×10^{-5}
Weak corrections	TBD	TBD
Total (TEMPORARY)	2×10^{-5}	5×10^{-5}

TABLE 5.11: Relative systematic uncertainties on the energy and momentum scale measurement, from higher-order EW corrections in $Z \to ee$ events [79].

Source (W events)	p_T^e	$m_T^{e\nu}$
FSR (real)	neg.	neg.
FSR (pair production)	4.1	0.8
Weak corrections	TBD	TBD
Total (TEMPORARY)	4.1	0.8

TABLE 5.12: Systematic uncertainties on the m_W measurement (in MeV), from higher-order EW corrections in $W \to e\nu$ events [79].

5.4.2 Polarization

For W bosons, the polarization effects manifest themselves in the angular and transverse momentum distributions of the decay lepton as well as the missing transverse energy. Like all massive spin-1 particles, the W has three polarization states. At the LHC, the polarization of the W is mainly determined by the momentum of the colliding quark and antiquark: it is left-handed if the quark has more momentum than the antiquark, and right-handed otherwise.

The general structure of the angular distribution is given by nine helicity cross sections:

$$\begin{aligned}\frac{d\sigma}{dp_T^2 dy d\cos\theta d\phi} = \frac{3}{16\pi}\frac{d\sigma}{dp_T^2 dy} \times [&(1+\cos^2\theta) + A_0\,\frac{1}{2}(1-3\cos^2\theta) \\ &+ A_1\ \sin 2\theta\cos\phi \\ &+ A_2\,\frac{1}{2}\sin^2\theta\cos 2\phi \\ &+ A_3\ \sin\theta\cos\phi \\ &+ A_4\ \cos\theta \\ &+ A_5\ \sin^2\theta\sin 2\phi \\ &+ A_6\ \sin 2\theta\sin\phi \\ &+ A_7\ \sin\theta\sin\phi]\end{aligned} \tag{5.20}$$

where p_T and y denote the transverse momentum and rapidity of the boson. The polar and azimuthal angles of the lepton in the rest frame of the boson are denoted as θ and ϕ, respectively. The A_i coefficients are helicity cross section ratios with respect to unpolarized production, and are functions of the boson kinematic variables. The interest in the use of cross-section ratios is that they suffer less from theoretical and experimental uncertainties.

The A_i coefficients vanish at $p_T = 0$, except for the electroweak part of A_4 responsible for the forward-backward lepton asymmetry in $\cos\theta$. The $A_5 - A_7$ coefficients appear at second order in the QCD strong coupling, α_S, and are small in the Collins-Soper (CS) frame, they are therefore not considered here. The CS rest frame is reached from the laboratory frame via a Lorentz boost

along the laboratory z axis into a frame where the z component of the lepton pair momentum is zero, followed by a boost along the transverse momentum of the pair. At $p_{\mathrm{T}} = 0$, the CS and laboratory coordinate systems are the same.

The angular coefficients obtained from POWHEG [72] and DYNNLO [89] (used for comparison to the baseline MC *i.e.* POWHEG+PYTHIA8), computed in the CS frame, and used both at NLO and NNLO, are shown in Figure 5.10 for Z, W^+ and W^- events, as a function of $p_{\mathrm{T}}(W, Z)$.

However, the MC generators used in the analysis do not have a clear definition of the angular decompositions and polarization coefficients. Instead, the numbers involve indirect calculations and the results rely therefore on the calculations accuracy and implementation choices, and are missing higher order calculations. It is possible to modify the prediction of a generator (called "source") by defining a reweighting towards another generator ("target"), knowing the values of the coefficients for both generators, according to:

$$w = \frac{1 + \cos^2\theta + \sum_i A'_i \, f_i(\theta, \phi)}{1 + \cos^2\theta + \sum_i A_i \, f_i(\theta, \phi)}, \tag{5.21}$$

where A'_i and A_i are the coefficients for the target and source generator respectively, and the $f_i(\theta, \phi)$ can be read off of Eq. 5.20.

Looking at Fig. 5.10, DYNNLO shows the correct behavior for A_i which tends to zero at $p_{\mathrm{T}} = 0$, except for A_4 in Z events. Therefore, POWHEG is reweighted to DYNNLO for all A_i coefficients except for A_4 in Z events. In DYNNLO, A_4 is predicted from the leading-order relation $\sin^2\theta_W = 1 - M_W^2/M_Z^2$, while POWHEG+PYTHIA8 uses the effective mixing angle measured at LEP $\sin^2\theta_W^{\mathrm{eff}}$ which is more accurate. The performance of the reweighting procedure is illustrated in Figure 5.11 for Z, W^+ and W^- events, and the impact on the lepton transverse momentum is shown in Figures 5.12 and 5.13.

The measurement of polarization angular coefficients in $Z \to \ell\ell$ processes is used to probe the underlying QCD dynamics in Z production. This measurement can be used to assess the systematic uncertainties coming from polarization and angular distributions. A preliminary approximation is discussed in Section 8.1.

5.4.3 Parton Distribution Functions

The incomplete knowledge of parton distribution functions induces the dominant theoretical uncertainty on the W-mass measurement. The PDF uncertainty is correlated to the uncertainty on the non-perturbative QCD modeling of the W boson p_{T} spectrum and connected to various aspects of the W boson production: the uncertainty on the valence and sea PDFs and the corresponding uncertainty on the average polarization of the W boson, the uncertainty on the strange PDF and the corresponding uncertainty on the amount of W production initiated by charm quarks, the uncertainty on the charm and bottom quarks PDFs and the corresponding uncertainty on the transverse momentum spectrum of the W boson.

In Ref. [90] and [91], the estimate of the uncertainty due to PDFs at the LHC used by the ATLAS and CMS collaborations is ±25 MeV.

Without improvement in the PDF uncertainties, the contribution of the LHC to the world average would not be significant. Therefore, huge efforts are being devoted in this particular area to

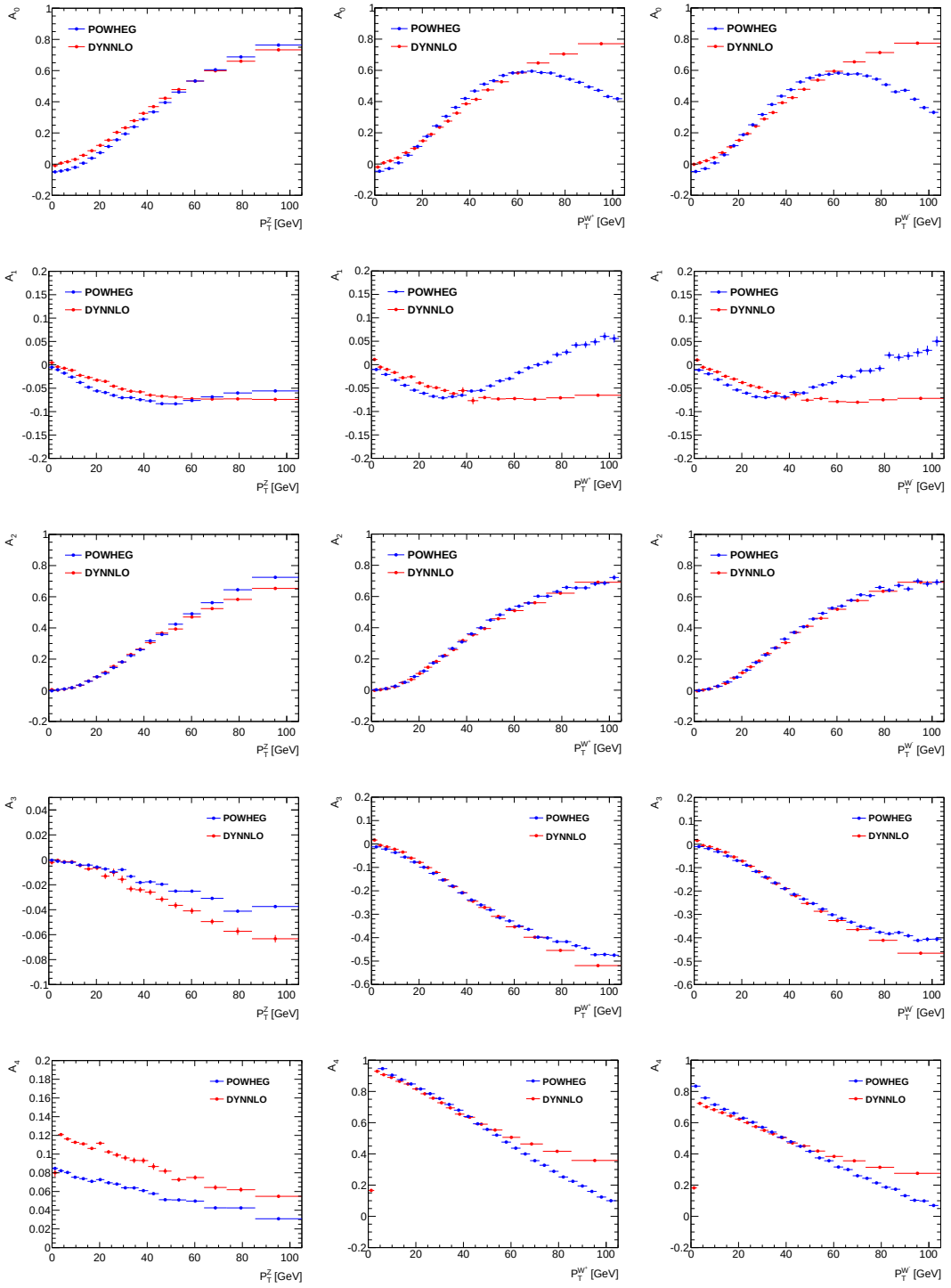

FIGURE 5.10: Angular coefficients for the Z, W^+ and W^- bosons for POWHEG+PYTHIA8 (blue) and DYNNLO (red) [79].

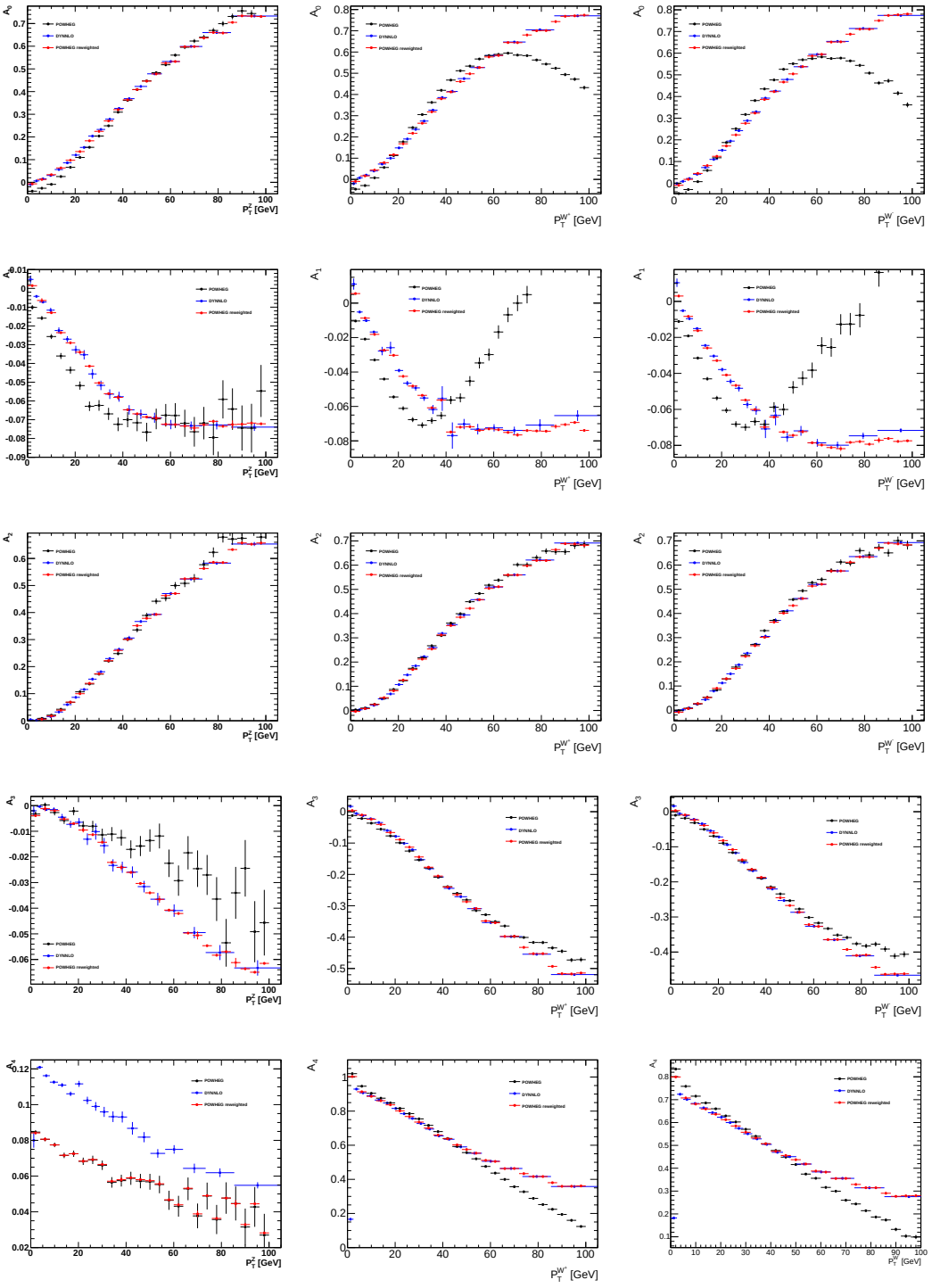

FIGURE 5.11: Angular coefficients for the Z, W^+ and W^- bosons before (black) and after (red) polarization reweighting of all angular coefficients except A_4 for Z [79]. Black points show the target DYNNLO coefficients.

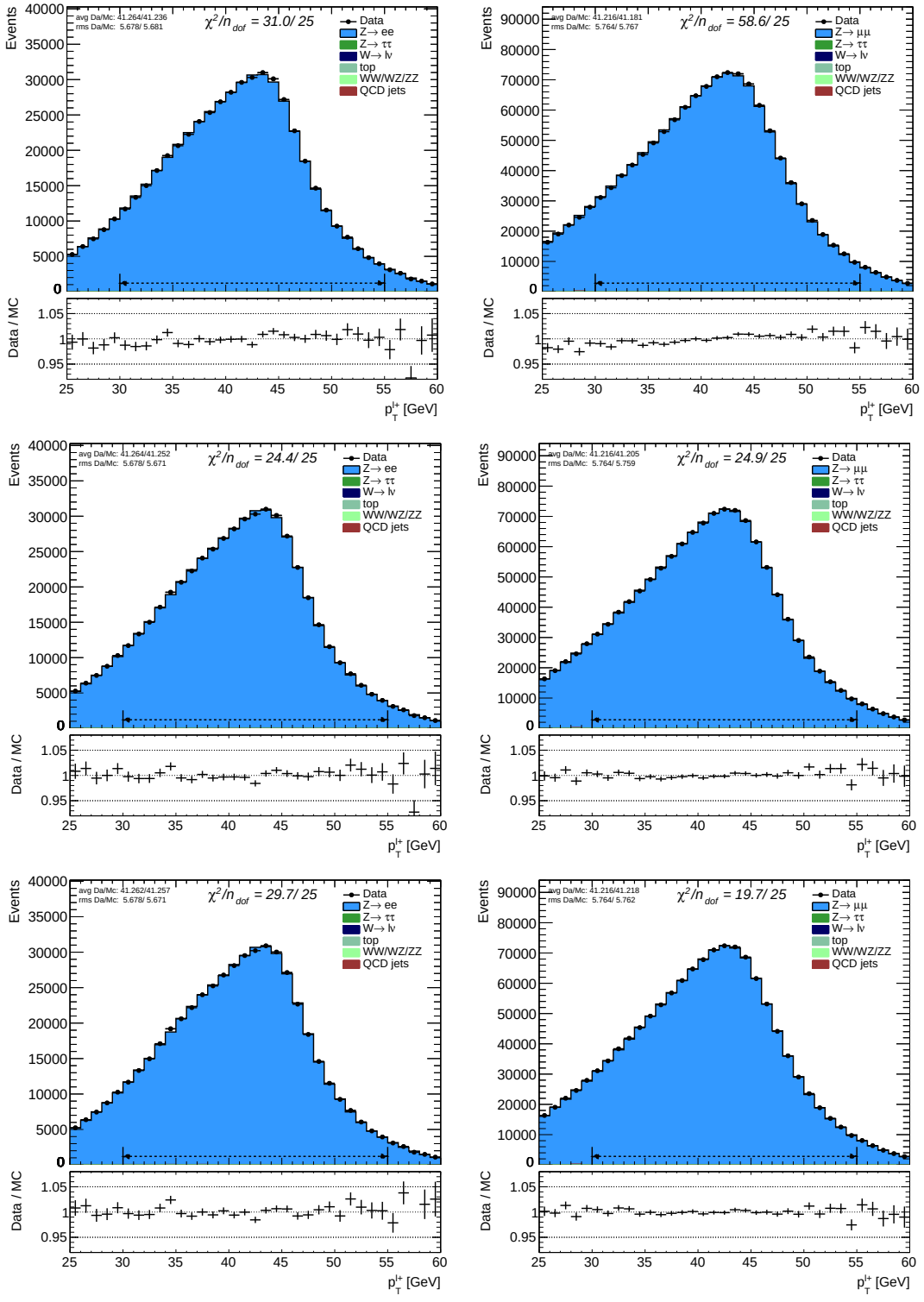

FIGURE 5.12: p_T^{l+} distributions before reweighting (top), after polarization reweighting (middle) and after polarization reweighting except A4 (bottom), for $Z \to ee$ (left) and $Z \to \mu\mu$ (right) events.

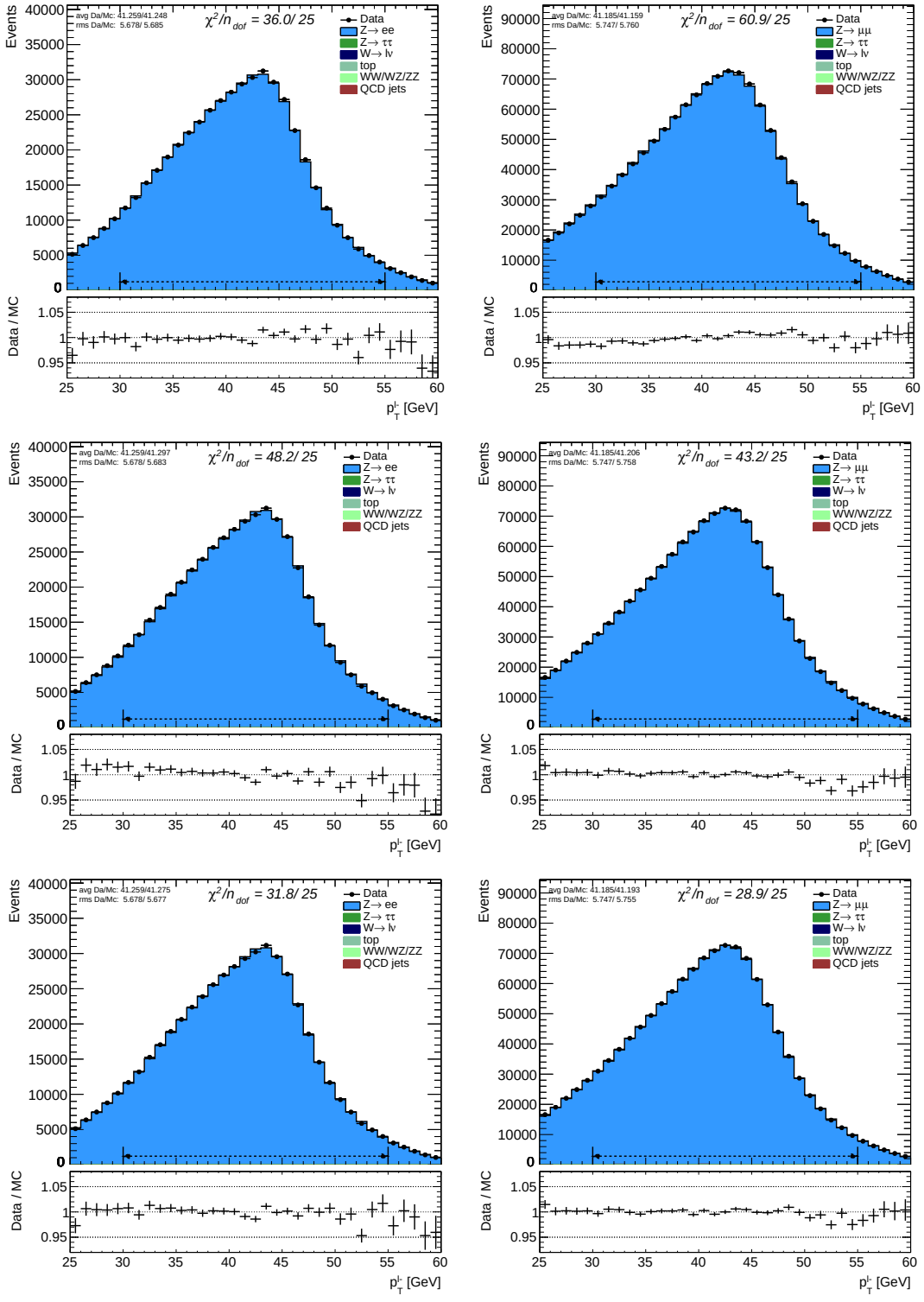

FIGURE 5.13: p_T^{l-} distributions before reweighting (top), after polarization reweighting (middle) and after polarization reweighting except A4 (bottom), for $Z \to ee$ (left) and $Z \to \mu\mu$ (right) events.

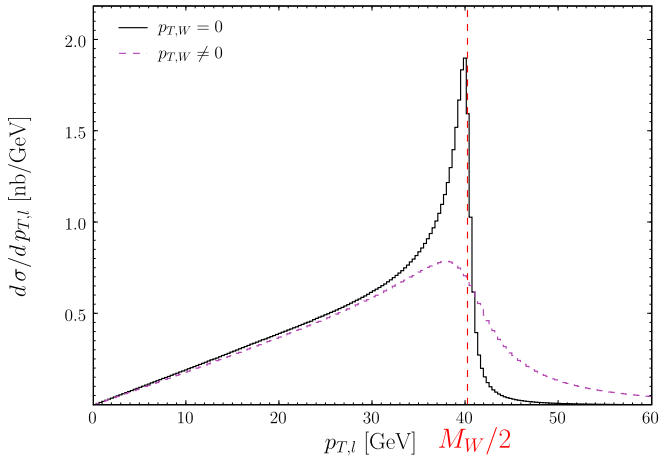

FIGURE 5.14: Simulation of the p_T spectrum of charged leptons from the $W \to \ell\nu$ decay. The full line is generated with zero p_T of the W, the dashed line represents the effect of a non-zero p_T as predicted by the PYTHIA generator. [52]

improve the theoretical and statistical treatment of PDFs, and also to study the impact of PDF uncertainties on the extraction of m_W from p_T^ℓ [56] and m_T [92, 93].

5.4.4 W-transverse momentum distribution

This observable has a weak impact on the m_T distribution. It mostly affects p_T^ℓ. Ideally, when the W is at rest, the lepton p_T has a clear Jacobian peak at exactly $m_W/2$ at detector level. But in reality, the W coming from hadronic collisions usually has a non-zero transverse momentum, due to initial state parton radiation during the collision and the intrinsic transverse momentum of the incoming partons. The non-zero boson-p_T smears the Jacobian peak of the lepton-p_T. These effects are shown in Fig. 5.14.

A p_T^W reweighting based on Parton Shower parameters tuning is discussed in Chapter 6. The corrections were derived and cross-checked on Z-events and applied to the W.

5.5 Cross-checks with the Z-boson

Due to the fact that the Z mass and width are known with high precision [94], and since the lepton transverse momentum and the transverse mass distributions are similar in Z and W events, the Z is used to define and implement corrections used with the W: it is used to determine the lepton energy scale and resolution, and allows to determine the linearity of the detector response, and the energy dependent resolution function. The Z-boson transverse momentum helps scaling the measured hadronic recoil to the Z, which together with the measured lepton transverse momentum define the missing transverse energy. The QCD mechanisms in the boson production affect the W and the Z similarly, the Z distributions are used to control the W's.

W-like distributions are built using Z samples as cross-checks. The recoil u, represented by the transverse momentum of the Z boson and reconstructed from the the hadronic activity in the detector is illustrated in Figure 5.15, and a pseudo-transverse mass, reconstructed from the

Channel	δm_Z : $p_{\mathrm{T}}^{\ell+}$ [MeV]	δm_Z : $p_{\mathrm{T}}^{\ell-}$ [MeV]	δm_Z : $p_{\mathrm{T}}^{\ell\pm}$ [MeV]
Electron	7 ± 29	-34 ± 29	-13 ± 20
Muon	33 ± 21	-18 ± 21	8 ± 14
Combined	24 ± 17	-23 ± 17	1 ± 12

TABLE 5.13: Z boson mass fit results in the electron and muon channels, all corrections applied. The $p_{\mathrm{T}}^{\ell+,-,\pm}$ distributions are used.

Channel	δm_Z : $m_{\mathrm{T}}^{\ell+}$ [MeV]	δm_Z : $m_{\mathrm{T}}^{\ell-}$ [MeV]	δm_Z : $m_{\mathrm{T}}^{\ell\pm}$ [MeV]
Electron	-86 ± 35	1 ± 35	-33 ± 23
Muon	22 ± 23	36 ± 23	29 ± 15
Combined	-11 ± 19	25 ± 19	7 ± 13

TABLE 5.14: Z boson mass fit results in the electron and muon channels, all corrections applied. The $m_{\mathrm{T}}^{\ell+,\ell-,\ell\pm}$ distributions are used.

recoil and one of the two selected electrons is illustrated in Figure 5.16. m_{T}^{e+} denotes the Z boson transverse mass reconstructed from the recoil and the positively charged electron, and m_{T}^{e-} is with the negatively charged electron. All performance and physics corrections are applied.

Z mass fits are also performed using the $m_{\ell\ell}$, p_{T}^{ℓ} and m_{T} observables, by comparing data to a set of templates built by varying the mass in steps of 2 MeV within ±100 MeV of the reference mass value fixed to the world average $m_Z = 91187.6$ MeV. This fitting method is explained in § 5.2.1. The results of the fits are summarized in Figure 5.17 for p_{T}^{ℓ} fits and Figure 5.18 for m_{T}^{ℓ} fits at different correction steps: energy/momentum corrections, sagitta bias corrections (specific to the muon channel [76]), polarization reweighting of all coefficients, and polarization reweighting of all coefficients except for A_4, and after isolation cuts applied as a final selection for electrons only.

The mass fits performed for positive and negative leptons (leptons = electrons and muons) are expected to be correlated as they use the same samples and the same recoil corrections. The final fit results are given in Tables 5.13 and 5.14 separately for the electron and muon channels, and after statistical combination including the above correlation. These table show the differences between the $m_{\ell\ell}$ and $p_{\mathrm{T}}^{\ell}/m_{\mathrm{T}}^{\ell}$ fit results, as the $m_{\ell\ell}$ fits agree with m_Z by construction and the compatibility between the invariant mass and transverse momentum/mass observables is tested here. The combined results are also shown.

The final p_{T}^{ℓ} fits after the above mentioned corrections give a mass value compatible within 0.8σ with the reference mass value. The difference between the combined $p_{\mathrm{T}}^{\ell+}$ and $p_{\mathrm{T}}^{\ell-}$ fits is compatible with 0 within 1.9 standard deviations. For the $m_{\mathrm{T}}^{\ell+,\ell-,\ell\pm}$ fits, the compatibility with the reference mass is at the level of 1.2 standard deviations. The corrections that we apply improve the Z fits and our understanding of the Z distributions and can therefore be applied to W.

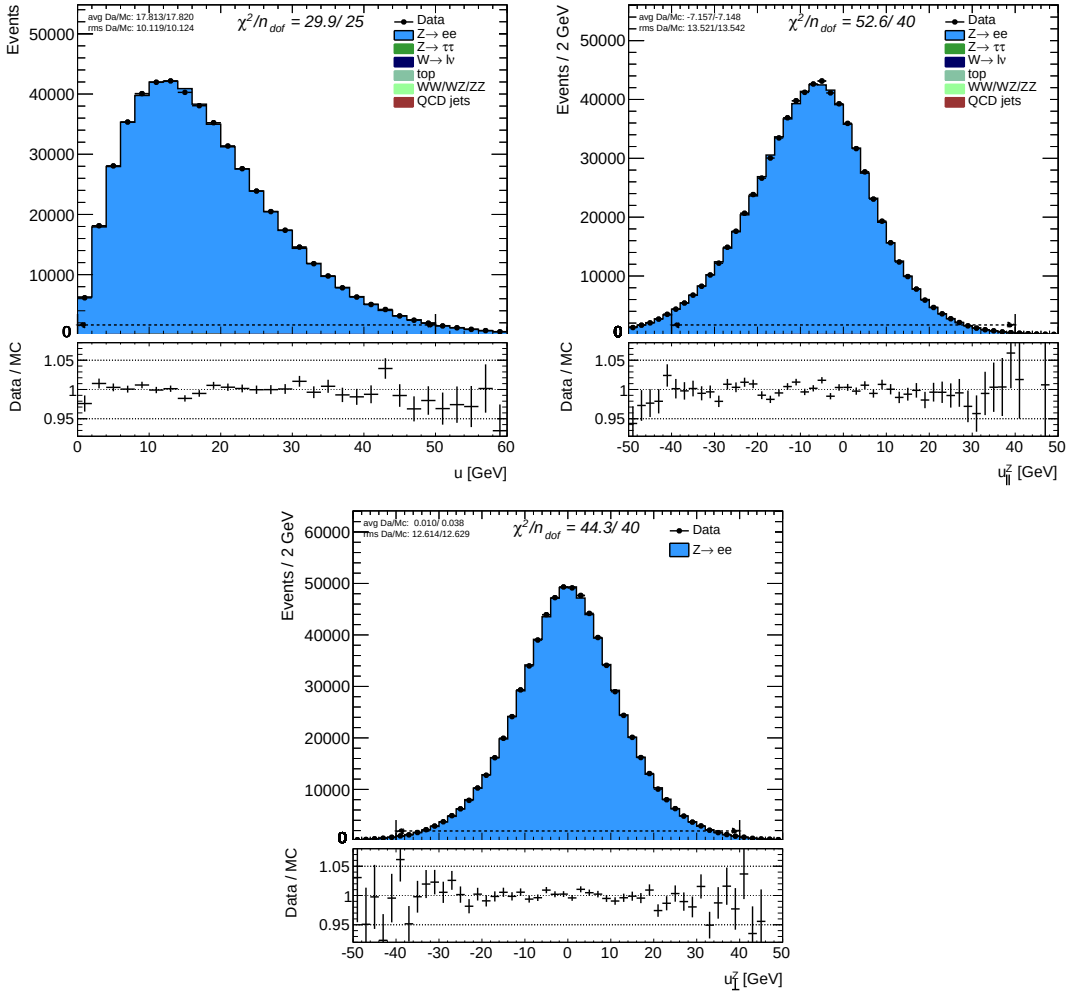

FIGURE 5.15: u, $u_{\parallel}^{Z}$ and $u_{\perp}^{Z}$ in the electron channel, after all corrections. The dashed line indicates the range over which the averages, RMS and χ^2 values are computed.

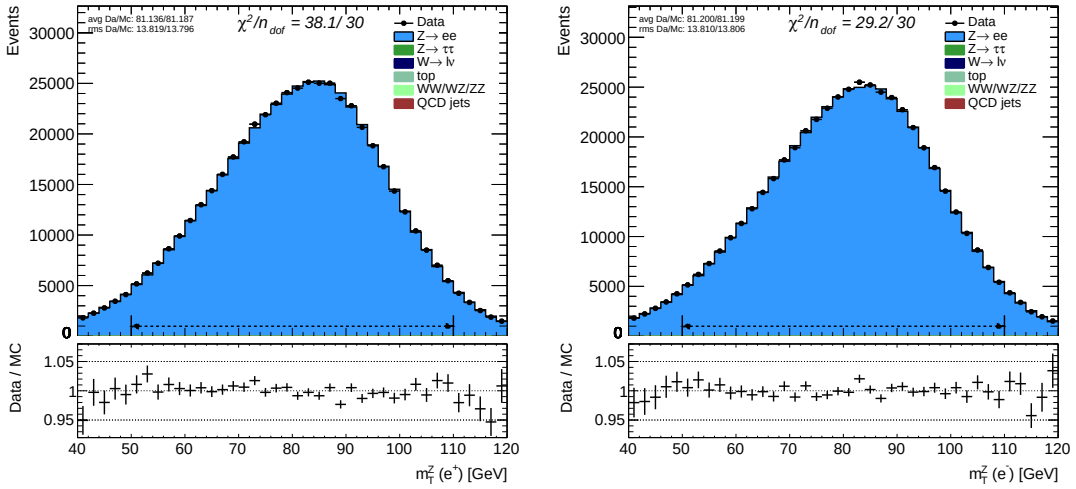

FIGURE 5.16: $m_{\mathrm{T}}^{e^+}$ and $m_{\mathrm{T}}^{e^-}$, after all corrections. The dashed line indicates the range over which the averages, RMS and χ^2 values are computed.

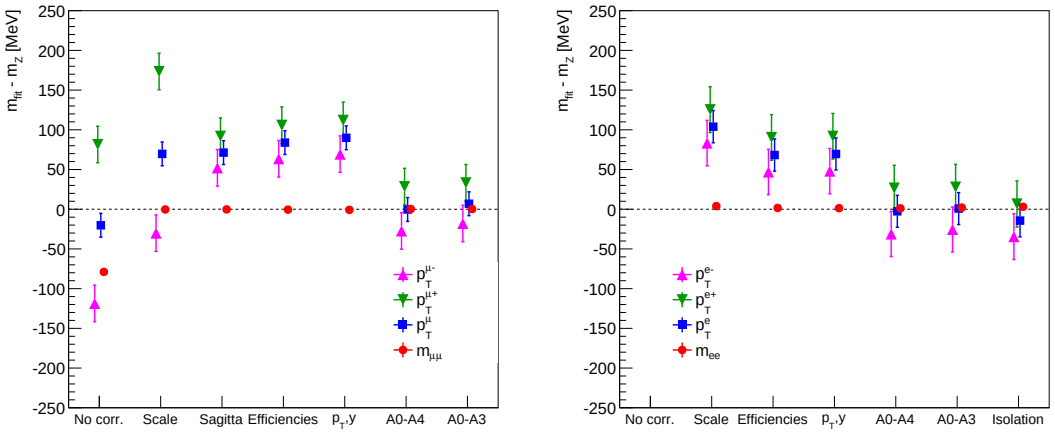

FIGURE 5.17: Summary of the p_T^{ℓ}-based mass fits results for muons (left) and electrons (right). The error bars are statistical only.

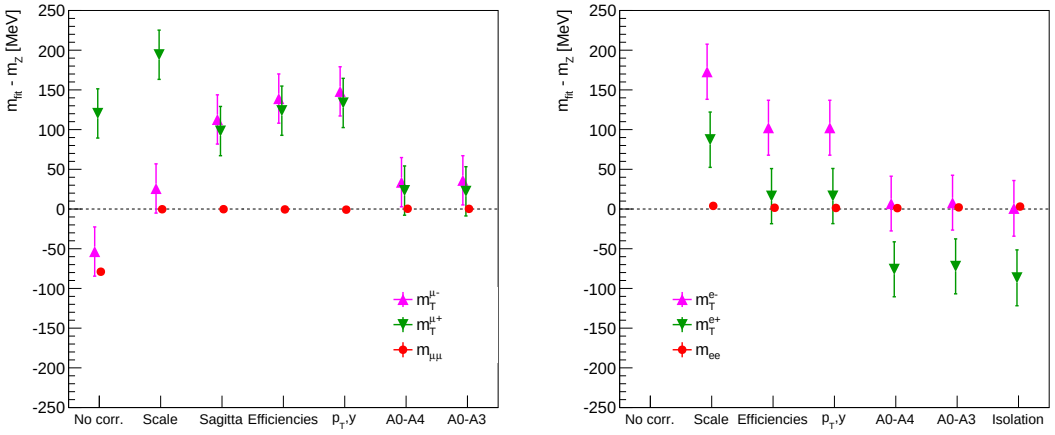

FIGURE 5.18: Summary of the m_T^{ℓ}-based mass fits results for muons (left) and electrons (right). The error bars are statistical only.

Chapter 6

Modeling of the boson p_{T}

6.1 Boson transverse momentum studies

The boson's transverse momentum is an important source of systematic uncertainty when measuring the boson's mass, due to the impact it makes on the lepton p_{T}, which is directly used in the mass measurement.

The effect seen in Fig. 5.14 shows the usefulness of accurately modeling the p_{T}^{W} distribution in the measurement of the W-mass. For this purpose, we can take advantage of our knowledge of the p_{T}^{Z}, since it is more precisely measured [95] and it involves the same QCD radiation effects as the p_{T}^{W}.

6.2 ϕ^* angle

In the p_{T} modeling, another variable, ϕ^*, can be measured with fine granularity at low p_{T}, and can therefore be exploited due to its high correlation to p_{T}^{Z}, shown in Fig. 6.1.

The acoplenary angle (Figure 6.2), ϕ_{acop}, was introduced in [100] with in head the goal of limiting the impact of uncertainties on the p_{T}^{Z} measurements. ϕ_{acop} is the complementary angle of the one between the two leptons: $\phi_{\mathrm{acop}} = \pi - \Delta\phi_{ll}$. Another variable was introduced, $\phi^* = \tan(\phi_{\mathrm{acop}}/2)\sin(\theta^*)$, where θ^* is the scattering angle of the leptons relative to the beam direction in the dilepton rest frame. ϕ^* provides an excellent experimental resolution, while providing essential informations about the momentum without having to measure the latter. Figure 6.3 represents a measurement of a ϕ^* distribution by ATLAS. The fine granularity at low p_{T}^{Z} gives a better precision in the parton shower region.

6.3 Tuning the parton shower parameters

An accurate modeling of p_{T}^{Z} was obtained by tuning three parton shower parameters in the Pythia8 [33] setup, and two in the Powheg+Pythia8 setup, during the event generation process. These parameters will later be used in the generation of W events. The tuning has been used on standalone Pythia8, with generator-level kinematics to minimize the dependence on QED Final

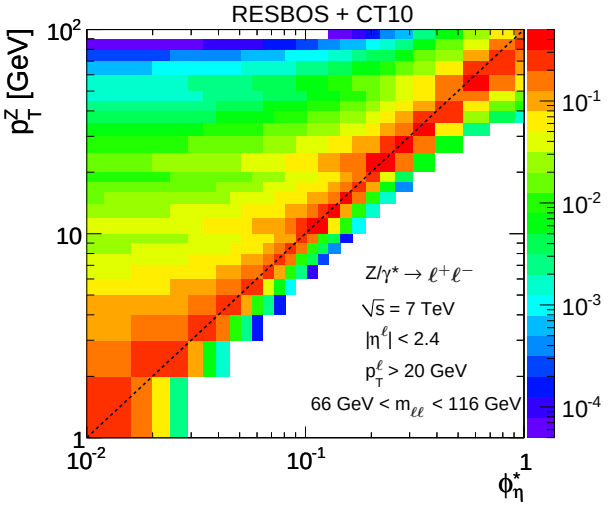

FIGURE 6.1: Correlation matrix between ϕ^* and p_T^Z variables, at born level, for $Z/\gamma^* \to \ell^+\ell^-$ decays. The ResBos [96–98] generator with the CT10 [51] PDF set has been used [99].

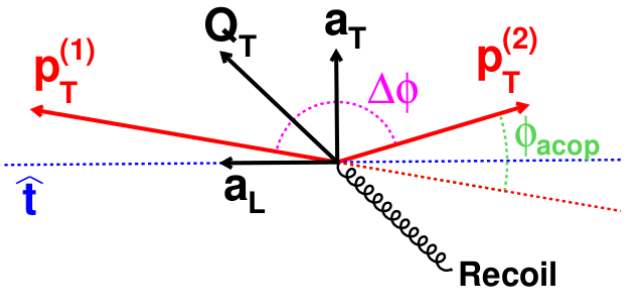

FIGURE 6.2: Graphical illustration in the plane transverse to the beam direction of the angular and kinematic variables defined in [100].

State Radiation. The tunes are performed for $p_T^Z < 26$ GeV and $\phi_\eta^* < 0.29$ covering a similar transverse momentum range, where parton shower effects dominate.

The PYTHIA [33] generator uses the parton shower approach to describe the low p_T^Z region. The phenomenological parameters used in the event generation are not constrained by the theory, but can be adjusted to improve the description of the measured distributions. The part of this study is about improving the parton shower parameters inside the PYTHIA generator. Also, another generator, Photos [86], is used in the process in addition to PYTHIA to simulate QED Final State Radiation (FSR). The tuning process is described in [95], and summarized in what follows. To define the tunings, the parameters are chosen randomly between a certain range. A χ^2 test is then performed between the generator and the data to determine the optimal parameters values. The final tune turned out to be an optimal combination between the muon channel p_T^Z measurement and the electron channel ϕ^* measurement.

The tuned parameters include p_{T0}, k_T and $\alpha_s^{ISR}(m_Z)$, which represent the parton shower lower cut-off in the non-perturbative regime, the primordial transverse momentum of the partons initiating the hard scattering process, and the strong-coupling constant value assumed for the initial-state radiation (ISR). This last parameter is left free only in the PYTHIA8 setup, while it is constrained to the value assumed for the NLO cross section calculation in POWHEG+PYTHIA8. The resulting tuned parameter sets are referred to as AZ for PYTHIA8 and AZNLO for POWHEG+PYTHIA8.

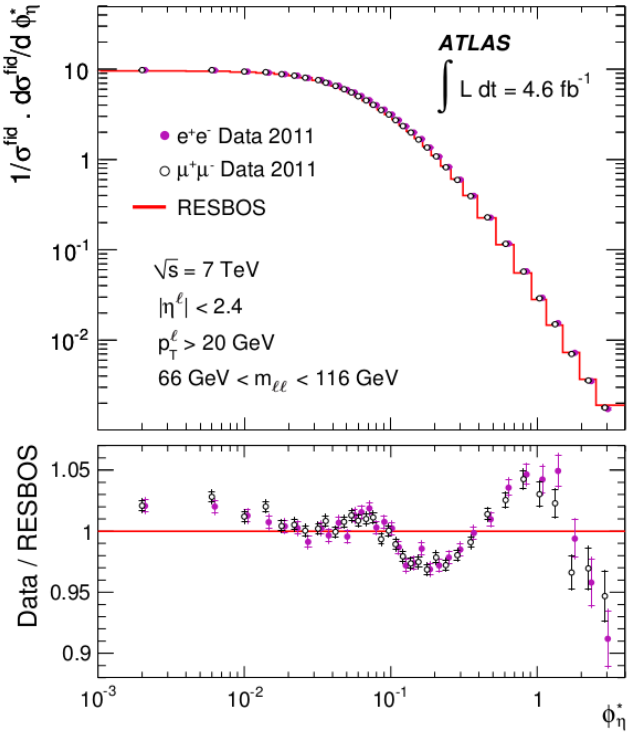

FIGURE 6.3: Measured normalized differential cross section as a function of ϕ^* for the Z decay into two electrons (closed dots) and two muons (open dots) [101], compared to predictions by the ResBos [96–98] generator.

Table 6.1 shows the tuned parameters values compared to the default tune used in PYTHIA8, 4C. The AZ tune has been compared to the data for different Z-boson rapidity regions, and the good agreement observed between predicted and measured p_T^Z distributions supports the validity of a single tune in a wide Bjorken x-range [95]. The parameters not used in the tuning are set to the default values of the PYTHIA8 baseline tune 4C. Figures 6.4 and 6.5 show the comparisons of tuned predictions to the data.

Tune	AZ	AZNLO	4C
Primordial k_T [GeV]	1.71 ± 0.03	1.75 ± 0.03	2.0
$\alpha_s^{ISR}(m_Z)$	0.1237 ± 0.0002	0.118 (fixed)	0.137
ISR cut-off [GeV]	0.59 ± 0.08	1.92 ± 0.12	2.0
χ^2_{min}/dof	45.4/32	46.0/33	-

TABLE 6.1: Central values and uncertainties of the set of tuning parameters for AZ (PYTHIA8) and AZNLO (POWHEG+PYTHIA8), compared to the base tune (4C) [95].

The AZ tune is used to propagate the uncertainties on the parton shower parameters computed from p_T^Z to the measurement of m_W. Three tuning eigenvectors and a pair of sets of parton shower parameters associated with each eigenvector are extracted from the correlation between the tuned variables. Each pair corresponds to positive and negative 68% CL exclusion along the eigenvector. The different sets are referred to as 1+, 1−, 2+, 2−, 3+ and 3−. Figure 6.6 (6.7) shows the distortion of the p_T^μ (p_T^Z) distribution due to the tune variations. These distributions are computed at the detector level, and reweighted with respect to the parton shower parameter variations at the particle level.

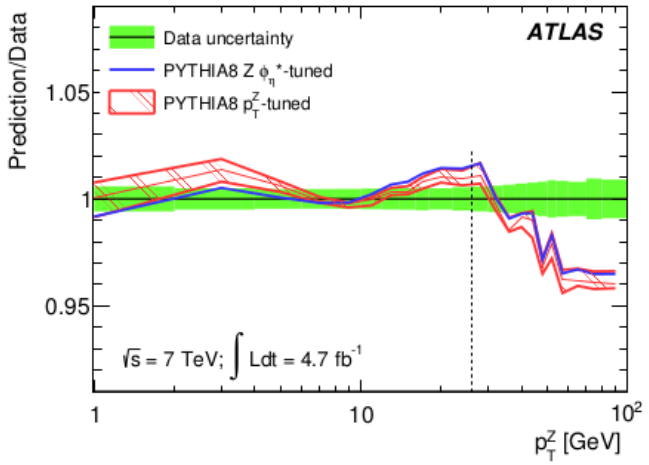

FIGURE 6.4: Tuned predictions for PYTHIA8 based on ϕ^* and p_{T}^Z measurements [95]. The vertical dashed lines show the upper limit of the tuning ranges.

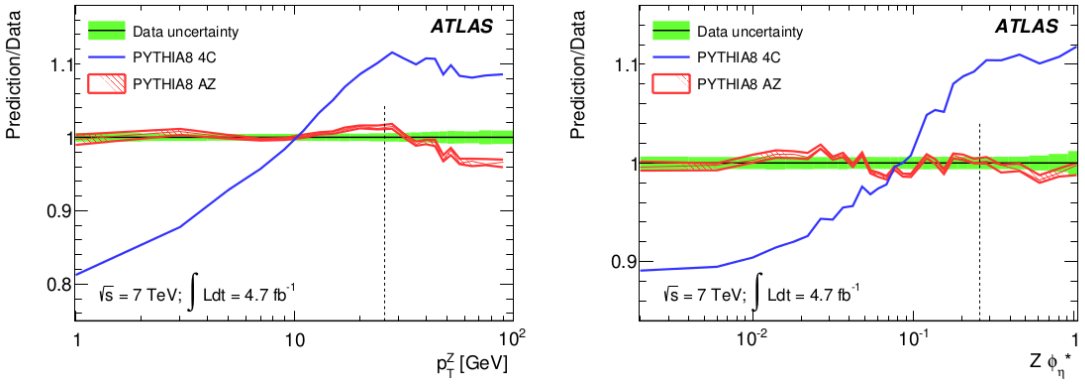

FIGURE 6.5: PYTHIA8 tuned predictions compared to data, for the muon (p_{T}^Z) and electron (ϕ^*) channels [95]. The base tune (4C) is shown in blue, the new tunes in red. The green fillings represent the uncertainty on the data (shown in black). The shown quantity is the differential cross section, for dressed kinematics and in the full rapidity range. The vertical dashed lines show the upper limit of the tuning ranges.

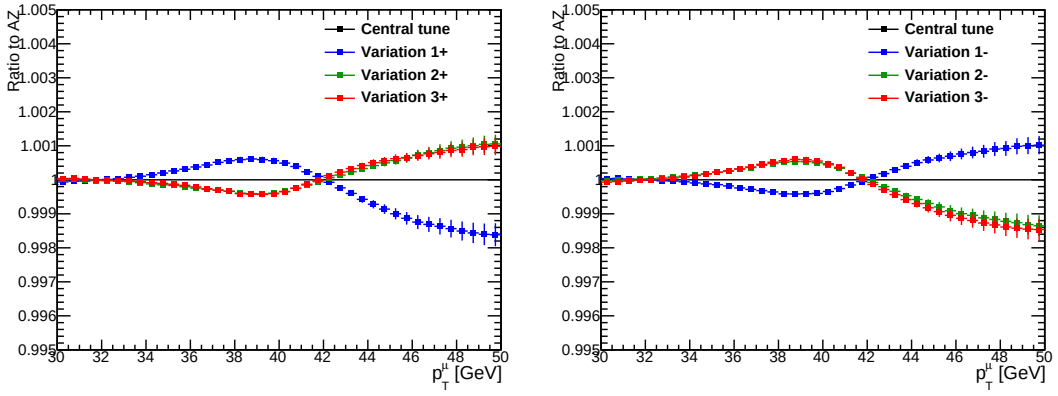

FIGURE 6.6: Ratios of p_{T}^μ using the tune variations ($1\pm,\ 2\pm,\ 3\pm$) with respect to the central tune.

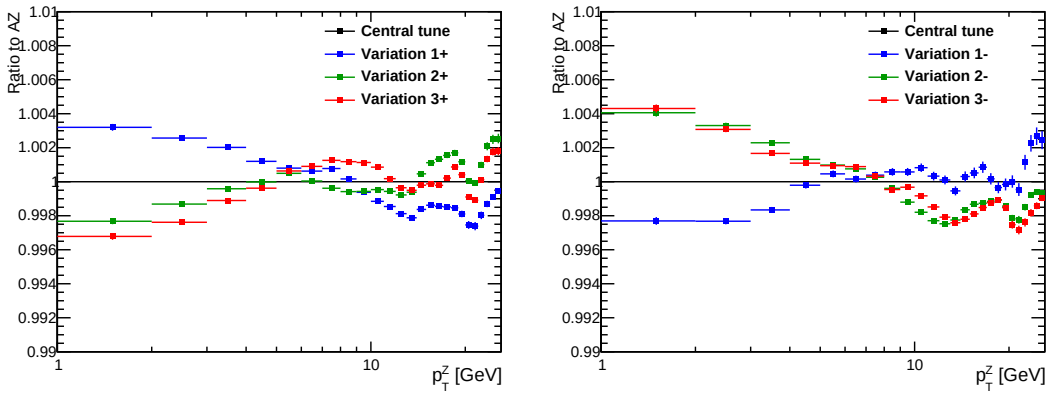

FIGURE 6.7: Ratios of p_T^Z using the tune variations (1±, 2±, 3±) with respect to the central tune.

6.4 Event selection and methodology for the uncertainty assessment

In this study, the muon channel was used while the electron channel is expected to behave similarly, since the boson-p_T is independent of its decay products. The parton shower uncertainties are evaluated separately for the p_T^μ spectrum from both W^+ and W^- decays. As discussed in section 5.2.1, the poor knowledge of the underlying physics mechanisms affecting the W-mass measurement leads us to use the template fitting method.

The AZ tune PS parameters set and the six pairs of variations were used to generate samples of W events, which are treated as data in the mass fits. Events are selected with a central muon such that $|\eta^\mu| < 2.4$ and $|p_T^\mu| > 25$ GeV, missing transverse energy $E_T^{\text{miss}} > 30$ GeV, transverse mass $M_T > 60$ GeV, and a W with a transverse momentum $p_T^W < 30$ GeV. The range of the p_T^μ distribution was varied in a way to scan $p_{T_{\text{min}}}^\mu$ between 30 and 35 GeV with steps of 0.5 GeV, and $p_{T_{\text{max}}}^\mu$ between 40 and 55 GeV with the same steps. This range scan was done in the purpose of finding an optimal fit interval for the uncertainty estimation, which is expected to vary according to the choice of such interval.

To determine the value of the W boson mass, a χ^2 profile as a function of M_W is evaluated by comparing the distributions obtained above to a set of templates built by varying the mass in steps of 0.02% within 0.5% of the reference mass value and assuming the central AZ tune. The χ^2 profile is fitted with a parabolic function, the value of m_W to minimize the χ^2 function corresponds to the result of the m_W extraction. The obtained differences with respect to the reference mass (fixed as the world average, $m_W = 80385$ MeV [31]) define the parton shower uncertainty. The uncertainties are evaluated with the hessian method, such that the positive (negative) uncertainty is the quadratic sum of positive (negative) biases with respect to the reference value of m_W [102].

One should stress that this uncertainty only covers the contribution of the parton shower parameters, while the p_T^W distribution is affected by additional uncertainties coming from the different quark flavour contributions to Z- and W-boson production. This aspect is discussed in § 1.3.4, where the potential impact of PDF uncertainties is illustrated. PDF uncertainties on the parton shower fit are not considered in the current estimation, only the experimental uncertainty of the p_T^Z measurement is propagated, *via* the fitted parton shower parameters, to the W-boson mass measurement. A more consistent procedure would involve a simultaneous fit of the PDF and parton shower parameters, which has not been attempted yet. The present estimate should thus

be considered as a first step in the derivation of a consistent set of parton shower parameters to describe W- and Z-boson production at the LHC.

The best fit range has been sought in a way to minimize the total uncertainty, i.e. systematic $\oplus$ statistical, where the statistical uncertainty is the one expected from data. The statistics of the combined electron-muon channel are assumed to be the double of the muonic channel alone. All the uncertainties are reported in Figure 6.8 and Figure 6.9, respectively representing the $p_{\mathrm{T}}^{\mu^-}$ and $p_{\mathrm{T}}^{\mu^+}$ fits. Figure 6.10 represents the minimal total uncertainty, as computed from the positive (blue) and negative (magenta) biases: each point illustrates the minimal error for each one of the Figures 6.8 and 6.9 plots. The uncertainties are noted on the y-axis, while the x-axis shows the ranges for positive and negative uncertainty.

6.5 Results

The optimal fitting range should take into account various experimental uncertainties, such as background uncertainty and reconstruction efficiency, and also all the relevant theoretical uncertainties such as the PDF. For the time being, this optimization only considers a compromise between the PS uncertainty and an estimate of the statistical uncertainty arising from data. Using the results in Figure 6.10, one can propose $[30, 46]$ GeV and $[30, 44.5]$ GeV as fitting ranges respectively for $p_{\mathrm{T}}^{\mu^-}$ and $p_{\mathrm{T}}^{\mu^+}$. This results in a systematic uncertainty of $+3$ and -3 MeV from $p_{\mathrm{T}}^{\mu^-}$ fit, and $+2$ and -2 MeV from $p_{\mathrm{T}}^{\mu^+}$ fit. The results are reported in Tables 6.2 and 6.3.

For the sake of comparison with previous results (cf. Ref. [103]), the fits were also performed with the combined $\mu^+ - \mu^-$ channel, and the optimal range was found to be $[30, 44.5]$ GeV, with a systematic uncertainty of $+2$ and -2 MeV. The uncertainties obtained in the default fitting range, i.e. $[30, 50]$ GeV, are $+5$ and -7 MeV for the $\mu^+ - \mu^-$ combined channel. Both these results as well as the expected statistical uncertainties are presented in Table 6.4.

Tune Variation	Positive	Negative
1±	2	−2
2±	2	−2
3±	2	−2
Tuning uncertainty	3	3
Statistics	10	10
Tuning ⊕ Stat	10	10

TABLE 6.2: Parton shower uncertainties induced by the modeling of p_{T}^{W-}. The first three rows show the differences in m_W associated to each tune variation, the last three rows show the total systematic uncertainty, the expected statistical uncertainty, and the quadratic sum of both. Values are given in MeV.

The differences in the extracted numbers show the importance of the chosen range towards the results of the fits, therefore implying the need to set on a common range when studying all the other systematic uncertainties.

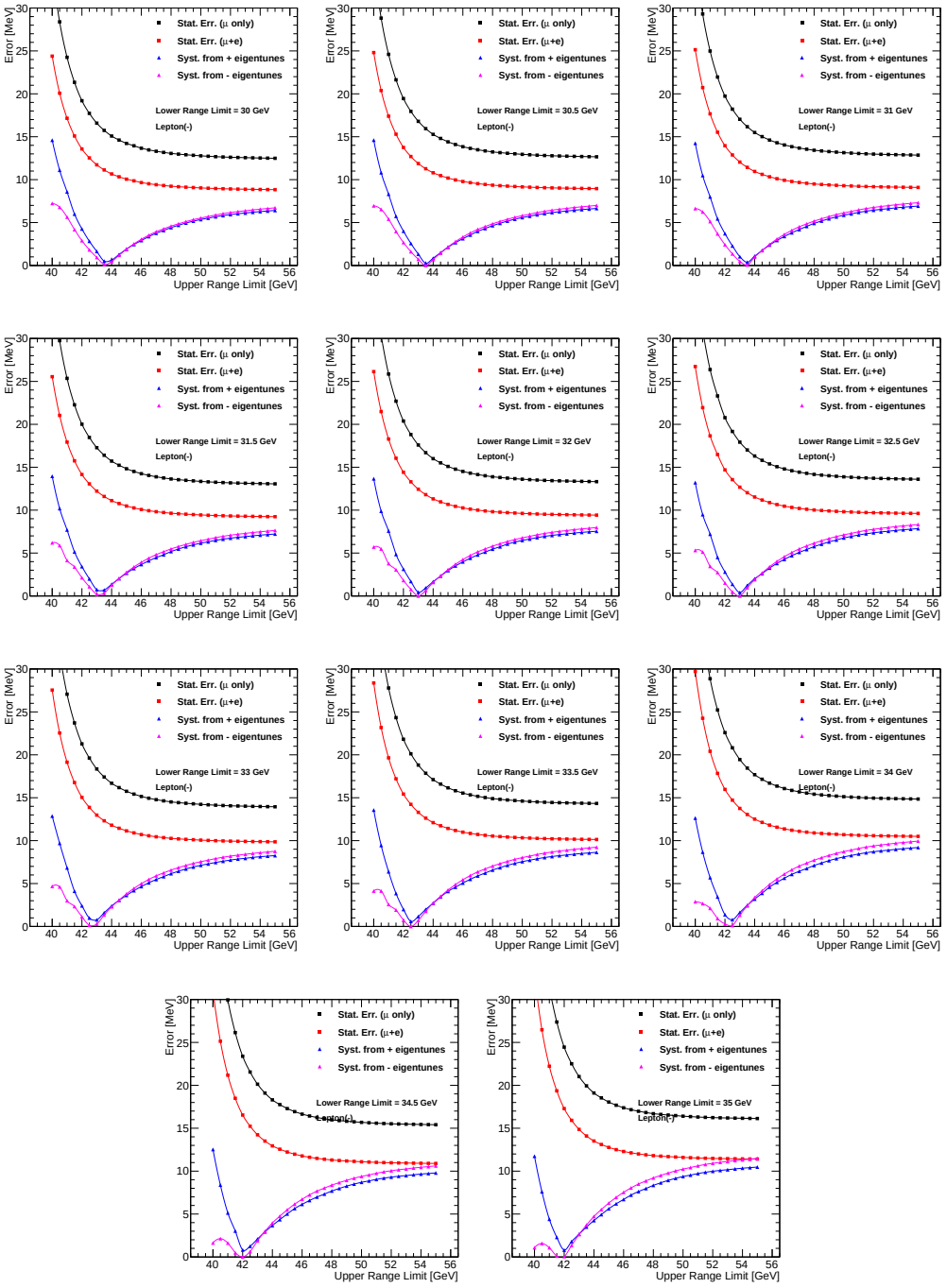

FIGURE 6.8: Computed systematic uncertainties from $p_{\mathrm{T}}^{\mu^-}$ and statistical uncertainties for the muonic channel only, and for the muon-electron combined channel, as expected from 2011 data samples. Each plot represents a different lower fit range limit, starting from 30 GeV (top left) to 35 GeV (bottom right) with steps of 0.5 GeV, and scans an upper range limit from 40 to 55 GeV with similar steps.

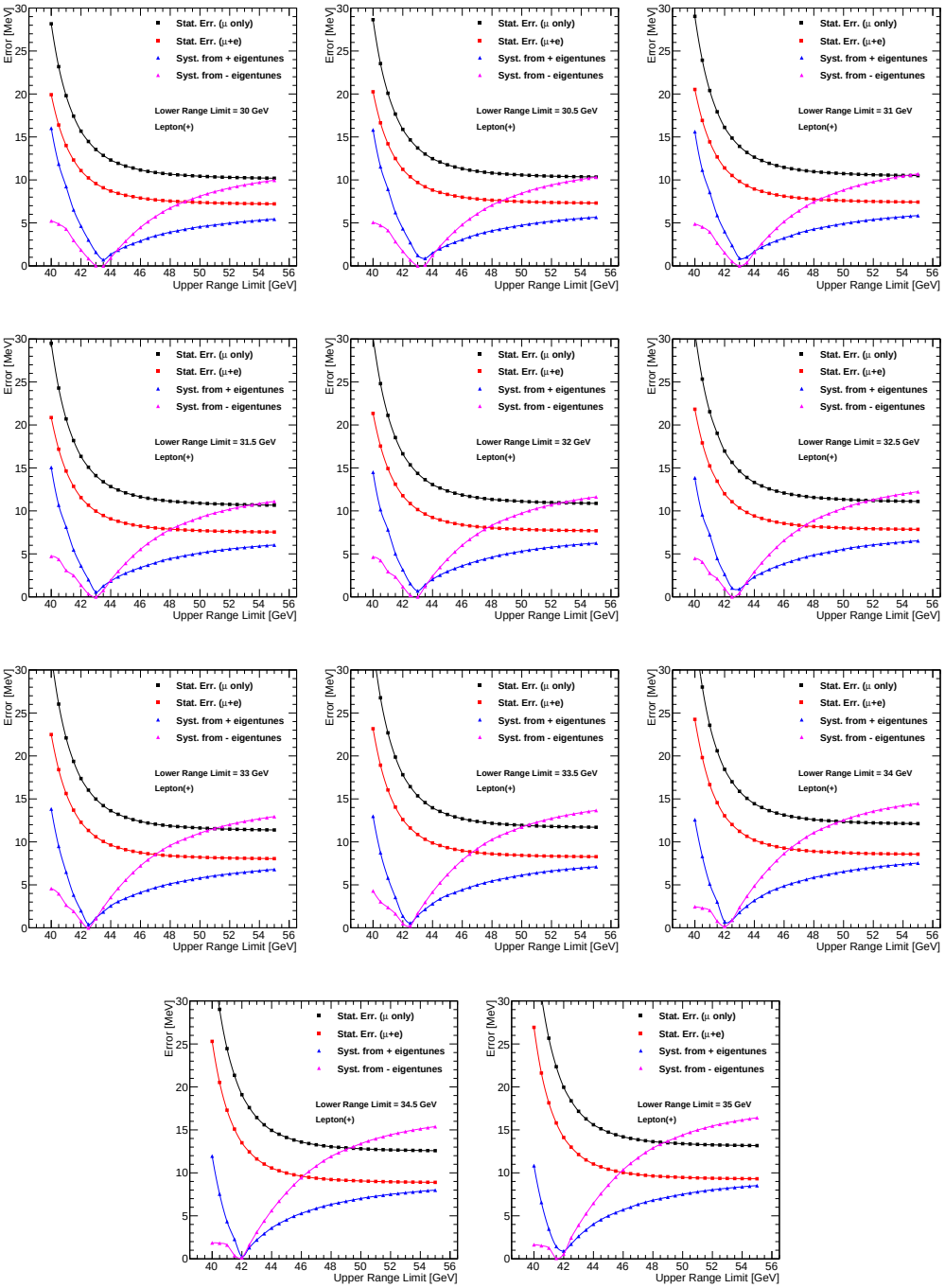

FIGURE 6.9: Computed systematic uncertainties from $p_T^{\mu^+}$ and statistical uncertainties for the muonic channel only, and for the muon-electron combined channel, as expected from 2011 data samples. Each plot represents a different lower fit range limit, starting from 30 GeV (top left) to 35 GeV (bottom right) with steps of 0.5 GeV, and scans an upper range limit from 40 to 55 GeV with similar steps.

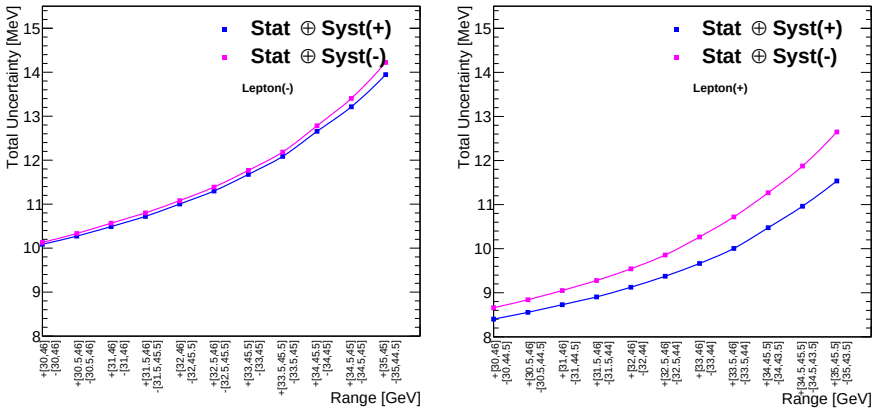

FIGURE 6.10: Minimization of the total uncertainty computed from the positive (blue) and the negative (magenta) systematic uncertainties, for μ^- (left) and μ^+ (right).

Tune Variation	Positive	Negative
1±	1	−1
2±	1	−1
3±	1	−1
Tuning uncertainty	2	2
Statistics	9	9
Tuning ⊕ Stat.	9	9

TABLE 6.3: Parton shower uncertainties induced by the modeling of p_{T}^{W+}. The first three rows show the differences in m_W associated to each tune variation, the last three rows show the total systematic uncertainty, the expected statistical uncertainty, and the quadratic sum of both. Values are given in MeV.

Fit Range	$30 < p_{\mathrm{T}}^{\mu} < 50$ GeV		$30 < p_{\mathrm{T}}^{\mu} < 44.5$ GeV	
Tune Variation	Positive	Negative	Positive	Negative
1±	3	−4	1	−1
2±	3	−4	1	−1
3±	3	−4	1	−1
Tuning uncertainty	5	7	2	2
Statistics	6	6	7	7
Tuning ⊕ Stat.	8	9	7	7

TABLE 6.4: Parton shower uncertainties induced by the modeling of combined p_{T}^{W+} and p_{T}^{W-}, for two different fitting ranges. The first three rows show the differences in m_W associated to each tune variation, the last three rows show the total systematic uncertainty, the expected statistical uncertainty, and the quadratic sum of both. Values are given in MeV.

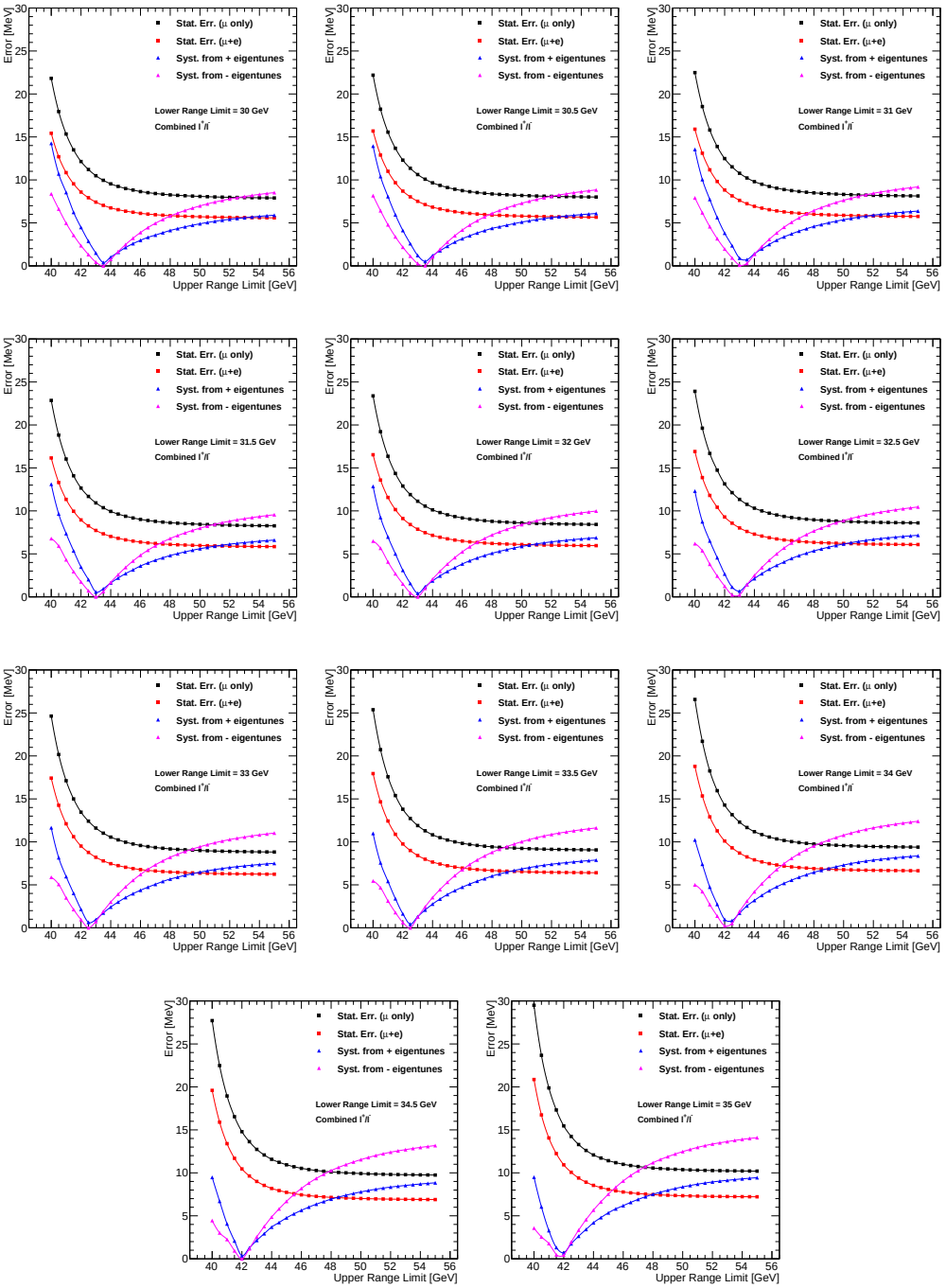

FIGURE 6.11: Computed systematic uncertainty from combined $p_{\mathrm{T}}^{\mu^+}$ and $p_{\mathrm{T}}^{\mu^-}$, and statistical uncertainties for the muonic channel only, and for the muon-electron combined channel, as expected from 2011 data samples. Each plot represents a different lower fit range limit, starting from 30 GeV (top left) to 35 GeV (bottom right) with steps of 0.5 GeV, and scans an upper range limit from 40 to 55 GeV with similar steps.

Chapter 7

W Event Selection, Signal and Background Extraction

7.1 Event selection

The signal event selection procedure conciliates between a high signal efficiency and a high background rejection. It consists of a sequence of requirements and selections applied on the event samples. Such requirements involve in a first step applying detector quality cuts to obtain clean samples containing well reconstructed events, without detector failures or similar problems. In a later step, and depending on the analysis, specific kinematic requirements are applied. In the case of a W analysis, considering only leptonic final states, the kinematic selections are based on the lepton's transverse momentum p_{T}^{ℓ}, the boson's transverse mass m_{T}^{W} and its transverse momentum p_{T}^{W}, and the missing transverse energy $E_{\mathrm{T}}^{\mathrm{miss}}$, reflecting the neutrino in the final state.

7.1.1 Collision data

The analysis discussed in this chapter is based on the 2011 pp collision data of $\sqrt{s} = 7$ TeV. The data samples used in the analysis are treated at several stages of the acquisition and processing chain, to make sure they pass the required quality criteria and to detect as early as possible any problem that could compromise this quality. An online monitoring takes place at first, to resolve problems such as data corruption or desynchronization, and to check the trigger rates and running conditions. After verification of the online data quality requirements, the total integrated luminosity of 2011 data corresponds to 4.7 fb^{-1}.

In a second step, an offline quality control is applied by imposing specific cuts and conditions on the data samples. These cuts exclude problematic luminosity blocks, and select events with a good primary vertex, and passing the relevant triggers. The quality monitoring and assessment algorithms are described in Ref. [104].

7.1.2 Simulated samples and cross sections

The main processes involved in the W-mass analysis are simulated using Monte Carlo. The signal, $W \to \ell\nu$, is generated using the POWHEG box [72, 105] (version 1.0), and events are showered using PYTHIA8 [33]. The POWHEG matrix element is interfaced to the CT10 PDF [51].An accurate modeling of the transverse momentum of the W boson, p_{T}^{W}, is obtained from the p_{T}^{Z} AZNLO tuning in POWHEG+PYTHIA8 as described in Chapter 6.

The backgrounds coming from vector bosons and top quark decays are also generated using Monte Carlo simulation. $Z \to \ell\ell$ and $W \to \tau\nu$ are simulated with POWHEG+PYTHIA8, and the top background sample is based on MC@NLO [106] interfaced to HERWIG+JIMMY [107, 108]. Backgrounds from weak boson pair production are simulated using HERWIG+JIMMY, tuned with AUET2 [109]. The generated events are processed through the full ATLAS detector simulation based on GEANT4 [110]. Multijet backgrounds are harder to model. They are determined using collision data, as described in § 7.2.

The signal and background MC samples include final state radiation effects (FSR), modeled using the PHOTOS [86] generator. The effect of multiple interactions per bunch crossing ("pile-up") is modeled by overlaying simulated minimum bias events over the original hard-scattering event. A reweighting is applied to reproduce the distribution of the average number of interactions per bunch crossing in data, this aspect is discussed in § 7.3.1. The MC samples used for the $W \to \ell\nu$ signal and background and their cross-sections, calculated to NNLO, are summarized in Table 7.1. The study discussed in this chapter concerns the $W \to e\nu$ channel only.

Process	Generator	$\sigma \times BR$[pb]
Signal Samples		
$W^+ \to \ell^+\nu$	Powheg+Pythia8	6160
$W^- \to \ell^-\nu$	Powheg+Pythia8	4300
Background Samples		
$W^+ \to \tau^+(\to e^+)\nu$	Powheg+Pythia8	930.04
$W^- \to \tau^-(\to e^-)\nu$	Powheg+Pythia8	603.63
$Z \to e^+e^-$	Powheg+Pythia8	990
$Z \to \tau^+\tau^-(\to e)$	Powheg+Pythia8	260.42
WW	Herwig	20.86
ZZ	Herwig	1.54
WZ	Herwig	6.97
$t\bar{t}$	MC@NLO	137.30
st_tchan_eν	MC@NLO	6.83
st_tchan_τν	MC@NLO	6.81
st_schan_eν	MC@NLO	0.46
st_schan_τν	MC@NLO	0.46
st_Wt	MC@NLO	14.37

Table 7.1: MC samples used in the analysis. Cross sections are normalized to NNLO.

7.1.3 Electron identification

The identification of the electrons is based on three levels of cuts: *loose*, *medium* and *tight* [111]. These cuts combine information from the calorimeter and from the tracking detector in order to maintain good signal efficiency and minimize the background. The variables used are defined in Table 7.2, and the cuts are summarized below:

Type	Description	Variable name
Loose cuts		
Acceptance of the detector	$\|\eta\| < 2.47$	
Hadronic leakage	Ratio of E_T in the first sampling of the hadronic calorimeter to E_T of the EM cluster	
Second layer of EM calorimeter	Ratio in η of cell energies in 3×7 versus 7×7 cells	R_η
	Ratio in Φ of cell energies in 3×3 versus 3×7 cells	R_ϕ
	Lateral width of the shower	
Medium cuts (include loose cuts)		
First layer of EM calorimeter	Difference between energy associated with the second largest energy deposit and energy associated with the minimal value between the first and second maxima.	ΔE_s
	Second largest energy deposit normalized to the cluster energy.	R_{max2}
	Total shower width	w_{stot}
	Shower width for three strips around maximum strip	w_{s3}
	Fraction of energy outside core of three central strips but within seven strips	F_{side}
Track quality	Number of hits in the pixel detector (at least one)	
	Number of hits in the pixel and SCT (at least nine)	
	Transverse impact parameter (< 1 mm)	
Tight (isol) cuts (include medium cuts)		
Isolation	Ratio of transverse energy in a cone $\Delta R < 0.2$ to the total cluster transverse energy	
Vertexing-layer	Number of hits in the vertexing-layer (at least one)	
Track matching	$\Delta\eta$ between the cluster and the track (< 0.005)	
	$\Delta\Phi$ between the cluster and the track (< 0.02)	
	Ratio of the cluster energy to the track momentum	E/p
TRT	Total number of hits in the TRT	
	Ratio of the number of high-threshold hits to the total number of hits in the TRT	
Tight (TRT) cuts (include tight (isol) except for isolation)		
TRT	Same as TRT cuts above, but with tighter values corresponding to about 90% efficiency for isolated electrons	

TABLE 7.2: Definition of variables used for *loose*, *medium* and *tight* electron identification cuts [111].

- **Loose cuts** perform a simple electron identification based on limited information from the calorimeter. They are applied on hadronic leakage and on shower shape variables derived

from only the middle layer of the EM calorimeter. This set of cuts provides excellent identification efficiency, but low background rejection.

- **Medium cuts** improve the quality by adding cuts on the strips in the first layer of the EM calorimeter and on the tracking variables, while including the *loose* requirements. These cuts are effective in rejecting $\pi^0 \to \gamma\gamma$ decays, and in increasing the jet rejection by factor 3-4 with respect to the *loose* cuts, while reducing the identification efficiency by 10%.
- **Tight cuts** make use of all the particle identification tools available for electrons. In addition to the *medium* selection, cuts are applied on the number of hits in the TRT and the ratio of high-threshold hits to the number of hits in the TRT to reject the dominant background from charged hadrons, on the difference between the cluster and the extrapolated track positions in η and ϕ, and on the ratio of cluster energy to track momentum. This selection rejects charged hadrons and secondary electrons coming from conversions.

7.1.4 W event selection

To select $W \to e\nu$ candidates in data, events are requested to pass good data quality and trigger requirements. The events are then required to have at least one primary vertex reconstructed from at least three tracks.

Electron candidates passing the identification criteria of § 7.1.3 are built from clusters of energy deposited in the electromagnetic calorimeter that are associated with at least one well-reconstructed track in the Inner Detector. They are required to have $p_{\mathrm{T}} > 15$ GeV and $|\eta| < 2.4$ excluding the region $1.2 < |\eta| < 1.82$, to avoid regions with high passive material. The electrons are required to pass the tight identification criterion. These conditions do not guarantee the absence of "fake" electrons, hence the need to apply additional cuts in the later steps of the selection.

The events passing the quality criteria and containing good electron candidates, are requested to contain exactly one tight electron with a transverse momentum $p_{\mathrm{T}} > 30$ GeV, missing transverse energy such that $E_{\mathrm{T}}^{\mathrm{miss}} > 30$ GeV, W boson transverse momentum $p_{\mathrm{T}}^{W} < 30$ GeV and a transverse mass $m_{\mathrm{T}} > 60$ GeV. Monte-Carlo events are corrected to take into account differences with data in lepton reconstruction, identification, isolation and trigger efficiencies, pile-up, energy and momentum.

Lastly, two additional cuts are applied simultaneously to the selected electron for further background reduction. These two cuts depend on electron pseudorapidity η and transverse momentum p_{T} to provide approximately constant signal efficiency in each $\eta \times p_{\mathrm{T}}$ bin. The first one acts on the calorimeter isolation variable called $E_{\mathrm{T}}\mathrm{cone20}/E_{\mathrm{T}}$ using calorimeter deposit within a cone $\Delta\mathrm{R} < 0.2$ and has a 98% signal efficiency, while the second one acts on the track isolation variable $p_{\mathrm{T}}\mathrm{cone40}/p_{\mathrm{T}}$ using tracks within $\Delta\mathrm{R} < 0.4$ and keeps 97% of the signal. A combination of both cuts turned out to be optimal, and their use is detailed in § 7.6.

Once all these selections are applied, the inclusive remaining numbers of $W \to e\nu$ data events is 3.4M for W^+, 2.4M for W^- and 5.8M charge-combined.

7.2 Simulated backgrounds: electroweak and top

The W events with leptonic final states are contaminated with relatively low background. In this chapter, only the $W \to e\nu$ channel is discussed. When extracting pure $W \to e\nu$ signals, one

should proceed carefully since the events passing the selections described in section 7.1.4 are not only $W \to e\nu$ signals but also events having a similar final state or where one or more particles have been mis-identified. The expected background for the electronic channel can result from $W \to \tau\nu$, $Z \to ee$, $Z \to \tau\tau$, as well as dibosons decays, top processes and multijet events. All of these are discussed in the paragraphs below.

The electroweak and top processes accompanying $W \to e\nu$ events are modeled with good accuracy: their respective cross-sections are measured with good agreement with the theoretical expectation [112–115], and Monte Carlo is used to implement them. They are described in 7.1.2 and listed hereafter:

- $Z \to ee$, where one of the final electrons is either not detected or not identified, thus creating a missing transverse energy. Reducing this background is done by requesting central $|\eta_e|$, vetoing a second electron and imposing a minimal m_{T}^{W} since it is mainly low for $Z \to ee$ events. After all selections, $Z \to ee$ represent 52% of the simulated background.
- $W \to \tau\nu$, where the τ decays into $e\nu_e\nu_\tau$. Since the final state is exactly identical to the signal (one electron and missing transverse energy), this background is irreducible. However, the p_{T}^{ℓ} and m_{T}^{W} are expected to be lower than with $W \to e\nu$ signal, hence the importance of applying p_{T}^{ℓ} and m_{T}^{W} cuts. Typically, $W \to \tau\nu$ processes constitute approximately 37% of the background.
- $Z \to \tau\tau$, which is similar to the previous process, but here one τ decays leptonically, and the other is not identified. This process has a small cross section, and can be reduced by cutting on the p_{T}^{ℓ}. It represents 4.5% of the background.
- $t\bar{t}$/single t, the top decaying into a W and a lighter quark (b, s, d), the W decaying into an isolated electron. This is a non-negligible source of background for this study, however it has a cross section which is significantly smaller than the signal: the number of top events after all selections constitute 4% of the background.
- Dibosons, which have a final state similar to the corresponding previous ones but here only one final electron is identified. They make up around 2.5% of the background.

7.3 Data-driven backgrounds: multijet events

The main challenge in the W background determination is the evaluation of the multijet background. The major contribution is dijet production via QCD processes, where the selected leptons in the final state can come from hadrons mis-identified as leptons, heavy quark decay, and multijet events where one jet is identified as an electron and the other falls outside of the acceptance region.

In a measurement requiring high precision like the W mass and the W,Z cross-sections, simulation of jet events faking electron is not sufficiently reliable. Therefore, a data-driven technique is used to determine them, by modifying the requirements on final electrons to select a background enriched sample: this technique consists of using collision data to isolate fake electron candidates. This is done in a jet-dominated region defined in the following sections.

The overall approach detailed in the following sections is represented in Fig. 7.1 and summarized hereafter. A jet-dominated region is defined with kinematic signal selections but background-enriching identification requirements. In this intent, we select electron candidates passing only

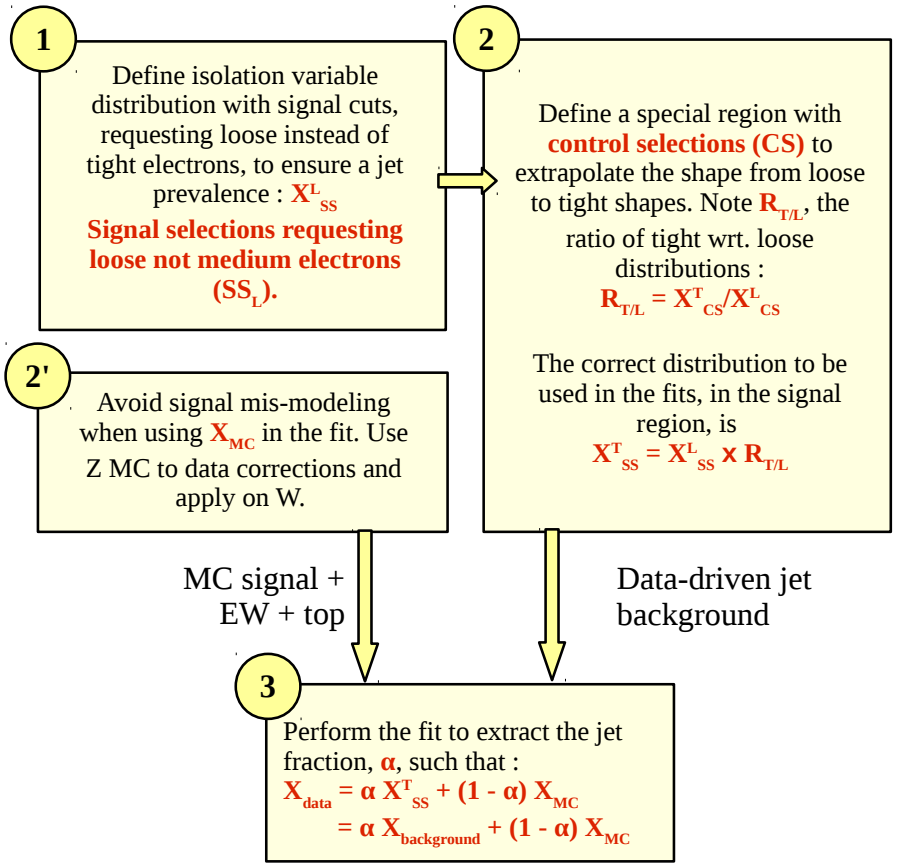

FIGURE 7.1: Jet background assessment approach. All the different steps are detailed in text.

the loose, but not the medium identification criteria, instead of tight electrons as in the signal. In the following, the term "loose" indicates electrons passing the loose but not the medium and tight selections.

The possibility of good electrons passing these selections is not negligible. To remove this contamination, the same requirements are imposed on the MC signal and EW background, and the selected simulated events are subtracted from the data-driven background. This step will later be referred to as "signal subtraction".

Once the jet background sample is defined, and the signal contamination is subtracted, one obtains clean jet-enriched distributions. In what follows, the data signal sample will be referred to as "signal", the clean jet-enriched sample as "background", and the rest of the samples (ie. MC signal, electroweak and top backgrounds) will be called "MC" for simplicity.

Next step consists of determining the fraction of the jet background with respect to the overall signal data distribution, assuming that the shape of the kinematic distributions are similar in signal and in background region. For that purpose, MC and the background are normalized to the signal distributions, in a jet-enriched range of an observable X not included in the event selections, used as a discriminant.

The aim of the normalization procedure is to find the jet background fraction, f_{jet}, representing the ratio of the number of background events (*i.e.* jet events) with respect to the number of signal data events, deduced from the following result of the fit:

$$H_{\text{signal}} = \alpha H_{\text{background}} + (1 - \alpha) H_{\text{MC}} \tag{7.1}$$

where H is the distribution of X, α is the results of the fit.

7.3.1 Background electron candidates

The selection of loose electron candidates is more efficient than selecting tight candidates. This high efficiency implies a larger amount of events passing the selections, and involves a larger volume of data to store. Due to the limited data storage, a prescaling is imposed at the trigger level: the prescale is a factor associated with a trigger at each level, indicating which fraction of events passing this trigger selection is actually accepted.

The primary triggers applying tight selections and used for physics measurements and searches are used without prescales. It is only when we request looser identification criteria, that the rate of the retained electrons is too large and would flood the storage system. In other terms, un-prescaled triggers are possible only for tighter selections, and prescaled triggers compensate for the loose selections. The prescales being different between early and late data taking periods [116], it is hence practical to separate in periods when using prescaled triggers.

In parallel, the multiple interactions per bunch crossing in one event, called "pile-up", depends on the luminosity (cf. Eq. 2.2). With higher luminosity, more jets are produced and reconstructed as electrons: the jet background therefore depends on the pile-up, hence the need to separate the study into bins of average number of interactions per bunch crossing, $\langle\mu\rangle$. The $\langle\mu\rangle$-based separation is at the same time in agreement with the recoil corrections (cf. § 5.3.4). The pile-up modeling is corrected as described in § 5.3.1.

As a first approach, the jet background estimation study was conducted separately in three data taking periods, corresponding to three different prescales: periods D-J (corresponding to a lower pile-up), period K, and period L-M (higher pile-up). The pile-up reweighting was also done separately in each period. Fig. 7.2 illustrates the pile-up distributions involved in the reweighting procedure, for the used prescaled triggers on the left, and the used physics triggers (without prescales) on the right. For each case, the average interactions per bunch crossing are shown for the three period groups. In a second approach, the study was repeated by separating in $\langle\mu\rangle$ bins, taking advantage of the optimized recoil correction in these bins as well. This part will be discussed in § 7.5.

The MC samples are listed in § 7.1.2. The same simulated events are launched six times, in parallel to data with and without prescales, times three period groups, each time reweighting the pile-up to one period group with a specific trigger, and normalizing the processes to their cross-sections according to the considered luminosity. Table 7.3 shows the luminosities in pb^{-1} for each period, and each trigger.

7.3.2 Discriminant variable choice - Signal subtraction

BOX (1) of Fig. 7.1

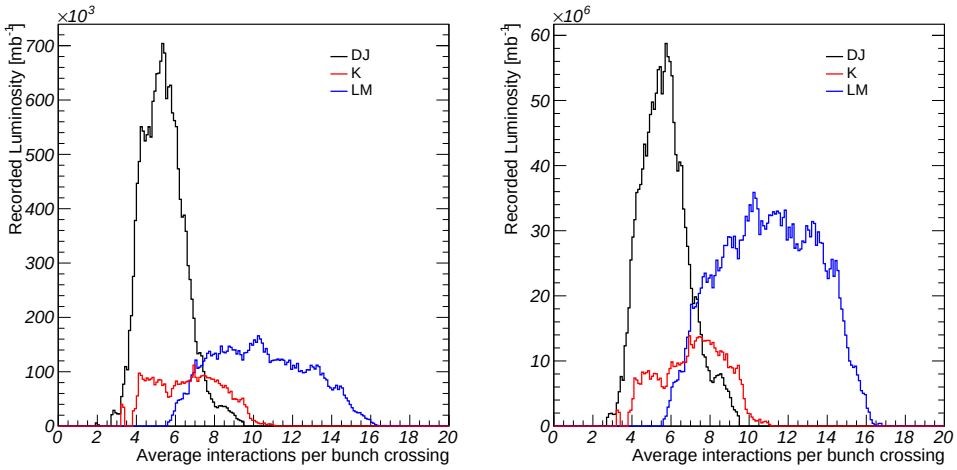

(a) $\langle\mu\rangle$ using prescaled triggers

(b) $\langle\mu\rangle$ using physics triggers

FIGURE 7.2: Average interactions per bunch crossing, $\langle\mu\rangle$. These histograms are used to correct the pile-up in the MC in different data taking periods. The plot on the left is used when handling prescaled triggers and the one on the right corresponds to physics triggers.

pb^{-1}	DJ	K	LM
Prescaled trigger	19.2	6.4	10.4
Physics trigger	1636	575	2368

TABLE 7.3: Luminosities vs. trigger and period.

The fits done to extract the jet background fraction need to be performed in a region with high jet prevalence, using a variable which can discriminate between jets and signal. This variable is chosen to be the electron isolation. Its discriminative nature is based on the fact that tight electron candidates selected in the signal are by definition more isolated than loose electron candidates selected in the background. To represent this aspect, Fig. 7.3 is an illustration of the sum of all tracks around the reconstructed electron in a cone of $\Delta R < 0.4$ (ΔR is defined in § 3.1), excluding the electron's momentum itself. The jet isolation tends to have higher values than the signal, which means that the jet has more activity around it and is thus less isolated than the signal.

To remove any signal contamination remaining in the jet samples, the same selections were applied on simulated samples (signal, EW and top background) which were subtracted from the jet distributions. Table 7.4 lists the approximate contamination (= $N_{contamination}/N_{jet\ events}$) level for each case. Fig. 7.4 illustrates the main distributions before and after signal subtraction.

Period	DJ	K	LM
Contamination (%)	4	6	4

TABLE 7.4: Signal contamination in the background region for each period.

The fit results rely non-exhaustively on the chosen fitting range, variable, and background control region. A test was performed on several variables, to check the impact of the fitting range on the results of the fits. An agreement between different results from fits in different ranges was observed within the uncertainties. The control region choice is discussed in § 7.3.3 and the variable choice is discussed hereafter.

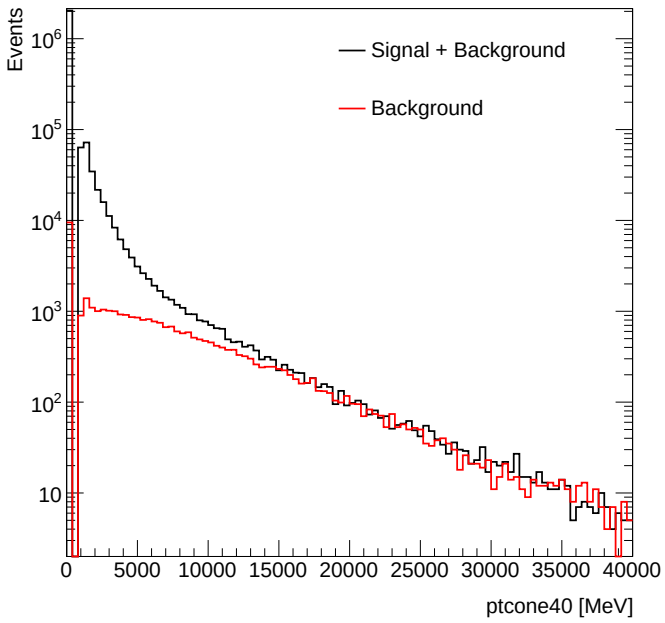

FIGURE 7.3: $p_T$cone40 distributions from data, in signal region (black) and background region (red). Signal events tend to have lower $p_T$cone40 values meaning less activity around the electron candidate showing that it's more isolated. Both distributions do not contain the same events, as tight electrons are requested for signal (black) and loose for background (red).

The track-based isolation variables ($p_T$coneXX) showed more stable fits with respect to the cone size than the calorimeter-based ones ($E_T$coneXX). The choice remains between the following variables: $p_T$cone20, $p_T$cone30 and $p_T$cone40 each representing the momentum sum of all tracks around the electron inside a cone of $\Delta R = 0.2, 0.3, 0.4$ respectively, without counting the electron momentum. The relative variable with respect to the electron p_T (ie. $p_T\text{cone20}/p_T$, $p_T\text{cone30}/p_T$ and $p_T\text{cone40}/p_T$) will not be considered due to the difficulty in correcting the p_T component in the simulation (this correction is discussed in § 7.3.4).

Since we are using the isolation variable as a jet discriminant, it is expected to have lower isolation values for the signal (tight) and higher for the background (loose). Fig. 7.5 shows that this is not the case for $p_T$cone40. This is due to electrons coming from conversions, where they are mostly detected in a small cone ($\Delta R < 0.2$) within each other. Removing the smaller cone removes both electrons from the calculation and lowers the isolation values. The variable used in the fit is therefore $p_T\text{cone40} - p_T\text{cone20}$, with $p_T\text{cone30} - p_T\text{cone20}$ used as a cross-check.

7.3.3 Jet shape correction

BOX (2) of Fig. 7.1

Requesting loose electrons to evaluate jets in a signal region where the electrons are tight is a tricky procedure, especially when using isolation variables in the fits. These variables are correlated with the electron identification, as shown in Fig. 7.6. In this figure, the events are from data samples with $p_T^e > 30$ GeV, m_T, E_T^{miss} and p_T^W cuts being relaxed. The signal, electroweak and top background contamination has also been subtracted, to focus solely on the

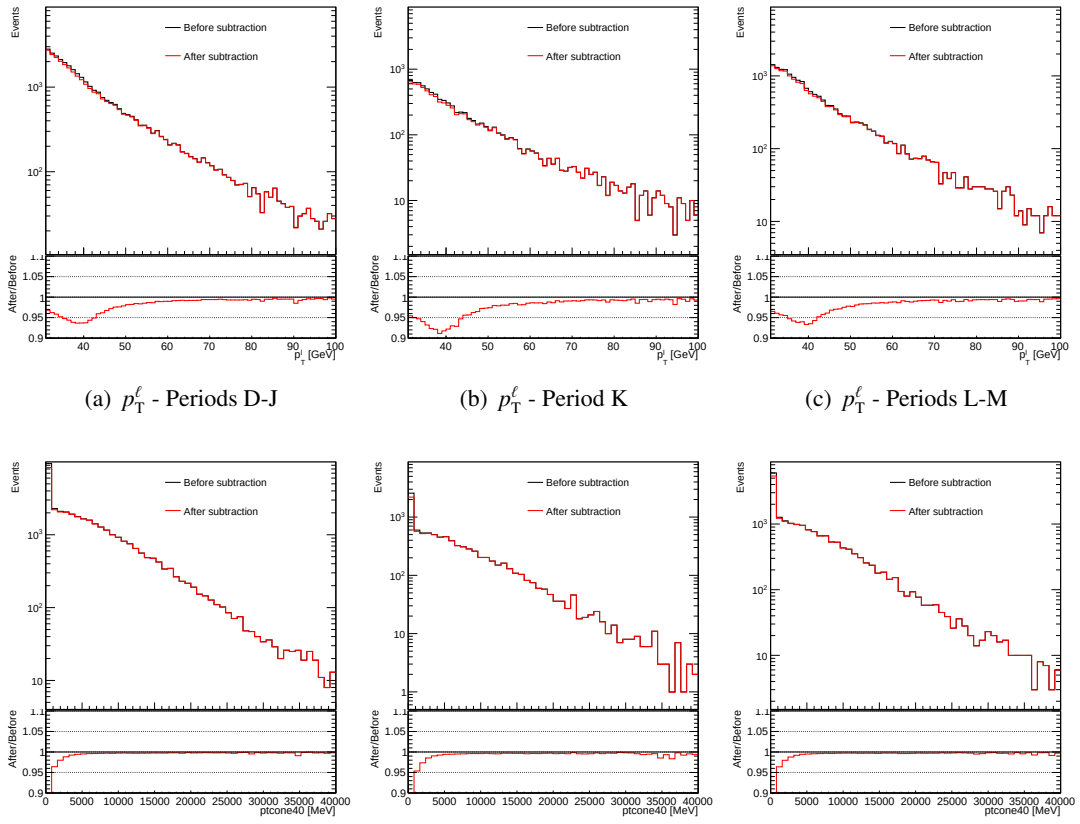

(a) p_{T}^{ℓ} - Periods D-J (b) p_{T}^{ℓ} - Period K (c) p_{T}^{ℓ} - Periods L-M

(d) p_{T}cone40 - Periods D-J (e) p_{T}cone40 - Period K (f) p_{T}cone40 - Periods L-M

FIGURE 7.4: p_{T}^{ℓ} (top) and p_{T}cone40 (bottom) distribution, in the background region, before and after signal subtraction, for different periods. Ratios are in agreement with the contamination level noted in Table. 7.4

effect of identification. Correcting the shape of the jet isolation distribution used in the fit is therefore considered.

In this purpose, we define an additional control region to study and correct for the effect of identification on the isolation, while being as orthogonal to the signal region as possible. Electron candidates are requested to pass the following control cuts:

$$p_{\mathrm{T}}^{e} > 30 \text{ GeV}, E_{\mathrm{T}}^{\mathrm{miss}} < 30 \text{ GeV}, m_{\mathrm{T}} \text{ and } p_{\mathrm{T}}^{W} \text{ cuts are relaxed.} \tag{7.2}$$

Table 7.5 schematizes the definitions of the signal and control regions.

In this newly defined control region, the ratio between tight and loose electrons ($R_{\mathrm{T/L}} = \mathrm{X}_{\mathrm{CS}}^{\mathrm{T}}/\mathrm{X}_{\mathrm{CS}}^{\mathrm{L}}$) is saved. The superscript T refers to tight electrons, and L to loose. The subscript CS indicates the region where Control Selections are applied.

The extrapolated jet distribution will therefore be $\mathrm{X}_{\mathrm{SS}}^{\mathrm{T}}(\mathrm{extrap}) = \mathrm{X}_{\mathrm{SS}}^{\mathrm{L}} \times R_{\mathrm{T/L}}$, where $\mathrm{X}_{\mathrm{SS}}^{\mathrm{L}}$ is built with *W* signal selections, but loose electron candidates, and $\mathrm{X}_{\mathrm{SS}}^{\mathrm{T}}$ does not represent the distribution directly extracted from the tight signal region, but is extrapolated from the control region as described above. The fitting procedure described in § 7.3.5 will be applied separately on the

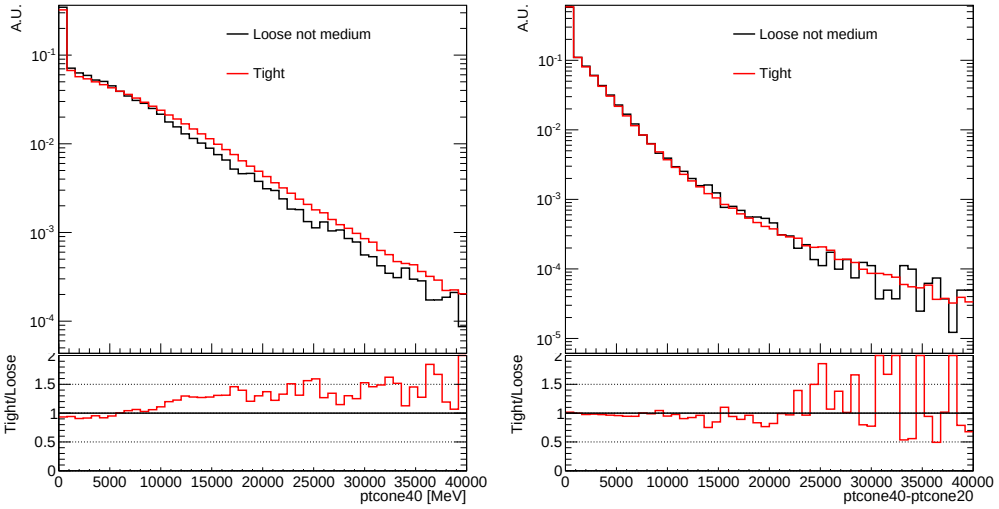

(a) p_{T}cone40 (b) p_{T}cone40 − p_{T}cone20

FIGURE 7.5: Ratios of distributions drawn with tight electrons with respect to loose electrons. With p_{T}cone40 on the left, the tight electrons seem to be less isolated than loose electrons. On the right, removing the inner cone of p_{T}cone20 reduces this effect. Distributions are plotted in background control regions, signal contamination is already subtracted everywhere.

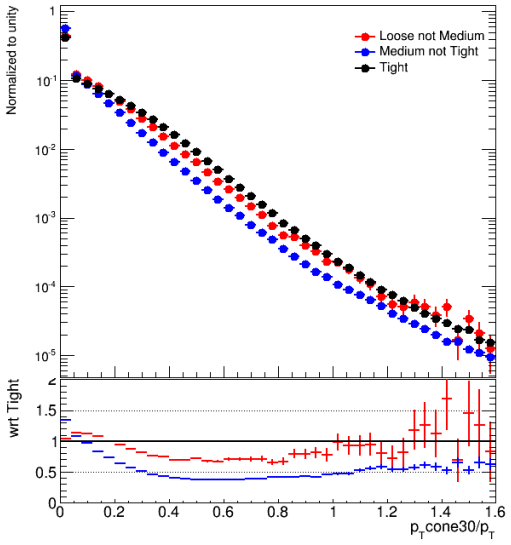

FIGURE 7.6: Example of the correlation between identification and isolation (p_{T}cone30/p_{T}). The events are from data samples, with only $p_{\mathrm{T}}^{e} > 30$ GeV, m_{T}, $E_{\mathrm{T}}^{\mathrm{miss}}$ and p_{T}^{W} cuts being relaxed. The signal, electroweak and top background contamination has also been subtracted, to focus solely on the effect of identification.

Usage	Name & Requirements	Additional Requirements	Description
Shape extrapolation in a control region poor in signal	**CS** **C**ontrol **S**election cuts: • $p_{\mathrm{T}}^{e} > 30$ GeV • $E_{\mathrm{T}}^{\mathrm{miss}} < 30$ GeV • $m_{\mathrm{T}} > 0$ GeV • $p_{\mathrm{T}}^{W} > 0$ GeV	$\mathrm{CS_T}$ Tight electron	The inverted $E_{\mathrm{T}}^{\mathrm{miss}}$ cut defines a signal-depleted region. Tight and Loose distributions are used to extrapolate the distributions shapes.
		$\mathrm{CS_L}$ loose electron	
Signal Regions	**SS** **S**ignal **S**election cuts: • $p_{\mathrm{T}}^{e} > 30$ GeV • $E_{\mathrm{T}}^{\mathrm{miss}} > 30$ GeV • $m_{\mathrm{T}} > 60$ GeV • $p_{\mathrm{T}}^{W} < 30$ GeV	$\mathrm{SS_T}$ Tight electron	$\mathrm{SS_T}$ defines the signal region, with tight electrons. $\mathrm{SS_L}$ is the background region, without any shape extrapolation.
		$\mathrm{SS_L}$ loose electron	

TABLE 7.5: Used signal and control regions.

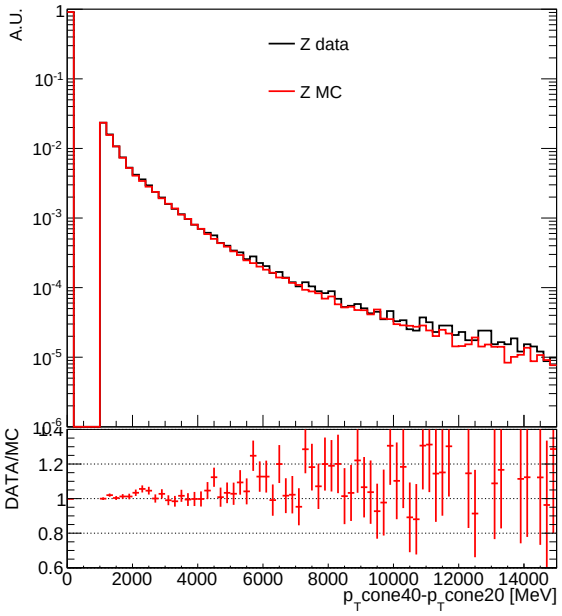

FIGURE 7.7: p_{T}cone40 $-$ p_{T}cone20 in Z events, illustrated up to 15 GeV. The ratio is used mainly to correct the bulk of the distribution. Errors are statistical.

background region ($\mathrm{SS_L}$) with and without jet shape extrapolation. The signal contamination level that is subtracted from the samples in these regions is noted in Table 7.6.

Period	DJ	K	LM
$\mathrm{CS_T}$	47%	46%	51%
$\mathrm{CS_L}$	1%	1 %	1%

TABLE 7.6: Signal contamination level in the tight and loose control regions for each period.

7.3.4 MC signal correction

BOX (2') of Fig. 7.1

It is essential to use a well measured variable in the fits, to have them as reliable as possible. Fig. 7.7 shows up to 8% of discrepancy in the bulk of the p_{T}cone40 $-$ p_{T}cone20 distribution between data and MC in Z events. The data to MC ratio is used to correct the distributions in W events, assuming that this ratio is similar in Z and W.

Now that the MC distribution is corrected, we can trust the fit if its range includes the signal dominated region. This procedure is beneficial from a statistical point of view, with a minimal risk of MC mismodeling. Table 7.7 shows the different fractions before and after correcting the MC isolation distribution.

On the other hand, table 7.8 shows an agreement within $\approx$ 20% between the results from fits performed in different ranges, which will be taken as a systematic uncertainty coming from the choice of the fitting range. The ranges also exclude bins with poor statistics.

Variable	w/o MC correction	w/ MC correction
Jet shape is not extrapolated		
p_{T}cone30 − p_{T}cone20	1.44 ± 0.03	1.24 ± 0.03
p_{T}cone40 − p_{T}cone20	1.65 ± 0.03	1.39 ± 0.03
Jet shape is extrapolated		
p_{T}cone30 − p_{T}cone20	1.42 ± 0.03	1.22 ± 0.03
p_{T}cone40 − p_{T}cone20	1.59 ± 0.03	1.33 ± 0.03

TABLE 7.7: Fit results obtained before and after MC correction. Results are shown for p_{T}cone40 − p_{T}cone20 and p_{T}cone30 − p_{T}cone20 variables, before and after extrapolating the jet shape.

Range	w/o shape extrapolation	w/ shape extrapolation
0-40 GeV	1.39 ± 0.03	1.33 ± 0.03
1-40 GeV	1.53 ± 0.04	1.42 ± 0.04
1-10 GeV	1.41 ± 0.05	1.37 ± 0.05
5-30 GeV	1.69 ± 0.13	1.13 ± 0.10

TABLE 7.8: Different fit results obtained from fitting in different ranges. Results are shown for p_{T}cone40 − p_{T}cone20 variable, and fits are performed with and without jet shape extrapolation.

7.3.5 Fitting procedure

BOX (3) of Fig. 7.1

At this point we now have a corrected jet shape (extrapolated from loose to tight) and a well modeled signal distribution, and we need to normalize these two distributions to match the data using the ROOFIT mathematical tool detailed in Ref. [117].

In the following, the superscript "^{range}" points to the variables inside the chosen fitting range, and no superscript points to the equivalent in the total distribution range. N_{data}, N_{MC} and N_{jets} refer to the number of events in the data, MC (signal+EW+top) and jet background distributions, which will be taken as inputs. The "prime" symbol represents the number after normalization.

The procedure goes as follows:

$$\mathrm{Fit}[\mathrm{N}_{\mathrm{data}}^{\mathrm{range}}, \mathrm{N}_{\mathrm{MC}}^{\mathrm{range}}, \mathrm{N}_{\mathrm{jets}}^{\mathrm{range}}] \rightarrow [\mathrm{N}_{\mathrm{data}}^{\mathrm{range}}, \mathrm{N}_{\mathrm{MC}}^{\prime\ \mathrm{range}}, \mathrm{N}_{\mathrm{jets}}^{\prime\ \mathrm{range}}] \tag{7.3}$$

and the jet background fraction:

$$\mathrm{f}_{\mathrm{jet}} = \frac{\mathrm{N}_{\mathrm{jets}}^{\prime}}{\mathrm{N}_{\mathrm{data}}} \tag{7.4}$$

Going from $\mathrm{N}_{\mathrm{jets}}^{\prime\ \mathrm{range}}$ (Eq. 7.3) to $\mathrm{N}_{\mathrm{jets}}^{\prime}$ (Eq. 7.4) is achieved by assuming that the fraction in the total range is equal to the one in the fitting range:

$$\mathrm{f}_{\mathrm{jet}} = \mathrm{f}_{\mathrm{jet}}^{\mathrm{range}} = \frac{\mathrm{N}_{\mathrm{jets}}^{\prime\ \mathrm{range}}}{\mathrm{N}_{\mathrm{data}}^{\mathrm{range}}} = \frac{\mathrm{N}_{\mathrm{jets}}^{\prime}}{\mathrm{N}_{\mathrm{data}}} \tag{7.5}$$

The normalization of the distributions is done in two steps:

1. The jet distribution is scaled to $\mathrm{N}_{\mathrm{jets}}^{\prime} = \mathrm{f}_{\mathrm{jet}} \times \mathrm{N}_{\mathrm{data}}$

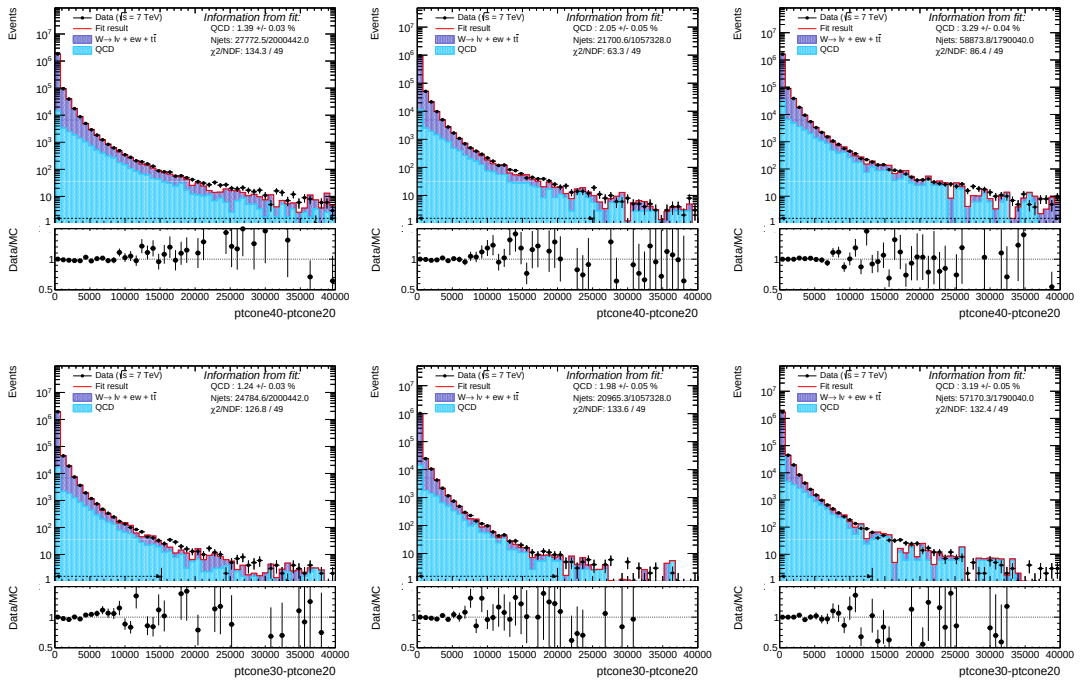

FIGURE 7.8: Fit results from the two variables, combined in charge and inclusively in pseudorapidity, before shape extrapolation. Top row represents $p_{\mathrm{T}}\mathrm{cone40} - p_{\mathrm{T}}\mathrm{cone20}$, bottom row represents $p_{\mathrm{T}}\mathrm{cone30} - p_{\mathrm{T}}\mathrm{cone20}$, and the three columns correspond to $2.5 < \langle\mu\rangle < 6.5$, $6.5 < \langle\mu\rangle < 9.5$ and $9.5 < \langle\mu\rangle < 16$ from left to right.

2. The MC distribution is scaled to $\mathrm{N}'_{\mathrm{MC}} = \mathrm{N}_{\mathrm{data}} - \mathrm{N}'_{\mathrm{jets}}$

Plots resulting from the fits are shown in Fig. 7.8 and 7.9, before and after shape extrapolation.

7.4 Background fractions

The fits were performed in a first step in three period bins, inclusively and in bins of pseudorapidity. Results are displayed for W, W^+ and W^-. Tables of fractions and numbers of jet events are detailed in Appendix A.

7.5 Results in bins of $\langle\mu\rangle$

As stated in § 7.3.1, the study was repeated in bins of average number of interactions per bunch crossing, $\langle\mu\rangle$. The chosen bins are $2.5 < \langle\mu\rangle < 6.5$, $6.5 < \langle\mu\rangle < 9.5$ and $9.5 < \langle\mu\rangle < 16$, with respectively 40%, 30% and 30% of the total statistics approximately.

Since the background fraction depends only on the pile-up, and for the sake of simplification, only the period D-J was studied for the first $\langle\mu\rangle$ bin, and L-M for the last two, since they are statistically dominant in these bins (cf. Fig 7.2).

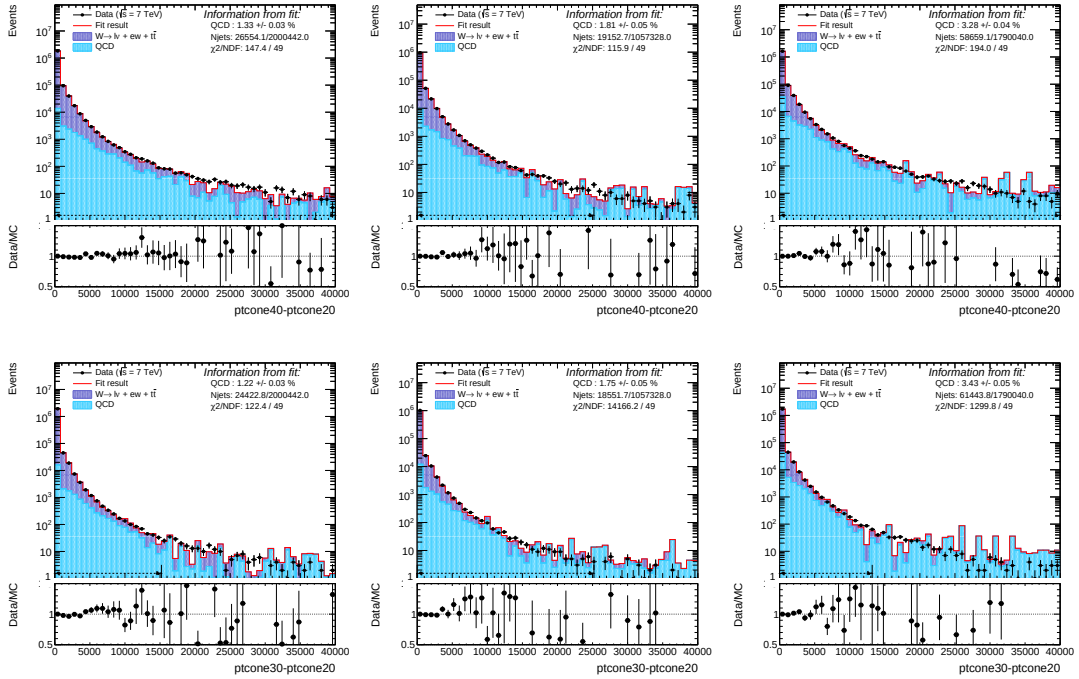

FIGURE 7.9: Fit results from the two variables, combined in charge and inclusively in pseudorapidity, after shape extrapolation. Top row represents $p_{\mathrm{T}}\mathrm{cone40} - p_{\mathrm{T}}\mathrm{cone20}$, bottom row represents $p_{\mathrm{T}}\mathrm{cone30} - p_{\mathrm{T}}\mathrm{cone20}$, and the three columns correspond to $2.5 < \langle\mu\rangle < 6.5$, $6.5 < \langle\mu\rangle < 9.5$ and $9.5 < \langle\mu\rangle < 16$ from left to right.

The study was repeated in bins of pseudorapidity. Results before isolation cuts are detailed in Appendix B and the average is shown in Table 7.9.

7.6 Reducing the background

In an attempt to reduce the background from non-isolated or fake electrons, additional isolation cuts to the central electron are applied. Two cuts, acting separately on track and calorimeter deposits, are applied simultaneously for optimal signal efficiency and background rejection. They involve cutting on the track isolation variable $p_{\mathrm{T}}\mathrm{cone40}$ and the calorimeter isolation variables $E_{\mathrm{T}}\mathrm{cone20}$. The efficiency of these cuts on the signal (tight electrons) was estimated in a parallel study [118] and was found to be 97% for the $p_{\mathrm{T}}\mathrm{cone40}$ cut and 98% for the $E_{\mathrm{T}}\mathrm{cone20}$ cut.

The estimation of the background reduction factor k was done by directly applying the cuts on the jet sample and the data sample as explained in Eq. 7.6, where f and f' are the fractions before and after isolation cuts, ε_i is the efficiency of the cut on the sample i, and N (N') is the number of events before (after) isolation cuts.

$$f = \frac{N_{QCD}}{N_{data}} \; ; \; f' = \frac{N'_{QCD}}{N'_{data}} = \frac{\varepsilon_{QCD} \times N_{QCD}}{\varepsilon_{data} \times N_{data}} = k \times f \; ; \; k = \frac{\varepsilon_{QCD}}{\varepsilon_{data}} \tag{7.6}$$

The reduction factors (Eq. 7.6) are noted in Table 7.10, and the final results are shown in Table 7.11.The relative uncertainties on the fractions are kept the same.

$\|\eta\|$-inclusive	$2.5 < \langle\mu\rangle < 6.5$	$6.5 < \langle\mu\rangle < 9.5$	$9.5 < \langle\mu\rangle < 16$
W	1.30 ± 0.02	1.90 ± 0.03	3.30 ± 0.02
W^+	0.99 ± 0.02	1.45 ± 0.03	2.57 ± 0.03
W^-	1.70 ± 0.03	2.43 ± 0.04	3.99 ± 0.04
$0.0 < \|\eta\| < 0.6$	$2.5 < \langle\mu\rangle < 6.5$	$6.5 < \langle\mu\rangle < 9.5$	$9.5 < \langle\mu\rangle < 16$
W	0.99 ± 0.02	1.28 ± 0.03	2.29 ± 0.03
W^+	0.68 ± 0.03	0.88 ± 0.04	1.44 ± 0.04
W^-	1.37 ± 0.04	1.59 ± 0.05	2.65 ± 0.05
$0.6 < \|\eta\| < 1.2$	$2.5 < \langle\mu\rangle < 6.5$	$6.5 < \langle\mu\rangle < 9.5$	$9.5 < \langle\mu\rangle < 16$
W	0.98 ± 0.02	1.63 ± 0.04	2.73 ± 0.04
W^+	0.75 ± 0.03	1.18 ± 0.05	1.82 ± 0.04
W^-	1.32 ± 0.04	2.07 ± 0.06	3.49 ± 0.05
$1.8 < \|\eta\| < 2.4$	$2.5 < \langle\mu\rangle < 6.5$	$6.5 < \langle\mu\rangle < 9.5$	$9.5 < \langle\mu\rangle < 16$
W	1.91 ± 0.04	2.70 ± 0.06	4.66 ± 0.06
W^+	1.42 ± 0.04	2.13 ± 0.07	3.46 ± 0.06
W^-	2.46 ± 0.06	3.11 ± 0.10	6.06 ± 0.10

TABLE 7.9: Average multijet background fraction (%) for W, W^+ and W^-, before isolation cuts, inclusively and in pseudo-rapidity bins.

$\|\eta\|$-inclusive	$2.5 < \langle\mu\rangle < 6.5$	$6.5 < \langle\mu\rangle < 9.5$	$9.5 < \langle\mu\rangle < 16$
W	0.26	0.31	0.34
W^+	0.26	0.31	0.34
W^-	0.26	0.30	0.34
$0.0 < \|\eta\| < 0.6$	$2.5 < \langle\mu\rangle < 6.5$	$6.5 < \langle\mu\rangle < 9.5$	$9.5 < \langle\mu\rangle < 16$
W	0.21	0.23	0.28
W^+	0.22	0.25	0.29
W^-	0.20	0.21	0.27
$0.6 < \|\eta\| < 1.2$	$2.5 < \langle\mu\rangle < 6.5$	$6.5 < \langle\mu\rangle < 9.5$	$9.5 < \langle\mu\rangle < 16$
W	0.21	0.25	0.27
W^+	0.21	0.25	0.27
W^-	0.21	0.26	0.27
$1.8 < \|\eta\| < 2.4$	$2.5 < \langle\mu\rangle < 6.5$	$6.5 < \langle\mu\rangle < 9.5$	$9.5 < \langle\mu\rangle < 16$
W	0.31	0.38	0.42
W^+	0.32	0.39	0.41
W^-	0.31	0.38	0.43

TABLE 7.10: Background reduction factor for W, W^+ and W^-, inclusively and in pseudo-rapidity bins.

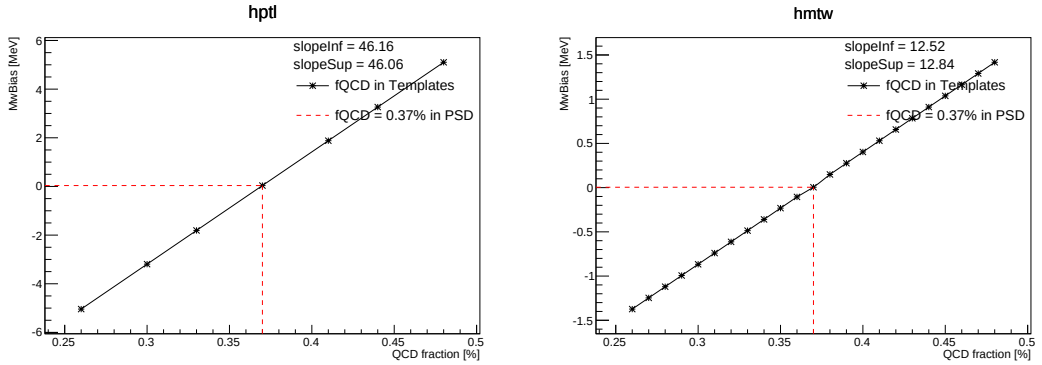

(a) $30 < p_{\mathrm{T}}^{\ell} < 50$ GeV (b) $65 < m_{\mathrm{T}}^{W} < 100$ GeV

FIGURE 7.10: $2.5 < \langle\mu\rangle < 6.5$ - η-inclusive.

7.7 Signal selection efficiency

The data and MC samples are treated separately in $\langle\mu\rangle$ bins as discussed in § 7.5. The relevant event cutflows are shown in Tables 7.12,7.13 and 7.14, inclusively in $|\eta|$. All MC cutflows are scaled to the number of data events. The cutflow in $|\eta|$ bins represents approximately 38%, 36% and 26% for $|\eta| \in [0.0, 0.6], [0.6, 1.2]$ and $[1.82, 2.4]$ respectively, with respect to the $|\eta|$-inclusive cutflow.

7.8 Mass fits and results

Template mass fits are performed based on the different background fractions. A pseudodata sample was defined using the nominal background fraction in each $\langle\mu\rangle \times |\eta|$ bin as reported in Table 7.11. A relative uncertainty of 20% was taken as coming from the choice of the fit range, and another 20% come from the variable choice, the MC correction, and the jet extrapolation procedures. A total uncertainty of 30% is therefore considered, and templates are built using variations of the nominal fraction within 30% of its value.

The resulting mass biases with respect to the pseudodata are illustrated as a function of the background fraction in Figures 7.10, 7.11, 7.12 and 7.13 corresponding to fits in the three $\langle\mu\rangle$ bins and inclusively, performed in the ranges $30 < p_{\mathrm{T}}^{\ell} < 50$ GeV and $65 < m_{\mathrm{T}} < 100$ GeV. These pictures show η-inclusive results, the results in η-bins are reported in Appendix C.

The variations of the W mass bias is an indicator on the systematic uncertainty coming from the background fraction value. These uncertainties are noted in Table 7.15, such that:

$$\Delta m_W = A \times \Delta f_{QCD} = \frac{\delta m_W}{\delta f_{QCD}} \times \Delta f_{QCD} \tag{7.7}$$

where A is the slope of the linear fit and $\Delta f_{QCD} = 30\% \times f_{QCD}$, f_{QCD} being the nominal background fraction. The slope A is reported in Table 7.16.

$\|\eta\|$-inclusive	$2.5 < \langle\mu\rangle < 6.5$	$6.5 < \langle\mu\rangle < 9.5$	$9.5 < \langle\mu\rangle < 16$	$\langle\mu\rangle$-inclusive
W	0.37 ± 0.01	0.62 ± 0.01	1.17 ± 0.01	0.68 ± 0.01
W^+	0.29 ± 0.01	0.48 ± 0.01	0.92 ± 0.01	0.53 ± 0.01
W^-	0.47 ± 0.01	0.76 ± 0.01	1.40 ± 0.01	0.84 ± 0.01
$0.0 < \|\eta\| < 0.6$	$2.5 < \langle\mu\rangle < 6.5$	$6.5 < \langle\mu\rangle < 9.5$	$9.5 < \langle\mu\rangle < 16$	$\langle\mu\rangle$-inclusive
W	0.24 ± 0.01	0.33 ± 0.01	0.68 ± 0.01	0.40 ± 0.01
W^+	0.18 ± 0.01	0.26 ± 0.01	0.48 ± 0.01	0.29 ± 0.01
W^-	0.29 ± 0.01	0.35 ± 0.01	0.74 ± 0.01	0.45 ± 0.01
$0.6 < \|\eta\| < 1.2$	$2.5 < \langle\mu\rangle < 6.5$	$6.5 < \langle\mu\rangle < 9.5$	$9.5 < \langle\mu\rangle < 16$	$\langle\mu\rangle$-inclusive
W	0.23 ± 0.01	0.44 ± 0.01	0.78 ± 0.01	0.46 ± 0.01
W^+	0.18 ± 0.01	0.33 ± 0.01	0.53 ± 0.01	0.33 ± 0.01
W^-	0.30 ± 0.01	0.57 ± 0.01	0.98 ± 0.01	0.59 ± 0.01
$1.8 < \|\eta\| < 2.4$	$2.5 < \langle\mu\rangle < 6.5$	$6.5 < \langle\mu\rangle < 9.5$	$9.5 < \langle\mu\rangle < 16$	$\langle\mu\rangle$-inclusive
W	0.61 ± 0.01	1.05 ± 0.02	1.98 ± 0.02	1.15 ± 0.01
W^+	0.47 ± 0.01	0.85 ± 0.02	1.44 ± 0.02	0.88 ± 0.02
W^-	0.78 ± 0.01	1.20 ± 0.03	2.63 ± 0.03	1.46 ± 0.02

TABLE 7.11: Average multijet background fraction (%) for W, W^+ and W^-, after isolation cuts, inclusively and in pseudo-rapidity bins.

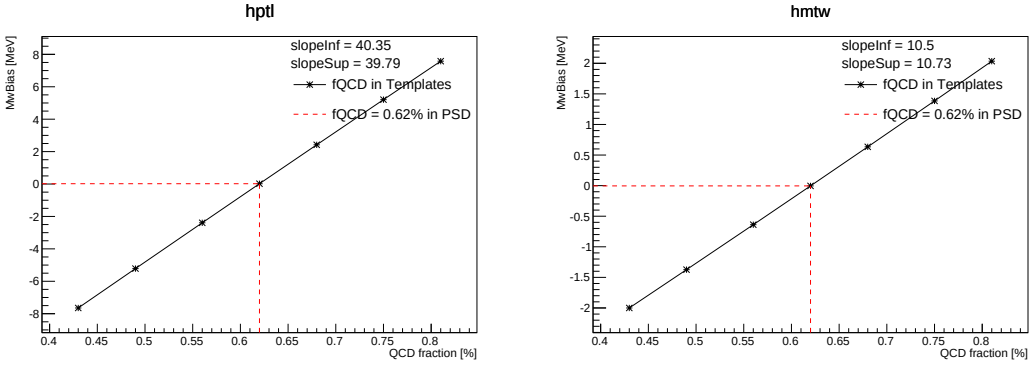

(a) $30 < p_{\mathrm{T}}^{\ell} < 50$ GeV (b) $65 < m_{\mathrm{T}}^{W} < 100$ GeV

FIGURE 7.11: $6.5 < \langle\mu\rangle < 9.5$ - η-inclusive.

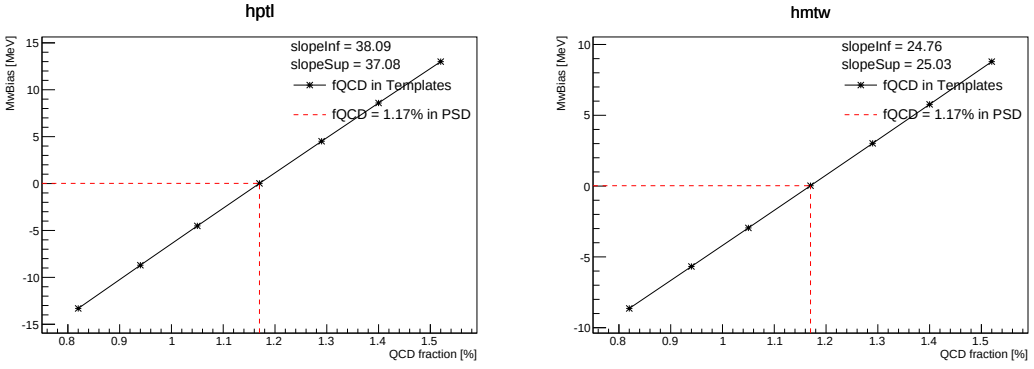

(a) $30 < p_{\mathrm{T}}^{\ell} < 50$ GeV (b) $65 < m_{\mathrm{T}}^{W} < 100$ GeV

FIGURE 7.12: $9.5 < \langle\mu\rangle < 16$ - η-inclusive.

Cut	Data	$W \to e\nu$	$W \to \tau\nu$	$Z \to ee$	$Z \to \tau\tau$	top	WW/WZ/ZZ	Total MC
$\langle\mu\rangle$ cut	4965741	3203399	64061	229415	14117	23368	5120	3539480
Cleaning	4922183	3192668	63603	220208	13912	22248	5011	3517650
$E_{\mathrm{T}}^{\mathrm{miss}} > 30$ GeV	2560206	2310891	33515	39421	4522	17555	3395	2409300
$p_{\mathrm{T}}^{W} < 30$ GeV	2010729	1927039	19900	25063	2272	2164	1364	1977802
$m_{\mathrm{T}}^{W} > 60$ GeV	1999308	1918485	19531	24777	2228	2152	1357	1968530
$E_{\mathrm{T}}^{\mathrm{cone20}}$ cut	1963943	1899782	19393	24499	2207	2081	1332	1949295
$p_{\mathrm{T}}^{\mathrm{cone40}}$ cut	1914816	1859893	19041	23993	2162	1921	1275	1908286

Cut	Data	$W \to e\nu$	$W \to \tau\nu$	$Z \to ee$	$Z \to \tau\tau$	top	WW/WZ/ZZ	Total MC
$\langle\mu\rangle$ cut	2764316	1853089	35611	117602	7034	12192	2650	2028178
Cleaning	2741488	1847117	35367	113028	6926	11621	2593	2016653
$E_{\mathrm{T}}^{\mathrm{miss}} > 30$ GeV	1471851	1333056	18808	19949	2239	9153	1746	1384950
$p_{\mathrm{T}}^{W} < 30$ GeV	1163847	1110391	11346	12666	1145	1139	692	1137379
$m_{\mathrm{T}}^{W} > 60$ GeV	1157017	1105131	11135	12519	1124	1132	688	1131728
$E_{\mathrm{T}}^{\mathrm{cone20}}$ cut	1137555	1094501	11057	12372	1111	1096	676	1120812
$p_{\mathrm{T}}^{\mathrm{cone40}}$ cut	1110080	1071469	10846	12110	1092	1011	648	1097175

Cut	Data	$W \to e\nu$	$W \to \tau\nu$	$Z \to ee$	$Z \to \tau\tau$	top	WW/WZ/ZZ	Total MC
$\langle\mu\rangle$ cut	2201425	1350310	28450	111813	7083	11176	2470	1511302
Cleaning	2180695	1345551	28236	107180	6985	10627	2418	1500997
$E_{\mathrm{T}}^{\mathrm{miss}} > 30$ GeV	1088355	977835	14707	19472	2283	8403	1649	1024350
$p_{\mathrm{T}}^{W} < 30$ GeV	846882	816648	8554	12397	1127	1025	671	840423
$m_{\mathrm{T}}^{W} > 60$ GeV	842291	813354	8397	12258	1105	1020	668	836802
$E_{\mathrm{T}}^{\mathrm{cone20}}$ cut	826388	805282	8336	12127	1096	985	656	828483
$p_{\mathrm{T}}^{\mathrm{cone40}}$ cut	804736	788424	8196	11883	1071	910	627	811111

TABLE 7.12: Cut-flow in the $W \to e\nu$ (top), $W^{+} \to e\nu$ (middle) and $W^{-} \to e\nu$ channel (bottom), in the $2.5 < \langle\mu\rangle < 6.5$ bin. MC samples are scaled to data.

Cut	Data	$W \to e\nu$	$W \to \tau\nu$	$Z \to ee$	$Z \to \tau\tau$	top	WW/WZ/ZZ	Total MC
$\langle\mu\rangle$ cut	2755125	1798501	35826	125392	7857	13242	2921	1983739
Cleaning	2752286	1797896	35813	125294	7846	13224	2918	1982993
$E_{\mathrm{T}}^{\mathrm{miss}} > 30$ GeV	1469904	1287600	19583	28070	2863	10508	2001	1350624
$p_{\mathrm{T}}^{W} < 30$ GeV	1064157	1008785	10940	15240	1329	1301	768	1038363
$m_{\mathrm{T}}^{W} > 60$ GeV	1056736	1003306	10703	15042	1301	1293	764	1032408
$E_{\mathrm{T}}^{\mathrm{cone20}}$ cut	1033573	992910	10611	14854	1290	1248	747	1021660
$p_{\mathrm{T}}^{\mathrm{cone40}}$ cut	1005770	972059	10425	14556	1262	1157	715	1000174

Cut	Data	$W \to e\nu$	$W \to \tau\nu$	$Z \to ee$	$Z \to \tau\tau$	top	WW/WZ/ZZ	Total MC
$\langle\mu\rangle$ cut	1533070	1040043	19903	64367	3952	6890	1522	1136677
Cleaning	1531454	1039683	19897	64316	3947	6880	1521	1136244
$E_{\mathrm{T}}^{\mathrm{miss}} > 30$ GeV	840621	743001	10883	14152	1447	5444	1038	775965
$p_{\mathrm{T}}^{W} < 30$ GeV	614495	581380	6155	7668	674	690	391	596959
$m_{\mathrm{T}}^{W} > 60$ GeV	610178	578040	6019	7563	661	685	389	593357
$E_{\mathrm{T}}^{\mathrm{cone20}}$ cut	597572	572181	5972	7470	655	662	380	587321
$p_{\mathrm{T}}^{\mathrm{cone40}}$ cut	582244	560061	5869	7318	643	614	364	574870

Cut	Data	$W \to e\nu$	$W \to \tau\nu$	$Z \to ee$	$Z \to \tau\tau$	top	WW/WZ/ZZ	Total MC
$\langle\mu\rangle$ cut	1222055	758458	15923	61025	3905	6351	1399	847061
Cleaning	1220832	758213	15916	60979	3899	6344	1397	846748
$E_{\mathrm{T}}^{\mathrm{miss}} > 30$ GeV	629283	544599	8700	13918	1415	5063	963	574658
$p_{\mathrm{T}}^{W} < 30$ GeV	449662	427406	4785	7571	655	611	376	441404
$m_{\mathrm{T}}^{W} > 60$ GeV	446558	425266	4684	7479	640	607	374	439051
$E_{\mathrm{T}}^{\mathrm{cone20}}$ cut	436001	420729	4639	7383	634	586	367	434339
$p_{\mathrm{T}}^{\mathrm{cone40}}$ cut	423526	411998	4556	7238	619	543	351	425305

TABLE 7.13: Cut-flow in the $W \to e\nu$ (top), $W^{+} \to e\nu$ (middle) and $W^{-} \to e\nu$ channel (bottom), in the $6.5 < \langle\mu\rangle < 9.5$ bin. MC samples are scaled to data.

Cut	Data	$W \to e\nu$	$W \to \tau\nu$	$Z \to ee$	$Z \to \tau\tau$	top	WW/WZ/ZZ	Total MC
$\langle\mu\rangle$ cut	4949879	3211098	64114	226043	14238	23855	5210	3544558
Cleaning	4942929	3209949	64086	225767	14218	23819	5204	3543042
$E_{\mathrm{T}}^{\mathrm{miss}} > 30$ GeV	2716930	2292948	36570	61605	5680	18963	3619	2419386
$p_{\mathrm{T}}^{W} < 30$ GeV	1803810	1681385	19029	29334	2428	2312	1321	1735808
$m_{\mathrm{T}}^{W} > 60$ GeV	1788933	1671086	18600	28901	2362	2297	1313	1724559
$E_{\mathrm{T}}^{\mathrm{cone20}}$ cut	1741338	1652347	18432	28497	2338	2217	1287	1705118
$p_{\mathrm{T}}^{\mathrm{cone40}}$ cut	1687124	1617093	18094	27882	2286	2053	1232	1668642

Cut	Data	$W \to e\nu$	$W \to \tau\nu$	$Z \to ee$	$Z \to \tau\tau$	top	WW/WZ/ZZ	Total MC
$\langle\mu\rangle$ cut	2752477	1858671	35659	115982	7185	12428	2713	2032638
Cleaning	2748554	1858005	35645	115836	7174	12408	2710	2031777
$E_{\mathrm{T}}^{\mathrm{miss}} > 30$ GeV	1547713	1323983	20336	31350	2885	9873	1876	1390303
$p_{\mathrm{T}}^{W} < 30$ GeV	1038560	969779	10749	14900	1241	1231	676	998577
$m_{\mathrm{T}}^{W} > 60$ GeV	1029919	963429	10507	14679	1207	1224	672	991718
$E_{\mathrm{T}}^{\mathrm{cone20}}$ cut	1004359	952770	10415	14473	1194	1183	658	980693
$p_{\mathrm{T}}^{\mathrm{cone40}}$ cut	974574	932329	10226	14162	1166	1098	630	959610

Cut	Data	$W \to e\nu$	$W \to \tau\nu$	$Z \to ee$	$Z \to \tau\tau$	top	WW/WZ/ZZ	Total MC
$\langle\mu\rangle$ cut	2197402	1352427	28455	110060	7053	11427	2497	1511921
Cleaning	2194375	1351944	28441	109931	7044	11410	2494	1511264
$E_{\mathrm{T}}^{\mathrm{miss}} > 30$ GeV	1169217	968965	16234	30255	2795	9091	1743	1029084
$p_{\mathrm{T}}^{W} < 30$ GeV	765250	711606	8280	14434	1186	1081	645	737231
$m_{\mathrm{T}}^{W} > 60$ GeV	759014	707657	8092	14222	1155	1073	641	732841
$E_{\mathrm{T}}^{\mathrm{cone20}}$ cut	736979	699578	8017	14024	1144	1034	628	724426
$p_{\mathrm{T}}^{\mathrm{cone40}}$ cut	712550	684765	7869	13720	1120	955	603	709031

TABLE 7.14: Cut-flow in the $W \to e\nu$ (top), $W^{+} \to e\nu$ (middle) and $W^{-} \to e\nu$ channel (bottom), in the $9.5 < \langle\mu\rangle < 16$ bin. MC samples are scaled to data.

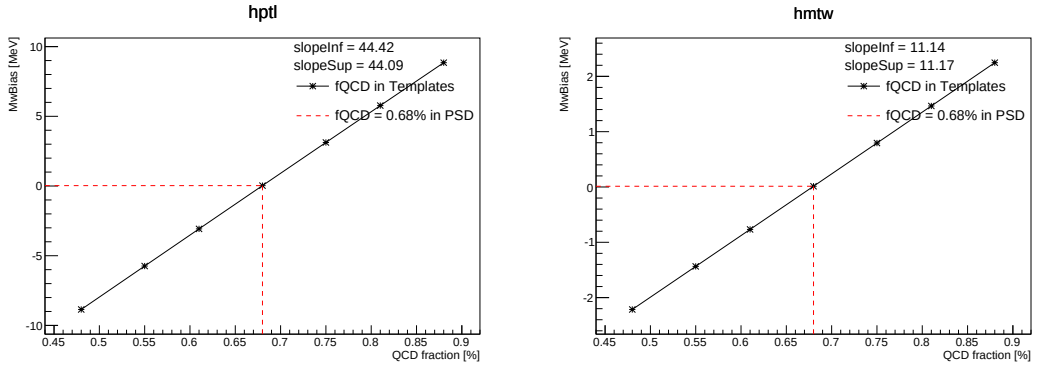

(a) $30 < p_{\mathrm{T}}^{\ell} < 50$ GeV (b) $65 < m_{\mathrm{T}}^{W} < 100$ GeV

FIGURE 7.13: $\langle\mu\rangle$-inclusive - η-inclusive.

$\lvert\eta\rvert$-inclusive	$2.5 < \langle\mu\rangle < 6.5$	$6.5 < \langle\mu\rangle < 9.5$	$9.5 < \langle\mu\rangle < 16$	$\langle\mu\rangle$-inclusive
p_{T}^{ℓ} fit	5.12	7.51	13.37	9.06
m_{T}^{W} fit	1.43	1.95	8.79	2.28
$0.0 < \lvert\eta\rvert < 0.6$	$2.5 < \langle\mu\rangle < 6.5$	$6.5 < \langle\mu\rangle < 9.5$	$9.5 < \langle\mu\rangle < 16$	$\langle\mu\rangle$-inclusive
p_{T}^{ℓ} fit	1.27	0.64	1.80	1.65
m_{T}^{W} fit	0.19	0.86	1.28	0.92
$0.6 < \lvert\eta\rvert < 1.2$	$2.5 < \langle\mu\rangle < 6.5$	$6.5 < \langle\mu\rangle < 9.5$	$9.5 < \langle\mu\rangle < 16$	$\langle\mu\rangle$-inclusive
p_{T}^{ℓ} fit	2.33	5.28	7.38	4.76
m_{T}^{W} fit	0.35	2.77	6.25	1.14
$1.8 < \lvert\eta\rvert < 2.4$	$2.5 < \langle\mu\rangle < 6.5$	$6.5 < \langle\mu\rangle < 9.5$	$9.5 < \langle\mu\rangle < 16$	$\langle\mu\rangle$-inclusive
p_{T}^{ℓ} fit	10.32	15.71	29.75	19.75
m_{T}^{W} fit	3.55	2.38	17.37	5.99

TABLE 7.15: Δm_W [MeV] in $\langle\mu\rangle$ bins and inclusively. Fits are performed in $30 < p_{\mathrm{T}}^{\ell} < 50$ GeV and $65 < m_{\mathrm{T}}^{W} < 100$ GeV, and the uncertainties take into account a variation of 30% in the multijet background fraction.

$\lvert\eta\rvert$-inclusive	$2.5 < \langle\mu\rangle < 6.5$	$6.5 < \langle\mu\rangle < 9.5$	$9.5 < \langle\mu\rangle < 16$	$\langle\mu\rangle$-inclusive
p_{T}^{ℓ} fit	46.16	40.35	38.09	44.42
m_{T}^{W} fit	12.84	10.5	25.03	11.17
$0.0 < \lvert\eta\rvert < 0.6$	$2.5 < \langle\mu\rangle < 6.5$	$6.5 < \langle\mu\rangle < 9.5$	$9.5 < \langle\mu\rangle < 16$	$\langle\mu\rangle$-inclusive
p_{T}^{ℓ} fit	17.67	6.49	8.81	13.76
m_{T}^{W} fit	2.68	8.68	6.27	7.63
$0.6 < \lvert\eta\rvert < 1.2$	$2.5 < \langle\mu\rangle < 6.5$	$6.5 < \langle\mu\rangle < 9.5$	$9.5 < \langle\mu\rangle < 16$	$\langle\mu\rangle$-inclusive
p_{T}^{ℓ} fit	33.78	40.03	31.52	34.52
m_{T}^{W} fit	5	20.95	26.73	8.23
$1.8 < \lvert\eta\rvert < 2.4$	$2.5 < \langle\mu\rangle < 6.5$	$6.5 < \langle\mu\rangle < 9.5$	$9.5 < \langle\mu\rangle < 16$	$\langle\mu\rangle$-inclusive
p_{T}^{ℓ} fit	56.37	49.86	50.09	57.26
m_{T}^{W} fit	19.42	7.54	29.25	17.37

TABLE 7.16: Slopes of δm_W vs. δf_{QCD} in $\langle\mu\rangle$ bins and inclusively. Fits are performed in $30 < p_{\mathrm{T}}^{\ell} < 50$ GeV and $65 < m_{\mathrm{T}}^{W} < 100$ GeV.

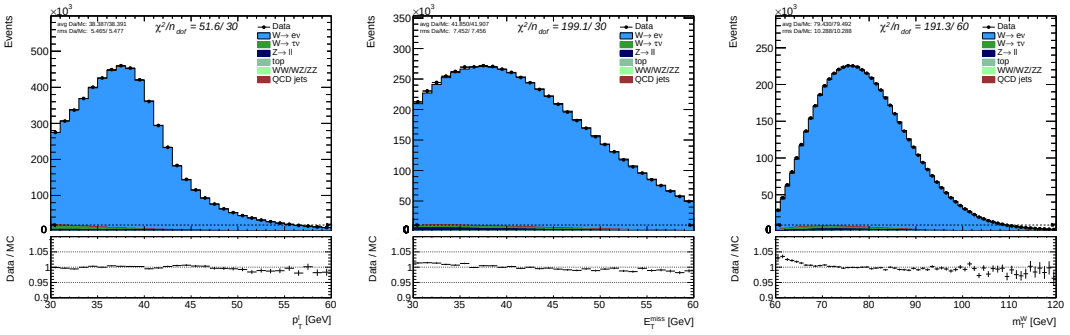

(a) p_{T}^{ℓ} (b) $E_{\mathrm{T}}^{\mathrm{miss}}$ (c) m_{T}

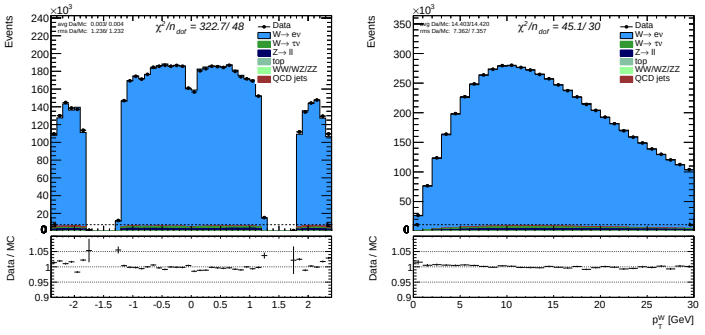

(d) $|\eta|$ (e) p_{T}^{W}

FIGURE 7.14: $\langle\mu\rangle$-inclusive - $W^{\pm}$ - η-inclusive

7.9 Control Plots

Control plots of the p_{T}^{ℓ}, $E_{\mathrm{T}}^{\mathrm{miss}}$, m_{T}, η and p_{T}^{W} distributions are shown in Figures 7.14, 7.15 and 7.16 inclusively in $\langle\mu\rangle$ and pseudorapidity. The error bars are statistical only. Plots in bins of $|\eta|$ are shown in Appendix D.

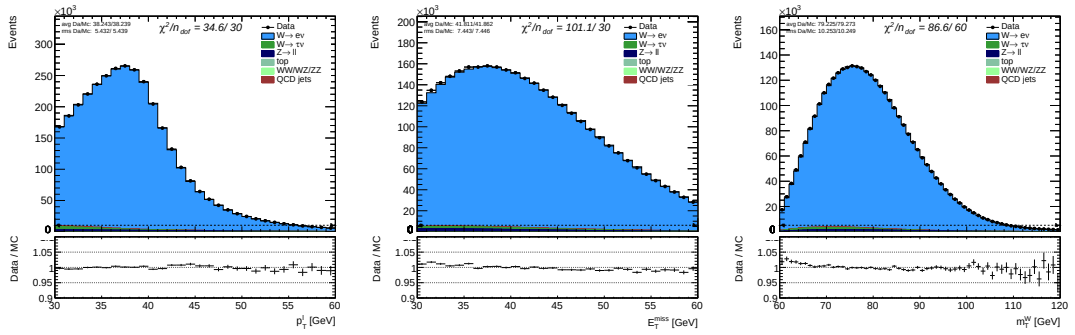

(a) p_{T}^{ℓ} (b) $E_{\mathrm{T}}^{\mathrm{miss}}$ (c) m_{T}

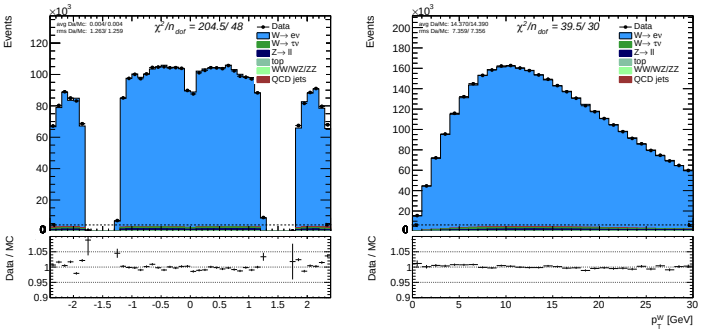

(d) $|\eta|$ (e) p_{T}^{W}

FIGURE 7.15: $\langle\mu\rangle$-inclusive - W^+ - η-inclusive

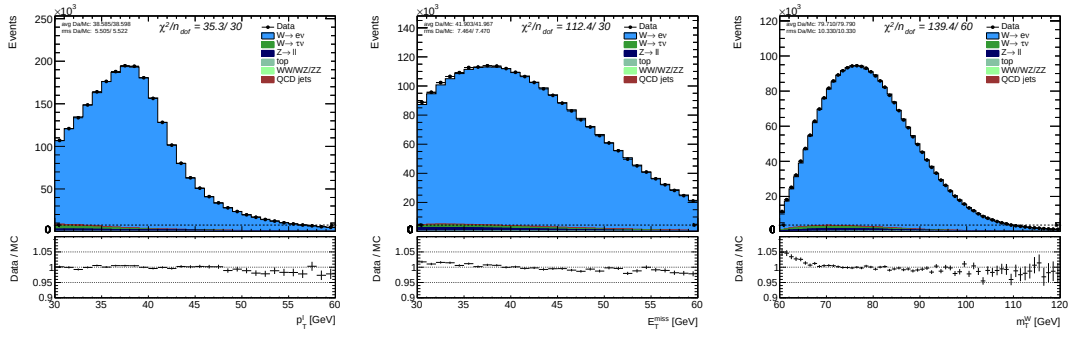

(a) p_{T}^{ℓ} (b) $E_{\mathrm{T}}^{\mathrm{miss}}$ (c) m_{T}

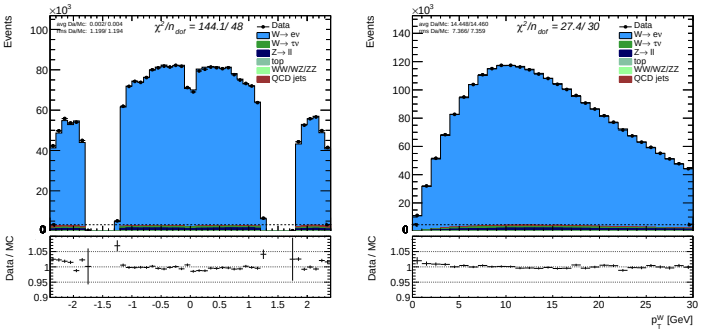

(d) $|\eta|$ (e) p_{T}^{W}

FIGURE 7.16: $\langle\mu\rangle$-inclusive - W^- - η-inclusive

Chapter 8

Results

This thesis focused on the $W \to e\nu$ channel in the background assessment study. The uncertainties involved in this channel are discussed in Chapter 5. In this section, a state-of-the-art of the electron analysis is presented, in terms of uncertainties on the W mass, and the treatment of the uncertainties case by case is discussed. Blinded mass fits are also shown, giving the results of the mass measurements at the writing of this thesis.

8.1 Sources and computations of the uncertainties

The uncertainties are treated differently whether they are extracted in bins of average number of interactions per bunch crossing $\langle\mu\rangle$, pseudorapidity η or inclusively. The goal is to have a full scope in bins of $\langle\mu\rangle \times |\eta|$. In other terms:

- **Electron calibration:**
  The calibration uncertainties involve detector and energy scale uncertainties. The extraction of the corresponding numbers was discussed in Chapter 5. In particular, Table 5.2 summarizes the main sources of uncertainty on the energy scale using $Z \to ee$ events, along with the expected impact on the W mass measurement. Tables 5.3 and 5.4 show the result of the W mass fits using p_{T}^{ℓ} and m_{T}^{W} distributions. All of the numbers are shown in bins of pseudorapidity.

  1. Energy scale uncertainties

  Looking at Table 5.2 one can notice that the statistical uncertainty is dominant, and thus the estimation of the uncertainties in bins of $\langle\mu\rangle$ is done assuming the following:

$$\frac{\delta\sigma_i}{\sigma} = \frac{\alpha}{\sqrt{N_i}}\,,\ \forall i \tag{8.1}$$

  where α is a constant, N_i is the number of events in bin i, and $\delta\sigma_i/\sigma$ is the relative uncertainty, where i represents the $\langle\mu\rangle$ bin: $2.5 < \langle\mu\rangle < 6.5$, $6.5 < \langle\mu\rangle < 9.5$, $9.5 < \langle\mu\rangle < 16$ or inclusively in $\langle\mu\rangle$. Knowing $\delta\sigma_{\mathrm{tot}}/\sigma$ from Table 5.2:

$$\alpha = \frac{\delta\sigma_{\mathrm{tot}}}{\sigma}\sqrt{N_{\mathrm{tot}}} \Leftrightarrow \frac{\delta\sigma_i}{\sigma} = \frac{\delta\sigma_{\mathrm{tot}}}{\sigma}\frac{\sqrt{N_{\mathrm{tot}}}}{\sqrt{N_i}} = \frac{\delta\sigma_{\mathrm{tot}}}{\sigma}\frac{1}{\sqrt{\varepsilon_i}} \tag{8.2}$$

where the efficiency ε_i is such that $\varepsilon = \{0.4, 0.3, 0.3\}$ considering a statistical distribution of 40%, 30% and 30% in the three bins of $\langle\mu\rangle$. The computed uncertainties in bins of $\langle\mu\rangle$ are therefore:

η-bin / $\langle\mu\rangle$-bin	[-2.4,-1.82]	[-1.2,-0.6]	[-0.6,0.0]	[0.0,0.6]	[0.6,1.2]	[1.82,2.4]	Total
$\delta^{\text{Escale}}m_W$ from the energy scales							
$\langle\mu\rangle$-inclusive(MeV)	22.0	15.1	15.6	13.3	15.5	23.0	7.7
$2.5 < \langle\mu\rangle < 6.5$ (MeV)	34.8	23.9	24.7	21.0	24.5	36.4	12.2
$6.5 < \langle\mu\rangle < 9.5$ (MeV)	40.2	27.6	28.5	24.3	28.3	42.0	14.1
$9.5 < \langle\mu\rangle < 16$ (MeV)	40.2	27.6	28.5	24.3	28.3	42.0	14.1

TABLE 8.1: Summary of electron energy scale uncertainties as estimated from $Z \to ee$ decays inclusively in $\langle\mu\rangle$ (Taken from Table 5.2), and calculated in bins of $\langle\mu\rangle$ (see text for details). Uncertainties coming from the Z mass and from FSR are treated separately.

2. Detector uncertainties

These uncertainties given in Tables 5.3 and 5.4 are considered to be independent of $\langle\mu\rangle$, and therefore the $\langle\mu\rangle$-inclusive values are taken as they are in the $\langle\mu\rangle$-bins.In Table 8.2, the first block is the combination of Table 8.1 and 5.3 (p_{T}^{ℓ} fits), and the second block is the combination of Table 8.1 with Table 5.4 (m_{T}^{W} fits).

η-bin / $\langle\mu\rangle$-bin	[-2.4,-1.82]	[-1.2,-0.6]	[-0.6,0.0]	[0.0,0.6]	[0.6,1.2]	[1.82,2.4]	Total
Total calib uncertainties from p_{T}^{ℓ} fits							
$\langle\mu\rangle$-inclusive (MeV)	22.5	16.8	16.4	14.2	17.2	23.5	8.8
$2.5 < \langle\mu\rangle < 6.5$ (MeV)	35.1	25.0	25.2	21.6	25.6	36.7	12.9
$6.5 < \langle\mu\rangle < 9.5$ (MeV)	40.5	28.6	28.9	24.8	29.3	42.3	14.7
$9.5 < \langle\mu\rangle < 16$ (MeV)	40.5	28.6	28.9	24.8	29.3	42.3	14.7
Total calib uncertainties from m_{T}^{W} fits							
$\langle\mu\rangle$-inclusive (MeV)	22.6	16.7	16.5	14.4	17.1	23.6	8.9
$2.5 < \langle\mu\rangle < 6.5$ (MeV)	35.2	25.0	25.3	21.7	25.5	36.8	13.0
$6.5 < \langle\mu\rangle < 9.5$ (MeV)	40.5	28.5	29.0	24.9	29.2	42.3	14.8
$9.5 < \langle\mu\rangle < 16$ (MeV)	40.5	28.5	29.0	24.9	29.2	42.3	14.8

TABLE 8.2: Uncertainty on W mass measurement obtained with transverse lepton momentum and transverse mass coming from the calibration procedure and the energy scales estimation. Values are shown in bins of $\langle\mu\rangle$and η.

- **Electron selection efficiency:**
  The impact of electron efficiency scale factor uncertainties on the measurement of m_W is quoted in Tables 5.6 and 5.7. This impact is considered independent on $\langle\mu\rangle$. The uncertainties taken in $\langle\mu\rangle$-bins are therefore equal to the $\langle\mu\rangle$-inclusive values.

- **Recoil calibration:**
  Uncertainties on the W mass are extracted in bins of $\langle\mu\rangle$ and quoted in Table 5.8. The recoil being η-independent, the uncertainty is taken the same regardless of the η region.

- **EW+top backgrounds:**
  The impact of varying the backgrounds is considered independent of the $\langle\mu\rangle \times \eta$ bin, and the inclusive values are taken everywhere. The total systematic uncertainty is considered to be the quadratic sum of the uncertainties coming from different backgrounds: δm = 2.8 MeV.

- **Jet backgrounds:**
  Jet background mass fits discussed in Section 7.8 are performed in bins of $\langle\mu\rangle \times |\eta|$. They are reported in Table 7.15.

- **m_Z uncertainty:**
  The uncertainty on the m_Z influences the measurement for its indirect impact through lepton scale calibration. This uncertainty of 2.1 MeV is taken as it is for all the bins, since it is yielded from Z events and does not depend on the W binning.

- **QED FSR:**
  The total FSR uncertainty is taken from Table 5.12, and has the same value regardless of the bin.

- **Polarization:**
  A first approximation was made in the purpose of estimating an order of magnitude to the relevant uncertainty. A more detailed and precise calculation is still ongoing. Reweighting the A_i coefficients in Powheg to match DYNNLO has an impact of $\approx$ 90 MeV on the Z mass, assumed to be the same on the W mass. It was verified that the dominant uncertainty on the Z polarization measurement comes from the A_0 coefficient, and therefore the 5% shift, between Powheg and DYNNLO, in A_0 at $p_T = 0$ seen in Figure 5.10 is considered as the dominant source of the 90 MeV impact.

  The DYNNLO predictions have been validated by the Z data, but only up to a level of precision matching the data accuracy dA_i. Having measured 10 data points of a $\approx 1\%$ accuracy each, the overall data accuracy is $1\%/\sqrt{10} \approx 0.32\%$, which gives a rough estimate for the contribution to the uncertainty on the W mass:

$$\delta m_W = \frac{dA_i}{A_i(Powheg) - A_i(DYNNLO)} \times 90 = \frac{0.32}{5} \times 90 \approx 6 \text{ MeV} \tag{8.3}$$

  This value is considered to be the same for all $|\eta|$ and $\langle\mu\rangle$ bins. In some cases, the DYNNLO prediction does not match the data accurately, so one should take into account this disagreement, and the Eq. 8.3 would therefore be:

$$\delta m_W = \frac{A_i(\text{Data}) - A_i(DYNNLO)}{A_i(Powheg) - A_i(DYNNLO)} \tag{8.4}$$

- **PDF:**
  The PDF are parametrized with 13 parameters, and evaluated with the hessian method [102]. 26 up and down variations along orthogonal directions in the 13 parameters space are evaluated with respect to the central PDF. In addition, four model variations are considered, corresponding to different values of the charm mass and different values of the ratio between the strange-quark PDF and the $\bar{d}$ PDF, giving a total of 30 variations.

  The uncertainties are assessed in $|\eta|$ bins, using p_T^ℓ and m_T^W fits, and considered to be independent of the $\langle\mu\rangle$ bin.

- **Parton showers and p_T^W modeling:**
  Taken from Table 6.4, these uncertainties are only computed using p_T^ℓ fits. They are considered to be independent of the $\langle\mu\rangle \times \eta$ bin, and as a first approximation the m_T^W fit results are considered to be the same as p_T^ℓ.

- **Statistics:**
  The statistical uncertainty is taken as the width of the fit parabola. It is represented by the red error bars in Figures 8.1 to 8.7.

Sources		$0.0 < \|\eta\| < 0.6$	$0.6 < \|\eta\| < 1.2$	$1.82 < \|\eta\| < 2.4$	η-inclusive
Experimental uncertainties					
Electron calibration		16.5/16.4	17.8/17.9	25.4/25.4	13.0/12.9
Electron selection efficiency		10.9/12.4	11.7/14.1	15.5/18.4	8.3/9.5
Recoil calibration		20.7/6.0			
EW+top backgrounds		2.8			
Jet backgrounds		0.2/1.3	0.4/2.3	3.6/10.3	1.4/5.1
Total Experimental		28.8/21.6	29.8/23.8	36.5/33.7	26.0/18.1
Theoretical uncertainties					
QED	Z-lineshape	2.1			
	QED FSR	0.8/4.1			
QCD	Polarization	≈ 6			
	PDF	26.0/27.0	22.0/24.0	23.0/26.0	18.0/20.0
	Parton showers (p_{T}^{ℓ} fits only)	+5 -7			
Total Theoretical		27.4/28.7	23.7/25.9	24.6/27.7	20.0/22.2
Statistics		28.4/22.6	28.3/23.5	31.8/25.1	16.9/13.6
Total		48.9/42.4	47.5/42.3	54.3/50.3	36.9/31.7

TABLE 8.3: Uncertainties (MeV) on m_W in the $2.5 < \langle\mu\rangle < 6.5$ bin, extracted from $60 < m_{\mathrm{T}}^{W} < 100$ GeV/30 $< p_{\mathrm{T}}^{e} <$ 50 GeV fits.

Sources		$0.0 < \|\eta\| < 0.6$	$0.6 < \|\eta\| < 1.2$	$1.82 < \|\eta\| < 2.4$	η-inclusive
Experimental uncertainties					
Electron calibration		18.9/18.8	20.4/20.4	29.3/29.2	14.8/14.7
Electron selection efficiency		10.9/12.4	11.7/14.1	15.5/18.4	8.3/9.5
Recoil calibration		13.9/4.3			
EW+top backgrounds		2.8			
Jet backgrounds		0.9/0.7	2.8/5.3	2.4/15.7	2.0/7.5
Total Experimental		26.0/23.1	27.6/25.9	36.1/38.3	22.2/19.7
Theoretical uncertainties					
QED	Z-lineshape	2.1			
	QED FSR	0.8/4.1			
QCD	Polarization	≈ 6			
	PDF	26.0/27.0	22.0/24.0	23.0/26.0	18.0/20.0
	Parton showers (p_{T}^{ℓ} fits only)	+5 -7			
Total Theoretical		27.4/28.7	23.7/25.9	24.6/27.7	20.0/22.2
Statistics		35.2/25.6	37.1/26.6	40.9/36.6	21.7/15.5
Total		51.7/44.8	52.0/45.2	59.9/59.8	36.9/33.5

TABLE 8.4: Uncertainties (MeV) on m_W in the $6.5 < \langle\mu\rangle < 9.5$ bin, extracted from $60 < m_{\mathrm{T}}^{W} < 100$ GeV/30 $< p_{\mathrm{T}}^{e} <$ 50 GeV fits.

- **Total uncertainty:**
  The uncertainties are reported in Tables 8.3, 8.4, 8.5 and 8.6 for the three $\langle\mu\rangle$-bins and inclusively.

8.2 Mass measurement

The current mass measurement being blinded, the following results do not represent the real and final measurement of the W-mass. Figures 8.1, 8.2, 8.3 show the fitted mass bias with respect to the blinded value in $\langle\mu\rangle \times |\eta|$ bins, and Figures 8.4 (8.5) illustrate the results inclusively in $\langle\mu\rangle$ ($|\eta|$). The statistical uncertainty is shown in red, the blue bars also take into account the experimental uncertainty, and the black bars represent the total uncertainty.

Sources		$0.0 < \|\eta\| < 0.6$	$0.6 < \|\eta\| < 1.2$	$1.82 < \|\eta\| < 2.4$	η-inclusive
Experimental uncertainties					
Electron calibration		18.9/18.8	20.4/20.4	29.3/29.2	14.8/14.7
Electron selection efficiency		10.9/12.4	11.7/14.1	15.5/18.4	8.3/9.5
Recoil calibration		11.9/3.4			
EW+top backgrounds		2.8			
Jet backgrounds		1.3/1.8	6.3/7.4	17.4/29.8	8.8/13.4
Total Experimental		25.0/23.0	27.2/26.2	39.4/45.8	22.7/22.5
Theoretical uncertainties					
QED	Z-lineshape	2.1			
	QED FSR	0.8/4.1			
QCD	Polarization	≈ 6			
	PDF	26.0/27.0	22.0/24.0	23.0/26.0	18.0/20.0
	Parton showers (p_{T}^{ℓ} fits only)	+5 -7			
Total Theoretical		27.4/28.7	23.7/25.9	24.6/27.7	20.0/22.2
Statistics		35.2/25.6	37.1/26.6	40.9/36.6	21.7/15.5
Total		51.2/44.8	51.8/45.4	61.9/64.8	37.2/35.2

TABLE 8.5: Uncertainties (MeV) on m_W in the $9.5 < \langle\mu\rangle < 16$ bin, extracted from $60 < m_{\mathrm{T}}^{W} < 100$ GeV/$30 < p_{\mathrm{T}}^{e} < 50$ GeV fits.

Sources		$0.0 < \|\eta\| < 0.6$	$0.6 < \|\eta\| < 1.2$	$1.82 < \|\eta\| < 2.4$	η-inclusive
Experimental uncertainties					
Electron calibration		10.8/10.7	12.0/12.0	16.3/16.2	8.9/8.8
Electron selection efficiency		10.9/12.4	11.7/14.1	15.5/18.4	8.3/9.5
Recoil calibration		13.0/4.6			
EW+top backgrounds		2.8			
Jet backgrounds		1.0/1.7	1.2/4.8	6.0/19.8	2.3/9.1
Total Experimental Syst.		20.3/17.3	21.4/19.9	26.8/31.9	18.2/16.7
Theoretical uncertainties					
QED	Z-lineshape	2.1			
	QED FSR	0.8/4.1			
QCD	Polarization	≈ 6			
	PDF	26.0/27.0	22.0/24.0	23.0/26.0	18.0/20.0
	Parton showers (p_{T}^{ℓ} fits only)	+5 -7			
Total Theoretical		27.4/28.7	23.7/25.9	24.6/27.7	20.0/22.2
Statistics		20.2/13.9	21.1/14.7	23.8/16.1	12.4/8.5
Total		39.7/36.3	38.3/35.8	43.5/45.3	29.7/29.1

TABLE 8.6: Uncertainties (MeV) on m_W in the inclusive $\langle\mu\rangle$ bin, extracted from $60 < m_{\mathrm{T}}^{W} < 100$ GeV/$30 < p_{\mathrm{T}}^{e} < 50$ GeV fits.

The fits show $|\eta|$-dependent results regardless of $\langle\mu\rangle$. A comparison with the muon channel using the same physics configurations showed a similar behavior, which lead to the conclusion that the $|\eta|$-dependence is most probably due to the physics modeling.

The results are unstable versus the pile-up bin (fig. 8.5). The first $\langle\mu\rangle$ bin is offset with respect to the last two, but the fit results are within the uncertainties.

These figures show the results of the fits in the $30 < p_{\mathrm{T}}^{\ell} < 50$ GeV and $65 < m_{\mathrm{T}}^{W} < 100$ GeV ranges. A consistency check with the result obtained in Chapter 6 is performed, by fitting the p_{T}^{ℓ} distribution in the $30 < p_{\mathrm{T}}^{\ell} < 44.5$ GeV range. The results are shown in Figure 8.6 and show somehow more stable fits versus $|\eta|$. This range could be considered in the coming mass measurement.

Concerning the m_{T}^{W} fits, the results from $60 < m_{\mathrm{T}}^{W} < 100$ GeV which is the default range where the systematic uncertainties have been computed are shown in Figure 8.7. The $65 < m_{\mathrm{T}}^{W} <$

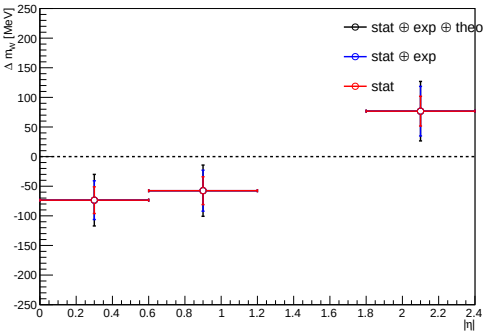

(a) $30 < p_{\mathrm{T}}^{\ell} < 50$ GeV

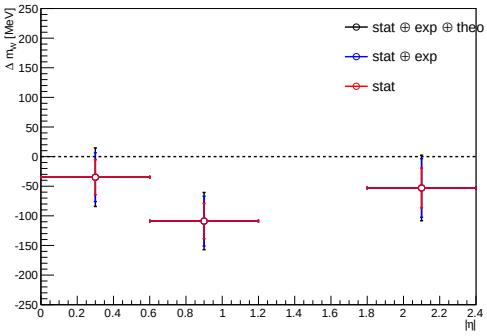

(b) $65 < m_{\mathrm{T}}^{W} < 100$ GeV

FIGURE 8.1: Mass bias [MeV] vs. $|\eta|$ bins, for $2.5 < \langle\mu\rangle < 6.5$.

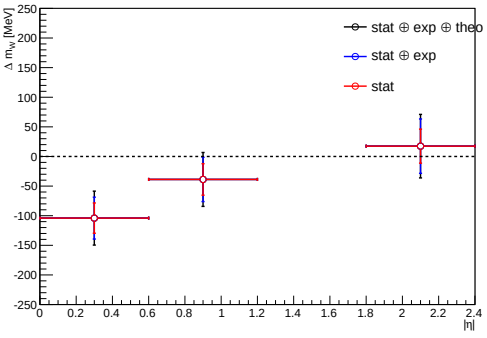

(a) $30 < p_{\mathrm{T}}^{\ell} < 50$ GeV

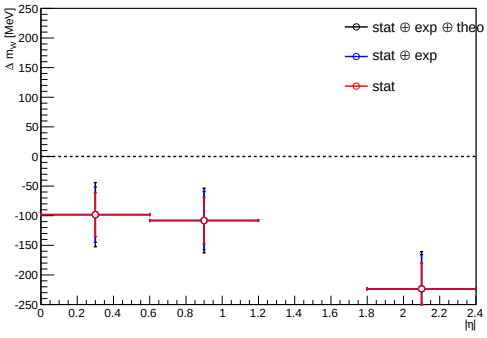

(b) $65 < m_{\mathrm{T}}^{W} < 100$ GeV

FIGURE 8.2: Mass bias [MeV] vs. $|\eta|$ bins, for $6.5 < \langle\mu\rangle < 9.5$.

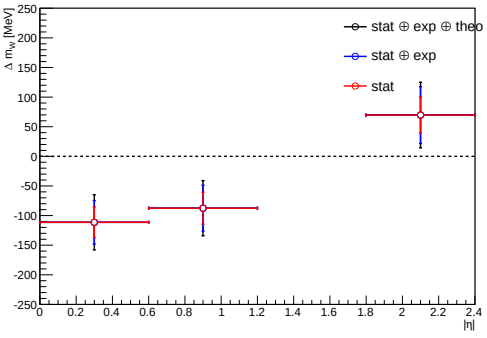

(a) $30 < p_{\mathrm{T}}^{\ell} < 50$ GeV

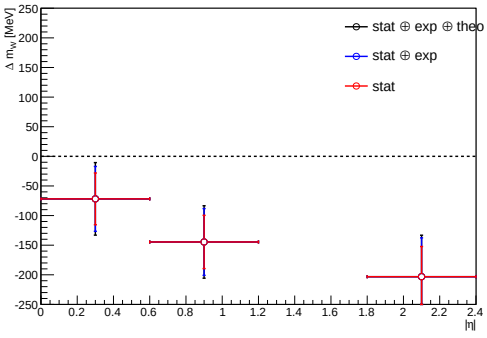

(b) $65 < m_{\mathrm{T}}^{W} < 100$ GeV

FIGURE 8.3: Mass bias [MeV] vs. $|\eta|$ bins, for $9.5 < \langle\mu\rangle < 16$.

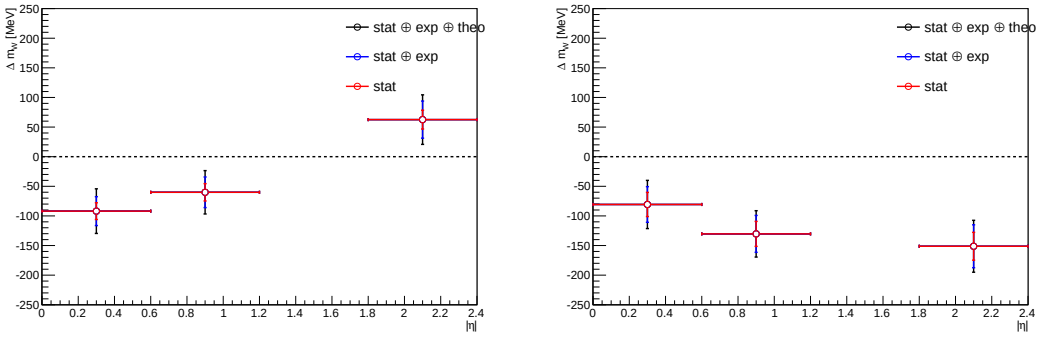

(a) $30 < p_{\mathrm{T}}^{\ell} < 50$ GeV (b) $65 < m_{\mathrm{T}}^{W} < 100$ GeV

FIGURE 8.4: Mass bias [MeV] vs. $|\eta|$ bins, $\langle\mu\rangle$-inclusive.

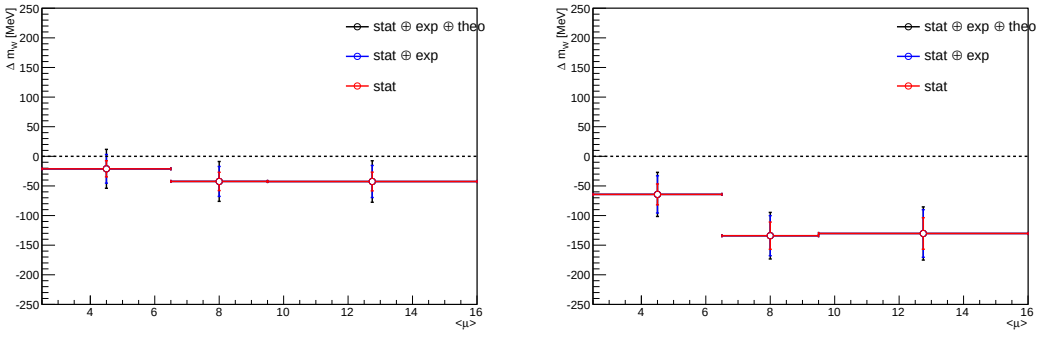

(a) $30 < p_{\mathrm{T}}^{\ell} < 50$ GeV (b) $65 < m_{\mathrm{T}}^{W} < 100$ GeV

FIGURE 8.5: Mass bias [MeV] vs. $\langle\mu\rangle$ bins, η-inclusive.

100 GeV range was chosen to be compared to $30 < p_{\mathrm{T}}^{\ell} < 50$ GeV fits since the biases appeared to be more realistic compared to with the default m_{T}^{W} fitting range. This is due to a mismodeling in the m_{T}^{W} distribution, which is seen in the control plots, illustrated in Figures 7.14, 7.15, 7.16 and in App. D where a slope in the 60-65 GeV range is observed. For both ranges, the systematic uncertainties are considered to be the same.

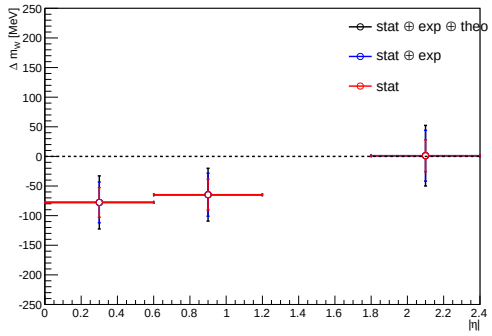

(a) $2.5 < \langle\mu\rangle < 6.5$

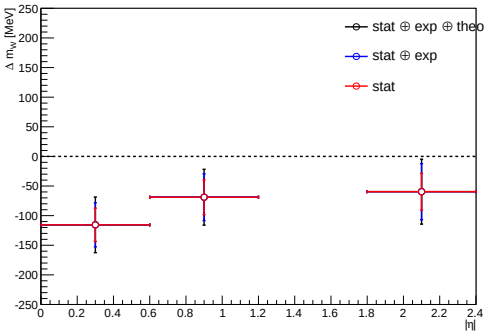

(b) $6.5 < \langle\mu\rangle < 9.5$

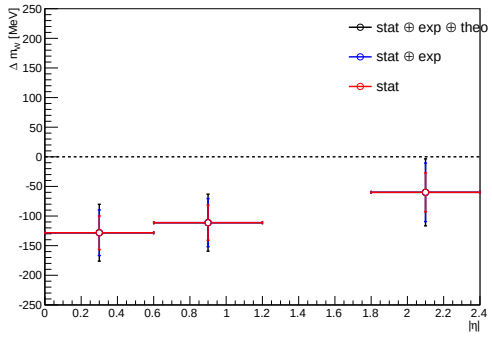

(c) $9.5 < \langle\mu\rangle < 16$

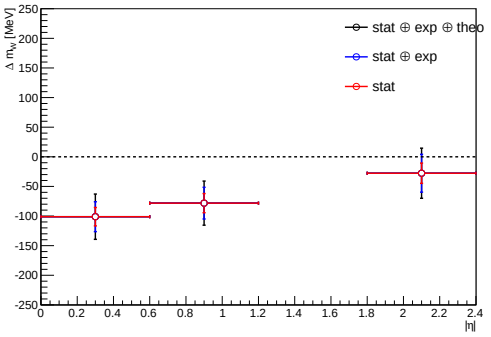

(d) $\langle\mu\rangle$-inclusive

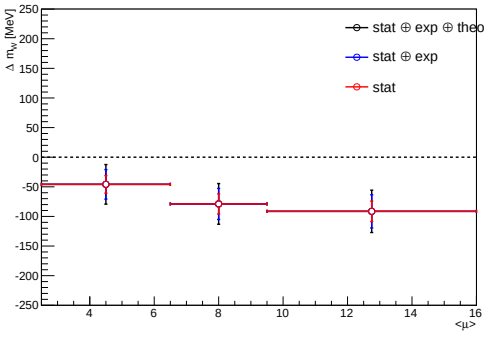

(e) $|\eta|$-inclusive

FIGURE 8.6: Mass bias [MeV] with $30 < p_{\mathrm{T}}^{\ell} < 44.5$ GeV.

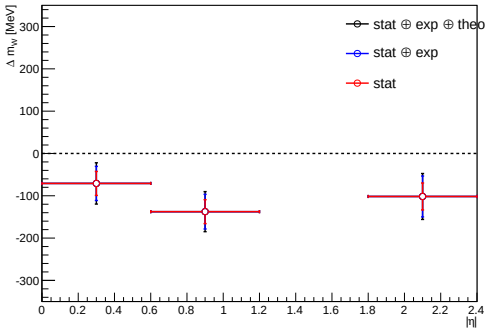

(a) $2.5 < \langle\mu\rangle < 6.5$

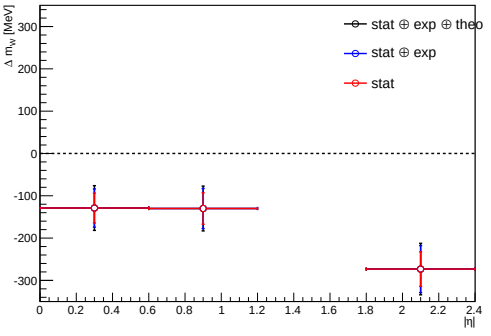

(b) $6.5 < \langle\mu\rangle < 9.5$

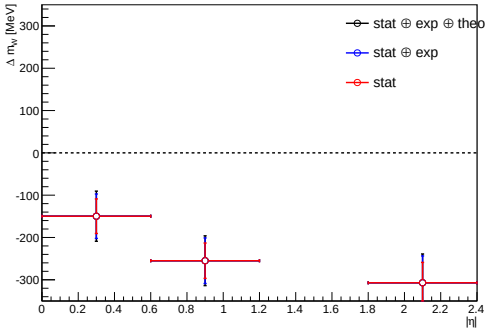

(c) $9.5 < \langle\mu\rangle < 16$

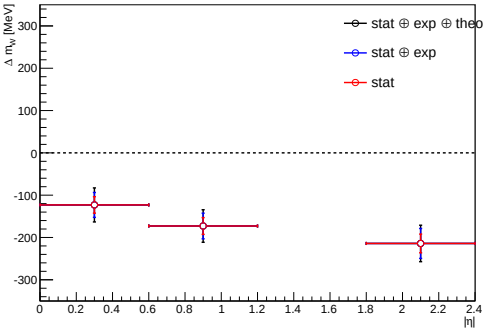

(d) $\langle\mu\rangle$-inclusive

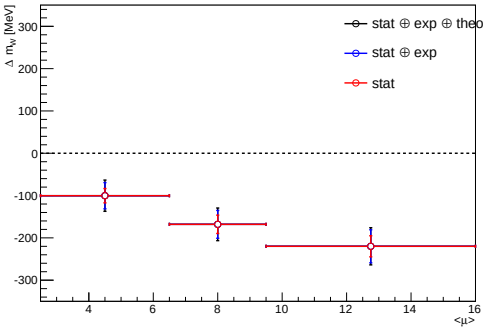

(e) $|\eta|$-inclusive

FIGURE 8.7: Mass bias [MeV] with $60 < m_{\mathrm{T}}^{W} < 100$ GeV. The y-axis range is wider than the previous figures.

Conclusion

In this thesis I discuss my contributions to a first measurement of the W boson mass with the ATLAS detector using 7 TeV data corresponding to an integrated luminosity of 4.37 fb^{-1} taken in 2011. The precision in such measurement is essential as it would test the internal consistency of the Standard Model.

In the first part of the thesis, a study of the performance of the electromagnetic calorimeter is shown. This analysis is performed on 8 TeV 2012 data. Lateral energy profiles, mainly used for particle identification and background rejection, are corrected in the simulation to remove discrepancies with the data. The correction is ready to be implemented in the ATLAS software and used for further analyses. Another study involved testing different physics simulations in GEANT4 and ended up in correcting the 10% lineshape discrepancy in Z events, observed in the 2012 data. These improvements help to better define electron energies, which is of a great importance in high precision measurements performed in the electron channel, such as the W mass measurement.

In the context of the W mass measurement, a modeling of the boson's transverse momentum is discussed. This observable is an important source of systematic uncertainty when measuring m_W, due to its impact on the lepton p_{T}, directly used in the mass measurement. The difficulty in modeling p_{T}^W relies mostly on the complexity of the PDFs in proton-proton collisions. Z events are used to model the boson p_{T}, by tuning parton shower parameters in the Pythia generator. The optimal tuning lead to an agreement with the data up to $p_{\mathrm{T}} = 30$ GeV. Systematic uncertainties coming from the parton shower parameters are assessed, and an optimal fitting range was found to be $30 < p_{\mathrm{T}}^{\ell} < 44.5$ GeV, resulting in an uncertainty of ± 2 MeV, smaller than the $^{+5}_{-7}$ MeV obtained with the default fitting range $30 < p_{\mathrm{T}}^{\ell} < 50$ GeV.

The last part concerns the jet background estimation in the $W \to e\nu$ channel. A new method is proposed, based on fits using the electron isolation. Several corrections and improvements, leading to stable results with respect to the cone size and the fitting range, are developed. The corrections are applied to the jet distribution shape to take into account the correlation with the electron identification requirements, and to the modeling of the isolation variable in Monte Carlo, which directly affects the quality of the fit. The jet background fraction is assessed inclusively and separately in charge, pseudorapidity and pile-up bins. The inclusive jet background fraction is found to be 0.68% with respect to the data events, and a relative uncertainty of approximately 30% on the fraction value is obtained, equivalent to 3(9) MeV on the W mass when extracted using the $m_{\mathrm{T}}^W(p_{\mathrm{T}}^{\ell})$ distribution.

A full breakdown of the systematic uncertainties on the W mass is finally shown, inclusively, and in bins of pseudorapidity and pile-up. At the moment of writing the thesis, Z kinematics are under control, and the experimental uncertainties on the W mass are fully assessed. Compatibilities between the $W \to e\nu$ and $W \to \mu\nu$ results after all experimental corrections

show that the open issues are related to the physics modeling. In fact, due to the incomplete knowledge of the physics modeling, the theoretical uncertainties are preliminary. The shown mass fit results are still blinded. The all-inclusive uncertainties are estimated to be $\delta m_W = 12.4_{\text{statistical}} \oplus 18.2_{\text{experimental}} \oplus 20.0_{\text{theoretical}}$ MeV from m_{T}^W fits and $\delta m_W = 8.5_{\text{statistical}} \oplus 16.7_{\text{experimental}} \oplus 22.2_{\text{theoretical}}$ MeV from p_{T}^{ℓ} fits. These numbers only represent the electron channel analysis, and they will be combined with the muon channel results.

Appendices

Appendix A

Jet background fractions and number of events in period bins

Multijet Fraction (%)	DJ	K	LM
$p_{\mathrm{T}}^{\mathrm{cone30}} - p_{\mathrm{T}}^{\mathrm{cone20}}(W)$	1.4 ± 0.03	1.83 ± 0.06	2.6 ± 0.03
$p_{\mathrm{T}}^{\mathrm{cone40}} - p_{\mathrm{T}}^{\mathrm{cone20}}(W)$	1.53 ± 0.03	1.91 ± 0.06	2.7 ± 0.03
$p_{\mathrm{T}}^{\mathrm{cone30}} - p_{\mathrm{T}}^{\mathrm{cone20}}(W^+)$	1.1 ± 0.04	1.54 ± 0.07	2.07 ± 0.04
$p_{\mathrm{T}}^{\mathrm{cone40}} - p_{\mathrm{T}}^{\mathrm{cone20}}(W^+)$	1.14 ± 0.04	1.52 ± 0.07	2.07 ± 0.04
$p_{\mathrm{T}}^{\mathrm{cone30}} - p_{\mathrm{T}}^{\mathrm{cone20}}(W^-)$	1.75 ± 0.05	2.06 ± 0.09	3.28 ± 0.05
$p_{\mathrm{T}}^{\mathrm{cone40}} - p_{\mathrm{T}}^{\mathrm{cone20}}(W^-)$	2.04 ± 0.05	2.29 ± 0.09	3.43 ± 0.05

TABLE A.1: Multijet background fraction after jet shape extrapolation for W, W^+ and W^-.

Multijet Fraction (%)	DJ	K	LM
$p_{\mathrm{T}}^{\mathrm{cone30}} - p_{\mathrm{T}}^{\mathrm{cone20}}(W)$	1.37 ± 0.03	1.79 ± 0.06	2.68 ± 0.03
$p_{\mathrm{T}}^{\mathrm{cone40}} - p_{\mathrm{T}}^{\mathrm{cone20}}(W)$	1.5 ± 0.03	1.89 ± 0.06	2.8 ± 0.03
$p_{\mathrm{T}}^{\mathrm{cone30}} - p_{\mathrm{T}}^{\mathrm{cone20}}(W^+)$	1.09 ± 0.04	1.51 ± 0.07	2.14 ± 0.04
$p_{\mathrm{T}}^{\mathrm{cone40}} - p_{\mathrm{T}}^{\mathrm{cone20}}(W^+)$	1.11 ± 0.04	1.48 ± 0.07	2.18 ± 0.04
$p_{\mathrm{T}}^{\mathrm{cone30}} - p_{\mathrm{T}}^{\mathrm{cone20}}(W^-)$	1.77 ± 0.05	2.12 ± 0.09	3.39 ± 0.05
$p_{\mathrm{T}}^{\mathrm{cone40}} - p_{\mathrm{T}}^{\mathrm{cone20}}(W^+)$	2.03 ± 0.05	2.37 ± 0.09	3.57 ± 0.05

TABLE A.2: Multijet background fraction before jet shape extrapolation for W, W^+ and W^-.

Number of jet events	DJ	K	LM
$p_{\mathrm{T}}^{\mathrm{cone30}} - p_{\mathrm{T}}^{\mathrm{cone20}}(W)$	32415	14634	71695
$p_{\mathrm{T}}^{\mathrm{cone40}} - p_{\mathrm{T}}^{\mathrm{cone20}}(W)$	35390	15221	74319
$p_{\mathrm{T}}^{\mathrm{cone30}} - p_{\mathrm{T}}^{\mathrm{cone20}}(W^+)$	14757	7112	32826
$p_{\mathrm{T}}^{\mathrm{cone40}} - p_{\mathrm{T}}^{\mathrm{cone20}}(W^+)$	15290	7030	32950
$p_{\mathrm{T}}^{\mathrm{cone30}} - p_{\mathrm{T}}^{\mathrm{cone20}}(W^-)$	17095	6939	38334
$p_{\mathrm{T}}^{\mathrm{cone40}} - p_{\mathrm{T}}^{\mathrm{cone20}}(W^-)$	19922	7742	40090

TABLE A.3: Number of multijet events for W, W^+ and W^- after jet shape extrapolation.

Number of jet events	DJ	K	LM
$p_{\mathrm{T}}^{\mathrm{cone30}} - p_{\mathrm{T}}^{\mathrm{cone20}}(W)$	31753	14293	73866
$p_{\mathrm{T}}^{\mathrm{cone40}} - p_{\mathrm{T}}^{\mathrm{cone20}}(W)$	34713	15101	77131
$p_{\mathrm{T}}^{\mathrm{cone30}} - p_{\mathrm{T}}^{\mathrm{cone20}}(W^+)$	14554	6972	34000
$p_{\mathrm{T}}^{\mathrm{cone40}} - p_{\mathrm{T}}^{\mathrm{cone20}}(W^+)$	14869	6834	34629
$p_{\mathrm{T}}^{\mathrm{cone30}} - p_{\mathrm{T}}^{\mathrm{cone20}}(W^-)$	17277	7167	39553
$p_{\mathrm{T}}^{\mathrm{cone40}} - p_{\mathrm{T}}^{\mathrm{cone20}}(W^-)$	19841	7986	41711

TABLE A.4: Number of multijet events for W, W^+ and W^- before jet shape extrapolation.

Multijet Fraction (W)	DJ	K	LM
	$p_{\mathrm{T}}^{\mathrm{cone30}} - p_{\mathrm{T}}^{\mathrm{cone20}}$		
$0.0 < \|\eta\| < 0.6$	1.06 ± 0.04	1.41 ± 0.07	1.95 ± 0.04
$0.6 < \|\eta\| < 1.2$	1.09 ± 0.06	1.2 ± 0.1	2.19 ± 0.06
$1.8 < \|\eta\| < 2.4$	2.14 ± 0.07	2.7 ± 0.14	4.05 ± 0.09
	$p_{\mathrm{T}}^{\mathrm{cone40}} - p_{\mathrm{T}}^{\mathrm{cone20}}$		
$0.0 < \|\eta\| < 0.6$	1.15 ± 0.04	1.31 ± 0.07	1.95 ± 0.04
$0.6 < \|\eta\| < 1.2$	1.2 ± 0.06	1.42 ± 0.1	2.38 ± 0.06
$1.8 < \|\eta\| < 2.4$	2.42 ± 0.07	3.09 ± 0.14	4.23 ± 0.08

TABLE A.5: Multijet background fraction after jet shape extrapolation for W, in pseudo-rapidity bins.

Multijet Fraction (W^+)	DJ	K	LM
	$p_{\mathrm{T}}^{\mathrm{cone30}} - p_{\mathrm{T}}^{\mathrm{cone20}}$		
$0.0 < \|\eta\| < 0.6$	0.77 ± 0.05	1.18 ± 0.09	1.48 ± 0.05
$0.6 < \|\eta\| < 1.2$	0.83 ± 0.07	0.61 ± 0.09	1.6 ± 0.07
$1.8 < \|\eta\| < 2.4$	1.69 ± 0.09	2.41 ± 0.17	3.06 ± 0.1
	$p_{\mathrm{T}}^{\mathrm{cone40}} - p_{\mathrm{T}}^{\mathrm{cone20}}$		
$0.0 < \|\eta\| < 0.6$	0.77 ± 0.05	1.13 ± 0.09	1.43 ± 0.05
$0.6 < \|\eta\| < 1.2$	0.79 ± 0.07	0.97 ± 0.11	1.71 ± 0.07
$1.8 < \|\eta\| < 2.4$	1.79 ± 0.09	2.34 ± 0.17	3.34 ± 0.1

TABLE A.6: Multijet background fraction after jet shape extrapolation for W^+, in pseudo-rapidity bins.

Multijet Fraction (W^-)	DJ	K	LM
	$p_{\mathrm{T}}^{\mathrm{cone30}} - p_{\mathrm{T}}^{\mathrm{cone20}}$		
$0.0 < \|\eta\| < 0.6$	1.32 ± 0.06	1.31 ± 0.09	2.37 ± 0.06
$0.6 < \|\eta\| < 1.2$	1.35 ± 0.09	1.42 ± 0.15	2.68 ± 0.09
$1.8 < \|\eta\| < 2.4$	2.78 ± 0.12	2.89 ± 0.21	5.11 ± 0.15
	$p_{\mathrm{T}}^{\mathrm{cone40}} - p_{\mathrm{T}}^{\mathrm{cone20}}$		
$0.0 < \|\eta\| < 0.6$	1.25 ± 0.06	1.34 ± 0.09	2.52 ± 0.06
$0.6 < \|\eta\| < 1.2$	1.69 ± 0.09	1.77 ± 0.15	3.0 ± 0.1
$1.8 < \|\eta\| < 2.4$	3.14 ± 0.12	3.68 ± 0.22	5.56 ± 0.14

TABLE A.7: Multijet background fraction after jet shape extrapolation for W^-, in pseudo-rapidity bins.

Multijet Fraction (W)	DJ	K	LM
	$p_{\mathrm{T}}^{\mathrm{cone30}} - p_{\mathrm{T}}^{\mathrm{cone20}}$		
$0.0 < \|\eta\| < 0.6$	1.1 ± 0.04	1.44 ± 0.07	2.09 ± 0.04
$0.6 < \|\eta\| < 1.2$	1.08 ± 0.06	1.34 ± 0.1	2.37 ± 0.06
$1.8 < \|\eta\| < 2.4$	1.89 ± 0.06	2.49 ± 0.12	3.7 ± 0.08
	$p_{\mathrm{T}}^{\mathrm{cone40}} - p_{\mathrm{T}}^{\mathrm{cone20}}$		
$0.0 < \|\eta\| < 0.6$	1.13 ± 0.04	1.47 ± 0.07	2.09 ± 0.04
$0.6 < \|\eta\| < 1.2$	1.22 ± 0.06	1.48 ± 0.1	2.6 ± 0.07
$1.8 < \|\eta\| < 2.4$	2.14 ± 0.06	2.76 ± 0.12	3.98 ± 0.08

TABLE A.8: Multijet background fraction before jet shape extrapolation for W, in pseudo-rapidity bins.

Multijet Fraction (W^+)	DJ	K	LM
	$p_{\mathrm{T}}^{\mathrm{cone30}} - p_{\mathrm{T}}^{\mathrm{cone20}}$		
$0.0 < \|\eta\| < 0.6$	0.86 ± 0.05	1.22 ± 0.09	1.72 ± 0.05
$0.6 < \|\eta\| < 1.2$	0.8 ± 0.07	0.88 ± 0.12	1.71 ± 0.08
$1.8 < \|\eta\| < 2.4$	1.5 ± 0.08	2.07 ± 0.15	2.88 ± 0.09
	$p_{\mathrm{T}}^{\mathrm{cone40}} - p_{\mathrm{T}}^{\mathrm{cone20}}$		
$0.0 < \|\eta\| < 0.6$	0.78 ± 0.05	1.24 ± 0.09	1.64 ± 0.05
$0.6 < \|\eta\| < 1.2$	0.84 ± 0.07	0.99 ± 0.12	1.97 ± 0.08
$1.8 < \|\eta\| < 2.4$	1.69 ± 0.08	2.16 ± 0.16	3.1 ± 0.09

TABLE A.9: Multijet background fraction before jet shape extrapolation for W^+, in pseudo-rapidity bins.

Multijet Fraction (W^-)	DJ	K	LM
	$p_{\mathrm{T}}^{\mathrm{cone30}} - p_{\mathrm{T}}^{\mathrm{cone20}}$		
$0.0 < \|\eta\| < 0.6$	1.42 ± 0.06	1.55 ± 0.1	2.48 ± 0.06
$0.6 < \|\eta\| < 1.2$	1.46 ± 0.09	1.68 ± 0.17	3.2 ± 0.11
$1.8 < \|\eta\| < 2.4$	2.51 ± 0.11	2.97 ± 0.21	4.83 ± 0.14
	$p_{\mathrm{T}}^{\mathrm{cone40}} - p_{\mathrm{T}}^{\mathrm{cone20}}$		
$0.0 < \|\eta\| < 0.6$	1.31 ± 0.06	1.69 ± 0.1	2.57 ± 0.06
$0.6 < \|\eta\| < 1.2$	1.76 ± 0.1	1.95 ± 0.16	3.29 ± 0.1
$1.8 < \|\eta\| < 2.4$	2.83 ± 0.11	3.46 ± 0.21	5.24 ± 0.13

TABLE A.10: Multijet background fraction before jet shape extrapolation for W^-, in pseudo-rapidity bins.

Number of jet events (W)	DJ	K	LM
$p_{\mathrm{T}}^{\mathrm{cone30}} - p_{\mathrm{T}}^{\mathrm{cone20}}$			
$0.0 < \|\eta\| < 0.6$	12153	5590	26741
$0.6 < \|\eta\| < 1.2$	5723	2198	13920
$1.8 < \|\eta\| < 2.4$	13413	5791	29487
$p_{\mathrm{T}}^{\mathrm{cone40}} - p_{\mathrm{T}}^{\mathrm{cone20}}$			
$0.0 < \|\eta\| < 0.6$	13111	5201	26750
$0.6 < \|\eta\| < 1.2$	6294	2596	15123
$1.8 < \|\eta\| < 2.4$	15149	6611	30823

TABLE A.11: Number of multijet events for W, in pseudo-rapidity bins, after jet shape extrapolation.

Number of jet events (W^+)	DJ	K	LM
$p_{\mathrm{T}}^{\mathrm{cone30}} - p_{\mathrm{T}}^{\mathrm{cone20}}$			
$0.0 < \|\eta\| < 0.6$	4950	2624	11410
$0.6 < \|\eta\| < 1.2$	2491	635	5815
$1.8 < \|\eta\| < 2.4$	6499	3153	13562
$p_{\mathrm{T}}^{\mathrm{cone40}} - p_{\mathrm{T}}^{\mathrm{cone20}}$			
$0.0 < \|\eta\| < 0.6$	4942	2510	11015
$0.6 < \|\eta\| < 1.2$	2381	1012	6211
$1.8 < \|\eta\| < 2.4$	6885	3070	14783

TABLE A.12: Number of multijet events for W^+, in pseudo-rapidity bins, after jet shape extrapolation.

Number of jet events (W^-)	DJ	K	LM
$p_{\mathrm{T}}^{\mathrm{cone30}} - p_{\mathrm{T}}^{\mathrm{cone20}}$			
$0.0 < \|\eta\| < 0.6$	6607	2280	14249
$0.6 < \|\eta\| < 1.2$	3023	1102	7276
$1.8 < \|\eta\| < 2.4$	6760	2407	14564
$p_{\mathrm{T}}^{\mathrm{cone40}} - p_{\mathrm{T}}^{\mathrm{cone20}}$			
$0.0 < \|\eta\| < 0.6$	6250	2326	15149
$0.6 < \|\eta\| < 1.2$	3791	1374	8147
$1.8 < \|\eta\| < 2.4$	7626	3065	15837

TABLE A.13: Number of multijet events for W^-, in pseudo-rapidity bins, after jet shape extrapolation.

Number of jet events (W)	DJ	K	LM
$p_{\mathrm{T}}^{\mathrm{cone30}} - p_{\mathrm{T}}^{\mathrm{cone20}}$			
$0.0 < \|\eta\| < 0.6$	12602	5706	28636
$0.6 < \|\eta\| < 1.2$	5670	2447	15085
$1.8 < \|\eta\| < 2.4$	11845	5328	26900
$p_{\mathrm{T}}^{\mathrm{cone40}} - p_{\mathrm{T}}^{\mathrm{cone20}}$			
$0.0 < \|\eta\| < 0.6$	12918	5828	28712
$0.6 < \|\eta\| < 1.2$	6413	2695	16530
$1.8 < \|\eta\| < 2.4$	13433	5907	28945

TABLE A.14: Number of multijet events for W, in pseudo-rapidity bins, before jet shape extrapolation.

Number of jet events (W^+)	DJ	K	LM
$p_{\mathrm{T}}^{\mathrm{cone30}} - p_{\mathrm{T}}^{\mathrm{cone20}}$			
$0.0 < \|\eta\| < 0.6$	5512	2699	13251
$0.6 < \|\eta\| < 1.2$	2421	926	6195
$1.8 < \|\eta\| < 2.4$	5774	2711	12743
$p_{\mathrm{T}}^{\mathrm{cone40}} - p_{\mathrm{T}}^{\mathrm{cone20}}$			
$0.0 < \|\eta\| < 0.6$	5016	2745	12640
$0.6 < \|\eta\| < 1.2$	2517	1032	7143
$1.8 < \|\eta\| < 2.4$	6503	2829	13709

TABLE A.15: Number of multijet events for W^+, in pseudo-rapidity bins, before jet shape extrapolation.

Number of jet events (W^-)	DJ	K	LM
$p_{\mathrm{T}}^{\mathrm{cone30}} - p_{\mathrm{T}}^{\mathrm{cone20}}$			
$0.0 < \|\eta\| < 0.6$	7113	2691	14962
$0.6 < \|\eta\| < 1.2$	3274	1303	8699
$1.8 < \|\eta\| < 2.4$	6096	2470	13773
$p_{\mathrm{T}}^{\mathrm{cone40}} - p_{\mathrm{T}}^{\mathrm{cone20}}$			
$0.0 < \|\eta\| < 0.6$	6572	2947	15492
$0.6 < \|\eta\| < 1.2$	3957	1517	8954
$1.8 < \|\eta\| < 2.4$	6875	2881	14938

TABLE A.16: Number of multijet events for W^-, in pseudo-rapidity bins, before jet shape extrapolation.

Appendix B

Jet background fractions and numbers of events in $\langle\mu\rangle$ bins

B.1 MC is not corrected

Multijet Fraction (%)	$2.5 < \langle\mu\rangle < 6.5$	$6.5 < \langle\mu\rangle < 9.5$	$9.5 < \langle\mu\rangle < 16$
${p_{\mathrm{T}}}^{\mathrm{cone30}} - {p_{\mathrm{T}}}^{\mathrm{cone20}}(W)$	1.44 ± 0.03	2.19 ± 0.05	3.42 ± 0.04
${p_{\mathrm{T}}}^{\mathrm{cone40}} - {p_{\mathrm{T}}}^{\mathrm{cone20}}(W)$	1.65 ± 0.03	2.32 ± 0.05	3.57 ± 0.04
${p_{\mathrm{T}}}^{\mathrm{cone30}} - {p_{\mathrm{T}}}^{\mathrm{cone20}}(W^+)$	1.18 ± 0.04	1.74 ± 0.06	2.79 ± 0.06
${p_{\mathrm{T}}}^{\mathrm{cone40}} - {p_{\mathrm{T}}}^{\mathrm{cone20}}(W^+)$	1.29 ± 0.04	1.81 ± 0.06	2.84 ± 0.05
${p_{\mathrm{T}}}^{\mathrm{cone30}} - {p_{\mathrm{T}}}^{\mathrm{cone20}}(W^-)$	1.82 ± 0.05	2.72 ± 0.08	4.2 ± 0.07
${p_{\mathrm{T}}}^{\mathrm{cone40}} - {p_{\mathrm{T}}}^{\mathrm{cone20}}(W^-)$	2.12 ± 0.05	2.89 ± 0.08	4.45 ± 0.07

TABLE B.1: Multijet background fraction before jet shape extrapolation for W, W^+ and W^-, without correcting the MC distribution.

Multijet Fraction (%)	$2.5 < \langle\mu\rangle < 6.5$	$6.5 < \langle\mu\rangle < 9.5$	$9.5 < \langle\mu\rangle < 16$
${p_{\mathrm{T}}}^{\mathrm{cone30}} - {p_{\mathrm{T}}}^{\mathrm{cone20}}(W)$	1.42 ± 0.03	1.95 ± 0.05	3.67 ± 0.05
${p_{\mathrm{T}}}^{\mathrm{cone40}} - {p_{\mathrm{T}}}^{\mathrm{cone20}}(W)$	1.59 ± 0.03	2.06 ± 0.05	3.58 ± 0.04
${p_{\mathrm{T}}}^{\mathrm{cone30}} - {p_{\mathrm{T}}}^{\mathrm{cone20}}(W^+)$	1.15 ± 0.04	1.58 ± 0.06	2.87 ± 0.06
${p_{\mathrm{T}}}^{\mathrm{cone40}} - {p_{\mathrm{T}}}^{\mathrm{cone20}}(W^+)$	1.25 ± 0.04	1.58 ± 0.06	2.79 ± 0.06
${p_{\mathrm{T}}}^{\mathrm{cone30}} - {p_{\mathrm{T}}}^{\mathrm{cone20}}(W^-)$	1.76 ± 0.05	2.58 ± 0.08	4.11 ± 0.07
${p_{\mathrm{T}}}^{\mathrm{cone40}} - {p_{\mathrm{T}}}^{\mathrm{cone20}}(W^-)$	1.98 ± 0.05	2.47 ± 0.07	4.22 ± 0.07

TABLE B.2: Multijet background fraction after jet shape extrapolation for W, W^+ and W^-, without correcting the MC distribution.

Multijet Fraction (W)	$2.5 < \langle\mu\rangle < 6.5$	$6.5 < \langle\mu\rangle < 9.5$	$9.5 < \langle\mu\rangle < 16$
	$p_{\mathrm{T}}^{\mathrm{cone30}} - p_{\mathrm{T}}^{\mathrm{cone20}}$		
$0.0 < \lvert\eta\rvert < 0.6$	1.17 ± 0.05	1.72 ± 0.07	2.57 ± 0.06
$0.6 < \lvert\eta\rvert < 1.2$	1.28 ± 0.05	1.93 ± 0.08	2.98 ± 0.07
$1.8 < \lvert\eta\rvert < 2.4$	1.79 ± 0.07	2.76 ± 0.12	4.51 ± 0.11
	$p_{\mathrm{T}}^{\mathrm{cone40}} - p_{\mathrm{T}}^{\mathrm{cone20}}$		
$0.0 < \lvert\eta\rvert < 0.6$	1.31 ± 0.05	1.69 ± 0.07	2.57 ± 0.06
$0.6 < \lvert\eta\rvert < 1.2$	1.38 ± 0.05	2.1 ± 0.08	3.25 ± 0.07
$1.8 < \lvert\eta\rvert < 2.4$	2.02 ± 0.07	2.94 ± 0.11	4.66 ± 0.1

TABLE B.3: Multijet background fraction before jet shape extrapolation for W, in pseudo-rapidity bins, without correcting the MC distribution.

Multijet Fraction (W^+)	$2.5 < \langle\mu\rangle < 6.5$	$6.5 < \langle\mu\rangle < 9.5$	$9.5 < \langle\mu\rangle < 16$
	$p_{\mathrm{T}}^{\mathrm{cone30}} - p_{\mathrm{T}}^{\mathrm{cone20}}$		
$0.0 < \lvert\eta\rvert < 0.6$	0.9 ± 0.06	1.35 ± 0.1	2.08 ± 0.08
$0.6 < \lvert\eta\rvert < 1.2$	1.07 ± 0.06	1.55 ± 0.09	2.35 ± 0.08
$1.8 < \lvert\eta\rvert < 2.4$	1.42 ± 0.08	2.25 ± 0.14	3.48 ± 0.12
	$p_{\mathrm{T}}^{\mathrm{cone40}} - p_{\mathrm{T}}^{\mathrm{cone20}}$		
$0.0 < \lvert\eta\rvert < 0.6$	0.97 ± 0.06	1.24 ± 0.1	2.1 ± 0.08
$0.6 < \lvert\eta\rvert < 1.2$	1.06 ± 0.06	1.62 ± 0.1	2.61 ± 0.09
$1.8 < \lvert\eta\rvert < 2.4$	1.6 ± 0.08	2.39 ± 0.14	3.55 ± 0.12

TABLE B.4: Multijet background fraction before jet shape extrapolation for W^+, in pseudo-rapidity bins, without correcting the MC distribution.

Multijet Fraction (W^-)	$2.5 < \langle\mu\rangle < 6.5$	$6.5 < \langle\mu\rangle < 9.5$	$9.5 < \langle\mu\rangle < 16$
	$p_{\mathrm{T}}^{\mathrm{cone30}} - p_{\mathrm{T}}^{\mathrm{cone20}}$		
$0.0 < \lvert\eta\rvert < 0.6$	1.53 ± 0.07	2.04 ± 0.11	2.96 ± 0.1
$0.6 < \lvert\eta\rvert < 1.2$	1.54 ± 0.08	2.3 ± 0.13	3.71 ± 0.11
$1.8 < \lvert\eta\rvert < 2.4$	2.39 ± 0.11	3.39 ± 0.2	6.02 ± 0.19
	$p_{\mathrm{T}}^{\mathrm{cone40}} - p_{\mathrm{T}}^{\mathrm{cone20}}$		
$0.0 < \lvert\eta\rvert < 0.6$	1.72 ± 0.08	2.01 ± 0.11	2.94 ± 0.09
$0.6 < \lvert\eta\rvert < 1.2$	1.82 ± 0.08	2.56 ± 0.12	3.89 ± 0.1
$1.8 < \lvert\eta\rvert < 2.4$	2.63 ± 0.11	3.51 ± 0.19	6.15 ± 0.18

TABLE B.5: Multijet background fraction before jet shape extrapolation for W^-, in pseudo-rapidity bins, without correcting the MC distribution.

Multijet Fraction (W)	$2.5 < \langle\mu\rangle < 6.5$	$6.5 < \langle\mu\rangle < 9.5$	$9.5 < \langle\mu\rangle < 16$
	$p_{\mathrm{T}}^{\mathrm{cone30}} - p_{\mathrm{T}}^{\mathrm{cone20}}$		
$0.0 < \lvert\eta\rvert < 0.6$	1.08 ± 0.04	1.31 ± 0.06	2.4 ± 0.06
$0.6 < \lvert\eta\rvert < 1.2$	1.12 ± 0.04	1.79 ± 0.08	2.91 ± 0.07
$1.8 < \lvert\eta\rvert < 2.4$	2.08 ± 0.08	2.76 ± 0.12	5.35 ± 0.13
	$p_{\mathrm{T}}^{\mathrm{cone40}} - p_{\mathrm{T}}^{\mathrm{cone20}}$		
$0.0 < \lvert\eta\rvert < 0.6$	1.21 ± 0.05	1.26 ± 0.06	2.44 ± 0.06
$0.6 < \lvert\eta\rvert < 1.2$	1.22 ± 0.05	1.89 ± 0.07	3.04 ± 0.07
$1.8 < \lvert\eta\rvert < 2.4$	2.17 ± 0.07	2.75 ± 0.12	4.8 ± 0.11

TABLE B.6: Multijet background fraction after jet shape extrapolation for W, in pseudo-rapidity bins, without correcting the MC distribution.

Multijet Fraction (W^+)	$2.5 < \langle\mu\rangle < 6.5$	$6.5 < \langle\mu\rangle < 9.5$	$9.5 < \langle\mu\rangle < 16$
	$p_{\mathrm{T}}^{\mathrm{cone30}} - p_{\mathrm{T}}^{\mathrm{cone20}}$		
$0.0 < \lvert\eta\rvert < 0.6$	0.76 ± 0.05	0.95 ± 0.08	1.46 ± 0.07
$0.6 < \lvert\eta\rvert < 1.2$	0.96 ± 0.06	1.47 ± 0.09	1.58 ± 0.07
$1.8 < \lvert\eta\rvert < 2.4$	1.5 ± 0.09	1.97 ± 0.15	3.89 ± 0.15
	$p_{\mathrm{T}}^{\mathrm{cone40}} - p_{\mathrm{T}}^{\mathrm{cone20}}$		
$0.0 < \lvert\eta\rvert < 0.6$	0.86 ± 0.06	0.81 ± 0.08	1.21 ± 0.06
$0.6 < \lvert\eta\rvert < 1.2$	0.94 ± 0.06	1.24 ± 0.09	2.15 ± 0.09
$1.8 < \lvert\eta\rvert < 2.4$	1.61 ± 0.09	2.32 ± 0.15	3.51 ± 0.13

TABLE B.7: Multijet background fraction after jet shape extrapolation for W^+, in pseudo-rapidity bins, without correcting the MC distribution.

Multijet Fraction (W^-)	$2.5 < \langle\mu\rangle < 6.5$	$6.5 < \langle\mu\rangle < 9.5$	$9.5 < \langle\mu\rangle < 16$
	$p_{\mathrm{T}}^{\mathrm{cone30}} - p_{\mathrm{T}}^{\mathrm{cone20}}$		
$0.0 < \lvert\eta\rvert < 0.6$	1.42 ± 0.07	1.57 ± 0.09	2.64 ± 0.09
$0.6 < \lvert\eta\rvert < 1.2$	1.35 ± 0.07	2.13 ± 0.13	3.45 ± 0.11
$1.8 < \lvert\eta\rvert < 2.4$	2.57 ± 0.13	3.11 ± 0.2	6.93 ± 0.24
	$p_{\mathrm{T}}^{\mathrm{cone40}} - p_{\mathrm{T}}^{\mathrm{cone20}}$		
$0.0 < \lvert\eta\rvert < 0.6$	1.64 ± 0.08	1.57 ± 0.1	2.88 ± 0.09
$0.6 < \lvert\eta\rvert < 1.2$	1.65 ± 0.08	2.4 ± 0.13	4.08 ± 0.12
$1.8 < \lvert\eta\rvert < 2.4$	2.63 ± 0.12	2.8 ± 0.19	5.87 ± 0.19

TABLE B.8: Multijet background fraction after jet shape extrapolation for W^-, in pseudo-rapidity bins, without correcting the MC distribution.

Number of jet events	$2.5 < \langle\mu\rangle < 6.5$	$6.5 < \langle\mu\rangle < 9.5$	$9.5 < \langle\mu\rangle < 16$
$p_{\mathrm{T}}^{\mathrm{cone30}} - p_{\mathrm{T}}^{\mathrm{cone20}}(W)$	28729	23170	61141
$p_{\mathrm{T}}^{\mathrm{cone40}} - p_{\mathrm{T}}^{\mathrm{cone20}}(W)$	33063	24535	63851
$p_{\mathrm{T}}^{\mathrm{cone30}} - p_{\mathrm{T}}^{\mathrm{cone20}}(W^+)$	13611	10594	28711
$p_{\mathrm{T}}^{\mathrm{cone40}} - p_{\mathrm{T}}^{\mathrm{cone20}}(W^+)$	14944	11079	29312
$p_{\mathrm{T}}^{\mathrm{cone30}} - p_{\mathrm{T}}^{\mathrm{cone20}}(W^-)$	15373	12141	31932
$p_{\mathrm{T}}^{\mathrm{cone40}} - p_{\mathrm{T}}^{\mathrm{cone20}}(W^-)$	17869	12925	33797

TABLE B.9: Average number of jets before jet shape extrapolation for W, W^+ and W^-, without correcting the MC distribution.

Number of jet events	$2.5 < \langle\mu\rangle < 6.5$	$6.5 < \langle\mu\rangle < 9.5$	$9.5 < \langle\mu\rangle < 16$
$p_{\mathrm{T}}^{\mathrm{cone30}} - p_{\mathrm{T}}^{\mathrm{cone20}}(W)$	28321	20661	65760
$p_{\mathrm{T}}^{\mathrm{cone40}} - p_{\mathrm{T}}^{\mathrm{cone20}}(W)$	31735	21756	64003
$p_{\mathrm{T}}^{\mathrm{cone30}} - p_{\mathrm{T}}^{\mathrm{cone20}}(W^+)$	13307	9652	29586
$p_{\mathrm{T}}^{\mathrm{cone40}} - p_{\mathrm{T}}^{\mathrm{cone20}}(W^+)$	14425	9661	28736
$p_{\mathrm{T}}^{\mathrm{cone30}} - p_{\mathrm{T}}^{\mathrm{cone20}}(W^-)$	14808	11545	31209
$p_{\mathrm{T}}^{\mathrm{cone40}} - p_{\mathrm{T}}^{\mathrm{cone20}}(W^-)$	16645	11058	32022

TABLE B.10: Average number of jets after jet shape extrapolation for W, W^+ and W^-, without correcting the MC distribution.

Number of jet events (W)	$2.5 < \langle\mu\rangle < 6.5$	$6.5 < \langle\mu\rangle < 9.5$	$9.5 < \langle\mu\rangle < 16$
	$p_{\mathrm{T}}^{\mathrm{cone30}} - p_{\mathrm{T}}^{\mathrm{cone20}}$		
$0.0 < \lvert\eta\rvert < 0.6$	8667	6790	17124
$0.6 < \lvert\eta\rvert < 1.2$	8975	7247	19031
$1.8 < \lvert\eta\rvert < 2.4$	9691	7703	21282
	$p_{\mathrm{T}}^{\mathrm{cone40}} - p_{\mathrm{T}}^{\mathrm{cone20}}$		
$0.0 < \lvert\eta\rvert < 0.6$	9660	6648	17145
$0.6 < \lvert\eta\rvert < 1.2$	9715	7911	20762
$1.8 < \lvert\eta\rvert < 2.4$	10959	8221	21992

TABLE B.11: Average number of jets before jet shape extrapolation for W, in pseudo-rapidity bins, without correcting the MC distribution.

Number of jet events (W^+)	$2.5 < \langle\mu\rangle < 6.5$	$6.5 < \langle\mu\rangle < 9.5$	$9.5 < \langle\mu\rangle < 16$
	$p_{\mathrm{T}}^{\mathrm{cone30}} - p_{\mathrm{T}}^{\mathrm{cone20}}$		
$0.0 < \lvert\eta\rvert < 0.6$	3733	2985	7748
$0.6 < \lvert\eta\rvert < 1.2$	4289	3327	8519
$1.8 < \lvert\eta\rvert < 2.4$	4705	3839	9978
	$p_{\mathrm{T}}^{\mathrm{cone40}} - p_{\mathrm{T}}^{\mathrm{cone20}}$		
$0.0 < \lvert\eta\rvert < 0.6$	4019	2742	7831
$0.6 < \lvert\eta\rvert < 1.2$	4271	3480	9459
$1.8 < \lvert\eta\rvert < 2.4$	5329	4068	10182

TABLE B.12: Average number of jets before jet shape extrapolation for W^+, in pseudo-rapidity bins, without correcting the MC distribution.

Number of jet events (W^-)	$2.5 < \langle\mu\rangle < 6.5$	$6.5 < \langle\mu\rangle < 9.5$	$9.5 < \langle\mu\rangle < 16$
	$p_{\mathrm{T}}^{\mathrm{cone30}} - p_{\mathrm{T}}^{\mathrm{cone20}}$		
$0.0 < \lvert\eta\rvert < 0.6$	4961	3533	8700
$0.6 < \lvert\eta\rvert < 1.2$	4640	3715	10207
$1.8 < \lvert\eta\rvert < 2.4$	5011	3693	11169
	$p_{\mathrm{T}}^{\mathrm{cone40}} - p_{\mathrm{T}}^{\mathrm{cone20}}$		
$0.0 < \lvert\eta\rvert < 0.6$	5594	3480	8649
$0.6 < \lvert\eta\rvert < 1.2$	5485	4137	10692
$1.8 < \lvert\eta\rvert < 2.4$	5534	3825	11399

TABLE B.13: Average number of jets before jet shape extrapolation for W^-, in pseudo-rapidity bins, without correcting the MC distribution.

Number of jet events (W)	$2.5 < \langle\mu\rangle < 6.5$	$6.5 < \langle\mu\rangle < 9.5$	$9.5 < \langle\mu\rangle < 16$
	$p_{\mathrm{T}}^{\mathrm{cone30}} - p_{\mathrm{T}}^{\mathrm{cone20}}$		
$0.0 < \lvert\eta\rvert < 0.6$	7993	5139	15986
$0.6 < \lvert\eta\rvert < 1.2$	7909	6727	18541
$1.8 < \lvert\eta\rvert < 2.4$	11292	7717	25236
	$p_{\mathrm{T}}^{\mathrm{cone40}} - p_{\mathrm{T}}^{\mathrm{cone20}}$		
$0.0 < \lvert\eta\rvert < 0.6$	8955	4977	16279
$0.6 < \lvert\eta\rvert < 1.2$	8565	7094	19378
$1.8 < \lvert\eta\rvert < 2.4$	11757	7698	22643

TABLE B.14: Average number of jets after jet shape extrapolation for W, in pseudo-rapidity bins, without correcting the MC distribution.

Number of jet events (W^+)	$2.5 < \langle\mu\rangle < 6.5$	$6.5 < \langle\mu\rangle < 9.5$	$9.5 < \langle\mu\rangle < 16$
	$p_{\mathrm{T}}^{\mathrm{cone30}} - p_{\mathrm{T}}^{\mathrm{cone20}}$		
$0.0 < \lvert\eta\rvert < 0.6$	3155	2093	5434
$0.6 < \lvert\eta\rvert < 1.2$	3871	3160	5737
$1.8 < \lvert\eta\rvert < 2.4$	4974	3363	11152
	$p_{\mathrm{T}}^{\mathrm{cone40}} - p_{\mathrm{T}}^{\mathrm{cone20}}$		
$0.0 < \lvert\eta\rvert < 0.6$	3566	1788	4499
$0.6 < \lvert\eta\rvert < 1.2$	3777	2651	7822
$1.8 < \lvert\eta\rvert < 2.4$	5346	3964	10066

TABLE B.15: Average number of jets after jet shape extrapolation for W^+, in pseudo-rapidity bins, without correcting the MC distribution.

Number of jet events (W^-)	$2.5 < \langle\mu\rangle < 6.5$	$6.5 < \langle\mu\rangle < 9.5$	$9.5 < \langle\mu\rangle < 16$
	$p_{\mathrm{T}}^{\mathrm{cone30}} - p_{\mathrm{T}}^{\mathrm{cone20}}$		
$0.0 < \lvert\eta\rvert < 0.6$	4609	2723	7744
$0.6 < \lvert\eta\rvert < 1.2$	4078	3440	9470
$1.8 < \lvert\eta\rvert < 2.4$	5400	3395	12860
	$p_{\mathrm{T}}^{\mathrm{cone40}} - p_{\mathrm{T}}^{\mathrm{cone20}}$		
$0.0 < \lvert\eta\rvert < 0.6$	5329	2722	8466
$0.6 < \lvert\eta\rvert < 1.2$	4964	3871	11219
$1.8 < \lvert\eta\rvert < 2.4$	5524	3054	10889

TABLE B.16: Average number of jets after jet shape extrapolation for W^-, in pseudo-rapidity bins, without correcting the MC distribution.

B.2 MC is corrected

Multijet Fraction (%)	$2.5 < \langle\mu\rangle < 6.5$	$6.5 < \langle\mu\rangle < 9.5$	$9.5 < \langle\mu\rangle < 16$
$p_{\mathrm{T}}^{\mathrm{cone30}} - p_{\mathrm{T}}^{\mathrm{cone20}}(W)$	1.24 ± 0.03	1.98 ± 0.05	3.19 ± 0.05
$p_{\mathrm{T}}^{\mathrm{cone40}} - p_{\mathrm{T}}^{\mathrm{cone20}}(W)$	1.39 ± 0.03	2.05 ± 0.05	3.29 ± 0.04
$p_{\mathrm{T}}^{\mathrm{cone30}} - p_{\mathrm{T}}^{\mathrm{cone20}}(W^+)$	0.98 ± 0.04	1.53 ± 0.06	2.57 ± 0.06
$p_{\mathrm{T}}^{\mathrm{cone40}} - p_{\mathrm{T}}^{\mathrm{cone20}}(W^+)$	1.03 ± 0.04	1.54 ± 0.06	2.57 ± 0.05
$p_{\mathrm{T}}^{\mathrm{cone30}} - p_{\mathrm{T}}^{\mathrm{cone20}}(W^-)$	1.63 ± 0.05	2.51 ± 0.08	3.98 ± 0.07
$p_{\mathrm{T}}^{\mathrm{cone40}} - p_{\mathrm{T}}^{\mathrm{cone20}}(W^-)$	1.87 ± 0.05	2.64 ± 0.08	4.18 ± 0.07

TABLE B.17: Multijet background fraction before jet shape extrapolation for W, W^+ and W^-.

Multijet Fraction (%)	$2.5 < \langle\mu\rangle < 6.5$	$6.5 < \langle\mu\rangle < 9.5$	$9.5 < \langle\mu\rangle < 16$
$p_{\mathrm{T}}^{\mathrm{cone30}} - p_{\mathrm{T}}^{\mathrm{cone20}}(W)$	1.22 ± 0.03	1.75 ± 0.05	3.43 ± 0.05
$p_{\mathrm{T}}^{\mathrm{cone40}} - p_{\mathrm{T}}^{\mathrm{cone20}}(W)$	1.33 ± 0.03	1.81 ± 0.05	3.28 ± 0.04
$p_{\mathrm{T}}^{\mathrm{cone30}} - p_{\mathrm{T}}^{\mathrm{cone20}}(W^+)$	0.95 ± 0.04	1.38 ± 0.06	2.62 ± 0.06
$p_{\mathrm{T}}^{\mathrm{cone40}} - p_{\mathrm{T}}^{\mathrm{cone20}}(W^+)$	1.0 ± 0.04	1.33 ± 0.06	2.5 ± 0.06
$p_{\mathrm{T}}^{\mathrm{cone30}} - p_{\mathrm{T}}^{\mathrm{cone20}}(W^-)$	1.57 ± 0.05	2.38 ± 0.08	3.87 ± 0.07
$p_{\mathrm{T}}^{\mathrm{cone40}} - p_{\mathrm{T}}^{\mathrm{cone20}}(W^-)$	1.73 ± 0.05	2.24 ± 0.07	3.94 ± 0.07

TABLE B.18: Multijet background fraction after jet shape extrapolation for W, W^+ and W^-.

Multijet Fraction (W)	$2.5 < \langle\mu\rangle < 6.5$	$6.5 < \langle\mu\rangle < 9.5$	$9.5 < \langle\mu\rangle < 16$
	$p_{\mathrm{T}}^{\mathrm{cone30}} - p_{\mathrm{T}}^{\mathrm{cone20}}$		
$0.0 < \lvert\eta\rvert < 0.6$	1.0 ± 0.05	1.55 ± 0.07	2.4 ± 0.06
$0.6 < \lvert\eta\rvert < 1.2$	1.01 ± 0.05	1.61 ± 0.08	2.68 ± 0.07
$1.8 < \lvert\eta\rvert < 2.4$	1.67 ± 0.07	2.63 ± 0.12	4.39 ± 0.11
	$p_{\mathrm{T}}^{\mathrm{cone40}} - p_{\mathrm{T}}^{\mathrm{cone20}}$		
$0.0 < \lvert\eta\rvert < 0.6$	1.06 ± 0.05	1.45 ± 0.07	2.33 ± 0.06
$0.6 < \lvert\eta\rvert < 1.2$	1.11 ± 0.05	1.82 ± 0.08	2.95 ± 0.07
$1.8 < \lvert\eta\rvert < 2.4$	1.93 ± 0.07	2.84 ± 0.11	4.56 ± 0.1

TABLE B.19: Multijet background fraction before jet shape extrapolation for W, in pseudo-rapidity bins.

Multijet Fraction (W^+)	$2.5 < \langle\mu\rangle < 6.5$	$6.5 < \langle\mu\rangle < 9.5$	$9.5 < \langle\mu\rangle < 16$
	$p_{\mathrm{T}}^{\mathrm{cone30}} - p_{\mathrm{T}}^{\mathrm{cone20}}$		
$0.0 < \lvert\eta\rvert < 0.6$	0.74 ± 0.06	1.17 ± 0.09	1.91 ± 0.08
$0.6 < \lvert\eta\rvert < 1.2$	0.8 ± 0.06	1.26 ± 0.09	2.05 ± 0.08
$1.8 < \lvert\eta\rvert < 2.4$	1.29 ± 0.08	2.11 ± 0.14	3.35 ± 0.12
	$p_{\mathrm{T}}^{\mathrm{cone40}} - p_{\mathrm{T}}^{\mathrm{cone20}}$		
$0.0 < \lvert\eta\rvert < 0.6$	0.72 ± 0.06	1.0 ± 0.09	1.86 ± 0.08
$0.6 < \lvert\eta\rvert < 1.2$	0.8 ± 0.06	1.35 ± 0.1	2.31 ± 0.09
$1.8 < \lvert\eta\rvert < 2.4$	1.51 ± 0.08	2.3 ± 0.14	3.45 ± 0.12

TABLE B.20: Multijet background fraction before jet shape extrapolation for W^+, in pseudo-rapidity bins.

Multijet Fraction (W^-)	$2.5 < \langle\mu\rangle < 6.5$	$6.5 < \langle\mu\rangle < 9.5$	$9.5 < \langle\mu\rangle < 16$
	$p_{\mathrm{T}}^{\mathrm{cone30}} - p_{\mathrm{T}}^{\mathrm{cone20}}$		
$0.0 < \lvert\eta\rvert < 0.6$	1.36 ± 0.07	1.89 ± 0.11	2.79 ± 0.1
$0.6 < \lvert\eta\rvert < 1.2$	1.28 ± 0.08	1.99 ± 0.13	3.42 ± 0.11
$1.8 < \lvert\eta\rvert < 2.4$	2.29 ± 0.11	3.26 ± 0.2	5.91 ± 0.2
	$p_{\mathrm{T}}^{\mathrm{cone40}} - p_{\mathrm{T}}^{\mathrm{cone20}}$		
$0.0 < \lvert\eta\rvert < 0.6$	1.49 ± 0.08	1.81 ± 0.11	2.72 ± 0.09
$0.6 < \lvert\eta\rvert < 1.2$	1.55 ± 0.08	2.3 ± 0.12	3.6 ± 0.1
$1.8 < \lvert\eta\rvert < 2.4$	2.56 ± 0.11	3.43 ± 0.19	6.04 ± 0.18

TABLE B.21: Multijet background fraction before jet shape extrapolation for W^-, in pseudo-rapidity bins.

Multijet Fraction (W)	$2.5 < \langle\mu\rangle < 6.5$	$6.5 < \langle\mu\rangle < 9.5$	$9.5 < \langle\mu\rangle < 16$
	$p_{\mathrm{T}}^{\mathrm{cone30}} - p_{\mathrm{T}}^{\mathrm{cone20}}$		
$0.0 < \lvert\eta\rvert < 0.6$	0.93 ± 0.04	1.16 ± 0.06	2.23 ± 0.06
$0.6 < \lvert\eta\rvert < 1.2$	0.87 ± 0.04	1.48 ± 0.08	2.57 ± 0.07
$1.8 < \lvert\eta\rvert < 2.4$	1.97 ± 0.08	2.62 ± 0.13	5.17 ± 0.13
	$p_{\mathrm{T}}^{\mathrm{cone40}} - p_{\mathrm{T}}^{\mathrm{cone20}}$		
$0.0 < \lvert\eta\rvert < 0.6$	0.98 ± 0.05	1.06 ± 0.06	2.2 ± 0.06
$0.6 < \lvert\eta\rvert < 1.2$	0.97 ± 0.05	1.61 ± 0.07	2.73 ± 0.07
$1.8 < \lvert\eta\rvert < 2.4$	2.08 ± 0.07	2.66 ± 0.12	4.69 ± 0.11

TABLE B.22: Multijet background fraction after jet shape extrapolation for W, in pseudo-rapidity bins.

Multijet Fraction (W^+)	$2.5 < \langle\mu\rangle < 6.5$	$6.5 < \langle\mu\rangle < 9.5$	$9.5 < \langle\mu\rangle < 16$
	$p_{\mathrm{T}}^{\mathrm{cone30}} - p_{\mathrm{T}}^{\mathrm{cone20}}$		
$0.0 < \|\eta\| < 0.6$	0.64 ± 0.05	0.8 ± 0.08	1.3 ± 0.07
$0.6 < \|\eta\| < 1.2$	0.7 ± 0.06	1.18 ± 0.09	1.32 ± 0.07
$1.8 < \|\eta\| < 2.4$	1.38 ± 0.09	1.84 ± 0.15	3.71 ± 0.15
	$p_{\mathrm{T}}^{\mathrm{cone40}} - p_{\mathrm{T}}^{\mathrm{cone20}}$		
$0.0 < \|\eta\| < 0.6$	0.65 ± 0.06	0.62 ± 0.08	1.03 ± 0.06
$0.6 < \|\eta\| < 1.2$	0.7 ± 0.06	0.97 ± 0.09	1.87 ± 0.08
$1.8 < \|\eta\| < 2.4$	1.52 ± 0.09	2.23 ± 0.15	3.4 ± 0.13

TABLE B.23: Multijet background fraction after jet shape extrapolation for W^+, in pseudo-rapidity bins.

Multijet Fraction (W^-)	$2.5 < \langle\mu\rangle < 6.5$	$6.5 < \langle\mu\rangle < 9.5$	$9.5 < \langle\mu\rangle < 16$
	$p_{\mathrm{T}}^{\mathrm{cone30}} - p_{\mathrm{T}}^{\mathrm{cone20}}$		
$0.0 < \|\eta\| < 0.6$	1.26 ± 0.07	1.43 ± 0.09	2.47 ± 0.09
$0.6 < \|\eta\| < 1.2$	1.11 ± 0.07	1.82 ± 0.13	3.15 ± 0.11
$1.8 < \|\eta\| < 2.4$	2.44 ± 0.13	2.97 ± 0.2	6.77 ± 0.24
	$p_{\mathrm{T}}^{\mathrm{cone40}} - p_{\mathrm{T}}^{\mathrm{cone20}}$		
$0.0 < \|\eta\| < 0.6$	1.42 ± 0.08	1.39 ± 0.09	2.66 ± 0.09
$0.6 < \|\eta\| < 1.2$	1.39 ± 0.08	2.11 ± 0.13	3.77 ± 0.11
$1.8 < \|\eta\| < 2.4$	2.54 ± 0.12	2.77 ± 0.19	5.77 ± 0.19

TABLE B.24: Multijet background fraction after jet shape extrapolation for W^-, in pseudo-rapidity bins.

Number of jet events	$2.5 < \langle\mu\rangle < 6.5$	$6.5 < \langle\mu\rangle < 9.5$	$9.5 < \langle\mu\rangle < 16$
$p_{\mathrm{T}}^{\mathrm{cone30}} - p_{\mathrm{T}}^{\mathrm{cone20}}(W)$	24784	20965	57170
$p_{\mathrm{T}}^{\mathrm{cone40}} - p_{\mathrm{T}}^{\mathrm{cone20}}(W)$	27772	21700	58873
$p_{\mathrm{T}}^{\mathrm{cone30}} - p_{\mathrm{T}}^{\mathrm{cone20}}(W^+)$	11348	9322	26445
$p_{\mathrm{T}}^{\mathrm{cone40}} - p_{\mathrm{T}}^{\mathrm{cone20}}(W^+)$	11964	9430	26494
$p_{\mathrm{T}}^{\mathrm{cone30}} - p_{\mathrm{T}}^{\mathrm{cone20}}(W^-)$	13747	11228	30230
$p_{\mathrm{T}}^{\mathrm{cone40}} - p_{\mathrm{T}}^{\mathrm{cone20}}(W^-)$	15734	11780	31714

TABLE B.25: Average number of jets before jet shape extrapolation for W, W^+ and W^-.

Number of jet events	$2.5 < \langle\mu\rangle < 6.5$	$6.5 < \langle\mu\rangle < 9.5$	$9.5 < \langle\mu\rangle < 16$
$p_{\mathrm{T}}^{\mathrm{cone30}} - p_{\mathrm{T}}^{\mathrm{cone20}}(W)$	24422	18551	61443
$p_{\mathrm{T}}^{\mathrm{cone40}} - p_{\mathrm{T}}^{\mathrm{cone20}}(W)$	26554	19152	58659
$p_{\mathrm{T}}^{\mathrm{cone30}} - p_{\mathrm{T}}^{\mathrm{cone20}}(W^+)$	11055	8402	27027
$p_{\mathrm{T}}^{\mathrm{cone40}} - p_{\mathrm{T}}^{\mathrm{cone20}}(W^+)$	11569	8119	25749
$p_{\mathrm{T}}^{\mathrm{cone30}} - p_{\mathrm{T}}^{\mathrm{cone20}}(W^-)$	13199	10648	29413
$p_{\mathrm{T}}^{\mathrm{cone40}} - p_{\mathrm{T}}^{\mathrm{cone20}}(W^-)$	14597	9995	29892

TABLE B.26: Average number of jets after jet shape extrapolation for W, W^+ and W^-.

Number of jet events (W)	$2.5 < \langle\mu\rangle < 6.5$	$6.5 < \langle\mu\rangle < 9.5$	$9.5 < \langle\mu\rangle < 16$
	$p_{\mathrm{T}}^{\mathrm{cone30}} - p_{\mathrm{T}}^{\mathrm{cone20}}$		
$0.0 < \lvert\eta\rvert < 0.6$	7417	6120	15974
$0.6 < \lvert\eta\rvert < 1.2$	7089	6046	17087
$1.8 < \lvert\eta\rvert < 2.4$	9041	7343	20719
	$p_{\mathrm{T}}^{\mathrm{cone40}} - p_{\mathrm{T}}^{\mathrm{cone20}}$		
$0.0 < \lvert\eta\rvert < 0.6$	7828	5717	15542
$0.6 < \lvert\eta\rvert < 1.2$	7817	6828	18816
$1.8 < \lvert\eta\rvert < 2.4$	10488	7943	21547

TABLE B.27: Average number of jets before jet shape extrapolation for W, in pseudo-rapidity bins.

Number of jet events (W^+)	$2.5 < \langle\mu\rangle < 6.5$	$6.5 < \langle\mu\rangle < 9.5$	$9.5 < \langle\mu\rangle < 16$
	$p_{\mathrm{T}}^{\mathrm{cone30}} - p_{\mathrm{T}}^{\mathrm{cone20}}$		
$0.0 < \lvert\eta\rvert < 0.6$	3077	2593	7113
$0.6 < \lvert\eta\rvert < 1.2$	3232	2702	7457
$1.8 < \lvert\eta\rvert < 2.4$	4278	3599	9604
	$p_{\mathrm{T}}^{\mathrm{cone40}} - p_{\mathrm{T}}^{\mathrm{cone20}}$		
$0.0 < \lvert\eta\rvert < 0.6$	2993	2208	6925
$0.6 < \lvert\eta\rvert < 1.2$	3222	2888	8372
$1.8 < \lvert\eta\rvert < 2.4$	5019	3927	9879

TABLE B.28: Average number of jets before jet shape extrapolation for W^+, in pseudo-rapidity bins.

Number of jet events (W^-)	$2.5 < \langle\mu\rangle < 6.5$	$6.5 < \langle\mu\rangle < 9.5$	$9.5 < \langle\mu\rangle < 16$
	$p_{\mathrm{T}}^{\mathrm{cone30}} - p_{\mathrm{T}}^{\mathrm{cone20}}$		
$0.0 < \lvert\eta\rvert < 0.6$	4402	3270	8195
$0.6 < \lvert\eta\rvert < 1.2$	3869	3205	9395
$1.8 < \lvert\eta\rvert < 2.4$	4808	3556	10953
	$p_{\mathrm{T}}^{\mathrm{cone40}} - p_{\mathrm{T}}^{\mathrm{cone20}}$		
$0.0 < \lvert\eta\rvert < 0.6$	4836	3123	7998
$0.6 < \lvert\eta\rvert < 1.2$	4664	3707	9907
$1.8 < \lvert\eta\rvert < 2.4$	5370	3738	11195

TABLE B.29: Average number of jets before jet shape extrapolation for W^-, in pseudo-rapidity bins.

Number of jet events (W)	$2.5 < \langle\mu\rangle < 6.5$	$6.5 < \langle\mu\rangle < 9.5$	$9.5 < \langle\mu\rangle < 16$
	$p_{\mathrm{T}}^{\mathrm{cone30}} - p_{\mathrm{T}}^{\mathrm{cone20}}$		
$0.0 < \lvert\eta\rvert < 0.6$	6866	4555	14844
$0.6 < \lvert\eta\rvert < 1.2$	6140	5565	16396
$1.8 < \lvert\eta\rvert < 2.4$	10679	7328	24422
	$p_{\mathrm{T}}^{\mathrm{cone40}} - p_{\mathrm{T}}^{\mathrm{cone20}}$		
$0.0 < \lvert\eta\rvert < 0.6$	7239	4164	14702
$0.6 < \lvert\eta\rvert < 1.2$	6838	6036	17402
$1.8 < \lvert\eta\rvert < 2.4$	11307	7434	22124

TABLE B.30: Average number of jets after jet shape extrapolation for W, in pseudo-rapidity bins.

Number of jet events (W^+)	$2.5 < \langle\mu\rangle < 6.5$	$6.5 < \langle\mu\rangle < 9.5$	$9.5 < \langle\mu\rangle < 16$
	$p_{\mathrm{T}}^{\mathrm{cone30}} - p_{\mathrm{T}}^{\mathrm{cone20}}$		
$0.0 < \lvert\eta\rvert < 0.6$	2634	1775	4864
$0.6 < \lvert\eta\rvert < 1.2$	2796	2522	4775
$1.8 < \lvert\eta\rvert < 2.4$	4583	3132	10643
	$p_{\mathrm{T}}^{\mathrm{cone40}} - p_{\mathrm{T}}^{\mathrm{cone20}}$		
$0.0 < \lvert\eta\rvert < 0.6$	2675	1359	3846
$0.6 < \lvert\eta\rvert < 1.2$	2812	2087	6782
$1.8 < \lvert\eta\rvert < 2.4$	5053	3810	9734

TABLE B.31: Average number of jets after jet shape extrapolation for W^+, in pseudo-rapidity bins.

Number of jet events (W^-)	$2.5 < \langle\mu\rangle < 6.5$	$6.5 < \langle\mu\rangle < 9.5$	$9.5 < \langle\mu\rangle < 16$
	$p_{\mathrm{T}}^{\mathrm{cone30}} - p_{\mathrm{T}}^{\mathrm{cone20}}$		
$0.0 < \lvert\eta\rvert < 0.6$	4079	2477	7257
$0.6 < \lvert\eta\rvert < 1.2$	3344	2945	8653
$1.8 < \lvert\eta\rvert < 2.4$	5133	3241	12558
	$p_{\mathrm{T}}^{\mathrm{cone40}} - p_{\mathrm{T}}^{\mathrm{cone20}}$		
$0.0 < \lvert\eta\rvert < 0.6$	4600	2412	7826
$0.6 < \lvert\eta\rvert < 1.2$	4200	3401	10368
$1.8 < \lvert\eta\rvert < 2.4$	5346	3022	10705

TABLE B.32: Average number of jets after jet shape extrapolation for W^-, in pseudo-rapidity bins.

Appendix C

Mass biases in pseudorapidity bins

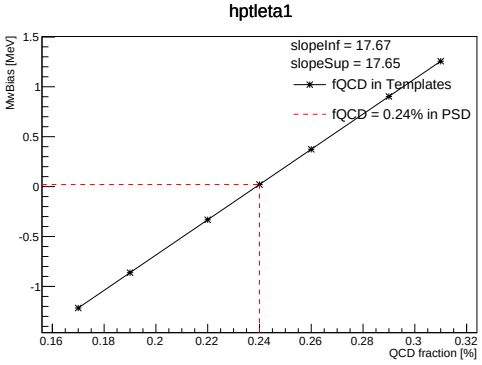

(a) $30 < p_{\mathrm{T}}^{\ell} < 50$ GeV

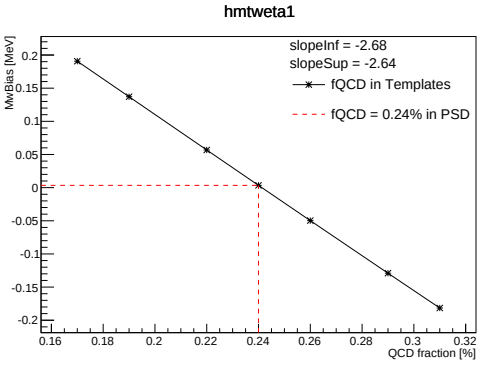

(b) $65 < m_{\mathrm{T}}^{W} < 100$ GeV

FIGURE C.1: $2.5 < \langle\mu\rangle < 6.5$ - $0.0 < |\eta| < 0.6$.

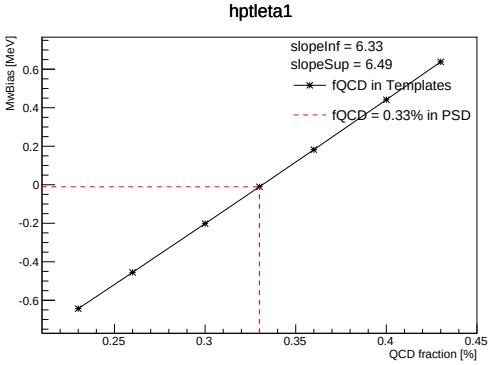

(a) $30 < p_{\mathrm{T}}^{\ell} < 50$ GeV

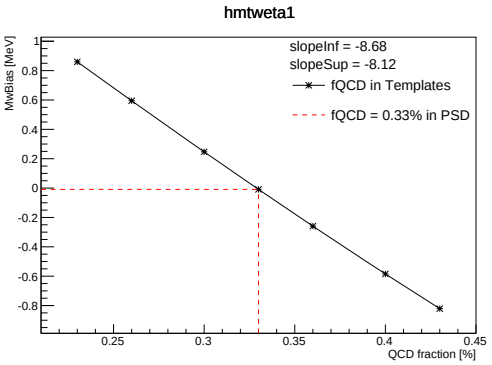

(b) $65 < m_{\mathrm{T}}^{W} < 100$ GeV

FIGURE C.2: $6.5 < \langle\mu\rangle < 9.5$ - $0.0 < |\eta| < 0.6$.

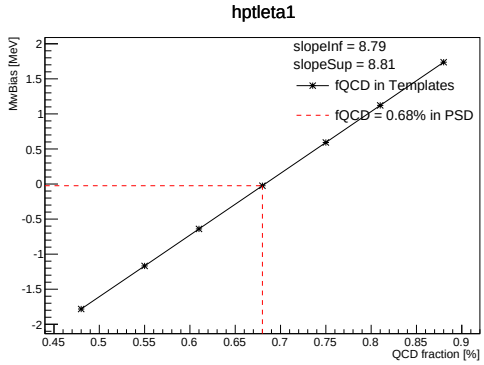

(a) $30 < p_{\mathrm{T}}^{\ell} < 50$ GeV

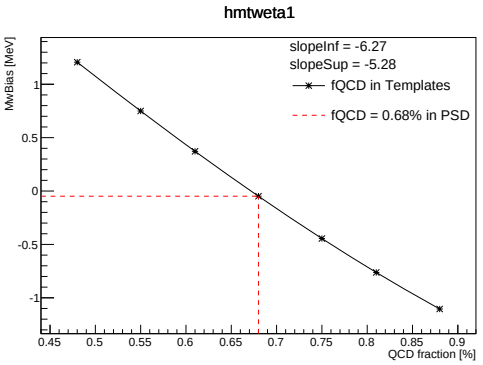

(b) $65 < m_{\mathrm{T}}^{W} < 100$ GeV

FIGURE C.3: $9.5 < \langle\mu\rangle < 16$ - $0.0 < |\eta| < 0.6$.

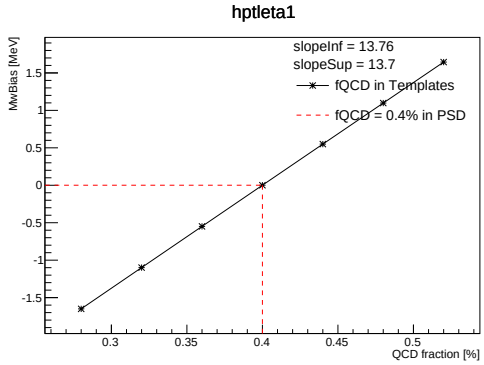

(a) $30 < p_{\mathrm{T}}^{\ell} < 50$ GeV

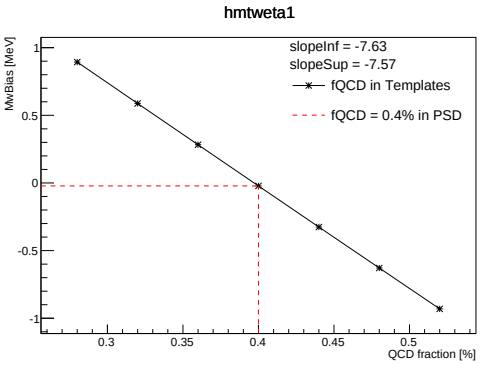

(b) $65 < m_{\mathrm{T}}^{W} < 100$ GeV

FIGURE C.4: $\langle\mu\rangle$-inclusive - $0.0 < |\eta| < 0.6$.

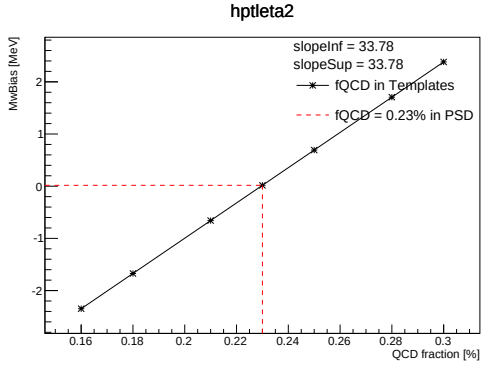

(a) $30 < p_{\mathrm{T}}^{\ell} < 50$ GeV

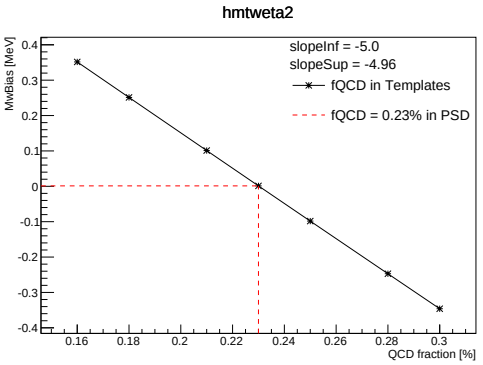

(b) $65 < m_{\mathrm{T}}^{W} < 100$ GeV

FIGURE C.5: $2.5 < \langle\mu\rangle < 6.5$ - $0.6 < |\eta| < 1.2$.

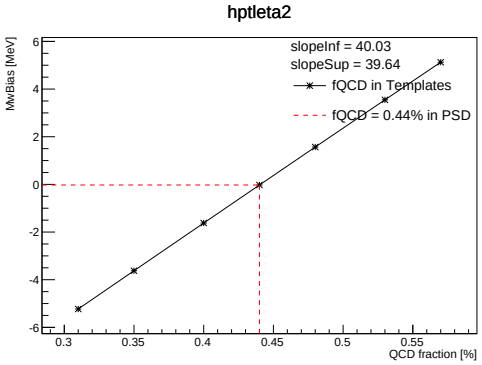

(a) $30 < p_{\mathrm{T}}^{\ell} < 50$ GeV

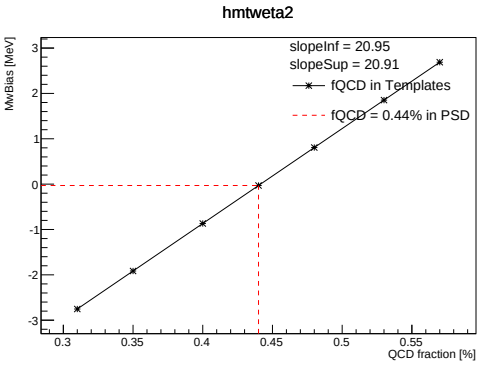

(b) $65 < m_{\mathrm{T}}^{W} < 100$ GeV

FIGURE C.6: $6.5 < \langle\mu\rangle < 9.5$ - $0.6 < |\eta| < 1.2$.

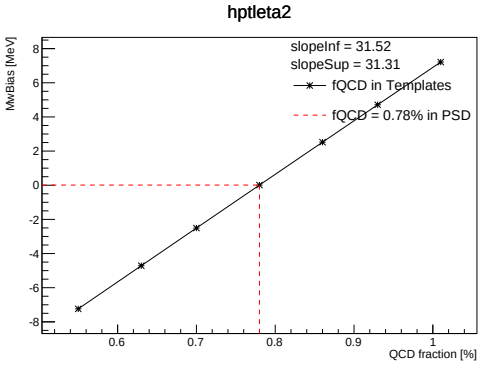

(a) $30 < p_{\mathrm{T}}^{\ell} < 50$ GeV

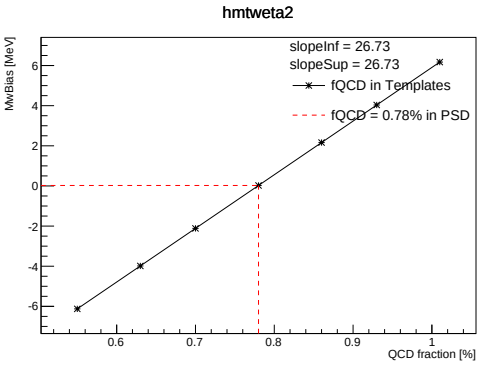

(b) $65 < m_{\mathrm{T}}^{W} < 100$ GeV

FIGURE C.7: $9.5 < \langle\mu\rangle < 16$ - $0.6 < |\eta| < 1.2$.

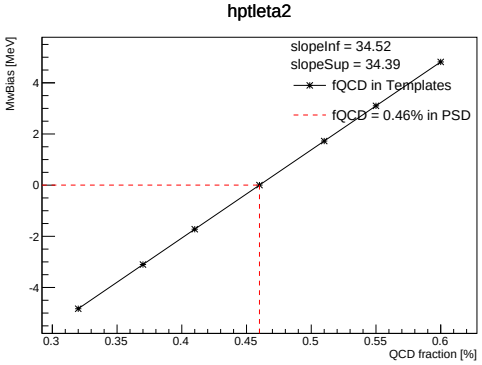

(a) $30 < p_{\mathrm{T}}^{\ell} < 50$ GeV

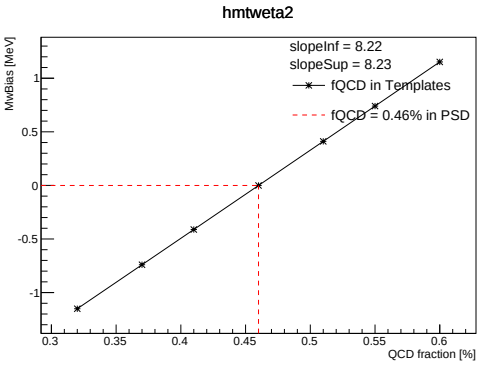

(b) $65 < m_{\mathrm{T}}^{W} < 100$ GeV

FIGURE C.8: $\langle\mu\rangle$-inclusive - $0.6 < |\eta| < 1.2$.

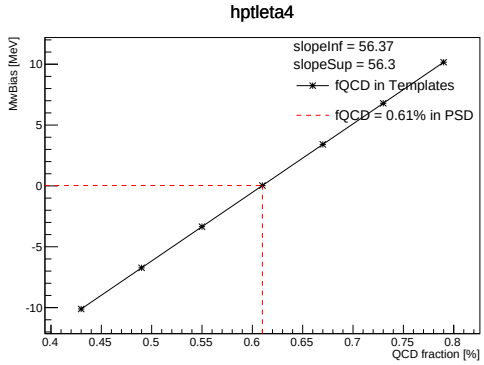

(a) $30 < p_{\mathrm{T}}^{\ell} < 50$ GeV

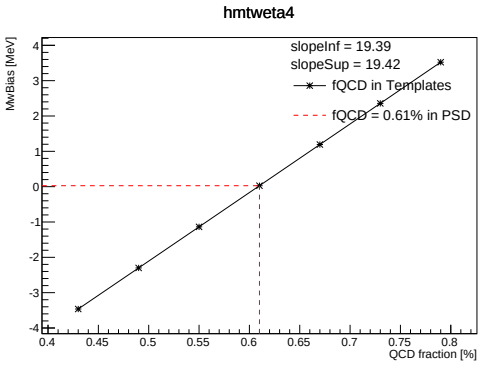

(b) $65 < m_{\mathrm{T}}^{W} < 100$ GeV

FIGURE C.9: $2.5 < \langle\mu\rangle < 6.5$ - $1.8 < |\eta| < 2.4$.

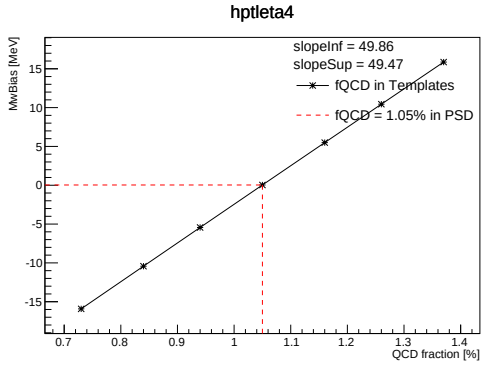

(a) $30 < p_{\mathrm{T}}^{\ell} < 50$ GeV

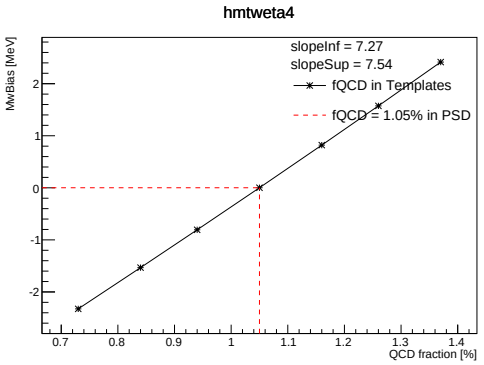

(b) $65 < m_{\mathrm{T}}^{W} < 100$ GeV

FIGURE C.10: $6.5 < \langle\mu\rangle < 9.5$ - $1.8 < |\eta| < 2.4$.

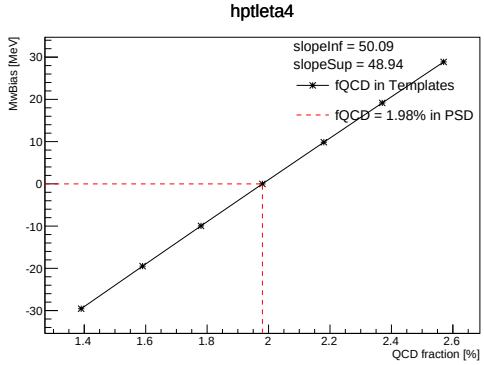

(a) $30 < p_{\mathrm{T}}^{\ell} < 50$ GeV

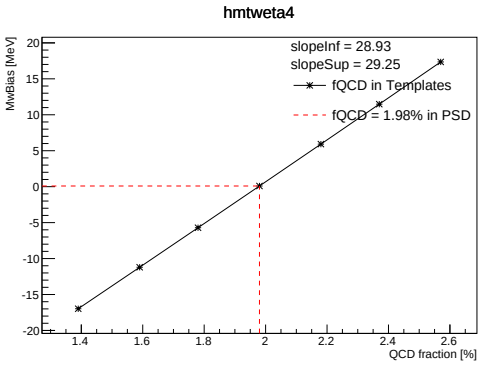

(b) $65 < m_{\mathrm{T}}^{W} < 100$ GeV

FIGURE C.11: $9.5 < \langle\mu\rangle < 16$ - $1.8 < |\eta| < 2.4$.

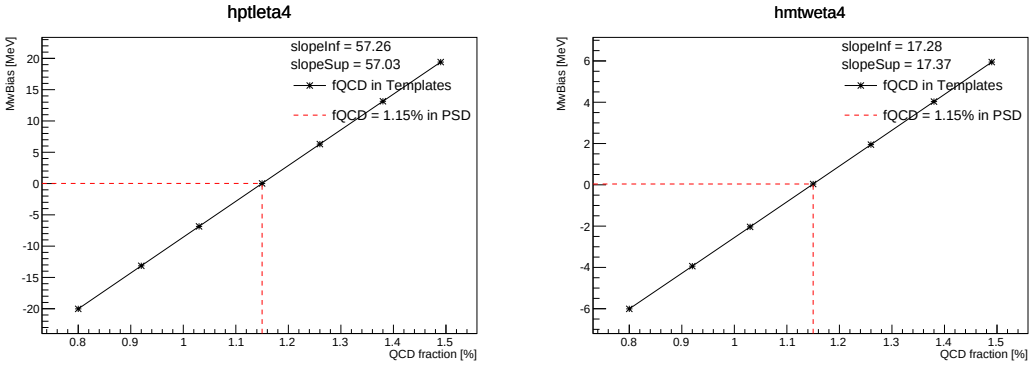

(a) $30 < p_{\mathrm{T}}^{\ell} < 50$ GeV

(b) $65 < m_{\mathrm{T}}^{W} < 100$ GeV

FIGURE C.12: $\langle\mu\rangle$-inclusive - $1.8 < |\eta| < 2.4$.

Appendix D

Control Plots in pseudorapidity bins

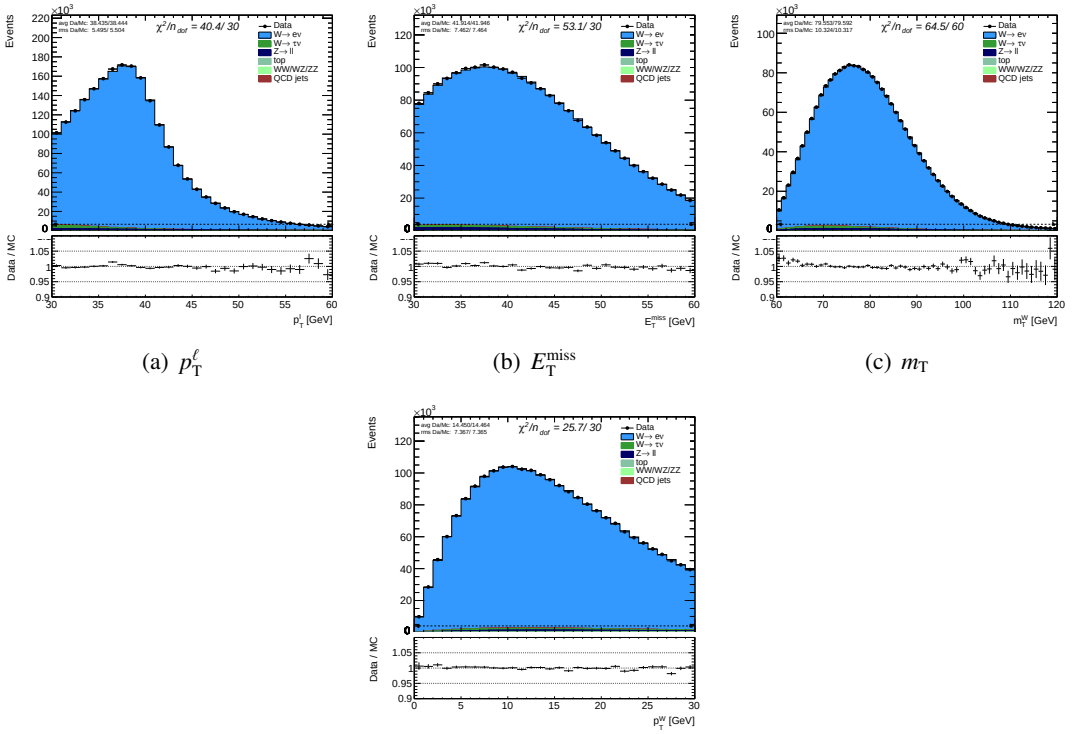

(a) p_{T}^{ℓ} (b) $E_{\mathrm{T}}^{\mathrm{miss}}$ (c) m_{T}

(d) p_{T}^{W}

FIGURE D.1: $\langle\mu\rangle$-inclusive - $W^{\pm}$ - $0.0 < |\eta| < 0.6$

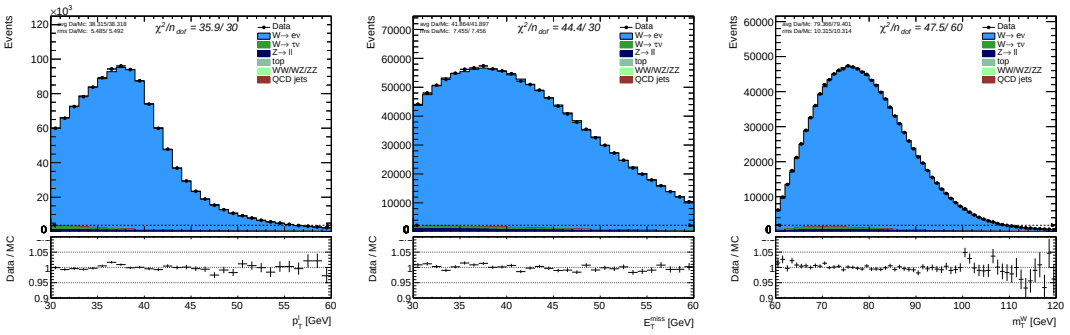

(a) p_{T}^{ℓ} (b) $E_{\mathrm{T}}^{\mathrm{miss}}$ (c) m_{T}

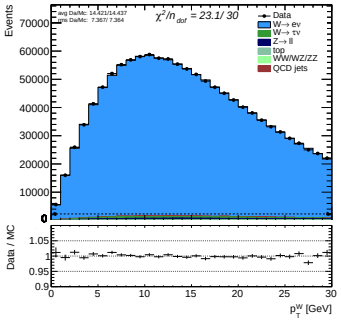

(d) p_{T}^{W}

FIGURE D.2: $\langle\mu\rangle$-inclusive - W^+ - $0.0 < |\eta| < 0.6$

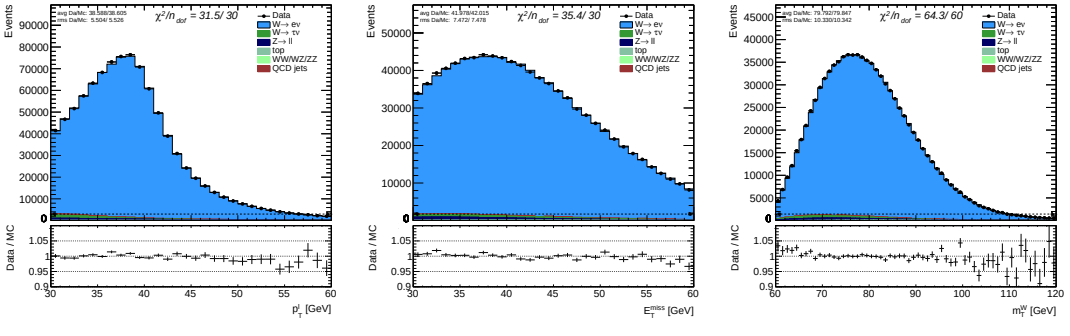

(a) p_{T}^{ℓ} (b) $E_{\mathrm{T}}^{\mathrm{miss}}$ (c) m_{T}

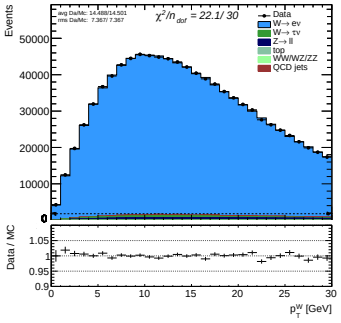

(d) p_{T}^{W}

FIGURE D.3: $\langle\mu\rangle$-inclusive - W^- - $0.0 < |\eta| < 0.6$

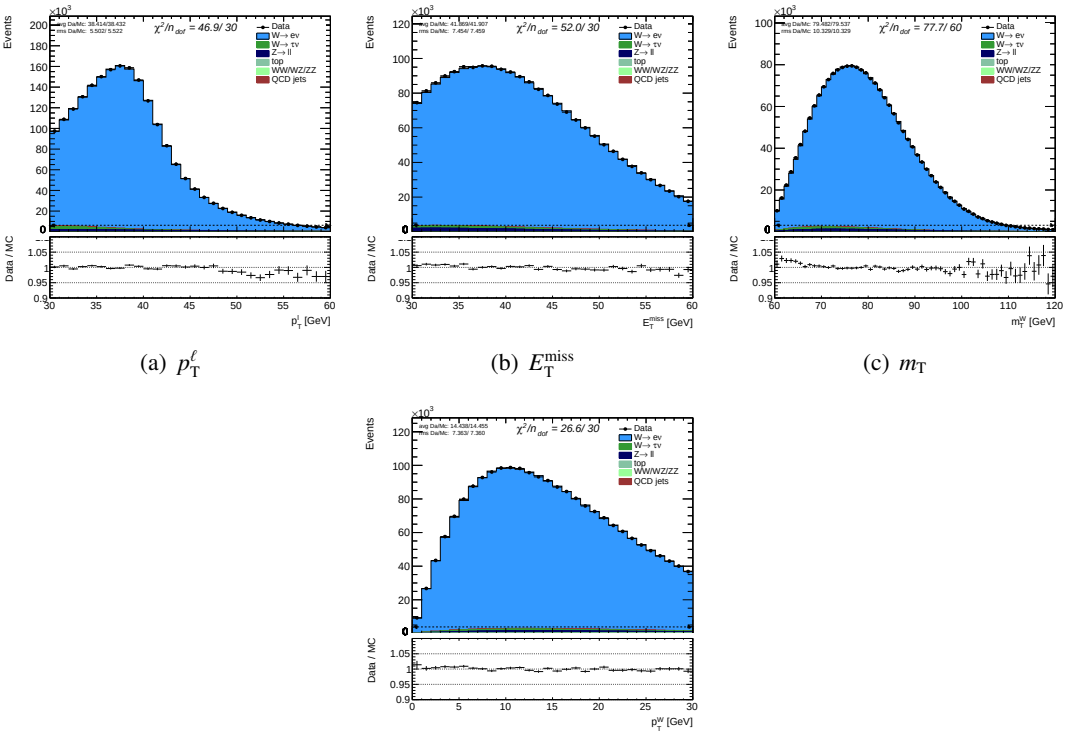

(a) p_{T}^{ℓ} (b) $E_{\mathrm{T}}^{\mathrm{miss}}$ (c) m_{T}

(d) p_{T}^{W}

FIGURE D.4: $\langle\mu\rangle$-inclusive - $W^{\pm}$ - $0.6 < |\eta| < 1.2$

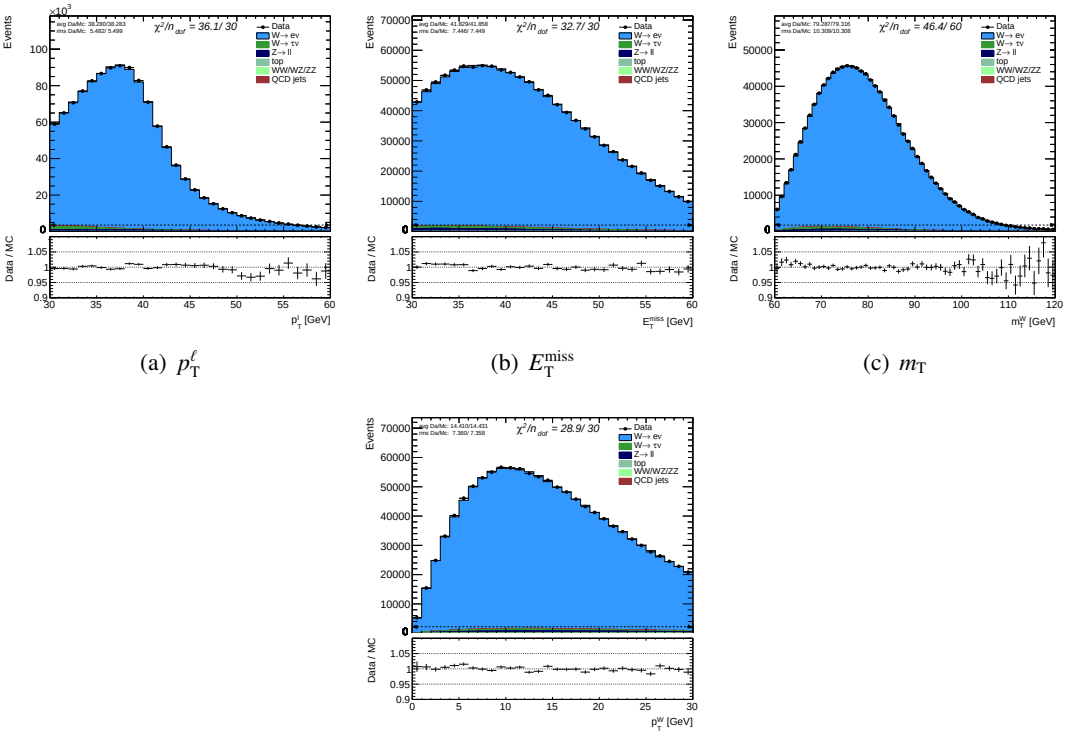

(a) p_{T}^{ℓ} (b) $E_{\mathrm{T}}^{\mathrm{miss}}$ (c) m_{T}

(d) p_{T}^{W}

FIGURE D.5: $\langle\mu\rangle$-inclusive - W^{+} - $0.6 < |\eta| < 1.2$

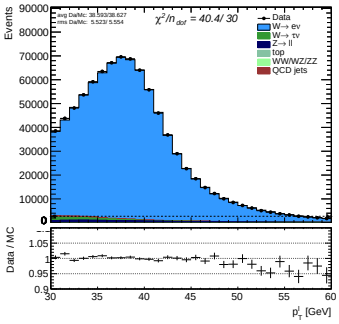

(a) p_{T}^{ℓ}

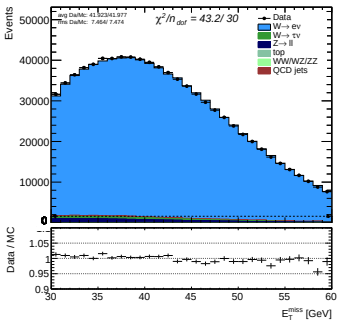

(b) $E_{\mathrm{T}}^{\mathrm{miss}}$

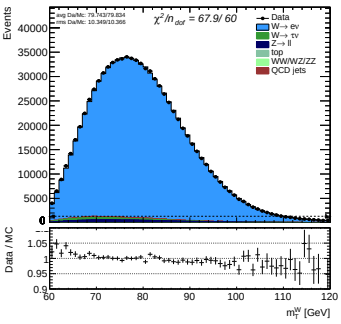

(c) m_{T}

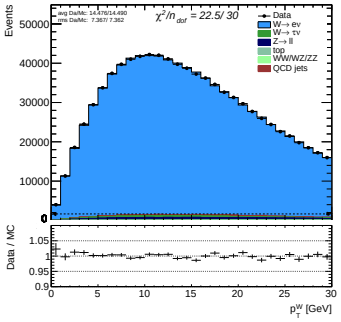

(d) p_{T}^{W}

FIGURE D.6: $\langle\mu\rangle$-inclusive - W^- - $0.6 < |\eta| < 1.2$

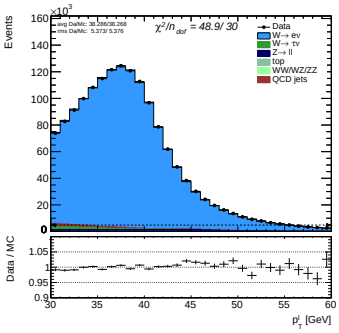

(a) p_{T}^{ℓ}

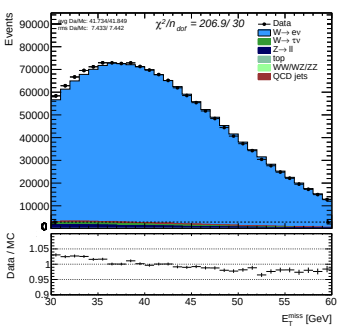

(b) $E_{\mathrm{T}}^{\mathrm{miss}}$

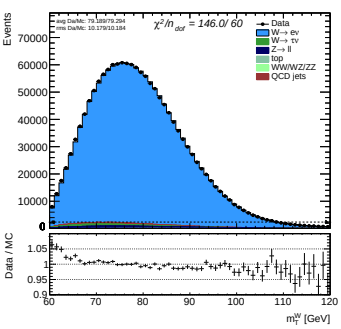

(c) m_{T}

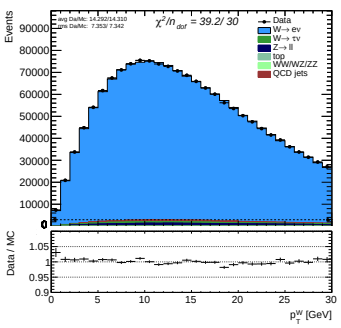

(d) p_{T}^{W}

FIGURE D.7: $\langle\mu\rangle$-inclusive - $W^{\pm}$ - $1.8 < |\eta| < 2.4$

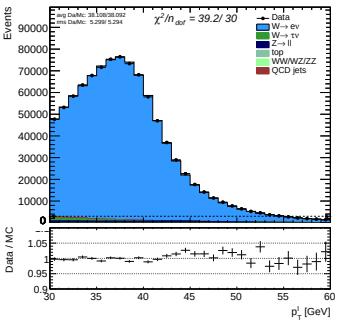

(a) p_{T}^{ℓ}

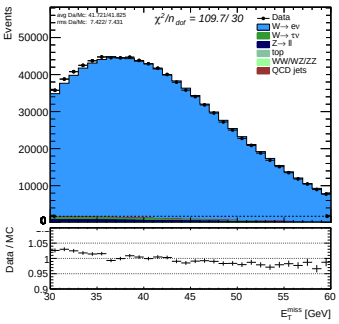

(b) $E_{\mathrm{T}}^{\mathrm{miss}}$

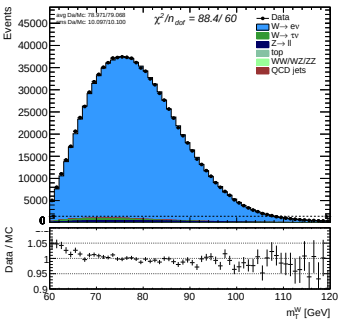

(c) m_{T}

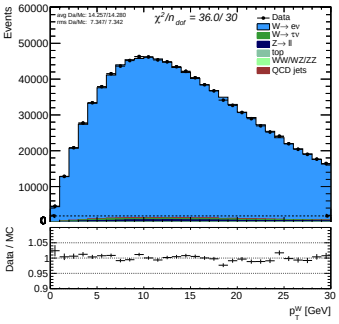

(d) p_{T}^{W}

FIGURE D.8: $\langle\mu\rangle$-inclusive - W^{+} - $1.8 < |\eta| < 2.4$

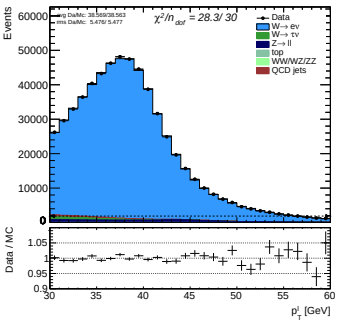

(a) p_{T}^{ℓ}

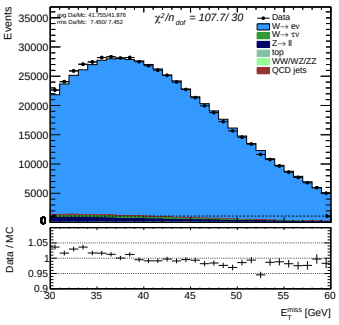

(b) $E_{\mathrm{T}}^{\mathrm{miss}}$

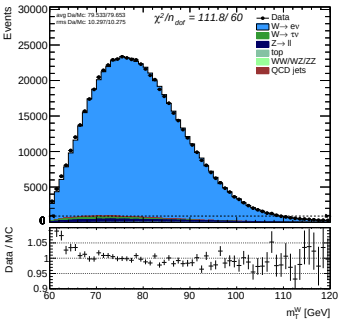

(c) m_{T}

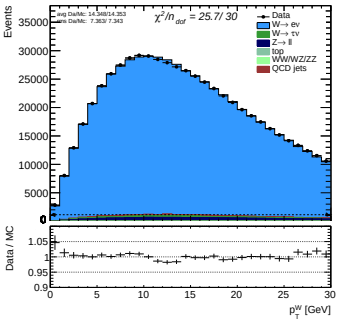

(d) p_{T}^{W}

FIGURE D.9: $\langle\mu\rangle$-inclusive - W^{-} - $1.8 < |\eta| < 2.4$

Bibliography

[1] C. N. Yang and R. L. Mills, *Conservation of Isotopic Spin and Isotopic Gauge Invariance*, Phys. Rev. **96** (1954) 191–195. http://link.aps.org/doi/10.1103/PhysRev.96.191. (Cited on pages 1 and 5.)

[2] M. Baker and S. L. Glashow, *Spontaneous Breakdown of Elementary Particle Symmetries*, Phys. Rev. **128** (1962) 2462–2471. http://link.aps.org/doi/10.1103/PhysRev.128.2462. (Not cited.)

[3] Y. Nambu, *Axial Vector Current Conservation in Weak Interactions*, Phys. Rev. Lett. **4** (1960) 380–382. http://link.aps.org/doi/10.1103/PhysRevLett.4.380. (Not cited.)

[4] J. Goldstone, A. Salam, and S. Weinberg, *Broken Symmetries*, Phys. Rev. **127** (1962) 965–970. http://link.aps.org/doi/10.1103/PhysRev.127.965. (Not cited.)

[5] F. Englert and R. Brout, *Broken Symmetry and the Mass of Gauge Vector Mesons*, Phys. Rev. Lett. **13** (1964) 321–323. http://link.aps.org/doi/10.1103/PhysRevLett.13.321. (Cited on pages 3 and 10.)

[6] P. W. Higgs, *Broken Symmetries and the Masses of Gauge Bosons*, Phys. Rev. Lett. **13** (1964) 508–509. http://link.aps.org/doi/10.1103/PhysRevLett.13.508. (Not cited.)

[7] P. W. Higgs, *Broken symmetries, massless particles and gauge fields*, Phys. Lett. **12** (1964) 132–133. (Cited on pages 3 and 10.)

[8] P. W. Higgs, *Spontaneous Symmetry Breakdown without Massless Bosons*, Phys. Rev. **145** (1966) 1156–1163. http://link.aps.org/doi/10.1103/PhysRev.145.1156. (Not cited.)

[9] G. S. Guralnik, C. R. Hagen, and T. W. B. Kibble, *Global Conservation Laws and Massless Particles*, Phys. Rev. Lett. **13** (1964) 585–587. http://link.aps.org/doi/10.1103/PhysRevLett.13.585. (Not cited.)

[10] T. W. B. Kibble, *Symmetry Breaking in Non-Abelian Gauge Theories*, Phys. Rev. **155** (1967) 1554–1561. http://link.aps.org/doi/10.1103/PhysRev.155.1554. (Not cited.)

[11] S. Weinberg, *A Model of Leptons*, Phys. Rev. Lett. **19** (1967) 1264–1266. http://link.aps.org/doi/10.1103/PhysRevLett.19.1264. (Cited on page 5.)

[12] A. Salam and J. C. Ward, *Electromagnetic and weak interactions*, Phys.Lett. **13** (1964) 168–171. (Not cited.)

[13] S. Glashow, *Partial Symmetries of Weak Interactions*, Nucl.Phys. **22** (1961) 579–588. (Cited on page 5.)

[14] A. Salam, *Weak and Electromagnetic Interactions*, Conf. Proc. **C680519** (1968) 367–377. (Not cited.)

[15] G. 'tHooft, *Renormalization of massless Yang-Mills fields*, Nuclear Physics B **33** no. 1, (1971) 173 – 199. http://www.sciencedirect.com/science/article/pii/0550321371903956. (Not cited.)

[16] G. 't Hooft and M. Veltman, *Regularization and Renormalization of Gauge Fields*, Nucl.Phys. **B44** (1972) 189–213. (Cited on pages 1 and 5.)

[17] P. Soding, B. Wiik, G. Wolf, and S. L. Wu, *The First evidence for three jet events in e+ e- collisions at PETRA: First direct observation of the gluon*, in *High-energy physics. Proceedings, International Europhysics Conference, HEP '95, Brussels, Belgium, July 27-August 2, 1995*. 1996. (Cited on page 1.)

[18] D. P. Barber, U. Becker, H. Benda, A. Boehm, J. G. Branson, J. Bron, D. Buikman, J. Burger, C. C. Chang, H. S. Chen, M. Chen, C. P. Cheng, Y. S. Chu, R. Clare, P. Duinker, G. Y. Fang, H. Fesefeldt, D. Fong, M. Fukushima, J. C. Guo, A. Hariri, G. Herten, M. C. Ho, H. K. Hsu, T. T. Hsu, R. W. Kadel, W. Krenz, J. Li, Q. Z. Li, M. Lu, D. Luckey, D. A. Ma, C. M. Ma, G. G. G. Massaro, T. Matsuda, H. Newman, J. Paradiso, F. P. Poschmann, J. P. Revol, M. Rohde, H. Rykaczewski, K. Sinram, H. W. Tang, L. G. Tang, S. C. C. Ting, K. L. Tung, F. Vannucci, X. R. Wang, P. S. Wei, M. White, G. H. Wu, T. W. Wu, J. P. Xi, P. C. Yang, X. H. Yu, N. L. Zhang, and R. Y. Zhu, *Discovery of Three-Jet Events and a Test of Quantum Chromodynamics at PETRA*, Phys. Rev. Lett. **43** (1979) 830–833. http://link.aps.org/doi/10.1103/PhysRevLett.43.830. (Cited on page 1.)

[19] G. A. et al., *Experimental observation of isolated large transverse energy electrons with associated missing energy at s=540 GeV*, Physics Letters B **122** no. 1, (1983) 103 – 116. http://www.sciencedirect.com/science/article/pii/0370269383911772. (Cited on page 1.)

[20] G. A. et al., *Experimental observation of lepton pairs of invariant mass around 95 GeV/c2 at the {CERN} {SPS} collider*, Physics Letters B **126** no. 5, (1983) 398 – 410. http://www.sciencedirect.com/science/article/pii/0370269383901880. (Cited on page 1.)

[21] DØ Collaboration, *Observation of the Top Quark*, Phys. Rev. Lett. **74** (1995) 2632–2637. http://link.aps.org/doi/10.1103/PhysRevLett.74.2632. (Cited on page 1.)

[22] CDF Collaboration, *Observation of Top Quark Production in $\overline{p}p$ Collisions with the Collider Detector at Fermilab*, Phys. Rev. Lett. **74** (1995) 2626–2631. http://link.aps.org/doi/10.1103/PhysRevLett.74.2626. (Cited on page 1.)

[23] ATLAS Collaboration, *Observation of a new particle in the search for the Standard Model Higgs boson with the ATLAS detector at the LHC*, Phys.Lett. **B716** (2012) 1–29, arXiv:1207.7214 [hep-ex]. (Cited on pages 1, 11, and 37.)

[24] CMS Collaboration, *Observation of a new boson at a mass of 125 GeV with the CMS experiment at the LHC*, Phys.Lett. **B716** (2012) 30–61, arXiv:1207.7235 [hep-ex]. (Cited on pages 1 and 11.)

[25] M. Gonzalez-Garcia and M. Maltoni, *Phenomenology with Massive Neutrinos*, Phys.Rept. **460** (2008) 1–129, arXiv:0704.1800 [hep-ph]. (Cited on page 1.)

[26] Super-Kamiokande Collaboration, Y. Fukuda et al., *Evidence for oscillation of atmospheric neutrinos*, Phys.Rev.Lett. **81** (1998) 1562–1567, arXiv:hep-ex/9807003 [hep-ex]. (Not cited.)

[27] Daya Bay Collaboration, F. An et al., *Observation of electron-antineutrino disappearance at Daya Bay*, Phys.Rev.Lett. **108** (2012) 171803, arXiv:1203.1669 [hep-ex]. (Not cited.)

[28] RENO Collaboration, J. Ahn et al., *Observation of Reactor Electron Antineutrino Disappearance in the RENO Experiment*, Phys.Rev.Lett. **108** (2012) 191802, arXiv:1204.0626 [hep-ex]. (Cited on page 1.)

[29] ALEPH, DELPHI, L3, OPAL, LEP Electroweak Collaboration, S. Schael et al., *Electroweak Measurements in Electron-Positron Collisions at W-Boson-Pair Energies at LEP*, Phys.Rept. **532** (2013) 119–244, arXiv:1302.3415 [hep-ex]. (Cited on pages 1, 11, and 13.)

[30] The CDF and DØ Collaborations, *Combination of CDF and D0 W-Boson Mass Measurements*, Phys.Rev. **D88** no. 5, (2013) 052018, arXiv:1307.7627 [hep-ex]. (Cited on pages 1, 11, 13, and 14.)

[31] Particle Data Group Collaboration, K. A. Olive et al., *Review of Particle Physics*, Chin. Phys. **C38** (2014) 090001. (Cited on pages 1, 8, 11, 14, and 97.)

[32] Gfitter Group Collaboration, M. Baak, J. Cúth, J. Haller, A. Hoecker, R. Kogler, K. Mönig, M. Schott, and J. Stelzer, *The global electroweak fit at NNLO and prospects for the LHC and ILC*, Eur. Phys. J. **C74** (2014) 3046, arXiv:1407.3792 [hep-ph]. (Cited on pages 1 and 12.)

[33] T. Sjostrand, S. Mrenna, and P. Z. Skands, *A Brief Introduction to PYTHIA 8.1*, Comput. Phys. Commun. **178** (2008) 852–867, arXiv:0710.3820 [hep-ph]. (Cited on pages 2, 57, 80, 93, 94, and 104.)

[34] A. Einstein, *Feldgleichungen der Gravitation, The Field Equations of Gravitation*, Königlich Preußische Akademie der Wissenschaften, Sitzungsberichte **part 2** (1915) 844–847. (Cited on page 3.)

[35] "The standard model of elementary particles (more schematic depiction), with the three generations of matter, gauge bosons in the fourth column, and the higgs boson in the fifth." https://en.wikipedia.org/?title=Standard_Model#/media/File:Standard_Model_of_Elementary_Particles.svg. Accessed: Feb 2015. (Cited on page 4.)

[36] M. Kobayashi and T. Maskawa, *CP Violation in the Renormalizable Theory of Weak Interaction*, Prog. Theor. Phys. **49** (1973) 652–657. (Cited on page 4.)

[37] N. Cabibbo, *Unitary Symmetry and Leptonic Decays*, Phys. Rev. Lett. **10** (1963) 531–533. http://link.aps.org/doi/10.1103/PhysRevLett.10.531. (Cited on page 4.)

[38] E. Noether, *Invariant Variation Problems*, Gott.Nachr. **1918** (1918) 235–257, arXiv:physics/0503066 [physics]. (Cited on page 5.)

[39] H. Weyl, *Elektron und Gravitation*, Zeit. für Physik **56** (1929) 330–352. (Cited on page 5.)

[40] D. J. Gross and F. Wilczek, *Ultraviolet Behavior of Non-Abelian Gauge Theories*, Phys. Rev. Lett. **30** (1973) 1343–1346. http://link.aps.org/doi/10.1103/PhysRevLett.30.1343. (Cited on page 5.)

[41] H. D. Politzer, *Reliable Perturbative Results for Strong Interactions?*, Phys. Rev. Lett. **30** (1973) 1346–1349. http://link.aps.org/doi/10.1103/PhysRevLett.30.1346. (Cited on pages 5 and 7.)

[42] C. Becchi, A. Rouet, and R. Stora, *Renormalization of Gauge Theories*, Annals Phys. **98** (1976) 287–321. (Cited on page 5.)

[43] T. H. V. Nguyen, *Mesure de la distribution de l'impulsion transverse des bosons W au LHC avec le détecteur ATLAS*. PhD thesis, Université Paris Diderot, 2011. (Cited on pages 7 and 10.)

[44] D. J. Gross and F. Wilczek, *Asymptotically Free Gauge Theories. I*, Phys. Rev. D **8** (1973) 3633–3652. http://link.aps.org/doi/10.1103/PhysRevD.8.3633. (Cited on page 7.)

[45] D. J. Gross and F. Wilczek, *Asymptotically free gauge theories. II*, Phys. Rev. D **9** (1974) 980–993. http://link.aps.org/doi/10.1103/PhysRevD.9.980. (Cited on page 7.)

[46] Q. Buat, *Recherche de nouveaux phénomènes dans les événements diphoton avec le détecteur ATLAS*. PhD thesis, Ecole doctorale de Physique - Grenoble, 2013. (Cited on page 9.)

[47] CDF Collaboration, T. Aaltonen et al., *Precise measurement of the W-boson mass with the CDF II detector*, Phys.Rev.Lett. **108** (2012) 151803, arXiv:1203.0275 [hep-ex]. (Cited on page 14.)

[48] D0 Collaboration, V. M. Abazov et al., *Measurement of the W Boson Mass with the D0 Detector*, Phys.Rev.Lett. **108** (2012) 151804, arXiv:1203.0293 [hep-ex]. (Cited on page 14.)

[49] D0 Collaboration, *Measurement of the W Boson Mass*, Phys. Rev. Lett. **103** (2009) 141801. http://link.aps.org/doi/10.1103/PhysRevLett.103.141801. (Cited on page 14.)

[50] G. Altarelli and G. Parisi, *Asymptotic Freedom in Parton Language*, Nucl.Phys. **B126** (1977) 298. (Cited on page 15.)

[51] J. Gao, M. Guzzi, J. Huston, H.-L. Lai, Z. Li, et al., *CT10 next-to-next-to-leading order global analysis of QCD*, Phys.Rev. **D89** no. 3, (2014) 033009, arXiv:1302.6246 [hep-ph]. (Cited on pages 15, 16, 94, and 104.)

[52] M. Krasny, F. Dydak, F. Fayette, W. Placzek, and A. Siodmok, $\Delta M_W \leq 10 MeV/c^2$ *at the LHC: a forlorn hope?*, Eur.Phys.J. **C69** (2010) 379–397, arXiv:1004.2597 [hep-ex]. (Cited on pages 16, 23, and 88.)

[53] J. M. Campbell, J. Huston, and W. Stirling, *Hard Interactions of Quarks and Gluons: A Primer for LHC Physics*, Rept.Prog.Phys. **70** (2007) 89, arXiv:hep-ph/0611148 [hep-ph]. (Cited on pages 17, 18, 19, and 21.)

[54] S. Drell and T.-M. Yan, *Massive Lepton Pair Production in Hadron-Hadron Collisions at High-Energies*, Phys.Rev.Lett. **25** (1970) 316–320. (Cited on page 17.)

[55] A. D. Martin, R. Roberts, W. J. Stirling, and R. Thorne, *Parton distributions and the LHC: W and Z production*, Eur.Phys.J. **C14** (2000) 133–145, arXiv:hep-ph/9907231 [hep-ph]. (Cited on page 20.)

[56] S. Camarda, R. Hanna, Y. Huang, S. Glazov, M. Boonekamp, N. Vranjes, J. Blanchard, V. Radescu, R. Strohmer, M. Schott, G. Siragusa, A. Dimitrievska, M. Karnevskiy, C. Zimmermann, N. Andari, O. Kivernyk, J. Cuth, and T.-H. Lin, *Studies of theoretical uncertainties on the measurement of the mass of the W boson at the LHC*, Tech. Rep. ATL-COM-PHYS-2014-875, CERN, Geneva, Jul, 2014. https://cds.cern.ch/record/1744695. (Cited on pages 22 and 88.)

[57] Lyndon Evans and Philip Bryant, *LHC Machine*, Journal of Instrumentation **3** no. 08, (2008) S08001. http://stacks.iop.org/1748-0221/3/i=08/a=S08001. (Cited on pages 25, 26, and 28.)

[58] O. S. Brüning, P. Collier, P. Lebrun, S. Myers, R. Ostojic, J. Poole, and P. Proudlock, *LHC Design Report*, vol. v.1 : the LHC Main Ring. CERN, Geneva, 2004. (Cited on page 25.)

[59] O. S. Brüning, P. Collier, P. Lebrun, S. Myers, R. Ostojic, J. Poole, and P. Proudlock, *LHC Design Report*, vol. v.2 : the LHC Infrastructure and General Services. CERN, Geneva, 2004. (Not cited.)

[60] M. Benedikt, P. Collier, V. Mertens, J. Poole, and K. Schindl, *LHC Design Report*, vol. v.3 : the LHC Injector Chain. CERN, Geneva, 2004. (Cited on page 25.)

[61] The ATLAS Collaboration, *The ATLAS Experiment at the CERN Large Hadron Collider*, Journal of Instrumentation **3** no. 08, (2008) S08003. http://stacks.iop.org/1748-0221/3/i=08/a=S08003. (Cited on pages 26, 33, and 39.)

[62] The CMS Collaboration, *The CMS experiment at the CERN LHC*, Journal of Instrumentation **3** no. 08, (2008) S08004. http://stacks.iop.org/1748-0221/3/i=08/a=S08004. (Cited on page 26.)

[63] The LHCb Collaboration, *The LHCb Detector at the LHC*, Journal of Instrumentation **3** no. 08, (2008) S08005. http://stacks.iop.org/1748-0221/3/i=08/a=S08005. (Cited on page 26.)

[64] The ALICE Collaboration, *The ALICE experiment at the CERN LHC*, Journal of Instrumentation **3** no. 08, (2008) S08002. http://stacks.iop.org/1748-0221/3/i=08/a=S08002. (Cited on page 26.)

[65] "The different interaction points of the lhc. the atlas detector is at point 1, alice at point 2, cms at point 5 and lhcb at point 8. the remaining points are strategic locations for technical purposes." http://te-epc-lpc.web.cern.ch/te-epc-lpc/machines/lhc/pagesources/LHC-Underground-Layout.png. Accessed: Feb 2015. (Cited on page 27.)

[66] "ATLAS Public Plots." https://twiki.cern.ch/twiki/bin/view/AtlasPublic/LuminosityPublicResults. (Cited on page 30.)

[67] M. Lamont, "The LHC's first long run." http://cerncourier.com/cws/article/cern/54381. (Cited on page 31.)

[68] "The ATLAS experiment." http://atlas.web.cern.ch/. Accessed: Feb 2015. (Cited on pages 34, 35, 36, 37, 40, 41, and 44.)

[69] W. Lampl, S. Laplace, D. Lelas, P. Loch, H. Ma, S. Menke, S. Rajagopalan, D. Rousseau, S. Snyder, and G. Unal, *Calorimeter Clustering Algorithms: Description and Performance*, Tech. Rep. ATL-LARG-PUB-2008-002. ATL-COM-LARG-2008-003, CERN, Geneva, Apr, 2008. (Cited on page 45.)

[70] ATLAS Collaboration, *ATLAS Calorimeter Performance - Technical Design Report*,. (Cited on page 45.)

[71] ATLAS Collaboration, *Performance of the ATLAS detector using first collision data*, J. High Energy Phys. **1009** (2010) 056, arXiv:1005.5254 [hep-ex]. (Cited on page 48.)

[72] S. Frixione, P. Nason, and C. Oleari, *Matching NLO QCD computations with Parton Shower simulations: the POWHEG method*, JHEP **0711** (2007) 070, arXiv:0709.2092 [hep-ph]. (Cited on pages 57, 80, 83, and 104.)

[73] H. Ma, "Correction for the eta width modulation in sampling 2 - egammaqweta2c.cxx." https://svnweb.cern.ch/cern/wsvn/atlasoff/Reconstruction/egamma/egammaCaloTools/trunk/src/egammaqweta2c.cxx. Accessed : February 2013. (Cited on page 61.)

[74] H. Ma, "Correction for the eta width modulation in sampling 2 - egammaqweta2c.h." https://svnweb.cern.ch/cern/wsvn/atlasoff/Reconstruction/egamma/egammaCaloTools/trunk/src/egammaqweta2c.h. Accessed : February 2013. (Cited on page 61.)

[75] R. Hanna, O. Kivernyk, C. Zimmermann, M. Boonekamp, M. Schott, N. Andari, N. Vranjes, J.-B. Blanchard, A. Dimitrievska, R. Stroehmer, G. Siragusa, C. Hays, M. Karnevskiy, and S. Camarda, *Measurement of m_W with 7 TeV data: W boson mass measurement*, Tech. Rep. ATL-COM-PHYS-2014-1569, CERN, Geneva, Dec, 2014. (Cited on page 67.)

[76] N. Vranjes, T. Petersen, and M. Karnevskiy, *Measurement of m_W at 7 TeV: Muon momentum corrections and uncertainties*, Tech. Rep. ATL-COM-PHYS-2014-1433, CERN, Geneva, Nov, 2014. (Cited on page 89.)

[77] M. Boonekamp and J.-B. Blanchard, *Measurement of m_W at 7 TeV: Electron energy corrections and uncertainties*, Tech. Rep. ATL-COM-PHYS-2014-1434, CERN, Geneva, Nov, 2014. (Cited on pages 75 and 76.)

[78] M. Schott, G. Siragusa, J. Cuth, and T.-h. Lin, *Measurement of m_W at 7 TeV: Reconstruction of the hadronic recoil*, Tech. Rep. ATL-COM-PHYS-2014-1435, CERN, Geneva, Nov, 2014. (Cited on page 77.)

[79] N. Andari, M. Boonekamp, R. Hanna, and S. Camarda, *Measurement of m_W at 7 TeV: Physics modeling*, Tech. Rep. ATL-COM-PHYS-2014-1436, CERN, Geneva, Nov, 2014. (Cited on pages 80, 81, 82, 84, and 85.)

[80] N. Andari, M. Boonekamp, J.-B. Blanchard, and N. Vranjes, *Measurement of m_W at 7 TeV: Z-based cross check measurements*, Tech. Rep. ATL-COM-PHYS-2014-1437, CERN, Geneva, Nov, 2014. (Not cited.)

[81] A. Dimitrievska, N. Vranjes, M. Schott, and M. Boonekamp, *Measurement of m_W at 7 TeV: Hadronic recoil corrections*, Tech. Rep. ATL-COM-PHYS-2015-344, CERN, Geneva, Apr, 2015. https://cds.cern.ch/record/2013274. (Cited on pages 67, 78, and 79.)

[82] G. Cowan, *Statistical Data Analysis*. Oxford University Press, 1998. (Cited on page 69.)

[83] ATLAS Collaboration, G. Aad et al., *Electron and photon energy calibration with the ATLAS detector using LHC Run 1 data*, Eur.Phys.J. **C74** no. 10, (2014) 3071, arXiv:1407.5063 [hep-ex]. (Cited on page 70.)

[84] J.-B. Blanchard, J.-B. de Vivie, and P. Mastrandrea, *In situ scales and smearings from Z and J/Ψ events*, Tech. Rep. ATL-COM-PHYS-2013-1653, CERN, Geneva, Dec, 2013. https://cds.cern.ch/record/1637533. (Cited on page 72.)

[85] ATLAS Collaboration, G. Aad et al., *Electron reconstruction and identification efficiency measurements with the ATLAS detector using the 2011 LHC proton-proton collision data*, Eur.Phys.J. **C74** no. 7, (2014) 2941, arXiv:1404.2240 [hep-ex]. (Cited on page 73.)

[86] E. Barberio, B. van Eijk, and Z. Was, *PHOTOS: A Universal Monte Carlo for QED radiative corrections in decays*, Comput.Phys.Commun. **66** (1991) 115–128. (Cited on pages 80, 94, and 104.)

[87] G. Nanava and Z. Was, *How to use SANC to improve the PHOTOS Monte Carlo simulation of bremsstrahlung in leptonic W boson decays*, Acta Phys.Polon. **B34** (2003) 4561–4570, arXiv:hep-ph/0303260 [hep-ph]. (Cited on page 81.)

[88] G. Nanava, Q. Xu, and Z. Was, *Matching NLO parton shower matrix element with exact phase space*, Eur.Phys.J. **C70** (2010) 673–688, arXiv:0906.4052 [hep-ph]. (Cited on page 81.)

[89] S. Catani, L. Cieri, G. Ferrera, D. de Florian, and M. Grazzini, *Vector boson production at hadron colliders: a fully exclusive QCD calculation at NNLO*, Phys.Rev.Lett. **103** (2009) 082001, arXiv:0903.2120 [hep-ph]. (Cited on page 83.)

[90] V. Büge, A. Ghezzi, C. Jung, M. Malberti, G. Quast, and T. T. de Fatis, *Prospects for the precision measurement of the W mass with the CMS detector at the LHC*, Journal of Physics G: Nuclear and Particle Physics **34** no. 5, (2007) N193. http://stacks.iop.org/0954-3899/34/i=5/a=N02. (Cited on page 83.)

[91] ATLAS Collaboration, N. Besson, M. Boonekamp, E. Klinkby, S. Mehlhase, and T. Petersen, *Re-evaluation of the LHC potential for the measurement of Mw*, Eur.Phys.J. **C57** (2008) 627–651, arXiv:0805.2093 [hep-ex]. (Cited on page 83.)

[92] G. Bozzi, J. Rojo, and A. Vicini, *The Impact of PDF uncertainties on the measurement of the W boson mass at the Tevatron and the LHC*, Phys.Rev. **D83** (2011) 113008, arXiv:1104.2056 [hep-ph]. (Cited on page 88.)

[93] J. Rojo and A. Vicini, *PDF uncertainties in the extraction of the W mass at LHC: a Snowmass Whitepaper*, arXiv:1309.1311 [hep-ph]. (Cited on page 88.)

[94] ALEPH, DELPHI, L3, OPAL, SLD, LEP Electroweak Working Group, SLD Electroweak Group, SLD Heavy Flavour Group Collaboration, S. Schael et al., *Precision electroweak measurements on the Z resonance*, Phys.Rept. **427** (2006) 257–454, arXiv:hep-ex/0509008 [hep-ex]. (Cited on page 88.)

[95] ATLAS Collaboration Collaboration, T. A. Collaboration, *Measurement of the Z/γ^* boson transverse momentum distribution in pp collisions at $\sqrt{s}$ = 7 TeV with the ATLAS detector*, arXiv:1406.3660 [hep-ex]. (Cited on pages 93, 94, 95, and 96.)

[96] S. Berge, P. M. Nadolsky, and F. I. Olness, *Heavy-flavor effects in soft gluon resummation for electroweak boson production at hadron colliders*, Phys. Rev. **D73** (2006) 013002, arXiv:hep-ph/0509023 [hep-ph]. (Cited on pages 94 and 95.)

[97] G. A. Ladinsky and C. P. Yuan, *The Nonperturbative regime in QCD resummation for gauge boson production at hadron colliders*, Phys. Rev. **D50** (1994) 4239, arXiv:hep-ph/9311341 [hep-ph]. (Not cited.)

[98] C. Balazs, J.-w. Qiu, and C. P. Yuan, *Effects of QCD resummation on distributions of leptons from the decay of electroweak vector bosons*, Phys. Lett. **B355** (1995) 548–554, arXiv:hep-ph/9505203 [hep-ph]. (Cited on pages 94 and 95.)

[99] *Measurement of angular correlations in Drell–Yan lepton pairs to probe boson transverse momentum at with the {ATLAS} detector*, Physics Letters B **720** no. 1–3, (2013) 32 – 51. http://www.sciencedirect.com/science/article/pii/S0370269313000956. (Cited on page 94.)

[100] A. Banfi, S. Redford, M. Vesterinen, P. Waller, and T. Wyatt, *Optimisation of variables for studying dilepton transverse momentum distributions at hadron colliders*, Eur.Phys.J. **C71** (2011) 1600, arXiv:1009.1580 [hep-ex]. (Cited on pages 93 and 94.)

[101] T. A. Collaboration, *Measurement of angular correlations in Drell–Yan lepton pairs to probe boson transverse momentum at with the ATLAS detector*, Physics Letters B **720** no. 1–3, (2013) 32 – 51. (Cited on page 95.)

[102] J. Pumplin, D. Stump, R. Brock, D. Casey, J. Huston, et al., *Uncertainties of predictions from parton distribution functions. 2. The Hessian method*, Phys.Rev. **D65** (2001) 014013, arXiv:hep-ph/0101032 [hep-ph]. (Cited on pages 97 and 131.)

[103] *Studies of theoretical uncertainties on the measurement of the mass of the W boson at the LHC*, Tech. Rep. ATL-PHYS-PUB-2014-015, CERN, Geneva, Oct, 2014. https://cds.cern.ch/record/1956455. (Cited on page 98.)

[104] T. A. collaboration, *Monitoring and data quality assessment of the ATLAS liquid argon calorimeter*, Journal of Instrumentation **9** no. 07, (2014) P07024. http://stacks.iop.org/1748-0221/9/i=07/a=P07024. (Cited on page 103.)

[105] S. Alioli, P. Nason, C. Oleari, and E. Re, *NLO vector-boson production matched with shower in POWHEG*, JHEP **0807** (2008) 060, arXiv:0805.4802 [hep-ph]. (Cited on page 104.)

[106] S. Frixione and B. R. Webber, *Matching NLO QCD computations and parton shower simulations*, JHEP **06** (2002) 029, arXiv:hep-ph/0204244 [hep-ph]. (Cited on page 104.)

[107] G. Corcella, I. Knowles, G. Marchesini, S. Moretti, K. Odagiri, et al., *HERWIG 6: An Event generator for hadron emission reactions with interfering gluons (including supersymmetric processes)*, JHEP **0101** (2001) 010, arXiv:hep-ph/0011363 [hep-ph]. (Cited on page 104.)

[108] J. M. Butterworth, J. R. Forshaw, and M. H. Seymour, *Multiparton interactions in photoproduction at HERA*, Z. Phys. **C72** (1996) 637–646, arXiv:hep-ph/9601371 [hep-ph]. (Cited on page 104.)

[109] *New ATLAS event generator tunes to 2010 data*, Tech. Rep. ATL-PHYS-PUB-2011-008, CERN, Geneva, Apr, 2011. https://cds.cern.ch/record/1345343. (Cited on page 104.)

[110] J. Allison, K. Amako, J. Apostolakis, H. Araujo, P. Dubois, et al., *Geant4 developments and applications*, IEEE Trans.Nucl.Sci. **53** (2006) 270. (Cited on page 104.)

[111] ATLAS Collaboration Collaboration, The ATLAS Collaboration, *Expected performance of the ATLAS experiment: detector, trigger and physics*,. (Cited on page 105.)

[112] ATLAS Collaboration Collaboration, The ATLAS Collaboration, *Measurement of the inclusive $W^{\pm}$ and Z/γ cross sections in the electron and muon decay channels in pp collisions at $\sqrt{s} = 7$ TeV with the ATLAS detector*, Phys.Rev. **D85** (2012) 072004, arXiv:1109.5141 [hep-ex]. (Cited on page 107.)

[113] ATLAS Collaboration Collaboration, The ATLAS Collaboration, *Measurement of the $W \to \tau\nu_\tau$ Cross Section in pp Collisions at $\sqrt{s} = 7$ TeV with the ATLAS experiment*, Phys. Lett. B **706** no. arXiv:1108.4101. CERN-PH-EP-2011-122, (2011) 276–294. 20 p. Comments: 8 pages (20 including author list), 10 figures, 4 tables, submitted to Phys. Lett. B. (Not cited.)

[114] ATLAS Collaboration Collaboration, The ATLAS Collaboration, *Measurement of the $Z \to \tau\tau$ Cross Section with the ATLAS Detector*, Phys. Rev. D **84** no. arXiv:1108.2016. CERN-PH-EP-2011-097, (2011) 112006. 28 p. Comments: 16 pages (28 including authorlist), 12 figures, 5 tables, submitted to Phys. Rev. D. (Not cited.)

[115] ATLAS Collaboration Collaboration, The ATLAS Collaboration, *Measurement of the top quark pair production cross-section with ATLAS in the single lepton channel*, Phys. Lett. B **711** no. arXiv:1201.1889. CERN-PH-EP-2011-201, (2012) 244–263. 20 p. Comments: 9 pages plus author list (20 pages total), 6 figures, 2 tables, submitted to Physics Letter B. (Cited on page 107.)

[116] J. Stelzer and the ATLAS collaboration, *The ATLAS High Level Trigger Configuration and Steering: Experience with the First 7 TeV Collision Data*, Journal of Physics: Conference Series **331** no. 2, (2011) 022026. http://stacks.iop.org/1742-6596/331/i=2/a=022026. (Cited on page 109.)

[117] W. Verkerke and D. Kirkby, *The RooFit toolkit for data modeling*, Tech. Rep. physics/0306116, SLAC, Stanford, CA, Jun, 2003. (Cited on page 116.)

[118] K. Bachas, M. Bellomo, F. Bührer, S. Camarda, A. Cooper-Sarkar, J. Dassoulas, R. S. Hickling, F. Ellinghaus, C. Issever, C. T. Jeske, D. Froidevaux, L. Iconomidou-Fayard, A. Glazov, T. Guillemin, A. Kapliy, M. Karnevskiy, M. Klein, U. Klein, J. Kretzschmar, T. Kono, A. Lewis, K. Lohwasser, M. Lisovyi, T. Matsushita, J. Maurer, P. Onyisi, E. Richter-Was, E. Rizvi, V. Radescu, P. Sommer, G. Sedov, T. Serre, A. Schaffer,

S. Schmitt, J. Sendler, M. Shochet, J. Tseng, M. Vincter, M. Wielers, and E. Yatsenko, *Measurement and QCD Analysis of Differential Inclusive W → ℓν and Z/gamma*→ ℓℓ ; ll Production and Leptonic Decay Cross Sections with ATLAS: Analysis STDM-2012-20: W and Z inclusive cross section with 2011 data*, Tech. Rep. ATL-COM-PHYS-2013-217, CERN, Geneva, Feb, 2012. https://cds.cern.ch/record/1517987. (Cited on page 118.)

ACKNOWLEDGEMENTS

The work done during the past three years wouldn't be what it is if it wasn't for the help, the support and the guidance of many people.

First of all, I would like to express my gratitude to my supervisor, Maarten. Thank you for your patience and your pertinent advices. You have always encouraged me to give the best I can, and never failed to explain all the physics topics in the most pedagogical way.

I also thank all the members of my jury, for accepting to review my work, Mr. Reza Ansari, Mr. Louis Fayard, Mr. Alessandro Vicini and particulary Ms. Manuella Vincter and Mr. Fabio Cossutti for taking the time to read, comment and evaluate the quality of my thesis.

Merci à Anne-Isabelle Etienvre, Georges Vasseur, et à toute l'administration du SPP pour l'aide que vous m'avez offerte. En particulier, Martine Oger et Béatrice Guyot, merci d'avoir toujours été patientes avec moi et de répondre à toutes mes demandes et questions administratives. Merci à l'Université Paris-Sud et l'ED517, en particulier à Messieurs Ansari et Khan.

Thanks to the CEA ATLAS team for welcoming me these three years, in Saclay and at CERN, and for always helping me knowingly and unknowingly. Thank you Rosy, Henri and Nenad for the good moments we shared in Building 40. Nathalie, thank you for waiting for me at Porte Nord and for going through all the administrative procedures with me in my first day at Saclay! Claude, Ahmimed, Andrea, Samira, Pierre-François, ... it was a pleasure being around you, thank you Laurent and Jean-François for validating the stereotype about physicists and how they love comics and zombie movies.

Merci Frédéric Déliot pour toute ton aide concernant les formalités auprès de l'ED. C'était aussi un plaisir de travailler avec toi au cours des MasterClasses, ainsi qu'avec Angèle Sene, Mylène Donnart-Barrail, Sophie Kerhoas-Cavata et Philippe Briet. Merci encore une fois à Sophie, Angèle et Philippe pour avoir couru avec moi lors de l'impression des manuscrits le jour de ma soutenance!

Vanina, merci d'avoir accepté d'être ma marraine malgré ton programme chargé, et d'avoir toujours été là (à l'autre côté du couloir!) quand j'avais besoin de conseil.

I should not forget the CERN people who helped me through my first year's task, namely Guillaume Unal, Christos Anastopoulos, Bruno Lenzi, Marco Delmastro, Leonardo Carminati and Kerstin Tackmann. Stefano, thank you for being patient with me during the writing of the pub note, and for all the advice and constructive comments you had for me!

A shout out for the youngsters of CEA: Jean-Baptiste, Sofia, Thibaut, Fabrice, Camilla, Dimitra, Homero, Joao, Oleg, Denys, Mathias, Romain, Marta, Anais, Laura, Maria, Alessandro and Aleksandra (even if you're not an authentic Saclayan), etc. etc. you made my stay in Saclay a really enjoyable one! I will never forget the great moments, lunches, coffees, and beers that we had! Maria, you still owe me a danish tiramisu, don't think I'll ever forget.

Another one for the youngsters of CERN: Quentin, Narei, Ludovica, Bruno, Ahmad, Mohammed, Yannis, I enjoyed every discussion and/or sip of coffee/beer I shared with you! Thank you!

The Lebanese Mafia of Saclay: here's to the laughs, the friendship, and the -bad- food we shared! Diana, Rawad, Charly, Maria, Josiane, Bakhos, Rita-Maria, Chirelle, Farah, Elias, Joelle, Reine, Karim, I'm so glad I met each one of you.

Jean-Baptiste and Nenad. The two persons I enjoyed annoying the most. You can never know how much your presence during these past years has been helpful to me. Nenad, sorry for always bugging you on Skype with my silly questions, you know how students can be. JB, thanks for all the help in debugging (sorry...), and for the macros and the music you shared with me :) but not the cups of coffee you spilled on my desk, I'm not gonna miss that.

Louis, merci pour ta bonne humeur continue. Ça m'a toujours fait plaisir de discuter avec toi (et ton appareil photo...). Tu m'as toujours traitée comme une de tes étudiantes et je t'en remercie. Tu as toujours une réponse à tout, et sinon tu fais tout pour la trouver. Merci infiniment pour ton support moral pendant les périodes difficiles de fin de thèse.

Oleg and Aleksandra, thank you for putting up with all my mood swings, especially in the last months! I admire your patience and your kind heart. Thanks as well for all the help/macros/plots you shared with me. I enjoyed working with you! Cyril, je n'oublierai jamais les moments de complicité qu'on a partagés (contre Nancy évidemment), ni la course au manuscrit et aux slides! Vagelis, j'espère qu'on aura l'occasion de revivre les moments inoubliables de Corfou!

Margaux, tu étais toujours un grand soutien pour moi. Merci d'avoir été à l'écoute et toujours de bon conseil. Je n'oublierai jamais les moments de convivialité avec Damien, ni les week-ends, ni les gâteaux ;)

Gilbert -The Muscled Man- El-Hajje, que ferais-je sans tes muscles? Mes valises et mes meubles te disent merci. Merci également pour ta disponibilité aux moments de déprime. Courage pour ta dernière année!

Merci à Fouzia, qui s'est occupée de moi ces derniers mois, ne serait-ce qu'avec quelques mots d'encouragement, tu ne sais pas à quel point ça m'a aidée de voir ton sourire et ta bonne humeur chaque jour!

Merci à celles qui ont failli m'étrangler tellement j'étais chiante (ie. Mira et Pascale). Je vous adore, et j'apprécie tout le support moral malgré les distances. Merci également à Mokhtar, dont la présence et l'encouragement m'ont toujours remonté le moral :) je te remercie pour les moments agréables qui m'ont beaucoup aidée à surmonter mon stress!

Merci à Barbara et Nicolas, Lamia et Melhem, Nadia et Sleiman, Louisa et Michel, pour m'avoir offert un "chez moi" en France et en Suisse.

I must not forget the Levanoooo team! Carol, Maya, Rozi, Rania, Lina, and my baby Reine, I adore you, to the moon and back! Maya and Georges, the only word that comes to my mind when I think about thanking you is "woof!"... I wonder why...

Le plus grand merci à la personne qui est devenue une super amie en un temps record! Nancy (NANSI), je ne trouve pas les mots. Si je commence à citer ce que tu as fait pour moi, je ne finirai jamais. Tout simplement, merci d'exister, je t'adore.

Last but not least, papa, maman, Tony et Roland, vous êtes ma joie de vivre. Je ne serai pas ici sans votre soutien et votre encouragement. Merci à Mimo, Lello, Johnny, Mirna et Rocky pour le support, les prières et les câlins. Thank you Teta Souad, 3amto, 3ammi 1, 3ammi 2, as well as May, Najjouta and "Salim El Tawfi" for loving and encouraging me. I love you all.

Vicky et Béchara, je pense à vous tous les jours.